SOME STUDIES ON EFFECTS OF HEAT TREATMENT AND HYDROGEN EMBRITTLEMENT IN P92 STEEL WELDS

Ph.D. THESIS

by

Nitin Saini

DEPARTMENT OF MECHANICAL AND INDUSTRIAL ENGINEERING
INDIAN INSTITUTE OF TECHNOLOGY ROORKEE
ROORKEE-247667 (INDIA)
November, 2019

SOME STUDIES ON EFFECTS OF HEAT TREATMENT AND HYDROGEN EMBRITTLEMENT IN P92 STEEL WELDS

A THESIS

Submitted in partial fulfilment of the
requirements for the award of the degree

of

DOCTOR OF PHILOSOPHY

in

MECHANICAL ENGINEERING

by

Nitin Saini

DEPARTMENT OF MECHANICAL AND INDUSTRIAL ENGINEERING
INDIAN INSTITUTE OF TECHNOLOGY ROORKEE
ROORKEE-247667 (INDIA)
November, 2019


भारतीय प्रौद्योगिकी संस्थान रुड़की
INDIAN INSTITUTE OF TECHNOLOGY ROORKEE

INDIAN INSTITUTE OF TECHNOLOGY ROORKEE

STUDENT'S DECLARATION

I hereby certify that the work presented in the thesis entitled "**SOME STUDIES ON EFFECTS OF HEAT TREATMENT AND HYDROGEN EMBRITTLEMENT IN P92 STEEL WELDS**" is my own work carried out during a period from December, 2015 to November, 2019 under the supervision of Dr. Rahul S. Mulik, Associate Professor, Department of Mechanical and Industrial Engineering, Indian Institute of Technology, Roorkee and Dr. Manas Mohan Mahapatra, Associate Professor, School of Mechanical Sciences, Indian Institute of Technology, Bhubaneswar.

The matter presented in the thesis has not been submitted for the award of any other degree of this or any other Institute.

Dated: ____________ **(Nitin Saini)**

SUPERVISOR'S DECLARATION

This is to certify that the above mentioned work is carried out under our supervision.

M. M. Mahapatra

Dated: ____________ **(Rahul S. Mulik)** **(M. M. Mahapatra)**

The Ph.D. Viva-Voce Examination of **Nitin Saini,** Research Scholar, has been held on ……………….

Chairman, DRC **Signature of External Examiner**

This is to certify that the student has made all the corrections in the thesis.

M. M. Mahapatra

Signature of Supervisor(s) **Head of the Department**

ABSTRACT

The Creep strength enhanced ferritic (CSEF) steels are developed to meet the demand by power generation organizations to increase efficiency by operating at higher temperature and pressure. The microstructural evolution and mechanical properties of CSEF steels are affected by various parameters; normalizing temperature is one of them. Grade P92 steel is considered as a candidate material for thermal and nuclear power plants operations at temperatures of up to 650 °C. In the present work, the effect of normalizing temperature on the microstructural evolution and mechanical properties of cast and forged (C&F) P92 steel was carried out. The C&F P92 steel was subjected to various normalizing temperatures (950 °C - 1150 °C) and followed by a fixed tempering temperature (760 ^{o}C). Considering observation for the optimum combination of strength, ductility, and toughness, the normalizing at 1050 ^{o}C and tempering at 760 ^{o}C has been suggested for C&F P92 steel.

The Laves phase evolution (at 650° C) with varying aging time (upto 3000 hours) in P92 steel have been performed and their effect on mechanical properties have been investigated. The strength and ductility decreased as a result of deprivation of solid solution strengthening and formation of Laves phase. The hardness of P92 steel was also affected by aging time but less pronounced as compared to strength. Charpy toughness was also reduced continuously with increase in aging time as a result of thermal straining of particles and Laves phase formation.

In the other work, the formation of Laves phase during aging in P92 steel and an effort to dissolve Laves phase using re-austenitization and tempering treatment was carried out. The as-received material is exposed to 620 ^{o}C for 4560 hrs. After aging, the specimens are subjected to austenitization at 1050 ^{o}C for 1 hr and followed by tempering at 760 ^{o}C for different times (2 hrs and 4 hrs). After re-austenitization and tempering, the dissolution of Laves phase is observed. A model is also suggested to quantify the dissolution of W containing Laves phase. Thermo Calc is used to predict driving forces for precipitation of Laves and $M_{23}C_6$ phases. The predicted driving force map shows that the nucleation and dissolution of Laves phase can be controlled at different temperatures for varying composition of the steel.

The double austenitization based normalizing and tempering (DNT) heat treatments have been performed and their effect on tensile behavior and microstructural morphology of P92 steel have been carried out and compared with conventional normalizing and tempering (CNT) heat treatment. The CNT treatment deals with the normalizing at 1040 ^{o}C/60 min followed by air cooling and tempering at 760 ^{o}C/120 min, followed by the air cooling. The

DNT treatment deals with the initial austenitizing in the temperature range of 950-1150 ^{o}C for 60 min followed by the water quenching and second austenitizing was performed at the 1040 ^{o}C for 60 min followed by the air cooling. After the double austenitization based normalizing, tempering was performed at 760 ^{o}C for 2 h followed by the air cooling. The fine grain structure was obtained for the DNT 3 treatment. The results of tensile tests were also obtained to be superior for the DNT treatment as compared to CNT treatment.

The effect of preheating on the weld bead geometry have been performed in autogenous gas tungsten arc welding (GTAW) and a relation between preheat temperature and thickness of welded plate using Rosenthal 2-D heat equation have been developed for thin plates. The effect of cooling rate on the retention of δ-ferrite was also studied in P92 steel welds. The full penetration was achieved with preheat temperature of 300 ^{o}C. A relation between preheat temperature and plate thickness was correctly predicted and a good correlation was found with our experimental data. The volume fraction of δ-ferrite was measured lowest with highest preheat temperature (300 ^{o}C) or lowest cooling rate.

The dissolution of δ-ferrite in the weld fusion zone using post-weld normalizing and tempering (PWNT) have been investigated and their effect on mechanical properties have also been performed. The autogenous GTAW was used to prepare double-sided welded joints of P92 steel. After welding, post-weld heat treatment (PWHT) at 760 ^{o}C for 2 hrs and post-weld normalizing at 1050 ^{o}C for 1 hr followed by tempering at 760 ^{o}C for 2 hrs were performed. The morphology, composition, structure and hardness of δ-ferrite are verified. In as-welded and PWHT conditions, the retention of δ-ferrite was observed while the dissolution of δ-ferrite was confirmed after PWNT. Dissolution kinetics of δ-ferrite is quantified using Thermo-Calc for Scheil's solidification calculation and DICTRA for calculating diffusion coefficients of Cr and W at 1050 ^{o}C in austenite.

In the other work, P92 steel weld joints were prepared using multi-pass shielded metal arc welding (SMAW) process using E911 and P92 filler. A comparative study was performed on microstructural evolution, tensile strength, microhardness and Charpy toughness across the P92 steel weldments in as-welded and PWHT condition. In as-welded condition, transverse tensile specimens were fractured from the fine grain heat affected zone or inter-critical heat affected zone (FGHAZ/ICHAZ) and after PWHT, the fracture location was shifted to over tempered base metal from FGHAZ/ICHAZ. The minimum required Charpy toughness of 47 J (EN1557: 1997) was achieved after the PWHT for both E911 and P92 filler.

The effect of PWHT and PWNT on mechanical properties of dissimilar SMAW welded joint of P911 and P92 steel using P911 filler have been performed. PWHT of weldments resulted in a negligible increase in ultimate tensile strength and yield strength while a significant change was measured after PWNT. The PWNT resulted in minimum hardness gradient and maximum homogenization of microstructure across the dissimilar weldments. The room temperature Charpy toughness value was also found to be maximum for PWNT treatment. In other work, P91 and P92 dissimilar multi-pass SMAW welded joints have been produced using the different filler rods. The microstructure of the welded joint has been studied for the different filler composition in various heat treatment condition. The room temperature Charpy impact toughness and tensile properties for the different welded joints (different filler) have been also studied and related with the microstructure of the welded joint. From the results, it has been concluded that a higher amount of ferrite stabilizer in P92 filler promotes the formation of the δ ferrite in the weld fusion zone.

Granjon implant test and mercury method (for diffusible hydrogen measurement) have been performed on Grade P92 steel welded specimens to study the effect of welding parameters as well as filler conditions on diffusible hydrogen levels and their subsequent effect on hydrogen-assisted cracking (HAC). The three different welding conditions and three different filler conditions are used to measure the diffusible hydrogen level in the deposited metal. Granjon implant test was performed to evaluate HAZ-HAC susceptibility with similar welding conditions which were used in the mercury method. Lower critical stress (LCS) was also evaluated using Granjon implant test. The higher susceptibility of P92 steel welded plate towards HAZ-HAC was observed in case of lower heat input or higher diffusible hydrogen content. However, by considering LCS, fracture mode, embrittlement index, and diffusible hydrogen content, the weld deposited using highest heat input offers great resistance to HAZ HAC. The P92 steel plate welded by the contaminated electrode with a high level of diffusible hydrogen was found to be more susceptible to HAC.

भारतीय प्रौद्योगिकी संस्थान रुड़की
INDIAN INSTITUTE OF TECHNOLOGY ROORKEE

ACKNOWLEDGEMENTS

This thesis symbolizes an important milestone in the journey of my life. Firstly, I would like to express my sincere gratitude and respect to my supervisor(s) *Dr. Rahul S.Mulik and Dr. M. M. Mahapatra* for their invaluable guidance, unlimited continuous support, constructive criticism and thought provoking discussions throughout the course of work and made this thesis possible. They have been a constant source of encouragement, inspiration, and motivation to me. Their in-depth knowledge of the subject and wealth of experience steered me to complete the work. I am immensely benefited by their devotion to the research, ability to see things that are not obvious and their perseverance to pursue creative leads in research. Besides being a source of immense knowledge and experience, they are very kind and caring with great compassion and love for the students. I could not have imagined having better advisors and mentors for my Ph.D. work. I will forever cherish my close association with him.

I take the opportunity to thank *Prof. B. K. Gandhi*, Head and *Prof. Navneet Arora* (Chairman DRC), Department of Mechanical and Industrial Engineering, Indian Institute of Technology Roorkee for providing the basic infrastructural facilities for carrying out this research work.

I am very thankful to my SRC members; *Prof. D. K. Dwivedi* (Chairman), *Dr. P.K. Jha* (Internal expert, MIED), *Dr. G. P. Chodhari* (External expert, MMED) for their constructive criticism and valuable guidance during the course of presentations. I wish to express my sincere thanks to all faculty members of the Department of Mechanical and Industrial Engineering, I.I.T. Roorkee. I am thankful to staff members, *Mr. S.M. Mishra, Mr. D.K. Kapil, Mr. Pardeep Kumar* and *Mr. Subodh Kumar* for providing me essential aids to complete my experiments.

I am thankful to my co-researchers at IITR, *Dr. Chandan Pandey, Mr. Jayant Thakre, Mr. Rajneesh, Mr. Ankur, Mr. Anup Kulkarni, Mr. Rohit Kumar, Mr. Naveen Kumar, Mr. Vineet Yadav, Mr. Rajeev Rana,* who were always there to lend a helping hand when it mattered most and for the camaraderie that took away all the pressures and made research work more enjoyable.

I am thankful to my friends for their company and for the quality time that I spent with them. I am thankful to everyone who helped me directly or indirectly to complete this work.

I would also like to express my sentiments for my family for their unconditional support, love and encouragement. I am indebted to my parents, *Mr. Sushil Saini, Mrs Babli Devi,* for their blessings, motivation and constant support throughout this period. I am thankful to my brother, *Sachin Saini* and my sister-in law *Preeti Saini* for providing me moral support and taking care of many social responsibilities, which helped me to focus on my work all the time.

I am also grateful to God, the almighty, for having blessed me to rise and take up this challenge.

(Nitin Saini)

CONTENTS

CANDIDATE'S DECLARATION i

ABSTRACT v

ACKNOWLEDGEMENTS ix

LIST OF FIGURES xvii

LIST OF TABLES xxv

ABBREVIATIONS xxvii

CHAPTER 1. INTRODUCTION 1

- 1.1 Organization of thesis 2

CHAPTER 2. LITRATURE REVIEW 5

- 2.1 Development of CSEF steels 5
- 2.2 Role of alloying elements in P92 steel 8
  - 2.2.1 Ferrite stabilizers 9
  - 2.2.2 Strong Carbide and nitride formers 9
  - 2.2.3 Austenite stabilizers 10
  - 2.2.4 Other alloying elements 10
- 2.3 Various phases formed in P92 steel 10
- 2.4 Precipitates morphology 11
  - 2.4.1 $M_{23}C_6$ 12
  - 2.4.2 Laves phase 12
  - 2.4.3 MX phase 13
  - 2.4.4 Z-phase 14
- 2.5 Heat treatments of P92 steel 14
  - 2.5.1 Effect of heat treatments on mechanical properties 14
    - 2.5.1.1 Conventional normalizing and tempering 14
    - 2.5.1.2 Double austenitization based normalizing and tempering 15
  - 2.5.2 Effect of long-term aging on mechanical properties 17
- 2.6 Weldability of P92 steel 19
  - 2.6.1 Retention of δ-ferrite 19
  - 2.6.2 Heterogeneity and depletion of Cr in the weldments 22
  - 2.6.3 Hydrogen embrittlement 25

2.7 Research gap 26
2.8 Objective 27
CHAPTER 3. HEAT TREATMENT OF GRADE P92 STEEL 29
3.1 Experimental details 29
3.1.1 As-received material 29
3.1.2 Heat treatments 29
3.1.2.1 Optimization of normalizing temperature 29
3.1.2.2 Long-term ageing 30
3.1.2.3 Effect of normalizing and tempering on dissolution of Laves phase 30
3.1.2.4 Double austenitization treatment 30
3.1.3 Material characterization 31
3.1.4 Material testing 31
3.2 Results and discussion 32
3.2.1 As-received material 32
3.2.2 Optimization of normalizing temperature 33
3.2.2.1 Microstructure evolution 33
3.2.2.2 Mechanical properties 40
3.2.2.3 Fracture surface morphology 44
3.2.3 Effect of long-term ageing 50
3.2.3.1 Material in normalized and tempered condition (as-received) 50
3.2.3.2 Effect of thermal ageing on grain size 50
3.2.3.3 Ageing effect on microstructure evolution and precipitate size 52
3.2.3.4 Laves phase characterization 57
3.2.3.5 XRD analysis and phase determination 59
3.2.3.6 Room temperature tensile properties 60
3.2.3.7 Fracture surface analysis 62
3.2.3.8 Microhardness and Charpy toughness 63
3.2.4 Effect of normalizing and tempering on the dissolution of Laves phase 64
3.2.4.1 Effect of normalizing and tempering on grain size 65
3.2.4.2 Effect of long-term aging on the nucleation of Laves phase and the effect of N&T on the evanesce of Laves phase 66
3.2.4.3 Effect of aging and N&T on the fraction of Laves phase 70
3.2.4.4 Effect of aging and N&T on precipitate size 73
3.2.4.5 Dissolution of Laves phase 76

3.2.5 Effect of double austenitization on the microstructural evolution and mechanical properties 82

3.2.5.1 Effect of conventional normalizing and tempering treatment on microstructure evolution 82

3.2.5.2 Effect of different heat treatments on mechanical properties 88

3.2.5.3 Effect of conventional normalizing and tempering on microstructure evolution 90

3.3 Conclusions 92

CHAPTER 4. SIMILAR WELDED JOINTS OF P92 STEEL 93

4.1 Experimental procedure 93

4.1.1 As-received material 93

4.1.2 Optimization of preheating temperature and prediction of preheating temperature for thin plates in autogenous TIG welds by using Rosenthal equation 94

4.1.2.1 Optimization of preheating temperature 94

4.1.2.2 Prediction of preheating temperature for thin plates using Rosenthal equation 95

4.1.3 Dissolution of δ-ferrite using post-weld heat treatments 95

4.1.4 Effect of different filler on microstructure evolution and mechanical properties of SMAW welded joints of P92 steel 96

4.1.5 Material characterization and testing 98

4.2 Results and discussion 99

4.2.1 As-received material 99

4.2.2 Optimization of preheating temperature and prediction of preheating temperature for thin plates in autogenous TIG welds by using Rosenthal equation 100

4.2.2.1 Effect of preheating temperature on weld bead geometry 100

4.2.2.2 Prediction of preheating temperature for thin plates by using Rosenthal equation 103

4.2.2.3 Effect of cooling rates on retained δ-ferrite 105

4.2.3 Dissolution of δ-ferrite using post-weld normalizing and tempering 108

4.2.4 Effect of different filler compositions on the microstructure evolution and mechanical properties of SMAW welded joints of P92 steel 120

4.2.4.1 Microstructure evolution in as-welded condition 120

4.2.4.2 Microstructure evolution of weldments after PWHT 122

4.2.4.3 Effect of fillers on tensile strength of welded joints 124

4.2.4.4 Effect of fillers on harness and Charpy toughness of welded joints 130

4.3 Conclusions 133

CHAPTER 5. DISSIMILAR WELDED JOINTS OF P92 STEEL 135

5.1 Experimental procedure 135

5.1.1 As-received material 135

5.1.2 Effect of post-weld heat treatments on the microstructure evolution and mechanical properties of dissimilar SMAW welded joints of P911 and P92 steel using P911 filler 136

5.1.3 Effect of filler compositions on mechanical properties of dissimilar SMAW welded joints of P91 and P92 steel 137

5.1.4 Material characterization and testing 138

5.2 Results and discussion 139

5.2.1 As-received material 139

5.2.2 Effect of post-weld heat treatments on the microstructure evolution and mechanical properties of dissimilar SMAW welded joints of P911 and P92 steel using P911 filler 141

5.2.2.1 Microstructure evolution in the weldments 141

5.2.2.2 Mechanical properties of weld fusion zone 147

5.2.3 Effect of filler compositions on mechanical properties of dissimilar SMAW welded joints of P91 and P92 steel 153

5.2.3.1 Microstructure evolution in the weldments 153

5.2.3.2 Mechanical properties of weldments 160

5.3 Conclusions 163

CHAPTER 6. HYDROGEN EMBRITTLEMENT OF P92 STEEL 165

6.1 Experimental procedure 165

6.1.1 Base Material and weld consumable 165

6.1.2 Process variations 165

6.1.2.1 Effect of filler conditions on diffusible hydrogen content 165

6.1.2.2 Welding process parameters 166

6.1.3 Mercury method 166

6.1.4 Granjon Implant test 168

6.1.5 Material characterization and testing 170

6.2 Results and discussion 170

6.2.1 Effect of electrode conditions on diffusible hydrogen content and their effect on embrittlement of P92 steel 170

6.2.1.1 Diffusible hydrogen measurement 170

6.2.1.2 Granjon implant test 171

6.2.2 Effect of welding conditions on diffusible hydrogen content and their effect on embrittlement of P92 steel 177

6.2.2.1 Diffusible hydrogen measurement 177

6.2.2.2 Granjon implant test 178
6.3 Conclusions 183
CHAPTER 7. CONCLUSIONS AND FUTURE SCOPE 185
7.1 Conclusions 185
7.2 Scope of future research work 192
LIST OF PUBLICATIONS 193
REFERENCES 195

भारतीय प्रौद्योगिकी संस्थान रुड़की
INDIAN INSTITUTE OF TECHNOLOGY ROORKEE

LIST OF FIGURES

Figure Caption **Page No.**

Figure 2.1 Development of ferritic and martensitic boiler steels based on their increased creep resistance from 35 MPa to 140 MPa over 10^5 hours at 600°C (Ennis and Czyrska-Filemonowicz, 2003) 6
Figure 2.2 Maximum service temperatures of CSEF steels for 100 MPa of average stress rupture strength over 10^5 hrs (Ennis and Czyrska-Filemonowicz, 2003) 7
Figure 2.3 (a) and (b) Equilibrium phases as a function of temperature for P92 steel calculated by Thermo-Calc 11
Figure 2.4 Driving force with respect to temperature for Laves phase precipitation simulated using Thermo-Calc 13
Figure 2.5 Schematic evolution of microstructure in P92 steel during CNT process 15
Figure 2.6 Schematic evolution of Laves phase (Wang et al., 2019) 17
Figure 2.7 (a) Scheil's solidification calculation and (b) isopleth of P92 steel calculated using Thermo-Calc 19
Figure 2.8 schematic showing retension of δ-ferrite (Liu et al., 2011). 22
Figure 2.9 Schematic of the subzones formed in the weldments and equilibrium phase diagram of P92 steel (C. Pandey et al., 2018) 23
Figure 2.10 Schematic showing various factors influencing HAC 26
Figure 3.1 As-received microstructure of P92 steel: (a) SEM at 5000x, (b) SEM at 50000x, (c) EDS in the matrix region as point-1, (d) EDS of precipitates present at PAGB as point-2, (e) EDS of precipitates located inside the matrix as point-3 32
Figure 3.2 (a) Secondary electron micrograph of sample normalized at 950 °C, (b) EDS in the matrix area (point 1), (c) EDS in the matrix (point 2), (d) EDS at PAGB (point 3) and (e) micrograph of sample normalized at 1150 °C 34
Figure 3.3 Optical micrographs of sample after N&T treatment: (a) 950 °C/760 °C (b) 1000 °C/760 °C, (c) 1050 °C/760 °C (d) 1100 °C/760 °C and (e) 1150 °C/760 °C 35
Figure 3.4 Variation in grain size with normalizing temperature 36
Figure 3.5 Micrographs of samples subjected to different N&T treatment: (a) 950 °C/760 °C (b) 1000 °C/760 °C, (c) 1050 °C/760 °C (d) 1100 °C/760 °C and (e) 1150 °C/760 °C 37
Figure 3.6 (a) SEM image of N&T sample (normalize at 950 °C; tempered at 760 °C) (b) EDS of white particles located at the PAGB (point 1) (c) EDS of selected area in the matrix (point 2) 38
Figure 3.7 Variation of Cr/Fe ratio with normalizing temperature 38
Figure 3.8 Variation of particle size present at the grain boundary and in the matrix region with varying normalizing temperature and fixed tempering temperature of 760 °C 39
Figure 3.9 (a) Variation in inter particle spacing and (b) variation of area fraction of precipitates with varying normalizing temperature and fixed tempering temperature 40
Figure 3.10 Engineering stress-strain curve for (a) normalized and (b) normalized and tempered specimen 41
Figure 3.11 Variation in Charpy toughness and grain size with normalizing temperature 42
Figure 3.12 Diffractogram for normalizing and tempering treatment at 950 °C/760 °C 43

Figure 3.13 Fracture surface morphology of tensile specimens (a) N at 950 °C, (b) N at 1000 °C, (c) N at 1050 °C,(d) N at 1100 °C and (e) N at 1150 °C 44
Figure 3.14 Fracture surface morphology of tensile specimens (a) As-received material, (b) EDX of as-received fracture surface, (c) N&T at 950 °C/760 °C,(d) N&T at 1000 °C/760 °C, (e) N&T at 1050 °C/760 °C, (f) N&T at 1100 °C/760 °C and (g) N&T at 1150 °C/760 °C......46
Figure 3.15 Fracture surface morphology of impact Charpy test of (a) N at 950 °C, (b) N at 1000 °C, (c) N at 1050 °C,(d) N at 1100 °C and (e) N at 1150 °C 48
Figure 3.16 Fracture surface morphology of impact Charpy test of (a) As-received material, (b) N&T at 950 °C/760 °C,(c) N&T at 1000 °C/760 °C, (d) N&T at 1050 °C/760 °C, (e) N&T at 1100 °C/760 °C and (f) N&T at 1150 °C/760 °C 49
Figure 3.17 Micrographs of N&T P92 steel at (a) lower and (b) higher magnification 50
Figure 3.18 Optical micrographs in various ageing conditions (a) as-received, (b) 720 hrs, (c) 1440 hrs, (d) 2160 hrs, (e) 3000 hrs and (f) variation in grain size with ageing time.................51
Figure 3.19 SEMs of P92 steel at lower magnification for various ageing conditions (a) as-received state, (b) 720 hrs, (c) 1440 hrs, (d) 2160 hrs and (e) 3000 hrs 52
Figure 3.20 Line mapping results for aging duration of (a) as-received, (b) 720 hrs and (c) 3000 hrs..53
Figure 3.21 SEMs of P92 steel at higher magnification for various ageing conditions (a) as-received state, (b) 720 hrs, (c) 1440 hrs, (d) 2160 hrs and (e) 3000 hrs 55
Figure 3.22 Effect of ageing time on (a) fraction area of precipitates and (b) precipitates size .56
Figure 3.23 EDS of particles present at PAGBs for ageing duration of (a) as-received, (b) 720 hrs, (c) 1440 hrs, (d) 2160 hrs, (e) 3000 hrs and (f) variation in Mo/Fe and W/Fe ratio with ageing time at 650 ^{o}C 57
Figure 3.24 Elemental mapping of P92 steel (a) as-received condition, (b) after ageing at 720 hrs, (c) after ageing at 3000 hrs...58
Figure 3.25 (a) Mixed microstructure after thermal ageing of 3000 h, (b) line mapping of the precipitates, (c) EDS spectra of the area 1, (d), (e), (f) and (g) area maps for elements Cr, Fe, W, and Mo, respectively 59
Figure 3.26 Diffractogram of P92 steel in as-received and aging condition 60
Figure 3.27 (a) Engineering stress-strain curve for various aged specimens, (b) variation of yield and ultimate tensile strength and (c) variation of % elongation and % reduction in area for various ageing time 61
Figure 3.28 Fracture surface morphology of tensile tested specimens after different ageing conditions (a) as-received, (b) 720 hrs, (c) 1440 hrs, (d) 2160 hrs and (e) 3000 hrs 63
Figure 3.29 (a) Variation in hardness and (b) variation in Charpy toughness with ageing time 64
Figure 3.30 Optical micrograph of (a) as-received P92 steel, (b) Aged at 620 ^{o}C for 4560 hrs, (c) Aged + normalized at 1040 ^{o}C for 1 hr + tempered ^{o}C at 760 ^{o}C for 2 hrs and (d) Aged + normalized at 1040 ^{o}C for 1 hr + tempered ^{o}C at 760 ^{o}C for 4 hrs 65
Figure 3.31 (a) Variation in grain size and (b) variation in microhardness for different heat treatment conditions 66
Figure 3.32 Secondary electron micrographs (SEMs) of (a) as-received P92 steel, (b) Aged at 620 ^{o}C for 4560 hrs, (c) Aged + normalized at 1040 ^{o}C for 1 hr + tempered ^{o}C at 760 ^{o}C for 2 hrs and (d) Aged + normalized at 1040 ^{o}C for 1 hr + tempered ^{o}C at 760 ^{o}C for 4 hrs.............67

Figure 3.33 (a) SEM of aged specimen at 620 ^{o}C for 4560 hrs, (b) line scans for different elements at point 1 and (c) line scans for different elements at point 2 68
Figure 3.34 (a) SEM of specimen (Aged + normalized at 1040 ^{o}C for 1 hr + tempered ^{o}C at 760 ^{o}C for 4 hrs), (b) and (c) line scans for different elements at point 1 and point 2 68
Figure 3.35 Mapping of precipitates present in (a) as-received P92 steel, (b) Aged at 620 ^{o}C for 4560 hrs and (c) Aged + normalized at 1040 ^{o}C for 1 hr + tempered ^{o}C at 760 ^{o}C for 4 hrs...... 69
Figure 3.36 XRD profiles after Rietveld refinement for the: (a) & (b) as-received, (c) & (d) Aged and (e) & (f) Aged+N&T4 71
Figure 3.37 XRD peaks of NaCl structure of $Cr_{23}C_6$ and hexagonal structure of Laves phase (a) Aging and (b) Aging+N&T4 72
Figure 3.38 EBSD phase map of P92 steel (a) 1% Laves phase (Fe_2W+Fe_2Mo) in Aged and (b) no Laves phase in Aged+N&T4 condition 73
Figure 3.39 SEM of (a) as-received P92 steel, (b) Aged at 620 ^{o}C for 4560 hrs and (c) Aged + normalized at 1040 ^{o}C for 1 hr + tempered ^{o}C at 760 ^{o}C for 4 hrs.. 74
Figure 3.40 Particle size of Laves phase and $M_{23}C_6$ precipitates measured from SEM images (a) as-received P92 steel, (b) Aged at 620 ^{o}C for 4560 hrs and (c) Aged + normalized at 1040 ^{o}C for 1 hr + tempered ^{o}C at 760 ^{o}C for 4 hrs 75
Figure 3.41 Mole fraction of phases as a function of temperature calculated using Thermo-Calc for the temperature range of 500-1200 ^{o}C 76
Figure 3.42 Mass fraction of elements in a phase with temperature calculated using Thermo-calc for: (a) $M_{23}C_6$ and (b) Laves phase 77
Figure 3.43 Schematic evolution of microstructure and precipitates during aging followed by normalizing and tempering process 78
Figure 3.44 Schematic for modeling the dissolution of a spherical particle, and (b) calculated particle radius of Laves phase as a function of time.. 79
Figure 3.45 Driving force for precipitation simulated using Thermo-Calc at 620 ^{o}C for (a) $M_{23}C_6$ with varying mass percent of Cr & Mn and (b) Laves Phase with varying mass percent of W and Mo 80
Figure 3.46 Driving force with respect to temperature for Laves phase precipitation simulated using Thermo-Calc 81
Figure 3.47 Driving force for Laves phase precipitation simulated using Thermo-Calc at 620 ^{o}C and 700 ^{o}C (a) for varying mass percent of W and (b) for varying mass percent of Mo 81
Figure 3.48 Typical micrograph of P92 steel after the conventional normalizing and tempering treatment (a) optical micrograph at 500x, (b) SEM micrograph at 1000x, (c) SEM micrograph at 10000x and (d) SEM micrograph at 50000x.. 83
Figure 3.49 (a) Processed image and (b) variation in particle size.. 84
Figure 3.50 Optical micrograph of P92 steel in (a) DNT 1, (b) DNT 2 and (c) DNT 3 condition 85
Figure 3.51 Secondary electron micrograph of P92 steel in (a) CNT, (b) DNT 1, (c) DNT 2 and (d) DNT 3 condition 86
Figure 3.52 Higher magnification micrograph for the CNT and DNT 2 treatment (a) and (b), respectively; EDS of white particles present at the triple point for (c) CNT and (d) DNT 2 condition 87
Figure 3.53 Engineering stress-strain curve for different heat treatments.................................. 88

Figure 3.54 (a) Variation in ultimate tensile strength and % elongation and (b) variation in hardness for varying heat treatments ... 89
Figure 3.55 Top view and detailed view of the tensile tested fracture specimen, (a) and (b) CNT, (c) and (d) DNT 1, (e) and (f) DNT 2, (g) and (h) DNT 3 ... 91
Figure 4.1 Two-dimensional heat flow during welding of thin sheets (Kou, 2002) ... 95
Figure 4.2 (a) Schematic of groove design, (b) schematic of the weld passes and (c) complete weld joints ... 97
Figure 4.3 Schematic of the welded plate showing locations and dimensions of Charpy toughness and tensile test specimens ... 98
Figure 4.4 (a) Secondary electron micrograph (SEM) of as-received P92 steel, (b) schematic of a prior austenite grain, (c) in-lens micrograph of as received P92 steel, (d) energy-dispersive X-ray spectra (EDS) of a white particle present at triple point, (e) EDS of a white particle present at PAGB and (f) EDS of a point present in the matrix ... 100
Figure 4.5 (a) Top and (b) backside of weld joint welded at different preheat temperatures ... 101
Figure 4.6 Cross-sectional macrographs of welded joints with preheating temperature of (a) No PH, (b) 200 ^{o}C, (c) 250 ^{o}C and (d) 300 ^{o}C ... 102
Figure 4.7 Effect of preheating temperature on DOP and DOP/BW ratio ... 102
Figure 4.8 Plot of modified Bessel function of zero-order ... 103
Figure 4.9 Predicted preheating temperature curve with a thickness of thin plates ... 105
Figure 4.10 Optical micrographs of the weld fusion zone with different preheating temperatures ... 107
Figure 4.111 Effect of cooling rate on the fraction of δ-ferrite in the weld fusion zone ... 108
Figure 4.122 (a) Weld design of double-sided GTAW weld, (b) complete welded joint after 1st pass and (c) cross-sectional view of the weld ... 109
Figure 4.133 Optical micrographs of weld fusion zone of second pass weld in (a) the as-welded, (b) PWHT, and (c) PWNT condition ... 109
Figure 4.144 Secondary electron micrographs of weld fusion zone of the second and first pass in (a) and (b) the as-welded, (c) and (d) PWHT, (e) and (f) PWNT condition, respectively ... 110
Figure 4.15 (a) Micrographs of weld fusion zone (second pass) in as-welded condition showing δ-ferrite and matrix region with their boundary, (b) EDX of area 1 present in the δ-ferrite, and (c) EdX of area 2 present in the matrix region. ... 111
Figure 4.166 XRD profiles after Rietveld refinement for (a) as-welded, (b) PWHT, and (c) PWNT ... 112
Figure 4.17 (a) peak shift in martensitic phase and (b) peak confirmation of ferrite phase ... 113
Figure 4.18 Fraction of δ-ferrite measured for different post-weld conditions from optical micrographs and from XRD Rietveld refinement ... 114
Figure 4.19 Optical micrographs of hardness indentation in (a) δ-ferrite and matrix region and (b) δ-ferrite region ... 115
Figure 4.20 Hardness variation across the welded joint in (a) as-welded, (b) PWHT, (c) PWNT condition, and (d) average microhardness of weld fusion zone and HAZ in all three conditions ... 115
Figure 4.21 (a) Tensile specimens before and after fracture, and (b) engineering stress-strain curves for welded joints welded with different post-weld conditions ... 116

Figure 4.22 Variation in Charpy impact toughness of weld fusion zone in different post-weld conditions....117
Figure 4.23 Optical micrographs of weld fusion zone of the first-pass weld at lower and higher magnification in (a) and (b) as-welded, (c) and (d) PWHT, (e) and (f) PWNT condition....118
Figure 4.24 Analytical solution with experimental data for dissolution kinetics of δ-ferrite at 1050 ^{o}C. 120
Figure 4.25 Secondary electron micrograph in as-welded condition (a) weld fusion zone for E911 filler, (b) FGHAZ for E911 filler, (c) weld fusion zone for P92 filler and (d) FGHAZ for P92 filler 121
Figure 4.26 Secondary electron micrograph in PWHT condition (a) weld fusion zone for E911 filler, (b) FGHAZ for E911 filler, (c) weld fusion zone for P92 filler and (d) FGHAZ for P92 filler....122
Figure 4.277 (a) Schematic showing microstructure evolutions after welding and PWHT, (b), (c), (d) micrographs of base metal, FGHAZ after welding, FGHAZ after PWHT, respectively, (e) fine MX particles in base material and (f) fine MX particles in FGHAZ after PWHT 123
Figure 4.28 Secondary electron micrograph of FGHAZ after PWHT (a) for E911 filler, (b) for P92 filler and (c) average particle size in FGHAZ for different filler....124
Figure 4.29 Tensile specimens before and after the transverse tensile test in (a) as-welded condition and (b) PWHT condition 125
Figure 4.30 Specimens before and after the longitudinal tensile test in as-welded condition..125
Figure 4.31 (a) Longitudinal engineering stress-strain curve for different fillers, (b) true and engineering stress-strain curve in longitudinal samples with different fillers and (c) transverse engineering stress-strain curve for different fillers and post weld conditions....126
Figure 4.32 For different fillers and post weld conditions: (a) ultimate tensile strength and (b) % elongation and % reduction in area 127
Figure 4.33 Fracture surface morphology of longitudinal tensile specimen (a) using E911 filler (b) using P92 filler....128
Figure 4.34 Fracture surface appearance across the welded specimen in as-welded condition (a), (b) & (c) using P92 filler and (d) & (e) using E911 filler 129
Figure 4.35 Fracture surface appearance across the welded specimen after PWHT (a) & (b) using E911 filler and (c) & (d) using P92 filler....130
Figure 4.36 Hardness variation for different filler and post weld conditions from center of the weld fusion zone to the base material....131
Figure 4.37 Charpy toughness of (a) weld fusion zone (b) HAZ for different filler in as-welded and PWHT condition 132
Figure 5.1 (a) Plates before welding, (b) weld groove design, (c) plate after completion of welding....136
Figure 5.2 A schematic of peak temperature profile and their typical microstructure in the HAZs of as-welded P911 and P92 weldment....137
Figure 5.3 (a) Groove design, (b) sequence of welding passes and (c) complete welded joint with tensile and Charpy toughness sample locations....138
Figure 5.4 (a) & (b) Micrograph of as-received P911 steel and (c) EDS of precipitates present at PAGB as point-1 and (d) EDS of matrix region as area-1....140
Figure 5.5 Secondary electron micrograph of N&T (a) & (c) P91 steel, (b) & (d) P92 steel ..140

Figure 5.6 Micrograph of sub-zones of dissimilar weldments (a) CGHAZ of P911 (b) CGHAZ of P92 (c) weld fusion zone, (d) FGHAZ of P911, (e) FGHAZ of P92....................................142
Figure 5.7 Micrograph of sub-zones of dissimilar weldments after PWHT and N&T treatment, respectively; (a), (b) weld fusion zone; (c), (d) CGHAZ; (e), (f) FGHAZ 144
Figure 5.8 Microstructure of HAZs of dissimilar weldments on P911 side (a) CGHAZ after PWHT, (b) CGHAZ after N&T, (c) FGHAZ after PWHT, (d) FGHAZ after N&T 145
Figure 5.9 XRD peaks for weld fusion zone in different operating condition..........................146
Figure 5.10 (a) Interrupted tensile specimens (b) engineering stress-strain curve 147
Figure 5.11 Variation in tensile properties for different heat treatment condition (a) YS and UTS, (b) % reduction in area (c) % elongation...148
Figure 5.12 Fractographs after room temperature static tensile testing for different condition (a) as-welded, (b) PWHT, (c) N&T..149
Figure 5.13 Hardness variation across the dissimilar weldments for different operating condition...150
Figure 5.14 Charpy toughness of weld fusion zone in different operating condition...............152
Figure 5.15 Fracture surface morphology after Charpy toughness tests (a) as-welded, (b) PWHT, (c) N&T...153
Figure 5.16 Secondary electron micrograph of weld fusion zone of the weld joints for (a) AW–P91, (b) AW–P92, (c) PWHT–P91 and (d) PWHT–P92 154
Figure 5.17 Schematic of transformation behavior in weld fusion zone after different weld thermal cycles...155
Figure 5.18 Secondary electron micrograph of PWHT-P91 weldment: (a) CGHAZ P91 side, (b) weld fusion zone at lower magnification, (c) CGHAZ P92 side, (d) FGHAZ P91 side, (e) weld fusion zone at higher magnification, (f) FGHAZ P92 side, (g) ICHAZ P91 side (h) EDS spectra of particles present in the weld fusion zone and (i) ICHAZ P92 side......................................156
Figure 5.19 Micrograph of PWHT-P92 weldment: (a) CGHAZ P91 side, (b) weld fusion zone showing δ ferrite, (c) CGHAZ P92 side, (d) FGHAZ P91 side, (e) weld fusion zone at higher magnification showing δ ferrite boundary, (f) FGHAZ P92 side, (g) ICHAZ P91 side, (h) line mapping of the δ ferrite boundary and (i) ICHAZ P92 side 157
Figure 5.20 Schematic of transformation behavior in FGHAZ after different weld thermal cycles...158
Figure 5.21 (a) Schematic of evolution of δ-ferrite, (b) Micrograph of the weld fusion zone for PWHT joint, (c), (d), (e), (f), (g) and (h) line mapping of the matrix and δ-ferrite boundary region...159
Figure 5.22 (a) Stress-strain curve for various welded specimens and (b) tensile strength......160
Figure 5.23 Microhardness profile across the welds joints..161
Figure 5.24 Charpy impact toughness of different welded joints 162
Figure 6.1 Diffusible hydrogen testing apparatus (mercury method)......................................166
Figure 6.2 (a) Schematic of mercury method test assembly, (b) test assembly fixed on copper jig during after the deposited metal and (c) hydrogen sample after broken out from test assembly...167
Figure 6.3 The schematic of implant test: (a) base plate, (b) implant specimen, and (c) test assembly...169
Figure 6.4 Implant test assembly (a) top view and (b) side view 171

Figure 6.5 Unfractured implant test specimen sectioned near implant axis for Case I 172
Figure 6.6 Fractured implant test specimen (a) Case II and (b) Case III................................ 173
Figure 6.7 Vickers hardness measurement along the axis of implant specimen: (a) Case I, (b) Case II and (c) Case III 173
Figure 6.8 Implant test results for different test cases: (a) case I, (b) case II and (c) case III .. 174
Figure 6.9 Effect of diffusible hydrogen content on embrittlement index and lower critical stress.. 176
Figure 6.10 Fracture surface morphology of implant specimen in: (a) & (b) case II under a stress of 325 MPa with failure after 2 min of loading, (c) & (d) case III under a stress of 325 MPa with failure after 1 min of loading 176
Figure 6.11 LCS for all welding conditions from applied stress versus failure time (min) curve 179
Figure 6.12 Fractured implant test samples showing line of fracture (a) condition I, (b) Condition II and (c) condition III 180
Figure 6.13 Schematic of crack propagation in the implant sample through (a) deposited weld metal (at higher stress levels), and (b) CGHAZ (at lower stress levels) 180
Figure 6.14 Microhardness of unfractured implant samples for different welding conditions 181
Figure 6.15 Effect of heat inputs on diffusible hydrogen content and on embrittlement index182
Figure 6.16 Fracture surface morphology of implant specimen under a stress of 280 MPa (a) condition I, (b) condition II and (c) condition III 183


भारतीय प्रौद्योगिकी संस्थान रुड़की
INDIAN INSTITUTE OF TECHNOLOGY ROORKEE

LIST OF TABLES

Table Caption **Page No.**

Table 2.1 Chemical compositions of ASTM A335/ASME SA335 steel (wt. %, Fe balanced) ... 8
Table 2.2 Transformation temperatures for P92 steel calculated using Thermo-Calc ... 11
Table 2.3 Various empirical formulas to predict δ-ferrite ... 20
Table 3.1 Chemical composition of P92 steel, (wt. %) ... 29
Table 3.2 Heat treatment matrix for specimens ... 29
Table 3.3 Heat treatment matrix for specimens ... 30
Table 3.4 Heat treatment matrix for samples ... 30
Table 3.5 Mechanical properties of P92 steel in as-received state ... 33
Table 3.6 Mechanical properties of as-received P92 steel and after various heat treatments ... 41
Table 3.7 Structure and lattice parameter of phases identified in XRD analysis of P92 steel ... 43
Table 3.8 Phase fractions calculated using Rietveld refinement of the raw XRD data for different aging conditions ... 72
Table 3.9 Grain size for different heat-treated conditions ... 84
Table 3.10 Fraction area of precipitates and precipitate diameter for different heat treatments 87
Table 4.1Chemical compositions of base metal, fillers and weld joints ... 93
Table 4.2 Mechanical properties of P92 steel in normalized and tempered condition ... 93
Table 4.3 Welding process parameters used for GTAW process ... 94
Table 4.4 Welding process parameters for root pass and filler pass ... 97
Table 4.5 Values of x calculated for different g and T_o ... 104
Table 4.6 Calculated values of Cr_{eq}, Ni_{eq} and FF for various empirical formulas ... 106
Table 4.7 Phase fractions calculated using Rietveld refinement of the raw XRD data for different post-weld heat treating conditions ... 113
Table 4.8 c/a ratios for martensite phase after different post-weld conditions ... 113
Table 5.1 Chemical compositions of base metals, fillers and weld joints ... 135
Table 5.2 Mechanical properties of the P91 and P92 steel in N&T condition ... 135
Table 5.3 Process parameters of welding ... 138
Table 5.4 XRD analysis report for the structure and lattice parameter of phases present in weld fusion zone in different conditions ... 146
Table 6.1 Weld filler conditions used for diffusible hydrogen measurement ... 165
Table 6.2 Welding process parameters ... 166
Table 6.3 Diffusible hydrogen content for different condition of weld consumable ... 171
Table 6.4 Implant test results for different condition of weld consumable ... 172
Table 6.5 Diffusible hydrogen values for different welding conditions ... 177
Table 6.6 Implant test results for different welding process parameters ... 178
Table 6.7 Embrittlement index calculation from Granjon implant test results ... 181

भारतीय प्रौद्योगिकी संस्थान रुड़की
INDIAN INSTITUTE OF TECHNOLOGY ROORKEE

ABBREVIATIONS

SMAW	Shielded Metal Arc Welding
CSEF	Creep Strength Enhanced Ferritic
PWHT	Post Weld Heat Treatment
PWNT	Post Weld Heat Treatment
Ac_1	Lower Critical Temperature
Ac_3	Upper Critical Temperature
HIC	Hydrogen Induced Cracking
HAZ	Heat Affected Zone
CGHAZ	Coarse Grained Heat Affected Zone
FGHAZ	Fine Grained Heat Affected Zone
ICHAZ	Inter-Critical Heat Affected Zone
BCC	Body Centered Cubic
FCC	Face Centered Cubic
BCT	Body Centered Tetragonal
PAGBs	Prior Austenite Grain Boundaries
N&T	Normalizing and Tempering
PAGs	Prior Austenite Grains
CNT	Conventional Normalizing and Tempering
LCS	Lower Critical Stress
GTAW	Gas Tungsten Arc Welding


भारतीय प्रौद्योगिकी संस्थान रुड़की
INDIAN INSTITUTE OF TECHNOLOGY ROORKEE

In recent years, to minimize the environmental pollution or to reduce the CO_2 emission from the power plants, renewed efforts have been carried out by enhancing the operating temperature and pressure which led to enhancement in the efficiency of thermal power plants (Hald, 2008; Yadav et al., 2016). To achieve favorable properties for high-temperature applications, several creep strength enhanced ferritic/martensitic (CSEF/M) steels such as P9, E911, P91 and P92 steel were developed (Kern et al., 2002; Sket et al., 2010). One of the largest applications of CSEF steels are found in power generating industries. Specifically, these steels have found use in main steam pipes, boilers, bolting and turbine blades, reheaters and superheaters tubing and rotors in power plants (Abson and Rothwell, 2013a). The CSEF steels are used for superheaters and steam generators in gas and sodium cooled nuclear reactors. These steels are also being considered for first-wall applications in fusion reactor systems (R L Klueh, 2005).

The suitability of material is the main problem because, at such high operating pressure and temperature, materials undergo microstructural changes and possible degradation such as hydrogen induced cracking (HIC), oxidation, creep, corrosion and embrittlement. CSEF/M steels offer high creep strength, good toughness, high ductility, good weldability, resistance to oxidation and resistance to stress corrosion cracking (Ennis and Czyrska-Filemonowicz, 2003). High creep strength of CSEF/M steels was derived from solid solution strengthening and precipitation hardening. To achieve the optimum combination of mechanical properties, CSEF/M steels treated for normalization and tempering (N&T) treatment which exhibits martensitic lath microstructure with coarse and fine precipitates. Grade P92 steel is one of the family member of CSEF steels.

Creep strength enhanced ferritic (CSEF) steels are candidate materials for header and main steam pipe in boilers due to their good corrosion and creep performance (Sklenicka et al., 2016). The maximum operating/service temperature of CSEF steels is considered in the range of 550 °C to 650 °C (Ennis and Czyrska-Filemonowicz, 2003). Grade P92 steel is a candidate material for nuclear power plants, besides being used widely in fossil fuel power plants in both pipe and plate forms for components operating at temperatures up to 620 °C. The mechanical properties of these steels are governed by several strengthening mechanisms such as precipitation hardening, solid solution strengthening and sub-grain hardening.

The precipitation of Laves phase (Fe_2M, where M may be Mo, W and Si) during service or aging at higher temperatures critical affects the mechanical properties, mainly creep strength of CSEF steels (Zhu et al., 2014). The effect of Laves phase is more pronounced in case of P92 steel due to its higher weight percentage of W, Mo and Si as compared to other CSEF steels. In the earliest stage, the nucleation of fine Laves phase may increase the creep strength through the precipitation strengthening mechanism (Lee et al., 2006). The subsequent growth or coarsening of Laves phase reduces the precipitation strengthening which affects the creep strength (Maddi et al., 2016). The coarsening of $M_{23}C_6$ precipitates also affects the mechanical properties of these steels (Y. Xu et al., 2016). Isik et al. (Isik et al., 2014) reported that the nucleating sites of Laves phase were close to $M_{23}C_6$ precipitates on sub-grain boundaries. In steel welds, the average particle size of Laves phase was measured in the range of 180-240 nm after 10,000 hrs at 650 ^{o}C (Wang et al., 2019). In P92 steel, the volume fraction of Laves phase precipitated after 10,000 hrs of aging at 600 ^{o}C was approximately 1.0% (Hättestrand and Andrén, 2001).

1.1 Organization of thesis

The content of thesis is briefly described chapter wise as below:

Chapter 1. It provides brief introduction and motivation for the research work.

Chapter 2. It deals with the reviewing of the research work done in the field of heat treatment of P92 steel, problems in similar and dissimilar welded joints and diffusible hydrogen in P92 deposited metal and their effect on performance.

Chapter 3. The detailed discussions about the as-received material and effect of varying normalizing and tempering treatment on microstructure evolution and mechanical properties of P92 steel, effect of long term aging on Laves phase evolution and dissolution of Laves phase have been included in this section.

Chapter 4. The effect of preheating temperatures (200-300 ^{o}C) on the weld geometry in autogenous-TIG welds have been discussed in this Chapter and a model is suggested to predict a preheating temperature for a given plate using Rosenthal equation. The dissolution of δ-ferrite using post-weld normalizing and tempering in the autogenous TIG welds of P92 steel has been studied and their effect on mechanical properties have also been studied. The effect of different filler compositions on the microstructure evolution and mechanical properties of P92 steel weldments welded using SMAW have been studied.

Chapter 5. This chapter deals with effect of post-weld heat treatments on the microstructure evolution and mechanical properties of dissimilar welded joints of P911 and P92 steel have been studied. The effect of filler compositions on the microstructure evolution and mechanical properties of dissimilar welded joints of P91 and P92 steel have also been studied.

Chapter 6. It deals with the measurement of diffusible hydrogen content in deposited weld and its effect on the performance of the P92 weld joints.

Chapter 7. The summarisations of the entire work and important concluding points have been presented in this Chapter.

भारतीय प्रौद्योगिकी संस्थान रुड़की
INDIAN INSTITUTE OF TECHNOLOGY ROORKEE

To minimize environmental pollution or to reduce the CO_2 emission from the power plants, renewed efforts have been carried out by enhancing the operating temperature and pressure which led to enhancement in the efficiency of thermal power plants (Danielsen and Hald, 2009; Yadav et al., 2016). To achieve favorable properties for high-temperature applications, several creep strength enhanced ferritic (CSEF) steels such as P9, E911, P91 and P92 steel were developed (Kern et al., 2002; Sket et al., 2010). One of the largest applications of CSEF steels is found in power generating industries. Specifically, these steels have found use in main steam pipes, boilers, turbine blades, reheaters and superheaters tubing and rotors in power plants (Abson and Rothwell, 2013a). The CSEF steels are used for superheaters and steam generators in gas and sodium-cooled nuclear reactors. These steels are also being considered for first-wall applications in fusion reactor systems (R L Klueh, 2005)(Mahesh et al., 2008a, 2008b).

The suitability of material is the main problem because at such high operating pressure and temperature, materials undergo microstructural changes and possible degradation such as hydrogen-induced cracking, oxidation, creep, corrosion and embrittlement. The CSEF steels are preferred over austenitic steels due to its low thermal expansion coefficient and cheaper due to lower Ni and Cr content (Babu et al., 2013; Coussement et al., 1991). CSEF steels offer high creep strength, good toughness, high ductility, good weldability, resistance to oxidation and resistance to stress corrosion cracking (Ennis and Czyrska-Filemonowicz, 2003; Kamal et al., 2010). To achieve the optimum combination of mechanical properties, CSEF steels treated for normalization and tempering (N&T) treatment which exhibits martensitic lath microstructure with coarse and fine precipitates. Grade P92 steel is one of the family members of CSEF steels.

2.1 Development of CSEF steels

The limitations in terms of economics and environmental aspects of power generating plants have focused on the development of low emission and high-efficiency systems. The ultra-supercritical power plants have advantage of decreased emission and increased thermal efficiency over subcritical and supercritical power plants due to rapid water to steam generation (high temperature and pressure). Such elevated steam conditions requirements formerly met the use of austenitic steels for older subcritical and supercritical power plants. The older power plants have potential problems (thermal stress) due to higher thermal expansion coefficients of austenitic steels. Austenitic steels have problems during a sudden change in temperatures often in a short span and frequent change in boiler heat input.

However, CSEF steels are preferable over austenitic steels due to excellent creep rupture strength, low thermal expansion coefficient and good thermal conductivity (Babu et al., 2013; Coussement et al., 1991). The steam conditions are major determinant for heat resistant capability of CSEF steels (Masuyama, 2001). The CSEF steels such as E911, P91 and P92 have been developed for supercritical and ultra-supercritical power plants (Shibli and Starr, 2007). The ferritic/martensitic steels are further divided into low alloy steels (2.25% Cr and 0.5 to 1.0 % Mo), medium alloy steels (2.25 to 10 % Cr) and high alloy steels (9 to 12 % Cr) (Masuyama, 2001). Figure 2.1 shows development of ferritic and martensitic boiler steels based on their increased creep resistance from 35 MPa to 140 MPa over 10^5 hours creep strength at 600°C (Ennis and Czyrska-Filemonowicz, 2003). The CSEF steels are also known as Cr-Mo steels.

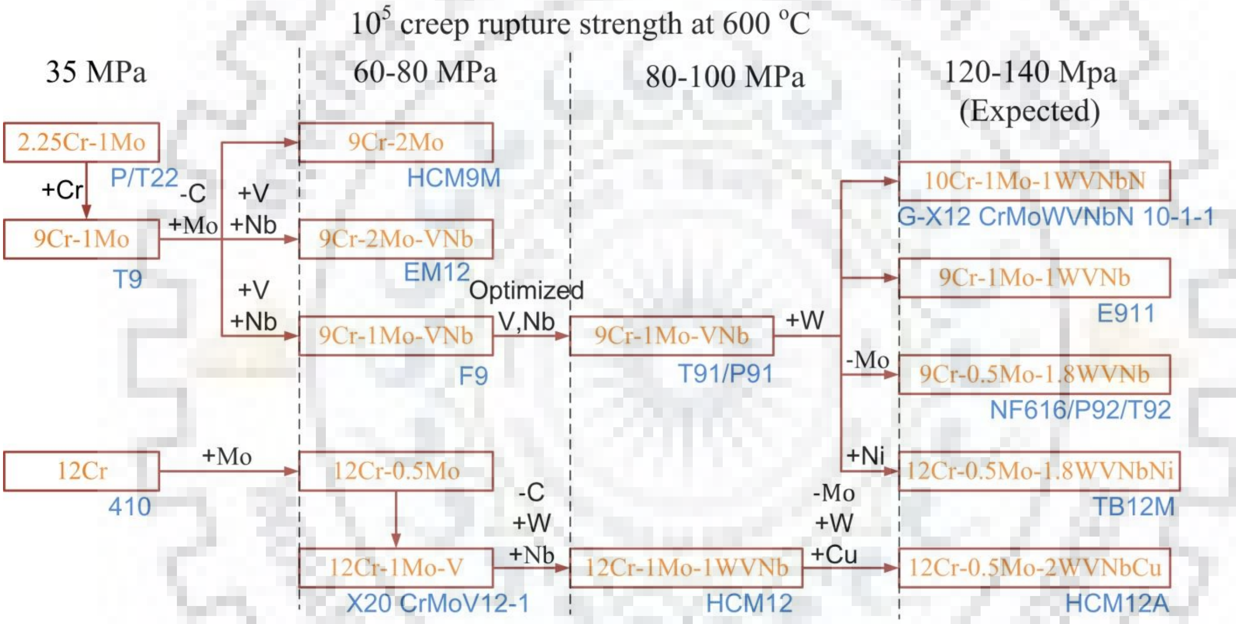

Figure 2.1 Development of ferritic and martensitic boiler steels based on their increased creep resistance from 35 MPa to 140 MPa over 10^5 hours at 600°C (Ennis and Czyrska-Filemonowicz, 2003)

In the 1950s, the 9Cr-1Mo steels were developed for fabrication of thick and thin-walled components with a maximum operating service temperature of 545 °C. In the 1960s, 12Cr- 1MoV steels were developed. The maximum service temperature for such steels was limited to 570 °C. The precipitation of z-phase [Cr(V, Nb)N] was the main reason for the failure of most of the 12% Cr steels during prolonged creep exposure (Cipolla et al., 2010; Zheng-fei and Zhen-guo, 2003). The higher Cr content is responsible for the precipitation of Z-phase precipitation (Golpayegani et al., 2008). The Cr percentage was brought down to 9 % from 12 % to further increase creep strength.

In the mid-1970s, there was considerable interest in 9% Cr steels due to increased creep strength. The 9Cr-1Mo with optimized addition of strong carbide and nitride forming elements (V and Nb) was developed at Oak Ridge National Laboratory and added into the ASTM specifications under the designation Grade P91 steel (Sikka and Patriarca, 1984). The CSEF P92 steel was originally developed by Nippon Steel in Japan under the company designation NF616, has been issued a data collection and based on the Nippon Steel data, the rupture strength is given as 130 MPa over 10^5 hrs (Sakthivel et al., 2015). The addition of W and optimization of V, Nb and Mo resulted in increased stress rupture strength which leads to the development of NF616 steel. Subsequently, this steel was included in the ASTM specifications under the designation of Grade P92 steel. Grade P92 steel is also known as 9Cr-0.5Mo-1.8W-V-Nb and designated as ASTM A335/ASME SA335 for plate, T92 for tube and P92 for pipe (Shrestha et al., 2015).

The maximum service temperature is affected by the increasing alloying elements in high alloys steel. The maximum service temperatures of CSEF steels over 10^5 hrs at 100 MPa of average stress rupture strength is presented in Fig. 2.2 (Ennis and Czyrska-Filemonowicz, 2003).

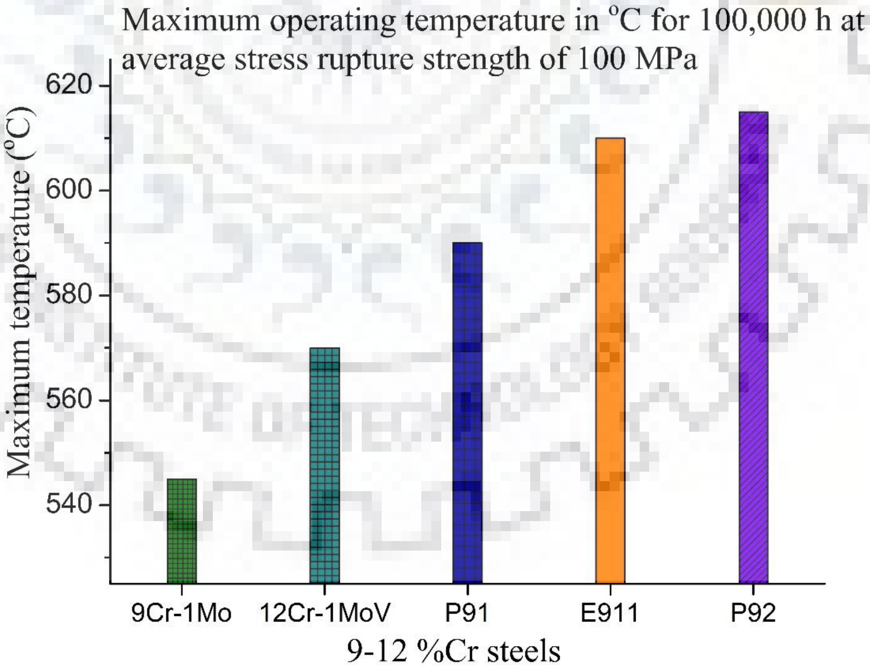

Figure 2.2 Maximum service temperatures of CSEF steels for 100 MPa of average stress rupture strength over 10^5 hrs (Ennis and Czyrska-Filemonowicz, 2003)

P92 steel differs from P91 steel due to the presence of 0.6%Mo, 1.8%W and 0.005% boron. The main advantage of P92 steel is its higher creep-rupture strength as compared to P91 steel, even though P92 steel is more expensive than P91 steel (C. Pandey et al., 2016). The demand for improved efficiency may increase the use of these alloy steels soon by increasing the operating conditions. Nowadays, P91 steel is cost-effective in power-plants, but P92 steel is now actively considered and installed in some power plants, because of its about 32 % reduction in thickness of the wall as compared to P91 steel for the same allowable stress and operating temperature (Thomas Paul et al., 2008).

2.2 Role of alloying elements in P92 steel

Each alloying element plays a critical role in the stability of microstructure during service. High creep strength of CSEF steels was derived from solid solution strengthening and precipitation hardening mechanisms. The strengthening mechanisms are depending upon alloying elements. In CSEF steels, the major alloying element is chromium (Cr) which acts as oxidation resistance and provides high-temperature strength. Nickel (Ni) is added to enhance the ductility and strength. Ferrite is counteracted by Ni because both Cr and Fe have the tendency to form ferrite.

Some other alloying elements are added to integrative properties at elevated temperature, such as molybdenum (Mo), tungsten (W), manganese (Mn), vanadium (V), aluminum (Al), niobium (Nb), silicon (Si), carbon (C), nitrogen(N), phosphorus (P) and boron (B) (Mayr et al., 2019). Mo enhances creep-rupture strengths. Mo is used in combination with Cr to prevent graphitization. Due to an increase of Cr to above 7 %, these steels containing martensite, which is characterized by a fine lath structure stabilized by $M_{23}C_6$ precipitates and high dislocation density. Creep strength has been achieved by alloying with V, W, Nb and B (Kafexhiu et al., 2012). The chemical composition of P92 steel is depicted in Table 2.1.

Table 2.1 Chemical compositions of ASTM A335/ASME SA335 steel (wt. %, Fe balanced)

Elements	C	Cr	Mo	W	Nb	V	Mn	Al	Si	N	Ni	P	B
ASTM A335/ ASME SA335	0.07 to 0.13	8.5 to 9.5	0.3 to 0.6	1.5 to 2.0	0.04 to 0.09	0.15 to 0.25	0.3to 0.6	0.04 max	0.5 max	0.03 to 0.07	0.4 max	0.02 max	0.001 to 0.006
P92 steel (measured)	0.09	8.7	0.4	1.8	0.04	0.19	0.5	0.01	0.22	0.04	0.11	0.01	-

2.2.1 *Ferrite stabilizers*

Chromium (Cr), tungsten (W) and molybdenum (Mo) are ferrite stabilizing elements in the P92 steel. Cr is a major alloying element in P92 steel and is generally added for corrosion and oxidation resistance of steel at elevated temperatures. It combines with Fe and contributes to solid solution strengthening. In P92 steel, the strengthening effect is governed by the formation of Cr-rich $M_{23}C_6$ precipitates from the solid solution, which increases the creep strength of the steel by restricting the movement of dislocations and sub-grain boundaries (Wang et al., 2009). The precipitation of Cr-rich $M_{23}C_6$ precipitates occurs during tempering and remains throughout service. The $Cr \geq 10$ % resulted in the retention of δ-ferrite which has a negative impact on Charpy toughness (Liu and Fujita, 1989). In P92 steel, Cr-rich M_2X type nitrides can also form (R. L. Klueh, 2005).

W and Mo also increase the solid solution strengthening effect in the P92 steel. Mo can affect the creep strength negatively by accelerating the coarsening of $M_{23}C_6$ precipitates. W is used as a substitute for Mo to reduce the detrimental effects of Mo. To avoid the formation of intermetallic Laves phase [$Fe_2(Mo, W)$] and retention of δ-ferrite, the weight % of Mo and W must be limited. Klueh (R. L. Klueh, 2005) reported that if structural steel has a Mo equivalent ($Mo_{eq} = Mo\% + 0.5\ W\%$) greater than 1% then tendency to form Laves phase is high at service temperature in the range of 600-650 ^{o}C.

The nucleation of the Laves phase resulted in reduction in Mo and W from the solid solution which decreases the solid solution strengthening effect (Dimmler et al., 2003). The W weight percentage greater than 2% accelerates the formation of the Laves phase. During short-term creep, the creep strength increases due to precipitation of Laves phase which increases the precipitation hardening effect while reduces during long-term creep due to growth of Laves phase which reduces the precipitation hardening effect (Cui et al., 2010; Hald and Korcakova, 2003; Korcakova et al., 2001).

2.2.2 *Strong carbide and nitride formers*

The niobium (Nb) and vanadium (V) are added to P92 steel to increase the precipitation strengthening effect by the precipitation of fine MX-type precipitates [M(C, N); M: V, Nb] within the matrix. The thermally stable MX precipitates can be in the form of MC (carbides), MN (nitrides), and M(C, N) (carbonitrides). These precipitates help in slow down the recovery rate and impede the movement of dislocations (Hofer et al., 1999). Maruyama (K Maruyama et al., 2001) observed the critical role of MX carbides with and without addition of W on increasing creep rupture strength.

2.2.3 *Austenite stabilizers*

Nickel (Ni) and manganese (Mn) acts as austenitic stabilizers, reducing the δ-BCC (ferrite) to γ-FCC (austenite) transformation temperature. During austenitizing, Ni and Mn ensure the formation of 100 % austenite and ensuring 100 % martensite during cooling (Knezevic et al., 2002). The Ni enhances the impact toughness of Grade P92 steel, but the weight percentage higher than the 0.4% accelerates the growth of $M_{23}C_6$ precipitates (Yin et al., 2008). Mn reduces the growth of $M_{23}C_6$ precipitates, when its weight percentage is limited to 0.5%. Further increase in Mn weight percentage accelerates the coarsening rate of $M_{23}C_6$ (Helis et al., 2009). Mn is also enhanced the nitrogen solubility in austenite (Sourmail, 2001).

2.2.4 *Other alloying elements*

Both carbon (C) and nitrogen (N) both are essential for the precipitation of $M_{23}C_6$ and MX type of precipitates which increases the creep strength by increasing the strengthening effects. C has higher solubility in austenite as compared to ferrite (Ennis et al., 1997). N has higher strengthening effect in solid solution (Pandey et al., 2007; Sourmail, 2001). In P92 steel, Al helps in precipitation of AlN nitrides. AlN formation reduces N in the system and helps in decreasing VN particles which are responsible for decreased creep strength (Gómez et al., 2009; Pandey et al., 2003). B is incorporated in grow of $M_{23}C_6$ and decreases its growing rate by decreasing interfacial energy (Abe, 2005; Ennis and Czyrska-Filemonowicz, 2003).

2.3 Various phases formed in P92 steel

The mole fractions of various phases formed in P92 steel have been calculated as a function of temperature by the Thermo-Calc with the TCFE6 database for the alloy composition (given in Table 2.1), as shown in Fig. 2.3(a). The predicted phases are γ-FCC (austenite), α-BCC (ferrite), $M_{23}C_6$, Laves phase, MX and Z-phase in the temperature range of 500 to 900 ^{o}C. At higher temperatures, δ-BCC (δ-ferrite) is also predicted which transformed into austenite during cooling. The predicted density of MX precipitates is very low in P92 steel. But MX precipitates are essential to increase creep strength and to maintain fine sub-grain during service (Abe, 2005). $M_{23}C_6$, α-ferrite, Laves phase and MX phases are dominant at 620 ^{o}C (maximum service temperature of P92 steel).

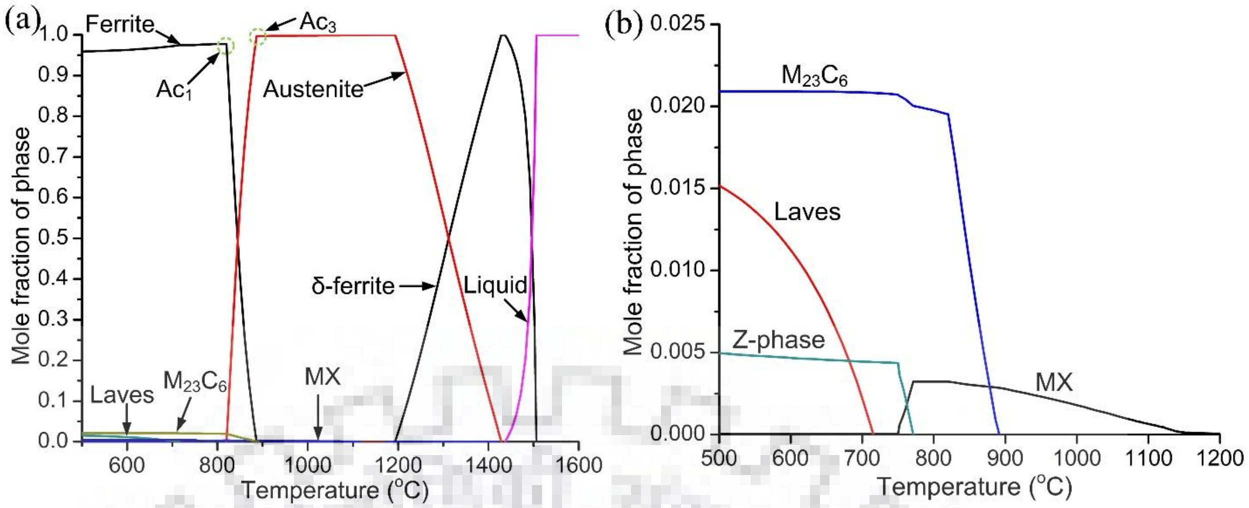

Figure 2.3 (a) and (b) Equilibrium phases as a function of temperature for P92 steel calculated by Thermo-Calc

An enlarged part of the mole fraction of the phase diagram is shown in Fig. 2.3(b). Figure 2.3(b) shows that the $M_{23}C_6$, Laves phase and Z-phase started to dissolve when the temperature is increased beyond the maximum operating temperature while MX-type particles remain same. The equilibrium composition of precipitates is also predicted using Thermo-Calc. The predicted $M_{23}C_6$ phases are enriched in Cr while MX phases are enriched in V and Nb. The Laves phase is enriched in W and Mo. The liquidus temperature of P92 steel is calculated as about 1505 °C. The estimated transformation temperatures for P92 steel using Thermo-Calc are tabulated in Table 2.2. The transformation temperature for ferrite to austenite is predicted as 820 ^{o}C.

Table 2.2 Transformation temperatures for P92 steel calculated using Thermo-Calc

Transformation reaction	Estimated temperature (^{o}C)
L starts to transform into δ	1505
δ starts to transform into γ	1436
δ finished transformation to γ	1193
γ starts to transform α (Ac_3)	887
α transformation completes (Ac_1)	820

2.4 Precipitates morphology

To achieve stable martensitic microstructure, P92 steel is subjected to austenitizing and tempering treatment. The evolution of un-tempered martensitic microstructure and dissolution of precipitates is observed after austenitization treatment (Jones et al., 1991). The homogenous distribution of precipitates is achieved after the tempering treatment (Li et al., 2006). The common phases formed during the tempering process in P92 steel are Cr, Fe and Mo-rich $M_{23}C_6$, M_7C_3 (M-Cr, Fe) and V and Nb-rich MX type carbide/carbonitrides [M:V, Nb; X:C, N] (Armaki et al., 2011; Baltusnikas et al., 2007; Kouichi Maruyama et al., 2001; Y. Wang et al., 2016a). After long-term creep exposure, the intermetallic phases such as Laves, and Z-phase are observed. A reduction in the service life of P92 steel observed due to the evolution of these intermetallic phases. The precipitates morphology is defined below:

2.4.1 $M_{23}C_6$

The Cr-rich $M_{23}C_6$ precipitates having FCC structure are precipitated along the grain boundaries in the initial stage of tempering (Y. Wang et al., 2016a). The composition of $M_{23}C_6$ also encountered with Fe, Mn, Mo and Ni. Further increase in tempering time up to 1 hr resulted in increasing Cr to Fe ratio which confirms the stability of Cr-rich $M_{23}C_6$ phase (Jones et al., 1991). These precipitates hindered the motion of sub-grain boundaries and provide the pinning effect during service or loading which results in increased creep strength (Kouichi Maruyama et al., 2001). Fine $M_{23}C_6$ particles are precipitated inside the matrix region while coarse $M_{23}C_6$ particles are precipitated along with lath and sub-grain boundaries. The driving force for precipitating $M_{23}C_6$ precipitate decreases with an increase in temperature.

2.4.2 *Laves phase*

The precipitation of the Laves phase (Fe_2M, where M may be Mo, W, and Si) during service or aging at higher temperatures affects the mechanical properties, mainly creep strength of CSEF steels (Zhu et al., 2014). The detrimental effect of Laves phase is more pronounced in P92 steel due to its higher weight percentage of W, Mo, and Si as compared to other steels. The Laves phase has a hexagonal structure in P92 steel. In the earliest stage, the nucleation of fine Laves phase may increase the creep strength through the precipitation strengthening mechanism (Lee et al., 2006). The subsequent growth or coarsening of the Laves phase reduces precipitation strengthening which affects the creep strength (Maddi et al., 2016). Isik et al. (Isik et al., 2014) reported that the preferential nucleating sites of the Laves phase were close to $M_{23}C_6$ precipitates on sub-grain boundaries.

The driving force map with varying temperature and mass percent of W for precipitating Laves phase is predicted using Thermo-Calc, as shown in Fig. 2.4. It is clearly seen from the calculation that the driving force for the precipitating Laves phase decreases with an increase in temperature. The precipitation of the Laves phase beyond 500 ^{o}C was mainly governed by W percentage in Grade P92 steel. A reduction in service life is observed due to the evolution of some detrimental phases like Z-phase and laves phase during long-term creep exposure (Danielsen et al., 2013; Li et al., 2006; Sawada et al., 2008).

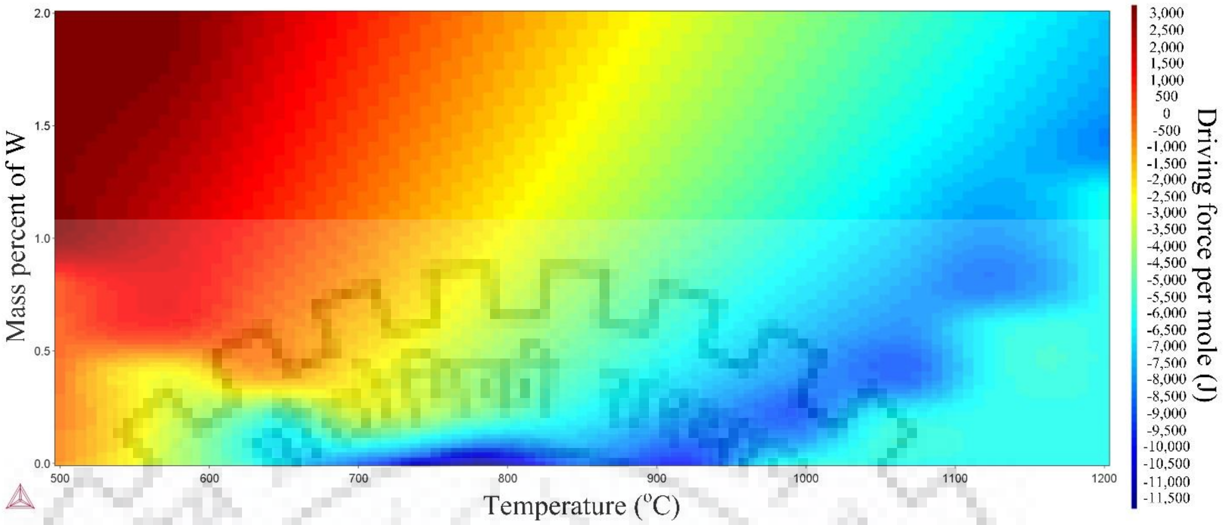

Figure 2.4 Driving force with respect to temperature for Laves phase precipitation simulated using Thermo-Calc

2.4.3 *MX phase*

In P92 steel, V, Nb, and Ti-rich carbides and nitrides are formed as MX precipitates. MX precipitates possessed FCC structure and precipitated mainly in the matrix or sub-grain interior region. The MX particles size is reported in the range of 10 to 50 nm (Srinivas Prasad et al., 2012). Though the density of these precipitates is low in P92 steel(as predicted from Fig. 2.3), the precipitates are mandatory to increase creep strength and to maintain fine sub-grains during service (Abe, 2005; K Maruyama et al., 2001). Three types of MX particles are reported in P92 steel. The relatively coarse and spherical NbX is the primary type of MX precipitates.

The NbX particles are randomly dispersed and remain undissolved after austenitization treatment due to higher mutual solubility of Nb and C or N in the austenite (Ennis et al., 1997; K Maruyama et al., 2001). The fine NbX and VX particles form during tempering, known as secondary MX precipitates. The secondary MX particles are finer in size (10 to 20 nm) as compared to primary MX particles (100 nm) (Shrestha et al., 2012). V-wing complex MX precipitates are the third type of these precipitates. They nucleate when NbX particles were dissolved during austenitization and act as a preferential site for nucleation of VN nitrides during tempering (Hu et al., 2010). These fine MX precipitates increase the creep life during service by pinning the motion of free dislocations while coarse NbX limits the growth of austenite grains (Abe, 2005; R. L. Klueh, 2005).

2.4.4 *Z-phase*

The precipitation of Z-phase [Cr(V, Nb)N] takes longer time during service as compared to Laves phase. The precipitation of Z-phase occurs in the temperature range of 600 to 750 ^{o}C. Z-phase possesses a body central tetragonal structure (Danielsen et al., 2006). The preferential sites for nucleation of Z-phase are observed as packet boundaries and prior austenite grain boundaries (Cipolla et al., 2010). The precipitation of Z-phase consumes the Nb and V-rich nitrides. To predict the driving force for precipitating Z-phase, a thermodynamic model is developed (Danielsen and Hald, 2007).

The weight percent of Cr strongly affects the precipitation of Z-phase as compared Nb and V. The large driving force for precipitating Z-phase is reported in 12-Cr steel as compared to 9-Cr steels. The precipitation of Z-phase is also accelerated by the N content (Yin et al., 2007). However, the precipitation of Z-phase is the reason for decreased creep life of components because it consumes Nb and V-rich nitrides from the matrix which reduces the pinning effect to move dislocations (Cipolla et al., 2010; Sawada et al., 2007).

2.5 Heat treatments of P92 steel

To obtain high-temperature strength that is associated with the tempered martensitic structure, these steels are generally used in conventional normalizing and tempering (CNT) state. To ensure the complete dissolution of precipitates/carbides in these steels, higher superheating above the upper critical temperature (Ac$_3$) is required to get complete austenite structure. But for a high degree of superheat, austenite grain growth follows a significantly higher rate than the conventional parabolic growth rate. In order to ensure complete dissolution of precipitates and to attain a martensitic structure on water quenching/air cooling, a higher degree of heating (100-150 ºC above Ac$_3$) is preferred. The recent development and finding related to the effect of heat treatments and effect of long-term aging on the microstructural evolution and mechanical properties of P92 steel are discussed below:

2.5.1 *Effect of heat treatments on mechanical properties*

2.5.1.1 Conventional normalizing and tempering

The stability of microstructure is governed by the tempered lath martensitic microstructure, precipitate size and their distribution inside the microstructure, dislocation density, prior-austenite grain boundaries (PAGBs), sub-grain size, lath boundaries, lath width, precipitate amount and their morphology (Mannan et al., 2003). The stable microstructure of P92 steel helps in developing the primary strength.

However, the stable microstructure was derived from the presence of solute atoms, high dislocation density and pinning precipitates like Cr-rich $M_{23}C_6$ [M: Cr, Fe, Mo], V and Nb-rich MX resulted in a large driving force required for recovery and required for high creep strength (Dudko et al., 2012; Tkachev et al., 2016). The dislocation barrier ability of precipitates reduces as precipitates coarsen while the finer precipitates lead to the higher strength of the steels. The temperature, as well as time of normalizing and tempering, are affecting the mechanical properties of these steels (Barbadikar et al., 2015; Penalba et al., 2016).

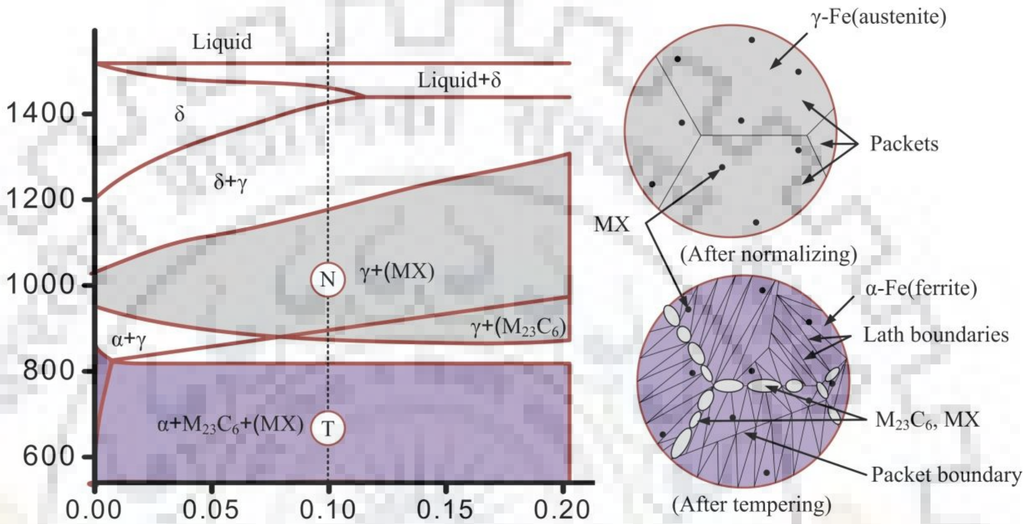

Figure 2.5 Schematic evolution of microstructure in P92 steel during CNT process

The properties of P92 steel are derived from precipitation hardening, sub-grain size hardening and solid solution hardening. Normalizing of P92 steel is carried out to develop the lath microstructure with high dislocation density while evolution of precipitates occurred during the tempering process. Tempering also led to precipitation hardening that enhanced the stability of the microstructure. Lath microstructure formation and evolution of precipitates during the CNT process are shown in the schematic diagram of Fig. 2.5**.**

The CNT process alters the microstructure as well as the precipitation of carbides/nitrides. In most of the research work, a normalizing of 1000-1080 ºC/30-60 min/air cooling and tempering of 750-780 ºC/60-240 min/air cooling is reported (Barbadikar et al., 2015). The components having weldments that are prone to type-IV cracking mainly depends on initial microstructure (Laha et al., 2007).

2.5.1.2 Double austenitization based normalizing and tempering

The fine prior austenite grain (PAG) size plays an important role in deciding the room temperature tensile behavior and Charpy toughness of the Grade P92 steel. It also plays an important role in deciding the long-term creep rupture life of the base metal. Double austenitization based treatment and some other heat treatment was recommended to refine the grain size (Karthikeyan et al., 2017; Liu et al., 2014; Narasimha Rao and Thomas, 1975). The main purpose of double austenitizing treatment is to obtain the fine PAG that leads to higher the strength and hardness of the P92 steel and provides the optimum combination of strength and Charpy toughness as compared to the conventional normalizing and tempering.

The double austenitizing based heat treatment deals with the austenitizing above A_{c3} in the initial step that results in the formation of untempered martensite that is devoid of carbide precipitates (Liu et al., 2014; Xiong et al., 2012). In the second step, the austenitizing is performed to make the homogeneous fine grain structure. After the second austenitizing, tempering was performed to reduce the brittleness of the untempered martensite and evolution of carbide precipitates.

Karthikeyan et al. (Karthikeyan et al., 2011) have studied the effect of ‘Double austenitization based Normalizing and Tempering (DNT)’ on grain refinement and its effect on the impact toughness 9Cr-1Mo steel and compared it with the ‘Conventional Normalizing and Tempering’ (CNT) treatment. The enhancement in Charpy impact toughness and a decrease in DBTT was reported as a result of the grain refinement through DNT treatment. Karthikeyan et al. (Karthikeyan et al., 2017) further studied the effect of DNT treatment on mechanical properties and thermal embrittlement of 9Cr-1Mo-0.1C steel. They reported the effect of DNT treatment (grain refinement) on creep rupture behavior, tensile behavior, and impact toughness.

The DNT treatment resulted in the superior tensile and creep strength of the material as compared to CNT treatment and this occurred mainly due to homogeneous fine-grained microstructure. The improved embrittlement was also reported for the DNT treatment. Liu et al. (Liu et al., 2014) have studied the microstructure and mechanical properties of a novel 5Cr steel for double quenching and tempering (DQT) treatment. The superior toughness was reported for the DQT treatment that was attributed to fine grain formation. It was also reported that fine grain formation hindered the crack propagation in the material. Effect of twice quenching and tempering on microstructure evolution and ductile-brittle transaction temperature of the SCRAM steel is also reported by the Xiong et al. (Xiong et al., 2012). The twice quenching has also resulted in the refined prior austenitic grain size and lath width that also reduced the ductile-brittle transition temperature.

2.5.2 *Effect of long-term aging on mechanical properties*

The schematic evolution of the Laves phase is shown in Fig. 2.6 (Wang et al., 2019). This schematic is used to explain the shape and nucleation of Laves phase. In the initial stage, no Laves phase particles are observed in the initial microstructure. In the first stage, the nucleation of Laves phase particles is observed in rod or needle-like shape during aging along the sub-grain boundaries and along the PAGBs. This stage is known as nucleation stage. In the second or final stage, the coarsening and growth of Laves phase particles at the sub-grain boundaries is observed. The rod/needle-like shape of Laves phase particles is transformed into bulky/chain-like shape with an increase in aging time.

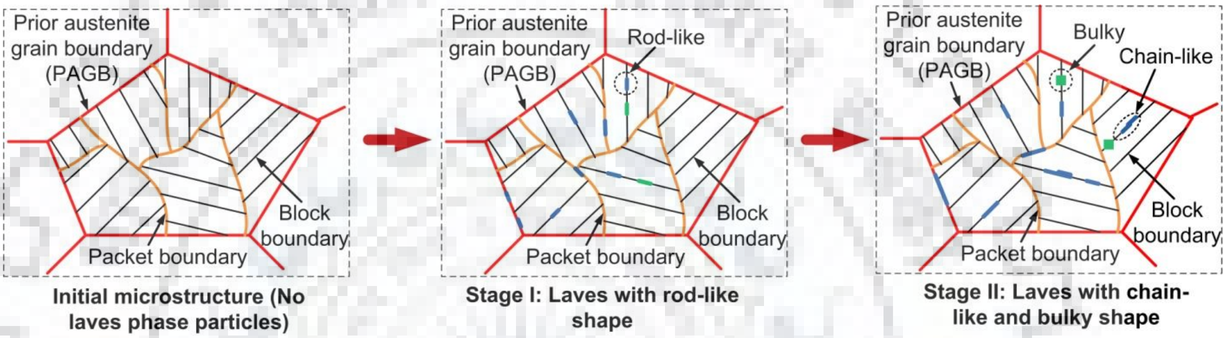

Figure 2.6 Schematic evolution of Laves phase (Wang et al., 2019)

During short-term aging, the nucleation of Laves phase increases the creep resistance by increasing the pinning effect (Swada et al., 1999). During long term aging, the coarsening of Laves phase starts which results in loss of W and Mo content in the matrix and decreases solid solution strengthening effect. The migration of lath boundaries indicates the weakened pinning effect after long-term aging, which is significantly affected by the average diameter of precipitates. In the AR material, the pinning effect of these precipitates on sub-grain boundaries attributed to higher creep properties by obstructing the movement of grain and sub-grain boundaries.

During aging, the coarsening of secondary phase precipitates started. During aging, the total number of secondary phase particles at boundaries is decreased due to coarsening of precipitates irrespective of nucleation of Laves phase. However, the overall pinning effect to impend the movement of grains reduced. The Laves phase shows higher coarsening rate as compared to intergranular coarse $M_{23}C_6$ precipitates during prolonged exposure to tempering. Both phases grow gradually with aging time, while it is observed that the size of Laves phase increases rapidly after 3400 hrs of tempering or more (Wang et al., 2015).

The nucleation and coarsening rate of Laves phase also depends on tempering temperature (Korcakova et al., 2001). The nucleation of coarse Laves phase particles acts as cavity trigger and limits the life of components (G. D. Janaki Ram et al., 2004; Janaki Ram et al., 2005; C. Panait et al., 2010). During long-term aging, the coarsening of $M_{23}C_6$ precipitates also affects the mechanical properties of these steels (Hald and Korcakova, 2003; Y. Xu et al., 2016). Isik et al. (Isik et al., 2014) reported that the nucleating sites of Laves phase were close to $M_{23}C_6$ precipitates on sub-grain boundaries. In steel welds, the average particle size of Laves phase was measured in the range of 180-240 nm after 10,000 hrs at 650 ^{o}C (Wang et al., 2019).

In P92 steel, the volume fraction of Laves phase precipitated after 10,000 hrs of aging at 600 ^{o}C was approximately 1.0% (Hättestrand and Andrén, 2001). Hattestrand et al. have also reported poor creep strength of P92 steel at 650 ^{o}C as compared to 600 ^{o}C due to rapid growth of Laves phase and rapid coarsening of $M_{23}C_6$ precipitates (Hättestrand and Andrén, 2001). During aging, the ductile-brittle transition temperature increases after precipitation of Laves phase in 9Cr-2Mo steel (Hosoi et al., 1986). Vyrostkova et al. (Vyrostkova et al., 2008) studied the effect of aging on the Charpy toughness of P92 and P911 dissimilar weldment. After aging, a decrease in impact energy was reported due to an un-favorable microstructure having very coarse Laves phase and $M_{23}C_6$ precipitates.

The Laves phase having size of more than 125 nm changes the fracture mode from ductile to brittle and resulted in decreased impact toughness (Kunimitsu et al., 1991). The precipitation of Laves phase with loss of strengthening elements affects the creep life of welds during service (Qiao et al., 2019). Abe et al. (Abe, 2005) studied the effect of W on the precipitation of Fe_2W Laves phase and their effect on creep rate and found that the W percentage of more than 1% in 9Cr steels accelerated the creep rate.

Abe et al. (Abe, 2004) have also observed that the coarsening of $M_{23}C_6$ precipitates depends mainly on volume diffusion-controlled process during creep. Wang et al. (Wang et al., 2015) have calculated coarsening constant for Laves phase by considering volume diffusion-controlled coarsening. A PWHT at 980 ^{o}C leads to the dissolution of Laves phase (G.D. Janaki Ram et al., 2004). The following Johnson Mehl Avrami equation can be used to describe volume fraction of a secondary phase (Laves phase) against time (Wang et al., 2015):

$$f(t) = 1 - e^{-(\frac{t}{t_o})^n} \qquad (2.1)$$

where f(t) is volume fraction of secondary phase particles at time t, t_o is time constant and n is time exponent. The value of n is determined by the nucleating mechanism. If the secondary phase particles are nucleating at boundaries then the value of n is 0.5 and 1.5 for nucleating rate rapidly decreasing to zero and constant nucleating rate, respectively.

2.6 Weldability of P92 steel

Retention of δ-ferrite, evolution of Cr-rich carbides or depletion of Cr and heterogeneous microstructure formation across the weldments, hydrogen embrittlement and residual stresses makes weldability of P92 steel a critical issue.

2.6.1 *Retention of δ-ferrite*

In P92 steel, the microstructure of the weld fusion zone consists of a martensitic matrix having a soft phase (δ-ferrite). The δ-ferrite is much soft, less strong, tougher and more ductile than the martensitic matrix. Both phases have an inverse effect on the mechanical properties of P92 steel (Wang et al., 2018a). The δ-ferrite phase increases the toughness and ductility while martensite decreases them. The mechanical properties of P92 steel welded joints are adversely affected by the δ-ferrite content in weld fusion zone. The evolution of solid-phase fraction from the liquid is predicted from Scheil's solidification calculation using Thermo-Calc, as shown in Fig. 2.7(a). δ-ferrite is the first solid phase that solidifies from the liquid metal during cooling as per the Scheil's solidification prediction. δ-ferrite starts solidifying at temperature of 1505 ^{o}C and the single-phase region (δ-ferrite) completes above 1426 °C.

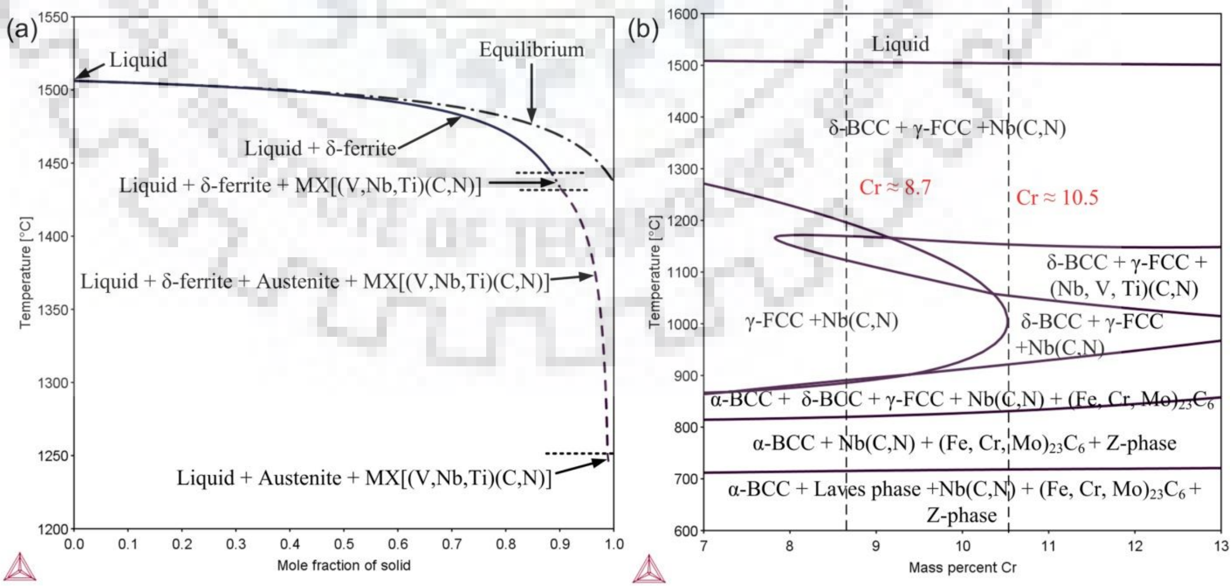

Figure 2.7 (a) Scheil's solidification calculation and (b) isopleth of P92 steel calculated using Thermo-Calc

Then, δ-ferrite starts to transform into austenite (γ-iron) at the temperature of 1426 °C and can continue till the weld metal cools down to below Ac_3 of this material which is 887 °C (above which 100% austenite is stable) (Wang et al., 2017). Sometimes, this transformation is not complete due to kinetic reasons. The main reason is the kinetics of allying elements that affect the chromium equivalent in the weld fusion zone. Further cooling results in retained δ-ferrite fraction in the austenite matrix. The Cr equivalent (Cr_{eq}) for CSEF steels can be calculated using eq. (2.2). If the value of $Cr_{eq}$is higher than 10 then the possibility of δ- ferrite retention is high (Wang et al., 2017; Y. Wang et al., 2016b).

$$Cr_{eq} = Cr + 6Si + 4Mo + 1.5W + 11\,V + 5Nb - 40C - 30N - 4Ni - 2Mn - 2Co \qquad (2.2)$$

An isopleth of Grade P92 steel is also calculated using Thermo-calc software (Fig. 2.7(b)). It also shows that δ-BCC (δ-ferrite) is the first phase that nucleates from the liquid and transforms into γ-FCC (austenite) during solidification. The formation of δ-ferrite is controlled by the concentrations of ferrite stabilizers, like Cr and W. At nominal Cr concentration (8.7 %), the δ-BCC (δ-ferrite) transforms completely into γ-FCC (austenite) during cooling, as shown in Fig. 2.7(b) by the left dash line. During initial solidification, micro-segregation may cause Cr enrichment. However, the Cr concentration exceeds the 10.5 % a duplex region of δ-ferrite and austenite are formed as shown by the right dash line. During further cooling when temperature decreases, the δ-BCC (δ-ferrite) grains will be retained in the austenite.

To predict δ-ferrite in the weld fusion zone, several empirical formulas available in literature such as Schaeffler, Schneider, Kaltenhauser and Newhouse are used which works on the chemical composition of the weld metal. Table 2.3 shows the various empirical formulas available in the literature.

Table 2.3 Various empirical formulas to predict δ-ferrite

Empirical formulas	Chromium equivalent (Cr_{eq})	Nickel equivalent (Ni_{eq})	Ferrite Factor (FF = Cr_{eq} - Ni_{eq})
Schaeffler	Cr_{eq} = Cr + Mo + 1.5Si + 0.5Nb	Ni_{eq} = Ni + 30C + 0.5Mn	≥ 10 than possibility of δ-ferrite
Schneider	Cr_{eq} = Cr + 2Si + 1.5Mo + 5V + 1.75Nb + 0.75W	Ni_{eq} = Ni + 0.5Mn + 30C + 25N + 0.3Cu	≥ 8 than possibility of δ-ferrite
Kaltenhauser	Cr_{eq} = Cr + 6Si + 4Mo + 8Ti + 2Al + 4Nb	Ni_{eq} = Mn + 4Ni + 40(C+N)	≥ 10 than possibility of δ-ferrite
Newhouse	Cr_{eq} = Cr + 6Si + 4Mo + 11V + 5Nb+ 1.5W + 12Al+ 8Ti	Ni_{eq} = 2Mn + 4Ni + 40C + 30N + 2Co+ Cu	≥ 10 than possibility of δ-ferrite

The ferrite factor (FF = Cr_{eq} - Ni_{eq}) is used as a parameter that can predict the presence of δ-ferrite in the weld fusion zone. To improve the accuracy of predicted δ-ferrite, these formulas have been developed subsequently by adding more weights/elements. The Kaltenhauser formula is not suited for P92 steel because W is not considered in this formula which is major alloying element in P92 steel. But the Newhouse formula was best suited to P92 steel because of the enhanced weight to elements like V, Nb and W which are major alloying elements in P92 steel.

The PWHT does not affect the δ-ferrite in the welds of P92 steel. To avoid the existence of room temperature stable δ-ferrite, the composition must be designed carefully to balance the ferrite and austenite stabilizer elements in the chemical composition. The higher percentage of ferrite stabilizing elements (W, Mo, Nb, and V) resulted in the retention of δ–ferrite (Arivazhagan et al., 2011). The retention of δ-ferrite is often observed adjacent to weld fusion line (weld fusion zone or/and heat affected zone) (Kuper and Alexandrov, 2019). The nucleation/growth of Laves phase in Grade P92 steel was observed faster in delta ferrite as compared to martensite due to higher solubility of W in delta ferrite (Baek et al., 2005).

The hardness of δ-ferrite reported in the range of 190-250 VHN while the hardness of matrix region was in the range of 420-490 VHN for dissimilar welded joint of P91 and P92 steel (Chandan Pandey et al., 2018a). The retention of δ-ferrite resulted in a reduction in strength and increase the toughness (not always fracture toughness) and ductility of martensitic steels (Schäfer, 1998). The presence of δ-ferrite patches in P92 steel welds has been observed a negative effect on mechanical properties due to notch sensitivity of the δ-ferrite (Onoro, 2006; Wang et al., 2017). It is possible to control the formation of retained austenite and δ-ferrite by optimizing the base and filler metal composition (Abson and Rothwell, 2013a). The high number of ferrite-forming elements resulted in excessive formation of δ-ferrite (Mandziej et al., 2011).

A schematic showing retension of δ-ferrite is shown in Fig. 2.8. δ-ferrite starts to transform into austenite at 1426 ^{o}C of tempearture. The δ-ferrite phase is dominated till 1250 ^{o}C of temperature. After that austenite phase is dominated over δ-ferrite. At higher temperature, the fast diffusion of solute atoms occurred along the boundaries (Liu et al., 2011). The austenite transforms into ferrite and further ferrite transforms to martensite. Below martensite start temperature (M_s), the δ-ferrite stripes are retained in the martensite microstructure.

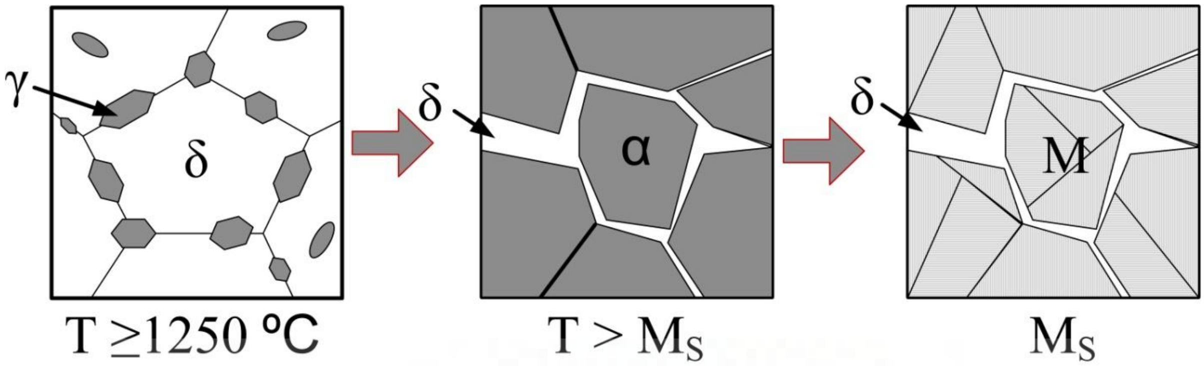

Figure 2.8 schematic showing retension of δ-ferrite (Liu et al., 2011).

2.6.2 *Heterogeneity and depletion of Cr in the weldments*

The mechanical properties of the P92 weldments are strongly influenced by the phase transformations occurring within the weldments of P92 steel. The optimized base material properties and microstructure are changed completely during the weld thermal cycle. Figure 2.9 shows the various heat-affected zones (HAZs) formed due to weld thermal cycle and equilibrium phase diagram of P92 steel (C. Pandey et al., 2018; Robson et al., 2010; Upadhyay and Reynolds, 2015). Based on Ac_1 and Ac_3 temperatures of P92 steel, the various sub-zones formed in the weldments are discussed below:

(a) Weld fusion zone (peak temperature (T_P) > melting temperature(T_M))

In P92 steel, according to the equilibrium phase diagram, austenite transformed to δ-ferrite at melting temperature. The lower solubility of C and other austenite stabilizing elements in ferrite resulted in the escape of these elements out of the δ-ferrite into the remaining austenite regions. Therefore, segregated regions differ locally in chemical composition. The austenite to martensite transformation on cooling can be incomplete, which results in the formation of retained δ-ferrite in the weld fusion zone. In P92 steel, the presence of ferrite stabilizer elements like W, Mo, V, and Nb also promotes the formation of δ-ferrite in the weld fusion zone. The higher weight percentage of C and N in solution matrix results in poor Charpy toughness and high strength of the weld fusion zone (Silwal et al., 2013).

(b) Coarse-grained heat affected zone (CGHAZ) (T_P >> Ac_3)

The zone adjacent to the weld fusion zone (i.e. CGHAZ) experienced temperatures much above the transformation temperature (Ac_3). At such high temperature, almost all precipitates are dissolved, except for some fine NbX type precipitates that resulted in the formation of the coarse austenite grains (Cao et al., 2011). After cooling, austenite gets transformed into the martensite. The dissolution of precipitates resulted in a higher weight percentage of C and N in the solid solution matrix. That leads to poor Charpy toughness and high hardness of CGHAZ among all HAZs.

(c) Fine-grained heat affected zone (FGHAZ) ($T_P > Ac_3$)

The zone adjacent to CGHAZ (i.e. FGHAZ) experienced the temperatures just above the Ac_3, which resulted in the formation of small grains of austenite. In FGHAZ, peak temperature is not too high to dissolve the precipitates completely, thus grain growth limited by the pinning austenite grain boundaries. On cooling, the fine-grained martensitic structure is achieved in the FGHAZ of the weldment. The coarse undissolved $M_{23}C_6$ precipitates are observed in the FGHAZ while the fine MX precipitates remain undissolved. The presence of coarse undissolved $M_{23}C_6$ precipitates and untempered martensite makes the FGHAZ more complex than the CGHAZ (Wang and Li, 2016).

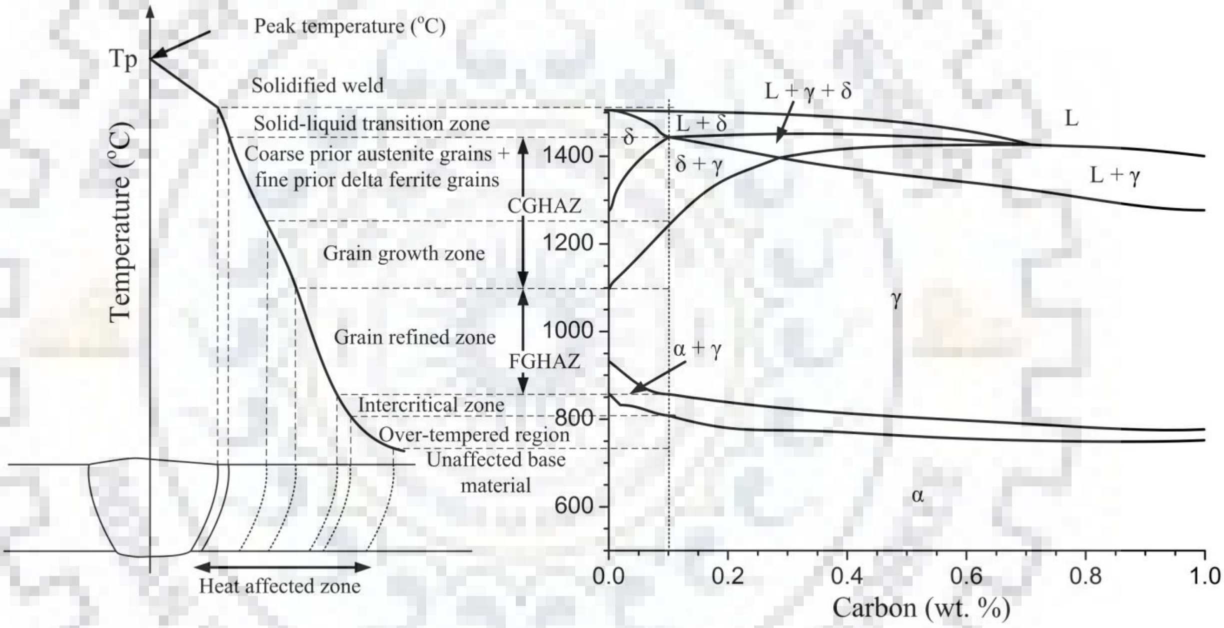

Figure 2.9 Schematic of the subzones formed in the weldments and equilibrium phase diagram of P92 steel (C. Pandey et al., 2018)

(d) Inter-critical heat affected zone (ICHAZ) ($Ac_1 < T_P < Ac_3$)

The next zone formed adjacent to the FGHAZ is the ICHAZ, which experienced the peak temperatures between the transformation temperatures Ac_1 and Ac_3. In this temperature range, the partial transformation of ferrite into austenite occurred during heating, whereas new austenite grains nucleated at prior austenite grain boundaries and the untransformed tempered martensitic microstructure is tempered for a second time by this weld thermal cycle. On cooling, both newly formed martensite and tempered original martensite microstructure were obtained. Partial dissolution of precipitates is observed in the ICHAZ. The ICHAZ is characterized by the small grain size and the combination of partially tempered and untempered martensite microstructure (Y. Wang et al., 2016b).

(e) Over-tempered base material ($T_P < Ac_1$)

The zone adjacent to ICHAZ (i.e. over-tempered base material) experienced temperatures below the Ac_1. Below Ac_1 temperature, the microstructure does not undergo any phase transformation. But the microstructure is locally tempered at higher temperatures as compared to tempering temperature of the base material which might be enhanced the coarsening of precipitates. The zone of unaffected base material experienced the peak temperature below 700 °C at which no visible changes in the microstructure of base material is observed (Milovic´ et al., 2013).

These zones develop heterogeneity in microstructure as well as in properties across the weldments, which result in reduced life of components. Therefore achieving uniform properties have been a concern and it is as well a technological challenge to heat treat each individual zone of the HAZat different tempering temperature. In the weldments especially in the heat-affected zone (HAZ), the depletion of Cr occurred on the grain boundaries in the temperature range of 450 °C to 850 °C due to the formation, growth and precipitation of Cr-rich carbide particles. Such evolution of Cr-rich carbides reduces the free Cr content and makes HAZ susceptible to intergranular cracking and drastically reduces the local corrosion resistance. To avoid the formation of Cr-rich carbides, the low C specification is made. In weldments, HAZ possesses lower creep rupture life as compared to P92 base metal due to its non-equilibrium microstructure (L. Xu et al., 2016).

Welding introduces localized changes in the microstructure, which become the life-limiting factor for these steels. In particular, type IV cracking is a phenomenon in which an enhanced rate of creep void formation occurs in the FGHAZ or ICHAZ (Bruscato, 1970). During the welding of P92 steel, the temper martensitic microstructure is adversely altered by the formation of fresh martensite in the weldments (weld fusion zone + HAZs) (C. Pandey et al., 2017). The nominal strength of P92 steel may be compromised by susceptibility to type-IV cracking in HAZs of welds while increasing contents of ferrite-forming elements like V, Nb, W, Mo, and Cr, may lead to excessive formation of δ-ferrite (Mandziej et al., 2011).

Due to type IV cracking, the premature failure in the cross welds is observed at an earlier stage of creep exposure as compared to the base materials (Wang et al., 2018b). The type IV cracking also reduces the creep rupture strength of cross-welds by 50% as compared to base materials (Falat et al., 2016). A post-weld heat treatment (PWHT) is a mandatory operation carried to reduce the non-equilibrium microstructure gradient and minimize the hardness mismatch across the weldment (Chalk et al., 2011; Xue et al., 2012).

The specification of preheating and PWHT conditions is an important concern because P92 steel is a high strength alloy steel that normally transforms completely to martensite during air cooling (Cerjak and Letofsky, 1996). To reduce the hardness and improve the ductility of the weld/HAZ, the PWHT is carried out just after welding at 760 ^{o}C (± 10 ^{o}C) for the P92 steel (Chhibber et al., 2012; Dodo et al., 2016). The PWHT resulted in a greater reduction in hardness, improved ductility and toughness of the weldments.

2.6.3 *Hydrogen embrittlement*

Stress corrosion cracking and hydrogen embrittlement are common threats to structural integrity (Alvaro et al., 2015). It is generally caused by the moisture present at the time of repair welding. Hydrogen damage generally occurs in boiler tubes (Dayal and Parvathavarthini, 2003). The diffusible hydrogen content in the deposited weld metal is determined by different methods like the Glycerin method, Gas chromatography method, Vaccum hot extraction method and Mercury method. For the measurement of lower hydrogen content, Mercury method is more precise than others (Fydrych, 2017). The diffusible hydrogen content is found much larger in arc welding processes (Kumar and Yu-ichi, 2013).

Welding consumables are the main source of hydrogen in the CSEF welds (Kumar and Yu-ichi, 2013). The actual hydrogen content depending primarily on the type of welding consumable, type of coating and/or on shielding gas (Chhibber et al., 2008; Sharma and Chhibber, 2019). Hydrogen-assisted cracking (HAC) is one of the most common problems encountered in CSEF steel welds and it is also known as under bead cracking or delayed cracking or cold cracking (Dayal and Parvathavarthini, 2003; Louthan, 2008). During service, the weldments of CSEF steels poses the danger of catastrophic failure due to HAC (Johnson, 1874; Woodtli and Kieselbach, 2000). It is known to noticeably degrade the mechanical properties mainly fracture toughness, fracture strength and ductility. It is widely known that hydrogen, tensile residual stresses and hard microstructure are three major aspects that are responsible to cause HAC in the weldment (Chandan Pandey et al., 2016).

The other factors influencing these three major factors to cause HAC are given in Fig. 2.10. Granjon implant test was utilized to determine susceptibility towards HAZ HAC. Lower critical stress (LCS) is a critical factor to evaluate the HAZ HAC susceptibility. LCS is maximum stress at which failure is not encountered after 24 hours of loading (Dickinson and

Ries, 1977). To decrease diffusible hydrogen or to prevent the HAC in the weld metal, use of low hydrogen fillers, baking of fillers, pre and post-weld heating are advisable (I A Shibli, 2006; Nisho et al., 1971).

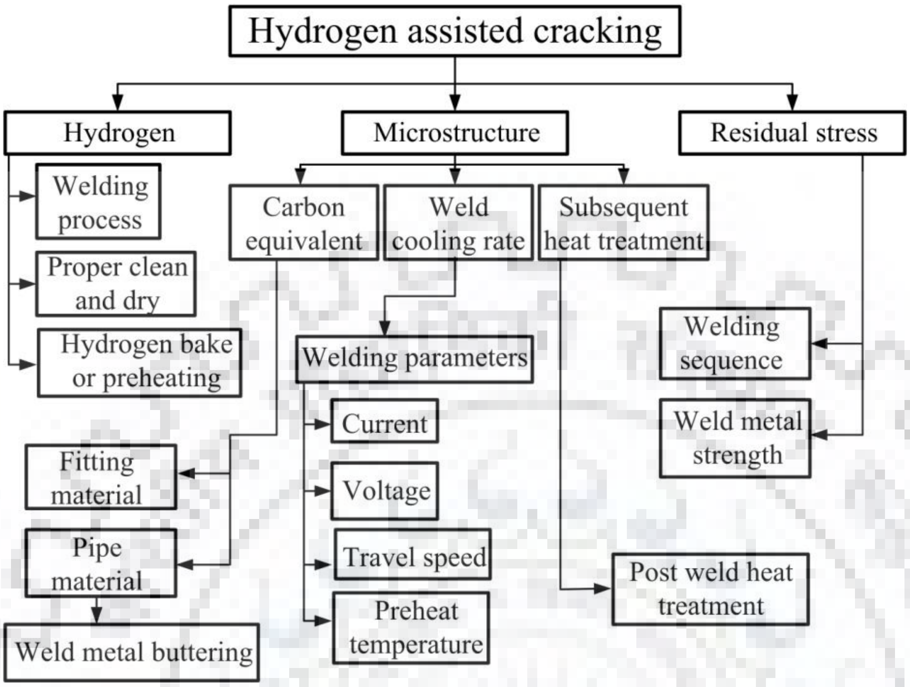

Figure 2.10 Schematic showing various factors influencing HAC

In underwater welding, the diffusible hydrogen content increased 54 to 87 % as compared to the diffusible hydrogen level in air welding (Fydrych and Rogalski, 2011). Gedeon et al. (Gedeon and Eagar, 1990) find maximum hydrogen absorption occurred around the outer edge of the weld pool instead of Sivert’s rule which suggests that the maximum absorption should occur at the center of the weld pool or in the high-temperature region. To prevent HAC in CSEF steel welds, the minimum recommended preheating temperature is 150 ^{o}C (J. Wang et al., 2016). The preheating of base plates is carried out in the temperature range of 200-250 ^{o}C to maximize the LCS value (Albert et al., 2011). To minimize the chances of HAC, the post-weld heat treatment (PWHT) also recommended which will temper the microstructure and facilitate diffusion of hydrogen from the deposited metal (Padhy et al., 2012; Pandey and Mahapatra, 2016a).

2.7 Research gap

- The optimum combination of normalizing and tempering temperatures for P92 steel has not been reported in the literature.
- The effect of Laves phase coarsening on the mechanical properties during long-term aging has not been reported yet.

- The dissolution of Laves phase has not been reported yet.
- A model to predict preheating temperatures for thin plates in autogenous TIG welds has not been observed in the literature.
- The dissolution of the delta ferrite phase in the weldments has not been reported yet.
- The effect of filler compositions on the microstructure evolution and mechanical properties of P92 steel welded joints has not been reported yet.
- The effect of post-weld heat treatments and filler compositions on the microstructure evolution and mechanical properties of dissimilar welded joints of P92 steel with P911 and P92 have not been observed in the literature.
- Effect of welding parameters and filler conditions on diffusible hydrogen content and embrittlement of P92 steel welds needs a relook.

2.8 Objective

- To study the effect of normalizing temperature on the microstructure evolution and mechanical properties of P92 steel.
- To study the effect of tempering time on the coarsening of Laves phase and their effect on the mechanical properties during long-term aging.
- To study the dissolution of Laves phase in the long-term aged specimens.
- To suggest a model to predict preheating temperatures for thin plates in autogenous TIG welds.
- To study the dissolution of delta ferrite phase in the weldments of P92 steel.
- To study the effect of filler compositions on the microstructure evolution and mechanical properties of P92 steel welded joints.
- To study the effect of post-weld heat treatment and filler compositions on the microstructure evolution and mechanical properties of dissimilar welded joints of P92 steel with P911 and P92.
- To study the effect of welding parameters and filler conditions on diffusible hydrogen content and their effect on embrittlement of P92 steel welds.

CHAPTER 3. HEAT TREATMENT OF GRADE P92 STEEL

In this chapter, the effect of varying normalizing temperatures and followed by a tempering temperature on microstructure evolution and mechanical properties of as-received P92 steel have been performed. The effect of long-term ageing on the microstructure and degradation of mechanical properties has been studied. The effect of normalizing followed by tempering on dissolution of Laves phase has been studied. The effect of double austenitization on the microstructural and mechanical properties have also been studied.

3.1 Experimental details

3.1.1 *As-received material*

The as-received material used for the investigation was 9Cr-1.8W-0.5Mo-VNb (Garde P92 steel) with the dimension of 300 mm × 60 mm × 12 mm. P92 steel designated as P92 for pipe and T92 for tube and ASTM A335 for the plate. The as-received material was in a cast forged (C&F) state. The chemical composition of P92 steel was analyzed using the inductively coupled plasma mass spectrometry (ICP-MS) and given in Table 3.1.

Table 3.1 Chemical composition of P92 steel, (wt. %)

	C	Cr	Mo	W	Nb	V	Mn	Al	Co	Si	N	Ni	Cu	Fe
P92 steel	0.09	8.7	0.41	1.81	0.04	0.19	0.51	0.01	0.03	0.22	0.04	0.11	0.01	balance

3.1.2 *Heat treatments*

3.1.2.1 Optimization of normalizing temperature

The as-received P92 steel was heated to an initial heat treatment of normalizing temperature in the range of 950 °C to 1150 °C for 1 h and then subjected to tempering temperature of 760°C for 2 hrs. The heat treatment matrix to optimize normalizing temperature is depicted in Table 3.2.

Table 3.2 Heat treatment matrix for specimens

Sample No.	Normalizing Temperature	Tempering Temperature
1	950 °C + AC*	760 °C + AC*
2	1000 °C + AC*	760 °C+ AC*
3	1050 °C + AC*	760 °C + AC*
4	1100 °C + AC*	760 °C + AC*
5	1150 °C + AC*	760 °C + AC*

AC*- Air cooled

3.1.2.2 Long-term ageing

The as-received material was normalized and tempered before subjected to long term ageing. The normalizing heat treatment was carried out for 1 h at 1000 °C. This was followed by tempering at 760 °C for 2 hrs. The long-term ageing treatment was conducted in a furnace under a protective layer of Al_2O_3 and FeCr powder mixture at 650 ^{0}C for 720 hrs, 1440 hrs, 2160 hrs and 3000 hrs ageing time.

3.1.2.3 Effect of normalizing and tempering on dissolution of Laves phase

The long-term ageing was performed in a furnace at 620 ^{0}C for 4560 h ageing time. After long-term ageing, normalizing and tempering was performed with varying tempering time from 2 hrs to 4 hrs. The heat treatment matrix is depicted in Table 3.3.

Table 3.3 Heat treatment matrix for specimens

Sample No.	Long-term ageing	Normalizing	Tempering	Abbreviation
1	620 ^{o}C/4560 hrs + FC*	-	-	Aged
2	620 ^{o}C/4560 hrs + FC*	1050 ^{o}C/1 h + AC**	760 ^{o}C/2 hrs + AC**	Aged+N&T2
3	620 ^{o}C/4560 hrs + FC*	1050 ^{o}C/1 h + AC**	760 ^{o}C/4 hrs+ AC**	Aged+N&T4

FC*-Furnace cooled; AC**-Air cooled

3.1.2.4 Double austenitization treatment

The two heat treatments such as conventional normalizing treatment (CNT) and double normalizing treatment (DNT) were carried out. The heat treatment conditions of as-received P92 steel is depicted in Table 3.4.

Table 3.4 Heat treatment matrix for samples

Condition(s)	First Normalizing temperature	Second normalizing temperature	Tempering
CNT	-	1040 ºC/1 h + AC**	760 ^{o}C/2 h + AC**
DNT 1	950 ºC/1 h + WC*	1040 ºC/1 h + AC**	760 ^{o}C/2 h + AC**
DNT 2	1050 ºC/1 h + WC*	1040 ºC/1 h + AC**	760 ^{o}C/4 h + AC**
DNT 3	1150 ºC/1 h + WC*	1040 ºC/1 h + AC**	760 ^{o}C/2 h + AC**

WC*-Water cooled; AC**-Air cooled`

3.1.3 *Material characterization*

In order to characterize the sample for field-emission scanning electron microscope and optical microscope, standard metallographic techniques were used. In the standard metallographic technique, initially grinding of samples was performed by using the silicon carbide paper upto grit size of 2000. After grinding, cloth polishing with alumina powder was performed to remove the paper scratches. After polishing, samples were etched in Vilella's reagent (1 g picric acid + 5 ml hydrochloric acid + 100 ml ethanol) for 80 sec. The microstructural examinations of heat-treated specimens were conducted using an optical microscope (OM) and QUANTA 200 Field-emission scanning electron microscope (FESEM) to calculate the precipitates size, fraction area of precipitates and grain size of the microstructure. The precipitate size was measured using Image J software.

3.1.4 *Material testing*

The microhardness measurement of as-received and heat-treated specimens of P92 steel was carried with Vickers Hardness Tester (Omnitech-S. Auto), at the load of 500 g and dwell time of 10 s. To find out, the various phase formed in different heat-treated condition, X-ray diffraction (XRD) of specimens was conducted on D-8 Bruker AXS diffractometer. XRD analysis was performed with 0.2^o speed by using Cu target. To perform a static tensile test for as received P92 steel and heat-treated conditions, flat sub size tensile specimens were prepared. The tensile specimens were prepared for gauge length of 25 mm and width 6.25 mm, as per ASTM A370-14. To perform the tensile test, the vertical tensile testing machine (Instron 5982) was used at room temperature. The crosshead speed was maintained 1 mm/min for all the specimens. The average of three tested specimens was noted for each heat-treated condition.

To study the impact toughness of heat-treated samples, the standard sub-size V-notch specimens were prepared according to ASTM A370 with dimensions 55mm × 10mm × 5mm and 55mm × 10mm × 7.5mm for Charpy impact test. Three specimens were prepared for each test and average of three test results was taken. The fracture surface of impact and tensile tested specimen were characterized by using FESEM. To characterize the effect of heat treatment on the element percentage, Energy-dispersive X-ray spectroscopy (EDS) of fracture surfaces was also carried out.

3.2 Results and discussion

3.2.1 *As-received material*

The as-received P92 steel was characterized with tempered martensitic microstructure with maximum coarse precipitates at the prior austenite grain boundaries (PAGBs) and fine precipitates within matrix region or subgrain boundaries as shown in Fig. 3.1(a-b).

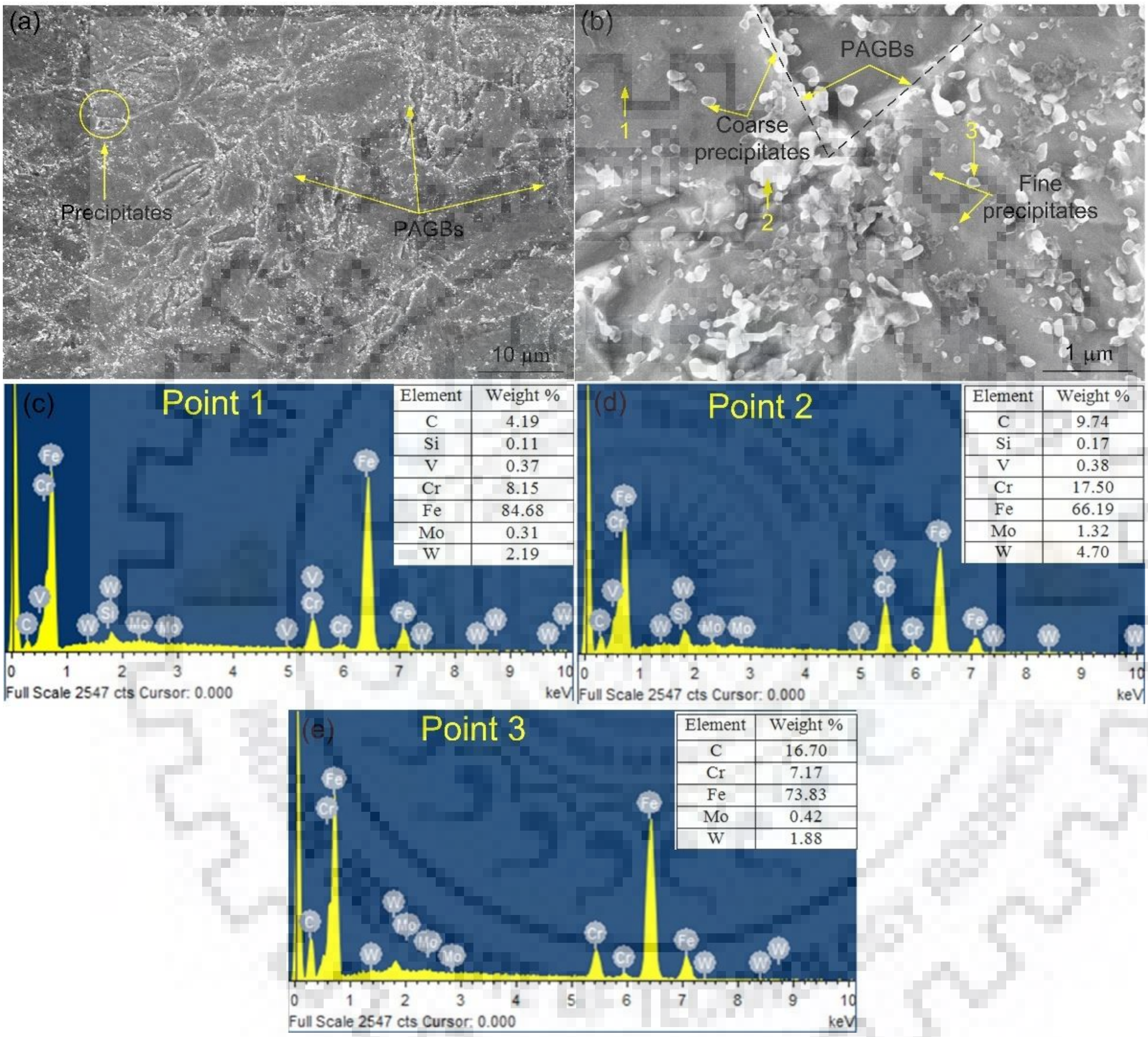

Element	Weight %
C	4.19
Si	0.11
V	0.37
Cr	8.15
Fe	84.68
Mo	0.31
W	2.19

Element	Weight %
C	9.74
Si	0.17
V	0.38
Cr	17.50
Fe	66.19
Mo	1.32
W	4.70

Element	Weight %
C	16.70
Cr	7.17
Fe	73.83
Mo	0.42
W	1.88

Figure 3.1 As-received microstructure of P92 steel: (a) SEM at 5000x, (b) SEM at 50000x, (c) EDS in the matrix region as point-1, (d) EDS of precipitates present at PAGB as point-2, (e) EDS of precipitates located inside the matrix as point-3

Precipitation hardening is the main strengthening mechanism in P92 steel. The formation of precipitates such as Mo, Fe and Cr-rich $M_{23}C_6$ and Nb, V and Ti-rich fine MX particles was promoted by fine alloying elements such as C, N, V, Nb, W, and Mo. The V, Ti, and Nb-rich MX precipitates were nearly spherical shape, while Cr-rich $M_{23}C_6$ precipitates were elongated block-like or rod-like particles as shown in Fig. 3.1(b). The $M_{23}C_6$ type precipitates were found at PAGBs and lath (Choudhary et al., 2013; Hurtado-noreña et al., 2015). The average precipitate size in as received Garde P92 steel was measured to be 150±66 nm at the PAGBs and 94±31 nm within the matrix region.

The FESEM-EDS analysis of the matrix confirms the presence of Cr and Mo-rich $M_{23}C_6$ type precipitates at PAGBs and indicates the presence of MX type precipitates in the matrix as shown in Fig. 3.1(c). The EDS analysis of precipitates at the PAGBs (point-2) confirms the presence Cr-rich $M_{23}C_6$ precipitates as shown in Fig. 3.1(d). It was also observed that coarse white particles present at the PAGBs were enriched with Cr and Mo as compared with fine precipitates present within the grain interior, i.e. lean in Cr and Mo as shown in Fig. Fig. 3.1(d) and (e). It was difficult to show the presence of small size precipitates of VC, NbN, VN, WC and NbC within the subgrain boundary and in the matrix but the EDS analysis of white particles at the PAGBs and in the matrix confirmed the presence of MX-type precipitates. The as-received P92 steel had measured grain size of about 39.50 µm. The similar results have also been reported by Wang et al. [6]. The mechanical properties of as-received C&F P92 steel are given in Table 3.5.

Table 3.5 Mechanical properties of P92 steel in as-received state

P92 steel	Yield strength (MPa)	Tensile strength (MPa)	Elongation, (%)	Microhardness (VHN)	Charpy toughness (Joules)
	670±12	801± 15	16±2	283±2	62±1

3.2.2 *Optimization of normalizing temperature*

3.2.2.1 Microstructure evolution

The SEM images of normalized specimens at 950 °C and 1150 °C are shown in Fig. 3.2(a) and 3.2(e), respectively. The effect of normalizing temperatures on the formation of fresh martensite has been analyzed by taking the SEM micrograph of P92 steel at different normalizing temperatures (950 °C-1150 °C). The normalized steel specimens mainly exhibited lath martensite type of structure with distinct PAGBs. Fig. 3.2(a) clearly indicates the presence of lath martensite in the form of group/packets inside the PAGBs. From Fig. 3.2(a) and 3.2(e), it can be observed that the formation of fresh martensite increases with an increase in normalizing temperature. The SEM micrograph reveals the presence of lath martensite patches in the local area of the martensitic matrix.

The P92 steel has a very strong tendency to form martensite under furnace or air cooling. The width of lath boundary and dissolution of precipitates were found to be enhanced with increasing the normalizing temperature from 950 °C to 1150 °C. EDS analysis of the normalized specimens was carried out to confirm the presence of $M_{23}C_6$ type and MX type precipitates at the PAGBs and in the matrix. EDS spectra of the matrix area (point 1), in the matrix (point 2) and at the PAGB (point 3) confirmed that the particles present in the matrix, lying along the lath boundaries and within the sub-grain boundaries are $M_{23}C_6$ type precipitates as shown in Fig. 3.3 (b), (c) and (d).

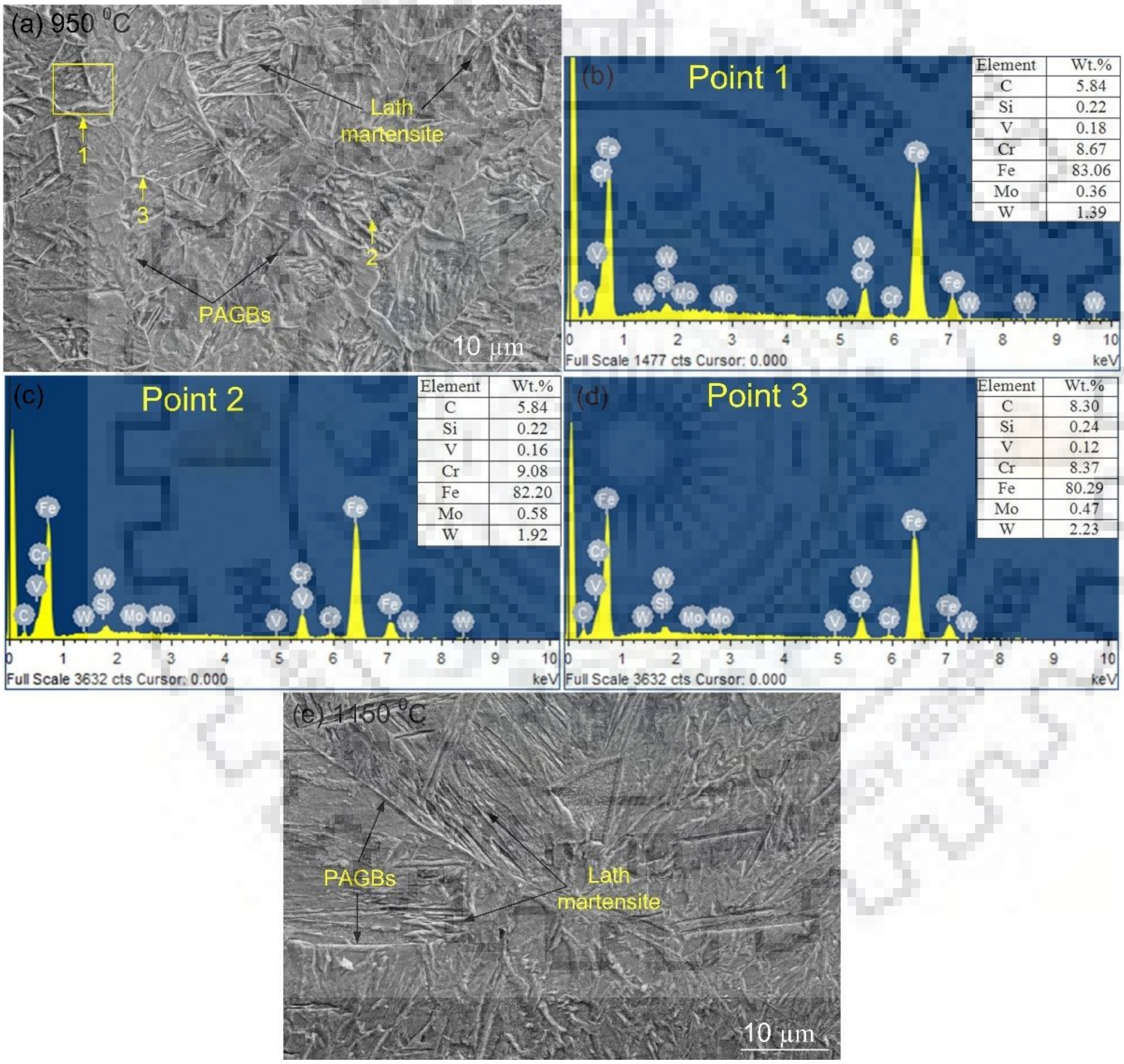

Element	Wt.%
C	5.84
Si	0.22
V	0.18
Cr	8.67
Fe	83.06
Mo	0.36
W	1.39

Element	Wt.%
C	5.84
Si	0.22
V	0.16
Cr	9.08
Fe	82.20
Mo	0.58
W	1.92

Element	Wt.%
C	8.30
Si	0.24
V	0.12
Cr	8.37
Fe	80.29
Mo	0.47
W	2.23

Figure 3.2 (a) Secondary electron micrograph of sample normalized at 950 °C, (b) EDS in the matrix area (point 1), (c) EDS in the matrix (point 2), (d) EDS at PAGB (point 3) and (e) micrograph of sample normalized at 1150 °C

The optical micrographs of C&F P92 steel for different N&T state are shown in Fig. 3.3(a-e). The optical micrograph showed in Fig. 3.3(a) is taken for sample normalized at 950 °C and tempered at 760 °C. The bulged and the straight boundary can be seen clearly from the optical micrograph at various normalizing temperatures as shown in Fig. 3.3(b-e). The consequence of tempering of normalized P92 steel was N and C rejection from the solution and formation of nitride and carbide precipitates. For normalized P92 steel at 1150 °C and tempered at 760 °C, a higher amount of coarsening was observed as shown in Fig. 3.3(e).

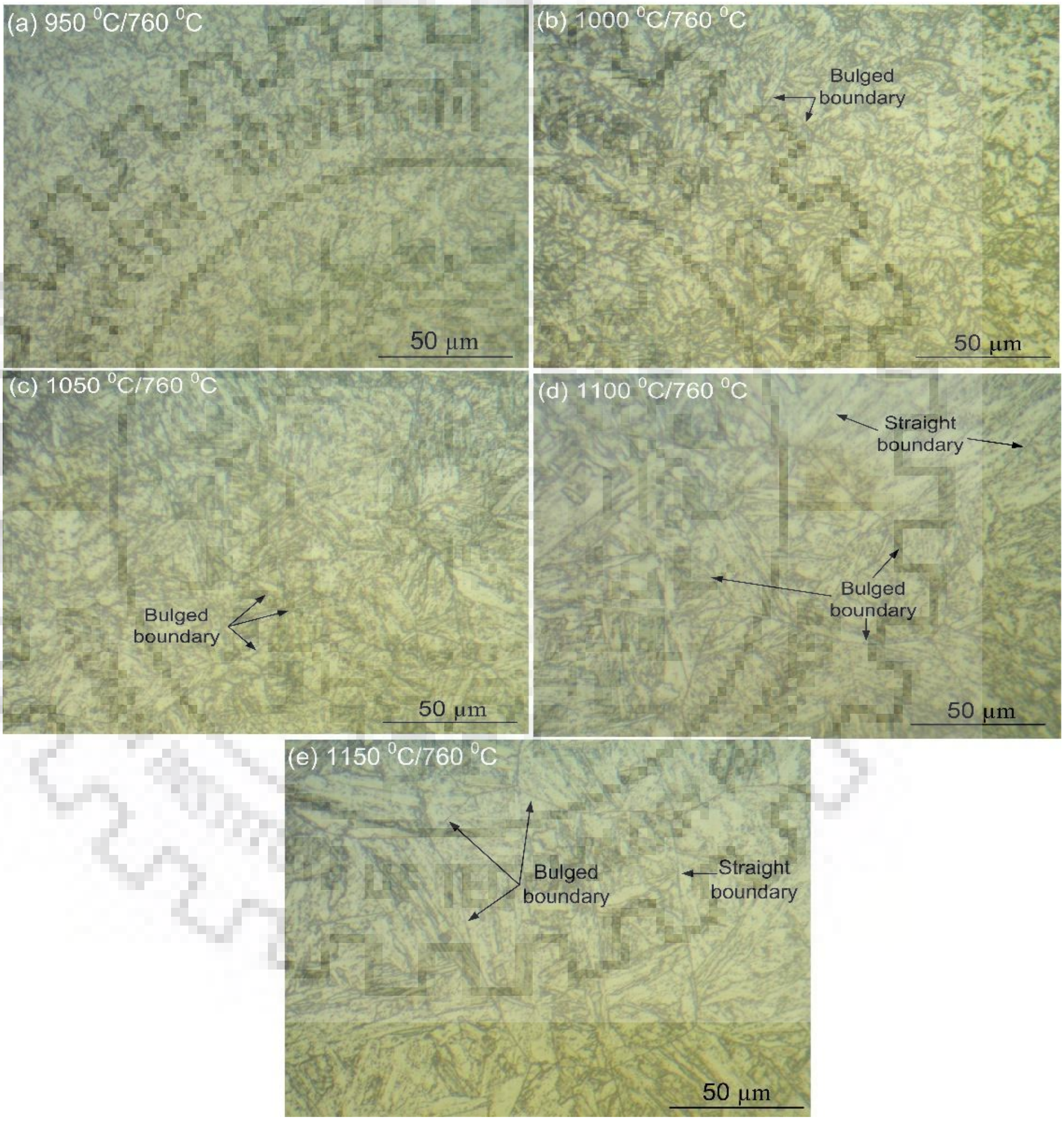

Figure 3.3 Optical micrographs of sample after N&T treatment: (a) 950 °C/760 °C (b) 1000 °C/760 °C, (c) 1050 °C/760 °C (d) 1100 °C/760 °C and (e) 1150 °C/760 °C

A small change was observed in grain size up to a normalizing temperature of 1000 °C and after that a considerable grain coarsening was found. The grain size was found to be increased with increasing normalizing temperature. The specimen normalized at 950 °C for 1 h and tempered at 760 °C for 2 h has a grain size of about 45 μm while the grain size was 61.2 for specimen normalized at 1150 °C for 1 h and tempered at 760 °C for 2 h. The variation in grain size for different N&T treatment is shown in Fig. 3.4.

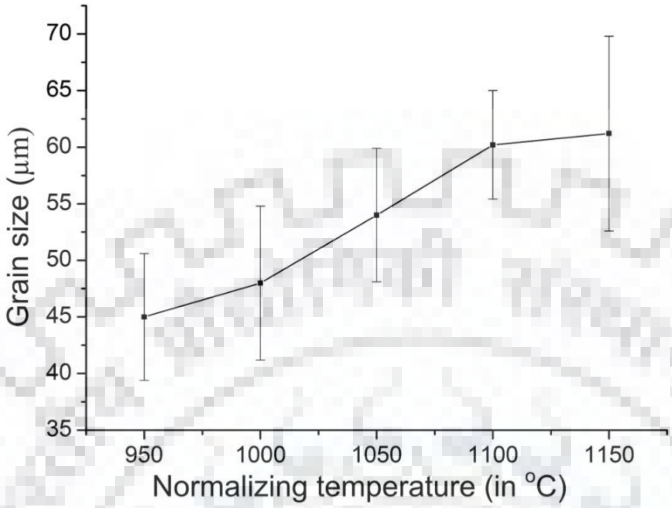

Figure 3.4 Variation in grain size with normalizing temperature

The SEM micrograph of C&F P92 steel for different N&T treatment is shown in Fig. 3.5(a–e). Fig. 3.5(a) shows very fine microstructure of specimen normalized at 950 °C and tempered at 760 °C. As the normalizing temperature increases, grain coarsening occurs. In the top right corner of every SEM image, higher magnification SEM micrograph (at 50,000x) is shown and rest micrograph is taken at low magnification (at 5,000x). Fig. 3.5(c-e) shows coarse microstructure of specimens normalized at 1050 °C, 1100 °C, and 1150 °C, respectively and tempered at 760 °C. Hence, the N&T C&F P92 steel has tempered lath martensitic structure with carbide precipitates along PAGBs as shown in Fig. 3.5. The accumulation of coarse $M_{23}C_6$ precipitates along the PAGBs are clearly seen from the micrograph. Fine MX precipitates are distributed uniformly inside the matrix region.

The SEM micrograph of sample normalized at 950 °C and tempered at 760 °C is shown in Fig. 3.6(a). The EDS spectra of precipitates located at the PAGB (point 1) and matrix area (point 2) is shown in Fig. 3.6(b-c). The EDS spectra confirmed that the particles present in the matrix, lying along the lath boundaries and within the sub-grain boundaries are $M_{23}C_6$ and MX type precipitates. The effect of normalizing temperature on the relative change in the $M_{23}C_6$ carbide composition has been calculated using EDS analysis. The chromium to the iron ratio (Cr/Fe) was calculated to be 0.2643 for as-received material.

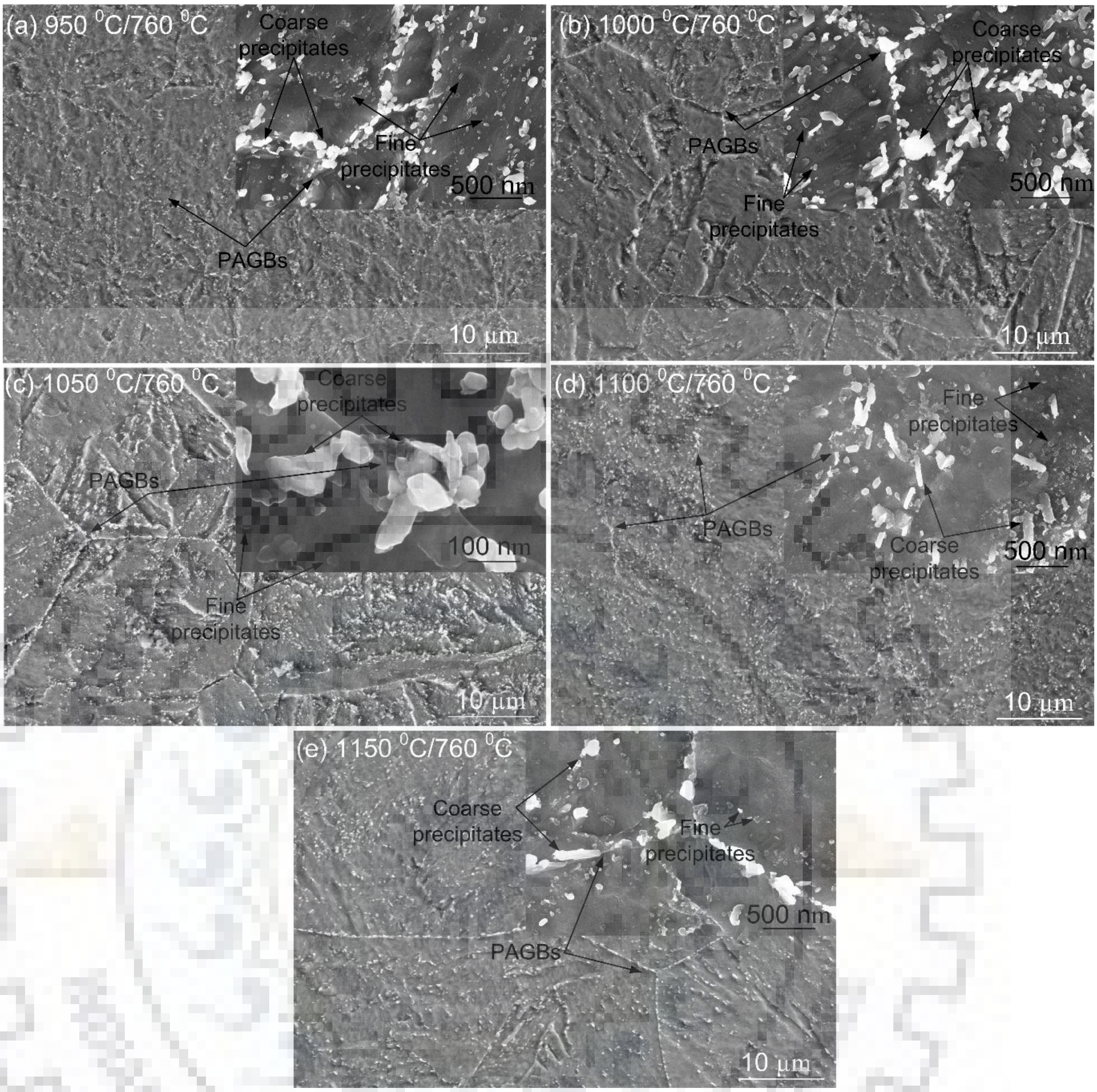

Figure 3.5 Micrographs of samples subjected to different N&T treatment: (a) 950 °C/760 °C (b) 1000 °C/760 °C, (c) 1050 °C/760 °C (d) 1100 °C/760 °C and (e) 1150 °C/760 °C

The variation of Cr/Fe ratio with various normalizing temperature is shown in Fig. 3.7. The Cr/Fe ratio was found to be on a continuous increase for normalizing at 950 °C and up to 1000 °C, and then, it started to decrease with normalizing temperature from 1050 °C to 1150 °C. The maximum and minimum Cr/Fe ratio were calculated for the normalizing temperature at 1050 °C and 950 °C respectively. The diffusion of Cr into the $M_{23}C_6$ carbides results in the evolution of meta-stable $Cr_{23}C_6$ phase, which is a consequence of the increase in Cr/Fe ratio.

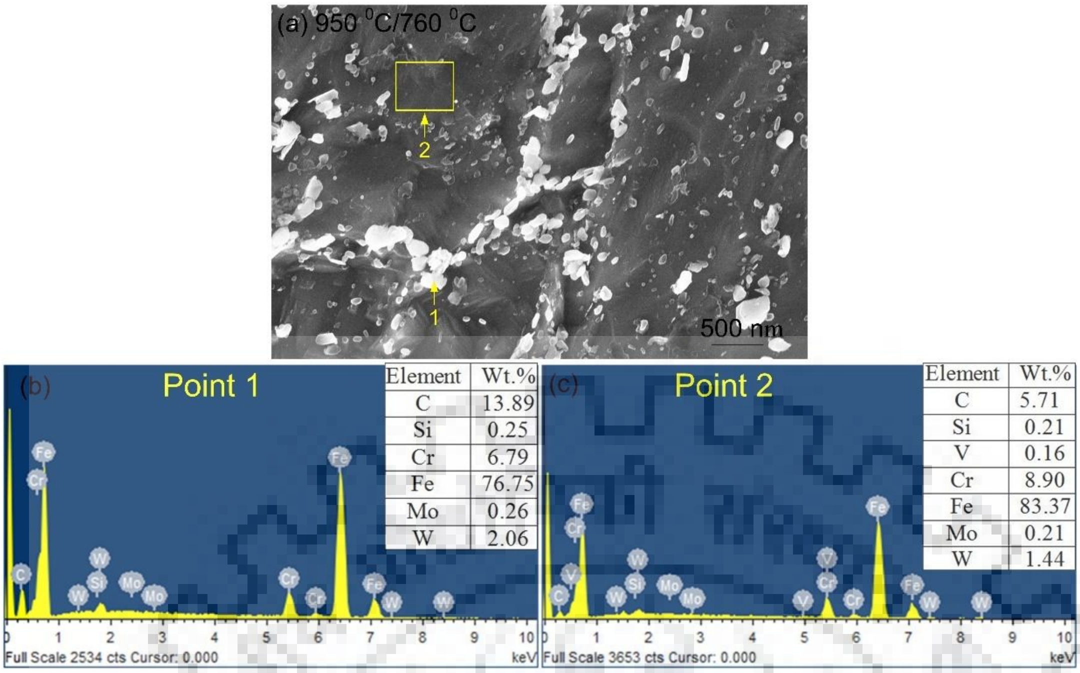

Element	Wt.%
C	13.89
Si	0.25
Cr	6.79
Fe	76.75
Mo	0.26
W	2.06

Element	Wt.%
C	5.71
Si	0.21
V	0.16
Cr	8.90
Fe	83.37
Mo	0.21
W	1.44

Figure 3.6 (a) SEM image of N&T sample (normalize at 950 °C; tempered at 760 °C) (b) EDS of white particles located at the PAGB (point 1) (c) EDS of selected area in the matrix (point 2)

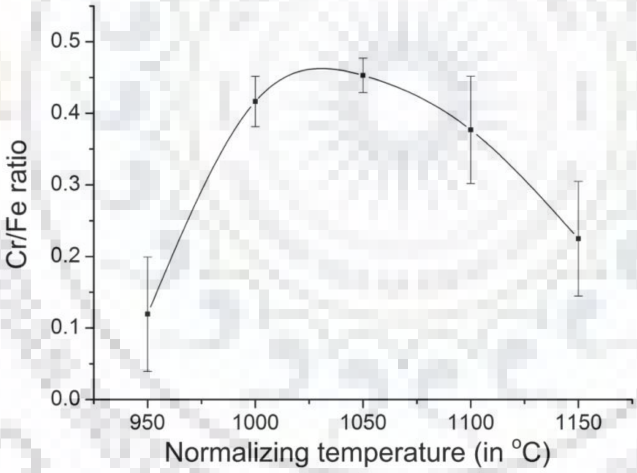

Figure 3.7 Variation of Cr/Fe ratio with normalizing temperature

To determine the precipitates distribution and their size present along PAGBs and grain interior, the SEM micrographs was used at higher magnification. The inter lath region was uniformly oriented in N&T C&F P92 steel with fine MX- type precipitates. The average precipitates size in the as-received material was observed to be 150 ± 66 nm and 94 ± 31 nm at PAGBs and within the grain boundaries, respectively. The variation of particles size present at PAGBs and within the grain is shown in Fig. 3.8. It was observed that the size of precipitates present at PAGBs increases with increase in normalizing temperature. The size of particles present inside the matrix region increases drastically with increase in normalizing temperature from 950 ^{o}C to 1000 °C after that remains constant up to 1150 °C.

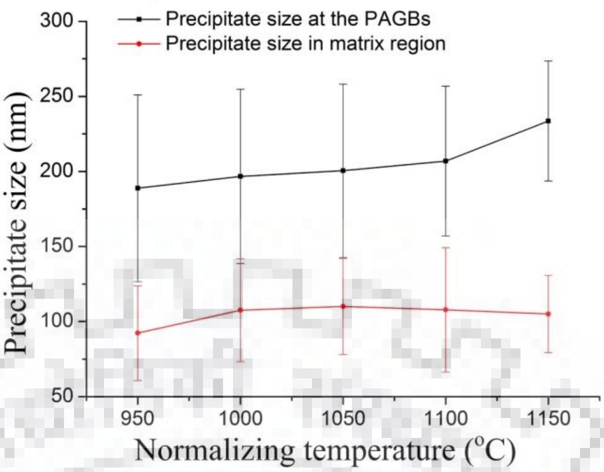

Figure 3.8 Variation of particle size present at the grain boundary and in the matrix region with varying normalizing temperature and fixed tempering temperature of 760 ^{o}C

A drastic increase in precipitate size after 1150 °C is quite harmful to creep strength, as shown in Fig. 3.8. To enhance the creep strength of C&F P92 steel, $M_{23}C_6$ precipitates are more effective as compared to other carbide precipitates because as the size of carbide precipitates are same as the thickness of sub-grain boundaries. It is difficult for sub-grains to cross the $M_{23}C_6$ precipitates. Hence, these carbide precipitates provide a pinning effect which prevents dislocation at subgrain boundaries and enhances creep strength.

The average interparticle spacing mainly depends on the size of precipitates (*d*) and carbide phase (*f*). The inter-particle spacing (particle-to-particle spacing) (L) is given by eq. (3.1) (Vodopivec et al., 2004);

$$L = \frac{4d}{\prod f^{\frac{1}{3}}} \tag{3.1}$$

The data relevant to as-received P92 steel in eq. (3.1) gives L= 3.86 d for the same quantity of carbide phase. Hence, according to this equation, the particle to particle spacing grow approximately four times than the precipitate size. The variation of inter-particle spacing for various N&T conditions is graphically represented in Fig. 3.9(a). The inter-particle spacing was calculated as 0.4709 µm for as- received material. The inter-particle spacing increased continuously with the increase in normalizing temperature.

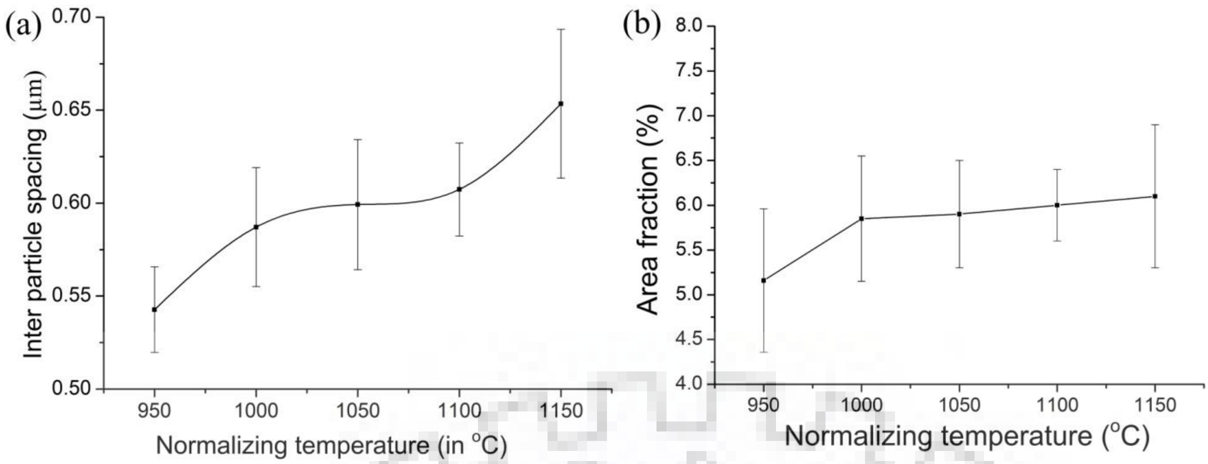

Figure 3.9 (a) Variation in inter particle spacing and (b) variation of area fraction of precipitates with varying normalizing temperature and fixed tempering temperature

The variation of % area fraction of precipitates for various N&T conditions is presented in Fig. 3.9(b). The % area fraction of precipitates for as received C&F material was 6.63%. As the normalizing temperature increases from 950 °C to 1000 °C, the fraction area of precipitates increases drastically. With further increase in normalizing temperature, a negligible change was observed in fraction area of precipitates.

3.2.2.2 Mechanical properties

The yield strength (YS), ultimate tensile strength (UTS), % reduction in area, % elongation, Vicker's hardness, Charpy toughness and average precipitate size of as-received P92 steel and for various heat treatments condition of P92 steel are depicted in Table 3.6. The YS, UTS, and % elongation for as-received P92 steel were measured as 670 MPa, 801 MPa, and 16% respectively. The engineering stress-strain curve for the tensile tested specimen is shown in Fig. 3.10.

The measured Vicker's hardness, impact toughness and average precipitate size were 283±5 HV, 62±4 Joules and 122±15 nm, respectively. The hardness of as-received P92 steel depends on solid solution strengthening, grain size, the fine MX precipitates and the higher dislocation density of fine precipitates. After the normalizing treatment the UTS, YS, and hardness were found to be increased due to the formation of un-tempered lath martensitic microstructure. The reduction in the % elongation and toughness is also caused by lath martensitic microstructure. The tempering of normalized sample produces the tempered lath martensitic microstructure and removed the quench stress and brittleness.

Table 3.6 Mechanical properties of as-received P92 steel and after various heat treatments

Heat treatment condition	Yield strength (MPa)	Tensile strength (MPa)	% elongation	Vickers Hardness (HV0.5)	Impact toughness (Joules)	Particle size (nm)
As received	670±12	801±15	16±2	283±5	62±4	122±15
N950	1255±15	1333±12	18±1.5	431±8	37±3	-
N1000	1190±13	1295±15	20±1.5	437±5	34±4	-
N1050	1120±12	1210±10	19±2.0	445±7	20±3	-
N1100	1150±14	1200±9	12±2.5	450±6	15±3	-
N1150	1250±15	1308±8	12±2	455±5	13±4	-
N&T 950/760	580±12	701±10	22±1.5	235±8	79±4	140±20
N&T 1000/760	530±10	678±10	23±2.0	227±7	77±3	152±18
N&T 1050/760	510±8	649±12	17±1.8	218±4	74±2	155±22
N&T 1100/760	490±10	618±12	18±2.0	215±6	72±3	157±25
N&T 1150/760	550±9	696±10	23±2.2	230±5	71±2	169±32
Notes: -	N950, N1000, N1050, N1100 and N1150 refer to normalizing treatments for 1 h each at 950, 1000, 1050, 1100 and 1150 °C, respectively. N&T 950/760 denotes 1 h normalizing at 950 °C and 2 h tempering at 760 °C. Likewise, for the other treatments shown.					

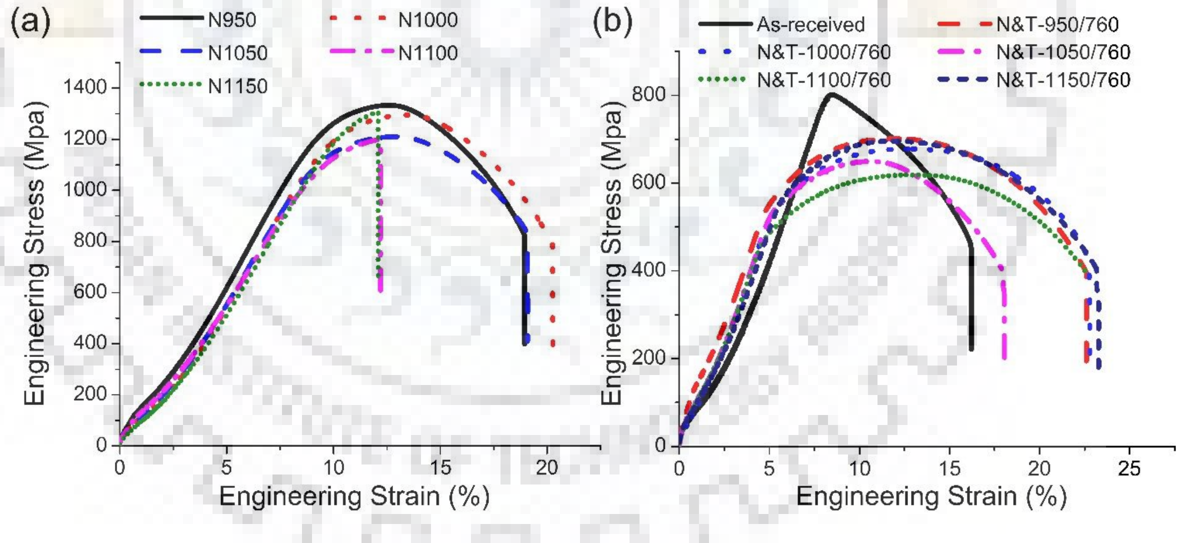

Figure 3.10 Engineering stress-strain curve for (a) normalized and (b) normalized and tempered specimen

Tempered lath martensitic microstructure is responsible for the reduction of YS, UTS, and hardness by a large value. During loading, decohesion and cracking of secondary phase carbide particles at the interface (precipitate/matrix) are possible mechanisms, which may be the reason for the deterioration of mechanical properties with normalizing temperature.

After tempering, the hardness was found to be decreased as normalizing temperature increases up to 1100 ^{o}C beyond that a drastic increase was observed. As the normalizing temperature increases, the hardness was found to be decreasing, due to tempering reaction. The variation in the degree of hardness between the samples normalized at 1000, 1050 and 1100 ^{o}C was found relatively lower as compared to normalized at 1150 ^{o}C. After tempering, the variation in hardness may occur due to fine grain size, evolution of fine MX and coarse $M_{23}C_6$ precipitates, and rejection of C and N from solid solution.

For fixed tempering temperature, the grain size was found to be increased with increase in normalizing temperature. The variation in grain size with normalizing temperature is shown in Fig. 3.11. For fixed tempering temperature, the average grain size measured for sample normalized at 950 ^{o}C and 1150 ^{o}C were 45 ± 5 and 61 ± 9, respectively. The Charpy toughness value of P91 steel depends on too many factors including grain size, precipitate size, fraction area of precipitates, thermal straining of particles and precipitate distribution. The variation in Charpy toughness value with grain size for different normalizing temperature (fixed tempering temperature) is shown in Fig. 3.11. The Charpy toughness value was found to be decreased with increase in grain size. The increase in grain size led to less availability of grain boundaries and ultimately less volume fraction of precipitates. This resulted in an increase in solid solution strengthening that led to higher strength and poor toughness.

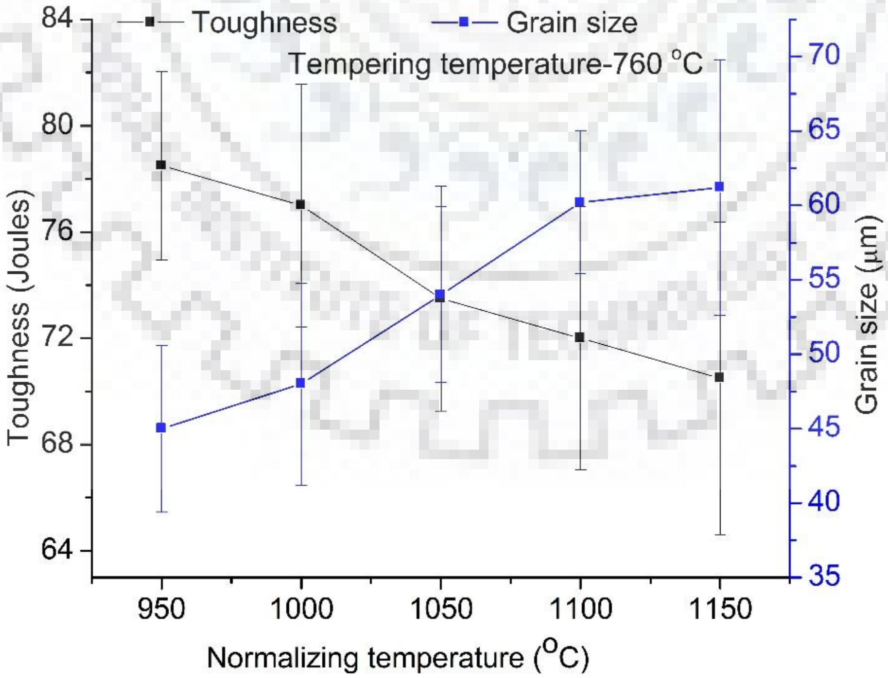

Figure 3.11 Variation in Charpy toughness and grain size with normalizing temperature

The phase identified in the as-received P92 steel are Cr-rich $Cr_{23}C_6$ and Cr_7C_3, V and Nb-rich MX particles, Cr-rich M_2X, Fe-rich M_3C and W-rich Fe_7W_6. The number of peaks and precipitates were reduced at various normalized specimens because at such a high temperature, some of the precipitates get dissolved. After tempering the number of peaks was found to be increased as compared to normalized samples. The XRD pattern of normalized and tempered (950 °C/760 ^{o}C) sample represents the presence of Cr-rich $M_{23}C_6$, Cr-rich M_7C_3, V and Nb-rich fine MX(M-V, Nb, and X-C, N), M_2X (M-Fe, Cr and X-C, N), M_3C (M-Fe) and W-rich Fe_7W_6 type precipitates as shown in Fig 3.12. The structure and lattice parameter for P92 steel obtained for each phase are represented in Table 3.7.

Table 3.7 Structure and lattice parameter of phases identified in XRD analysis of P92 steel

S.No.	Phase identified	Structure	Lattice parameter (A^{o})
1	$Cr_{23}C_6$	Cubic	a=10.65, b=10.65, c=10.65
2	Cr_7C_3	Orthorhombic	a=7.01, b=12.15, c=4.53
3	Cr_2N	Hexagonal	a=4.81, b=4.81, c=4.48
4	NbC	Cubic	a=11.15, b=11.15, c=11.15
5	NbN	Hexagonal	a=2.96, b=2.96, c=5.53
6	VN	Cubic	a=4.13, b=4.13, c=4.13
7	Fe_3C	Orthorhombic	a=4.51, b=5.04, c=6.73
8	Fe_2C	Monoclinic	a=2.79, b=2.79, c=4.36
9	Fe_7W_6	Rhombohedral	a=4.76, b=4.76, c=25.9

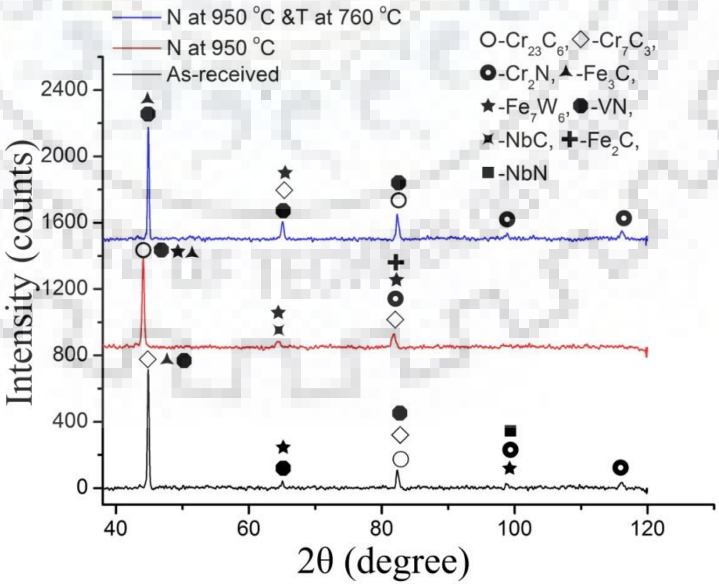

Figure 3.12 Diffractogram for normalizing and tempering treatment at 950 ^{o}C/760 ^{o}C

3.2.2.3 Fracture surface morphology

During tensile testing, the specimen has shear plane approximately 45° to the tensile axis along the peripheral of the specimen. The coalescence of microvoids results in equiaxed dimples normal to the loading axis on the tensile fracture surface. Hence during loading, it reveals elongated ellipsoidal dimples on the shear lips oriented at 45° and the equiaxed and spherical dimples on a flat crater bottom loaded in tension. The tensile fracture surfaces of various normalized conditions are shown in Fig. 3.13. Fig. 3.13(a) represents the final fracture zone of tensile tested specimen for normalized at 950 °C which was characterized by trans-granular dimples, ductile tear ridges and transgranular cleavage facets. However, the fracture surface mainly consisted ductile dimple tearing resulting from the micro-voids coalescence but also the fewer amount of ductile tear ridges and transgranular cleavage facets.

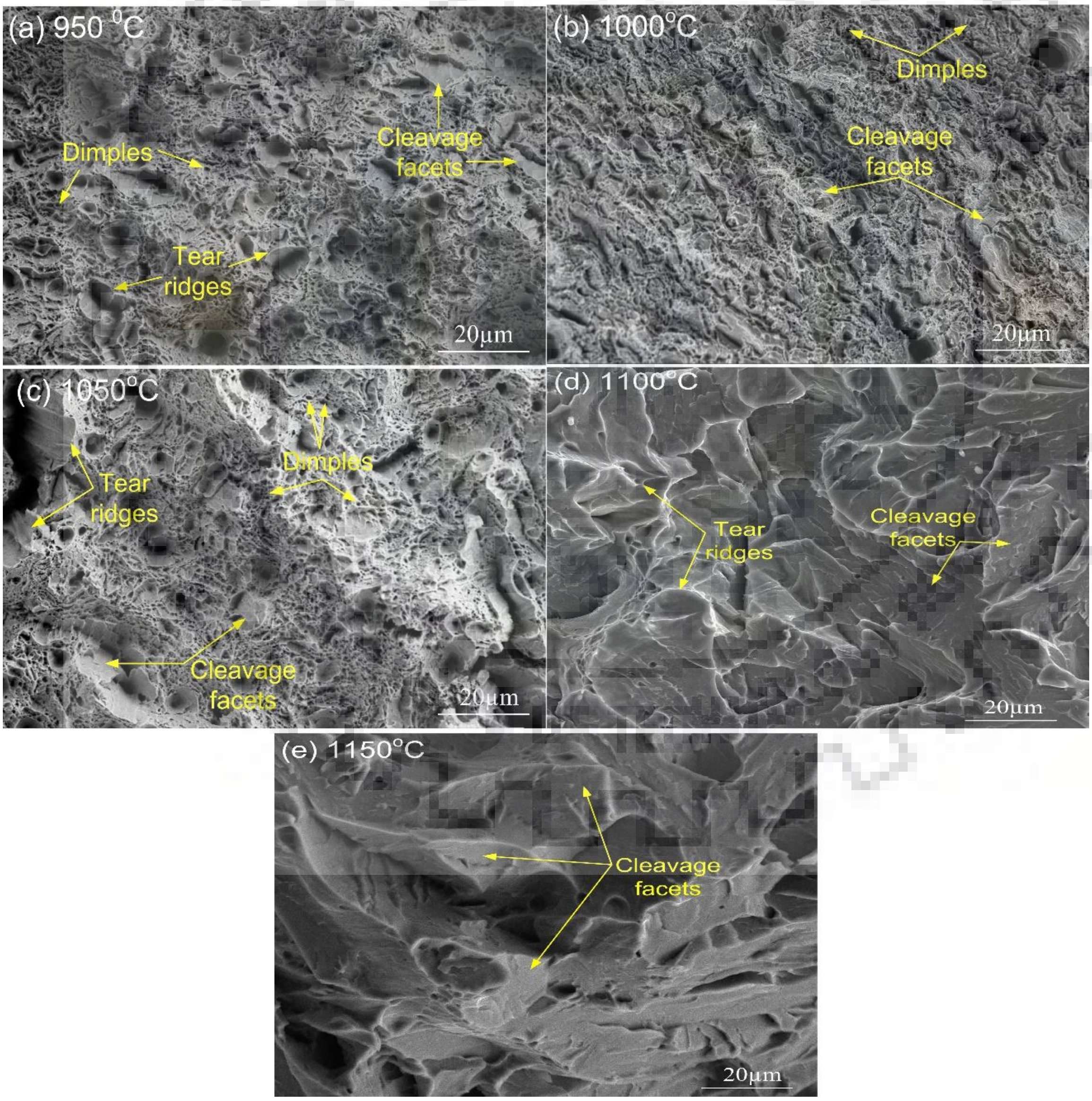

Figure 3.13 Fracture surface morphology of tensile specimens (a) N at 950 °C, (b) N at 1000 °C, (c) N at 1050 °C,(d) N at 1100 °C and (e) N at 1150 °C

A similar fracture surface morphology appears in normalized at 1000 °C and normalized at 1050 °C conditions, as shown in Fig. 3.13(b) and 3.13(c). But the % and area of transgranular cleavage facets and ductile tear ridges were increased as compared to normalize at 950 °C. The P92 steel is a mainly polycrystalline material which contains the inclusions, dislocations, grain boundaries and other imperfections. The cleavage facet propagates along the well-defined low-index crystallographic plane known as a cleavage plane and requires low energy for fracture. Fig. 3.13(d) and 3.13(e) represents the final fracture zone of P92 steel normalized at 1100 °C and normalized at 1150 °C respectively. Fig. 3.13(d) is characterized by transgranular cleavage facets and ductile tear ridges. The number of tear ridges and transgranular cleavage facets were higher as compared to previous conditions. Similarly, Fig. 3.13(e) represents the transgranular cleavage facets throughout the fracture surface. Hence as normalizing temperature increases, the mode of fracture was found the change from ductile to brittle.

Fig. 3.14(a–g) represents the fracture surface morphology of tensile tested specimen in different heat treatment conditions. Fig. 3.14(a) represents the tensile fracture surface of as-received C&F P92 steel which is characterized by cleavage facets, dimples and ductile tear ridges due to tempered lath martensitic type microstructure. The EDX of the tensile fracture surface of the as-received C&F P92 steel is shown in Fig. 3.14(b), which represents the presence of Cr-rich $M_{23}C_6$ type precipitates and V or Nb-rich fine MX(M-V, Nb, and X-C, N) type precipitates at the PAGBs and in the matrix. It also revealed the presence of secondary phase carbide particles, these particles act as the voids.

The void nucleation occurred at the PAGBs. The specimen is failed in a transgranular manner which shows that the voids do not extend along the PAGBs. After tempering, the fracture morphology of various normalized samples at 950 °C, 1000 °C, and 1050 °C are shown in Fig. 3.14(c–e) respectively, the dimples are observed from fracture surfaces, which is not completely equiaxed and somewhat little elongated. Small size dimples were observed for normalized at 950 °C as compared to others as shown in Fig. 3.14(c). After tempering, the % and area of ductile tear ridges and cleavage facets were increased from normalized at 950 °C to 1050 °C and dimples were decreased. The tensile fracture micrograph of P92 steel for normalized at 1100 °C with tempering at 760 °C is shown in Fig. 3.14(f), which shows the area of cleavage facets and size of dimples were enhanced. The fracture occurred in this condition is a mixed mode with a higher % of transgranular cleavage facets as compared to dimples.

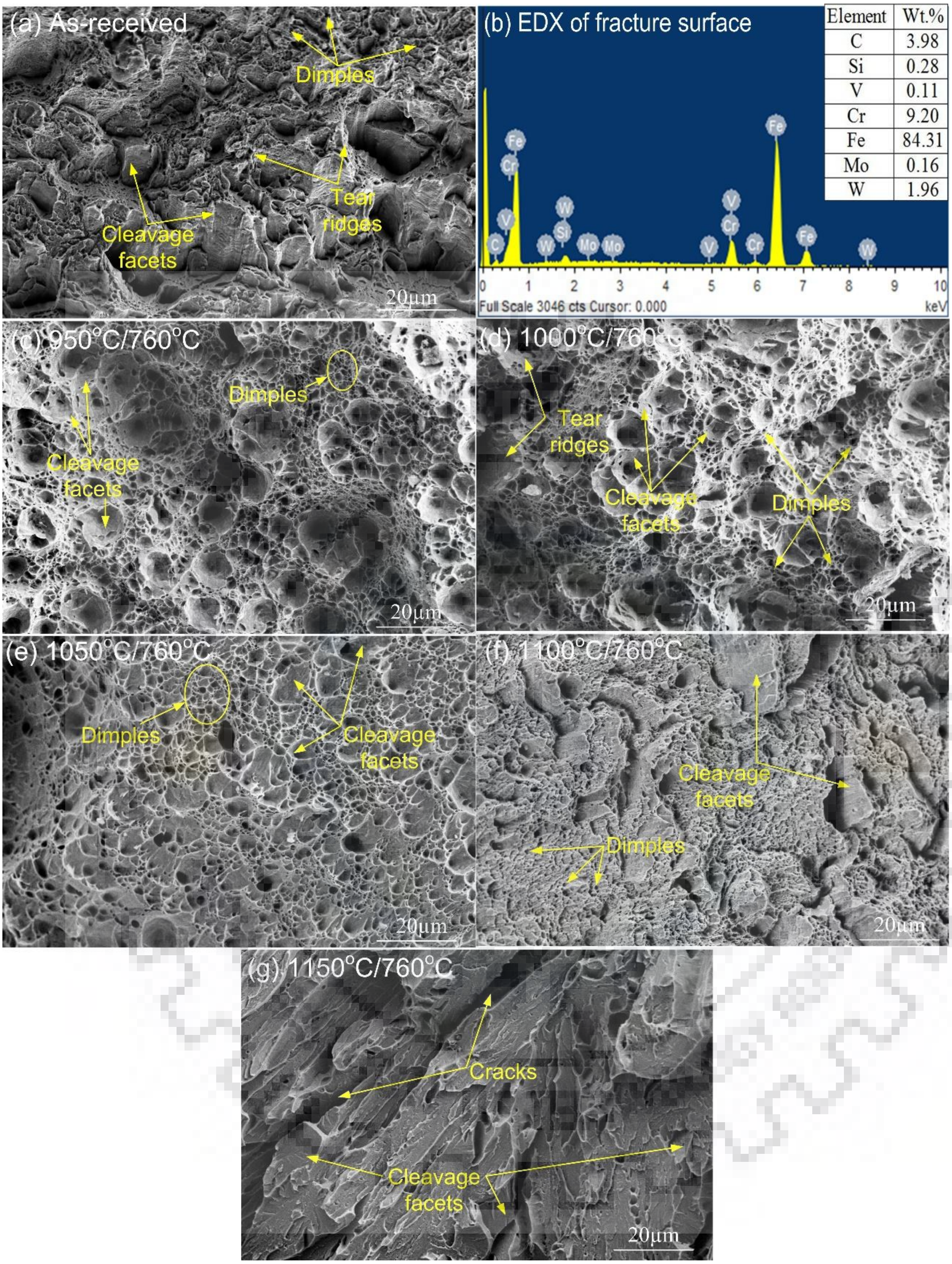

Figure 3.14 Fracture surface morphology of tensile specimens (a) As-received material, (b) EDX of as-received fracture surface, (c) N&T at 950 °C/760 °C,(d) N&T at 1000 °C/760 °C, (e) N&T at 1050 °C/760 °C, (f) N&T at 1100 °C/760 °C and (g) N&T at 1150 °C/760 °C

A completely different fracture surface morphology is observed in the normalized and tempered at 1150 °C/760 °C condition, as shown in Fig. 3.14(g). The almost negligible number of ductile dimples, bigger cracks and the large area of cleavage facets were observed in the tensile fracture zone. The mode of fracture is occurred completely brittle type for normalized and tempered at 1150 °C/ 760°C. At higher temperatures, coarsening of secondary phase carbide particles occurs at the PAGBs, which drops their strengthening effect and helpful for void nucleation and growth.

The fracture surface morphology of impact tested specimen for various normalized conditions is shown in Fig. 3.15(a–e). In Fig. 3.15(a), both quasi-cleavage facets and fine dimples were observed that shows the mixed mode fracture mechanism. There is no apparent boundary between dimples and the cleavage facet areas in quasi-cleavage. The coalescence of microvoids led to the final fracture. For a normalizing temperature of 1000 ^{o}C, fracture surface is characterized by the presence of cleavage facets and dimples but compared to previous one (normalized at 950 ^{o}C) the shallow dimples were observed, as shown in Fig. 3.15(b).

In the final failure region, heterogeneity in size of dimples was clearly observed. Fig. 3.15(c) shows the fracture surface morphology of the impact tested samples normalized at 1050 °C, which is characterized by cleavage facets and dimples in the final fracture zone that indicate the mixed mode of fracture. The area of cleavage facets was found to be increased and the number of dimples was reduced with an increase in normalizing temperature from 950 °C to 1050 °C. Normalizing beyond 1050 ^{o}C, the mixed mode of fracture transformed to brittle fracture. Cleavage facets and tear ridges were observed for sample normalized at 1100 °C and 1150 °C, respectively as shown in the Fig. 3.15(d) and 3.15(e). The negligible area of dimples was observed among the smooth intercrystalline area. In both cases, the mode of fracture was found to be the brittle type. The cleavage facets were found to be more pronounced at higher normalized temperature.

Fig. 3.16(a) represents the fracture surface morphology of Charpy tested as-received material P92 steel. The fracture surface revealed the presence of dimples, quasi-cleavage facets and tear ridges. To the crack growth direction, the tear ridges formed at the PAGBs are merged and it also useful to find the local crack ignition zone and the growth events. The fracture surfaces of Charpy tested specimen for different normalizing and tempering conditions are shown in Fig. 3.16(b-f). At the initial state of tempering, the final fracture zone revealed the mixed mode of fracture. Both shear dimples and cleavage facets were observed for sample normalized and tempered at 950 ^{o}C/760 ^{o}C and 1000 ^{o}C/760 ^{o}C. The number density of dimples was found to be increased for sample normalized and tempered at 1050 ^{o}C/760 ^{o}C.

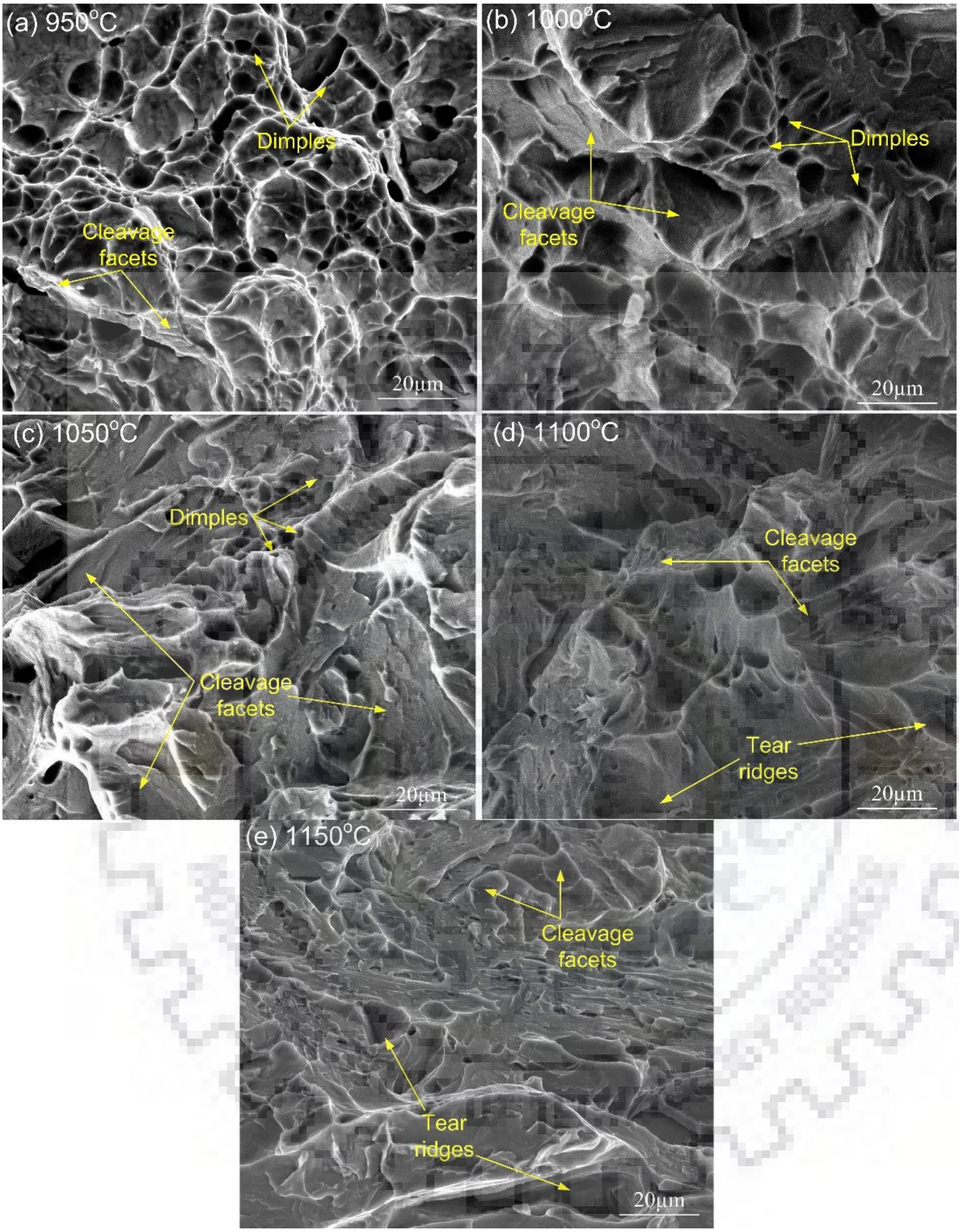

Figure 3.15 Fracture surface morphology of impact Charpy test of (a) N at 950 °C, (b) N at 1000 °C, (c) N at 1050 °C,(d) N at 1100 °C and (e) N at 1150 °C

For sample 1050 °C/760 °C, besides the shear dimples bigger size smooth intercrystalline are was observed, as shown in Fig. 3.16(d). The similar pattern of fracture surface was also observed for sample normalized and tempered at 1100 °C/760 °C, as shown in

Fig. 3.16(e). For the sample normalized and tempered at 1150 °C/760 °C, a completely different fracture surface appearance was observed, as shown in Fig. 3.16(f). The fracture surface was characterized with a negligible number of ductile dimples, some amount of tear ridges and the large area of cleavage facets. The fracture surface clearly indicates the brittle fracture mode. In C&F P92 steel after various thermal heat treatments, the embrittling effect occurs due to coarsening of secondary phase carbide precipitates present along the PAGBs and within the grain. This effect is more pronounced in impact toughness testing as compared to tensile testing. Due to the embrittling effect, the fracture surface shows the presence of smooth inter-crystalline area.

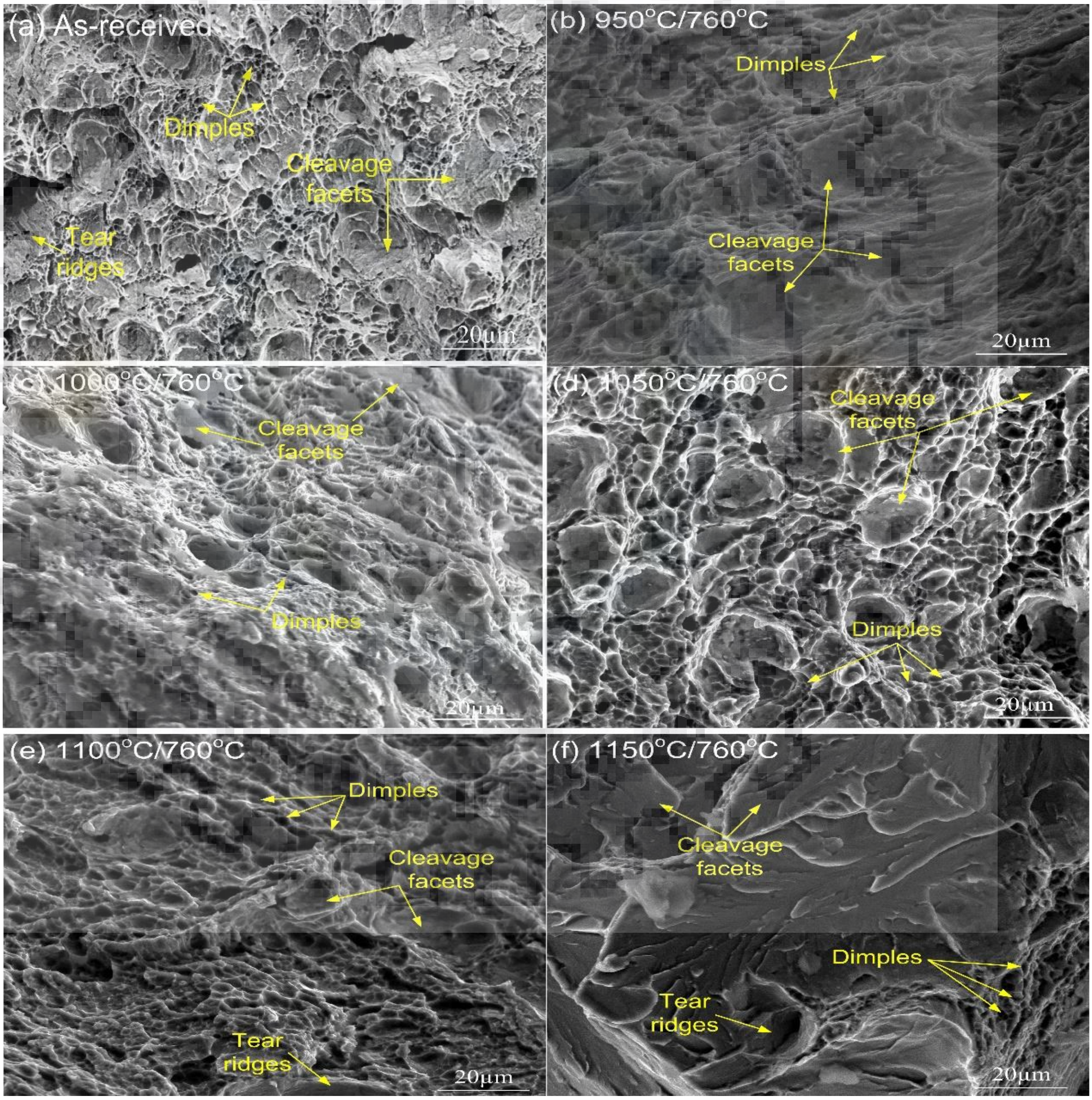

Figure 3.16 Fracture surface morphology of impact Charpy test of (a) As-received material, (b) N&T at 950 °C/760 °C,(c) N&T at 1000 °C/760 °C, (d) N&T at 1050 °C/760 °C, (e) N&T at 1100 °C/760 °C and (f) N&T at 1150 °C/760 °C

3.2.3 *Effect of long-term ageing*

The material had been heat treated in two steps before long-term ageing. In first step, normalizing heat treatment was carried out for 1 h at 1000 °C. This was followed by tempering at 760 °C for 2 hrs. The long-term ageing treatment was conducted in a furnace at 650 ^{0}C for 720 hrs, 1440 hrs, 2160 hrs and 3000 hrs ageing time.

3.2.3.1 Material in normalized and tempered condition (as-received)

Figure 3.17(a) and 3.17(b) shows the secondary electron micrographs of P92 steel (as-received) at lower and higher magnification, which clearly exhibits prior austenite grain boundaries (PAGBs), lath boundaries, blocks, fine MX and coarse $M_{23}C_6$ [M: Cr, Mo, Mn and Fe] precipitates. The fine V and Nb-rich carbo-nitrides were distributed within the PAGBs and higher density of coarse precipitates was observed at PAGBs. The yield strength (YS) and ultimate tensile strength (UTS) of as-received P92 steel were measured to be 530 ± 10 and 678 ± 10 MPa, respectively. The Charpy toughness and hardness of as-received P92 steel were measured to be 198 ± 8 J and 227 ± 4 HV, respectively.

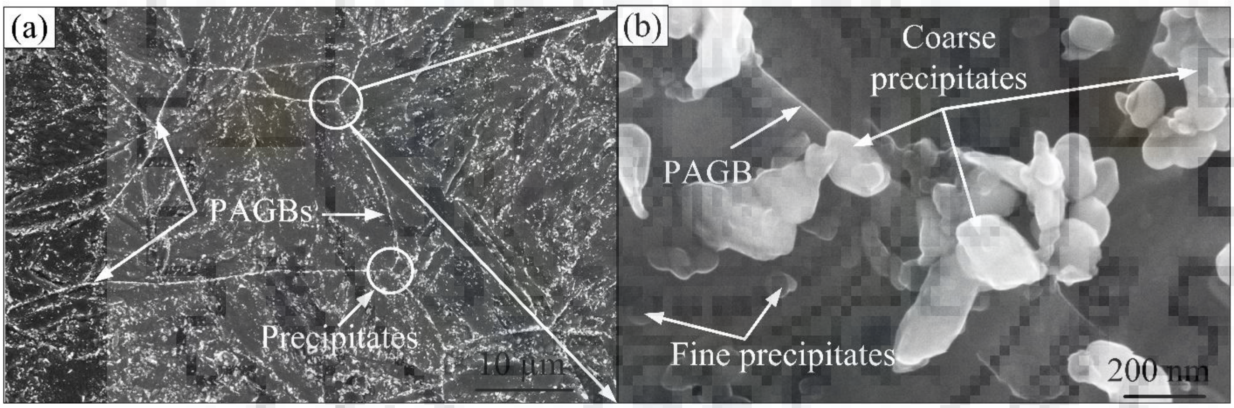

Figure 3.17 Micrographs of N&T P92 steel at (a) lower and (b) higher magnification

3.2.3.2 Effect of thermal ageing on grain size

Figure 3.18(a) represents the optical micrograph of N&T P92 steel which shows the average grain size of 16 ± 3 µm. To study the variation of grain size with respect to ageing time, the optical micrographs of P92 steel were analyzed after 720, 1440, 2160, and 3000 hrs of exposure at ageing temperature of 650 ^{o}C, as shown in Fig. 3.18(b-e). After ageing, the P92 steel microstructure shows precipitation of secondary phase and martensite in tempered form. After ageing of 720 hrs, the grain coarsening was observed (Fig. 3.18(b)).

High numbers of secondary phase particles were observed after ageing of 1440 hrs, as compared to the 720 hrs ageing (Fig. 3.18(c)). Figure 3.18(d) shows that after ageing of 2160 hrs, the microstructure consisted of coarse grains and carbide precipitates along the PAGBs and at the sub-grain boundaries. The grain coarsening was increased with an increase of ageing time as shown in Fig. 3.18(f). After 720 hrs of ageing, the grain size was measured 17 ± 4 μm. The grain size showed a decreasing trend as ageing time increases from 720 hrs to 1440 hrs and it was measured about 11 ± 3 μm. But, further enhance in ageing time resulted in a continuous increase in grain size. The adverse effect of increased grain size can be seen from the mechanical properties as discussed in the below section. The optical micrograph was observed to be similar in ageing range of 720 hrs to 3000 hrs.

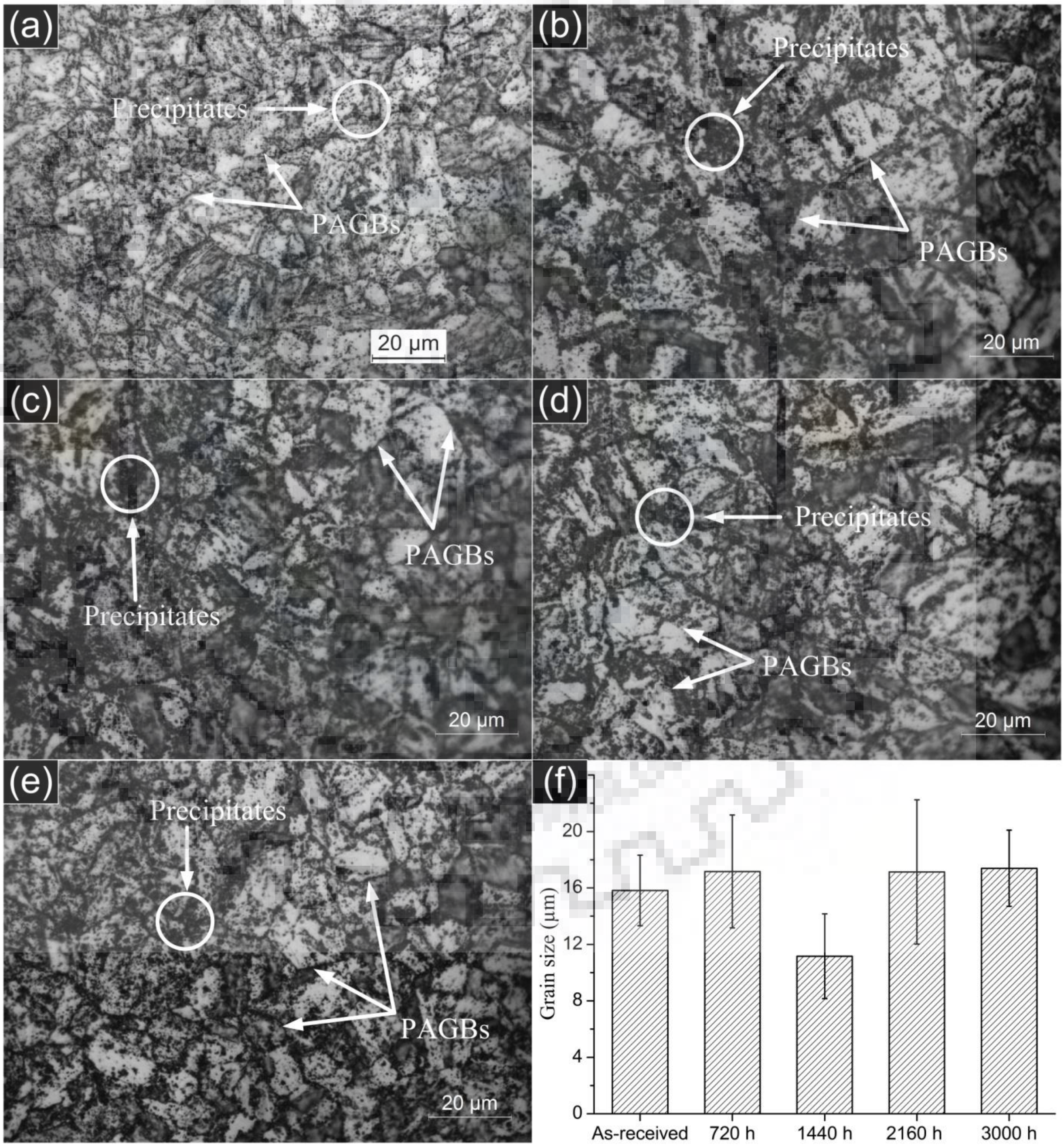

Figure 3.18 Optical micrographs in various ageing conditions (a) as-received, (b) 720 hrs, (c) 1440 hrs, (d) 2160 hrs, (e) 3000 hrs and (f) variation in grain size with ageing time

3.2.3.3 Ageing effect on microstructure evolution and precipitate size

The secondary electron micrographs of as-received and short term aged P92 samples are shown in Fig. 3.19(a-e). The micrograph of as-received P92 steel consisted of PAGBs, blocks, lath boundaries, $M_{23}C_6$ and MX type precipitates as shown in Fig. 3.19(a).

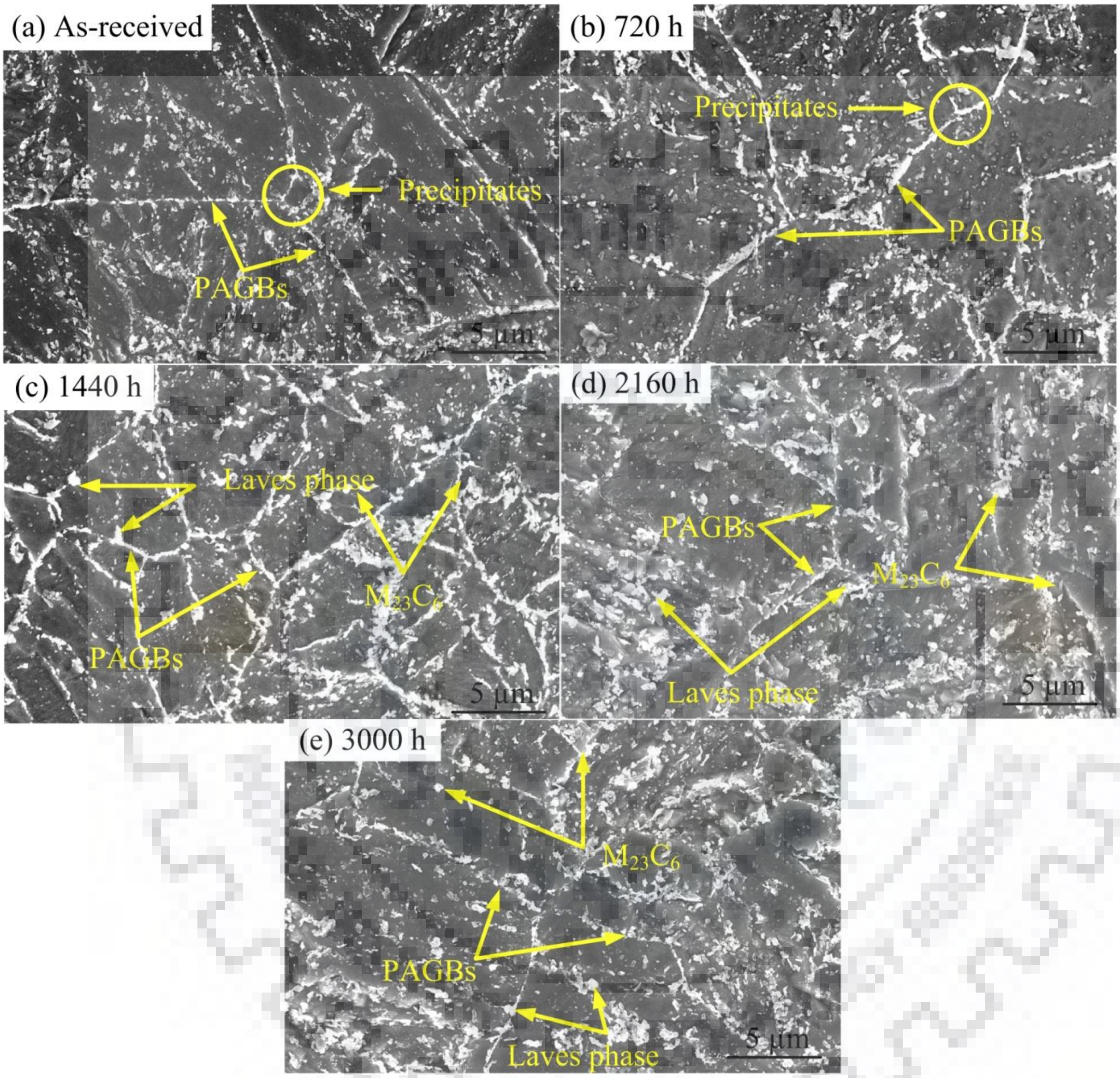

Figure 3.19 SEMs of P92 steel at lower magnification for various ageing conditions (a) as-received state, (b) 720 hrs, (c) 1440 hrs, (d) 2160 hrs and (e) 3000 hrs

Figure 3.19(b) confirms that the higher number of coarse ($M_{23}C_6$) precipitates at PAGBs and lath boundaries and grain coarsening was also observed after 720 hrs of ageing. The extent of grain coarsening was increased with enhance after 1440 hrs of exposure (Fig. 3.19(c)). After ageing of 1440 hrs, size and density of white precipitates increased at the sub-grain boundaries as-compared to 'as-received' material. The recovery of martensitic lath structure was very clear, but lath boundaries were not obvious enough after 3000 hrs of ageing

(Fig. 3.19(e)). The grain coarsening was clearly observed from the micrographs taken after long-term ageing. At the initial stage of ageing (720 hrs), the Mo and W segregation along the boundaries are clearly observed that leads to the nucleation of the Laves phase.

The nucleation of Laves phase is also confirmed from the line mapping of the PAGBs, as shown in Fig. 3.20. In as-received condition, line mapping of the precipitates confirmed the higher weight percentage of Cr in $M_{23}C_6$ composition.

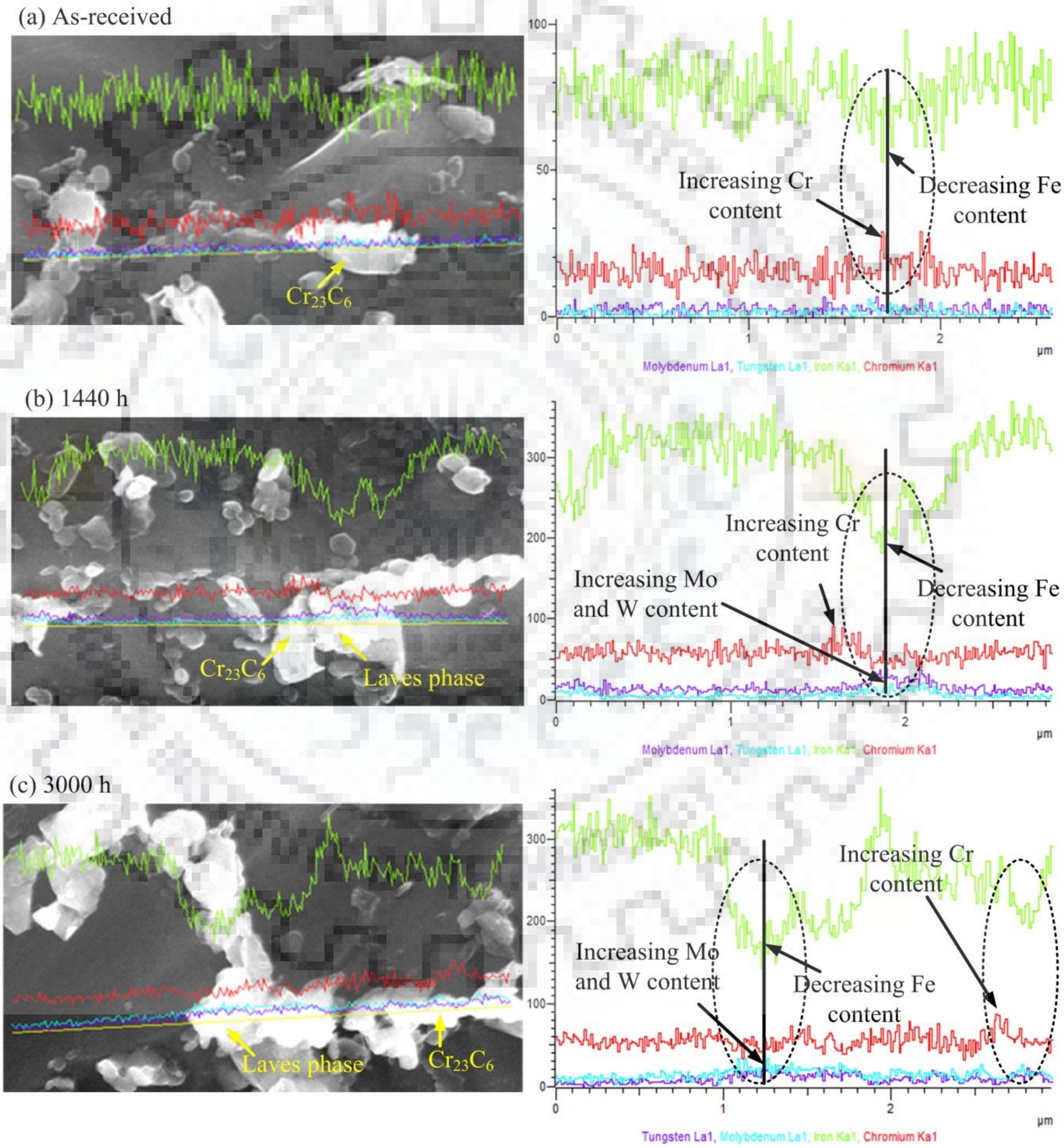

Figure 3.20 Line mapping results for aging duration of (a) as-received, (b) 720 hrs and (c) 3000 hrs

After the ageing of 720 hrs, the increase in weight percentage of W and Mo and simultaneous decrease in Fe at the PAGBs are clearly observed form Fig. 3.20(b). With further, increase in ageing time from 720 hrs to 3000 hrs, the coarse Laves phase are clearly observed along the PAGBs, as shown in Fig. 3.20(c). At the initial stage of nucleation, the size was observed to be low while at ageing time of 3000 hrs, the size was observed to be higher as compared to 720 hrs. In the initial stage of ageing, the size of Laves phase was measured in range of 190 to 220 nm while after the aging at 3000 hrs, it was in range of 250 to 300 nm. The similar results was also reported by the Panait et al. (C. G. Panait et al., 2010a). Fig. 3.20(c) confirms the segregation of Laves phase along the boundaries and near the $M_{23}C_6$ precipitates. The Laves phase generally nucleate at the $M_{23}C_6$ and after some time surround it.

After the 3000 hrs of ageing, Laves phase become the largest size precipitates in P92 steel microstructure as compared to $M_{23}C_6$. The size of fine MX precipitates was reported to be constant while size and composition of $M_{23}C_6$ phase were reported to be changed with ageing time (Gustafson and Hättestrand, 2002; C. G. Panait et al., 2010c; Chandan Pandey et al., 2017b). In P92 steel, the higher coarsening rate of Laves phase and growth and coarsening of $M_{23}C_6$ phase with ageing time was also reported by the Guo et al. (Guo et al., 2013). The EDS line mapping confirmed the Cr, Fe and Mo as the main constituents of $M_{23}C_6$. Guo et al. (Guo et al., 2013) reported rapid precipitation of Laves phase after 200 hrs of exposure. The Laves phase was found to increase continuously with increase in ageing duration. The $M_{23}C_6$ carbides were observed to be relatively stable as compared to Laves phase.

At the PAGBs, the accumulation of Laves phase in near area of the $M_{23}C_6$ is shown in Fig 3.21. PAGBs were denoted by yellow line (dotted) in the micrographs. The coarse $M_{23}C_6$ type precipitates were decorated at PAGBs and MX type precipitates were observed in the interior of PAGBs, as shown in Fig. 3.21(a). After the ageing of 720 hrs, the accumulation of the precipitates at the grain boundaries was observed to be increased (Fig. 3.21(b)). The area fraction of precipitates was decreased as compared to as-received base metal. This occurs as a result of grain coarsening. Further exposure leads to growth and coarsening of precipitates at PAGBs and at the sub-grain boundaries (Fig. 3.21(c)). The Laves phase formation is clearly seen in Fig. 3.21(c-e). The coarsening of precipitates and decrease in area fraction of precipitates are clearly observed from Fig. 3.21(b-e).

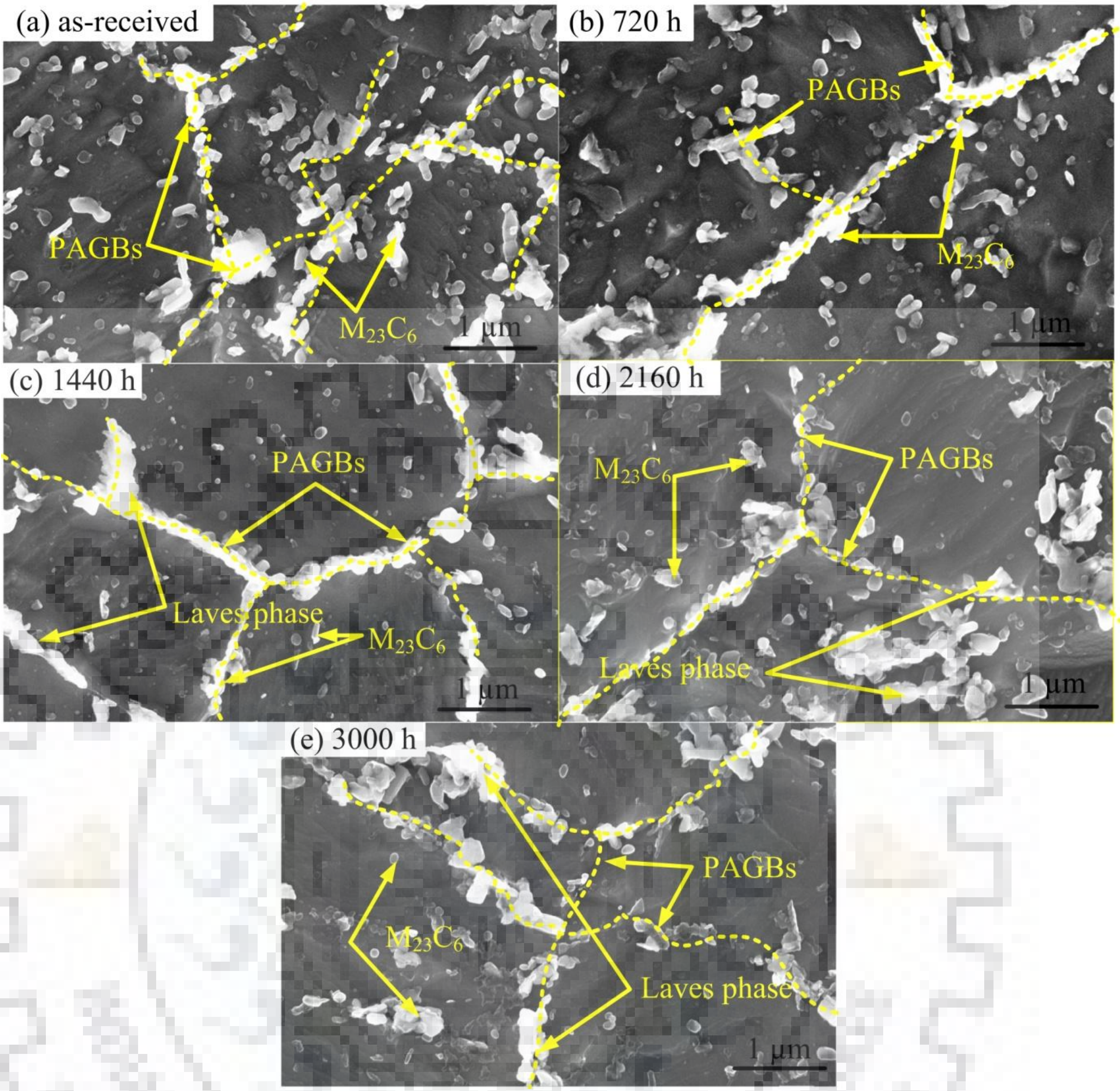

Figure 3.21 SEMs of P92 steel at higher magnification for various ageing conditions (a) as-received state, (b) 720 hrs, (c) 1440 hrs, (d) 2160 hrs and (e) 3000 hrs

Figure 3.22(a-b) shows variation in precipitate size, and fraction area of precipitates for varying ageing time. Figure 3.22(a) depicts the relationship between area fraction of precipitates and ageing time. The area fraction of precipitates was found to reduce continuously with increase in ageing time. After ageing, the area fraction of precipitates was measured 10 ± 2 % for 3000 hrs of ageing. The area fraction of precipitates depends greatly on the size of PAGBs and lath boundaries. The higher density of precipitates is generally observed along the lath and PAGBs. The coarsening of grains and lath boundaries results in lower availability of grain and lath boundaries per unit area that lead to reduction in area fraction of precipitates.

Hence, the reduction in area fraction of precipitates with ageing time is attributed to the grain coarsening, precipitate coarsening and increase in lath width.

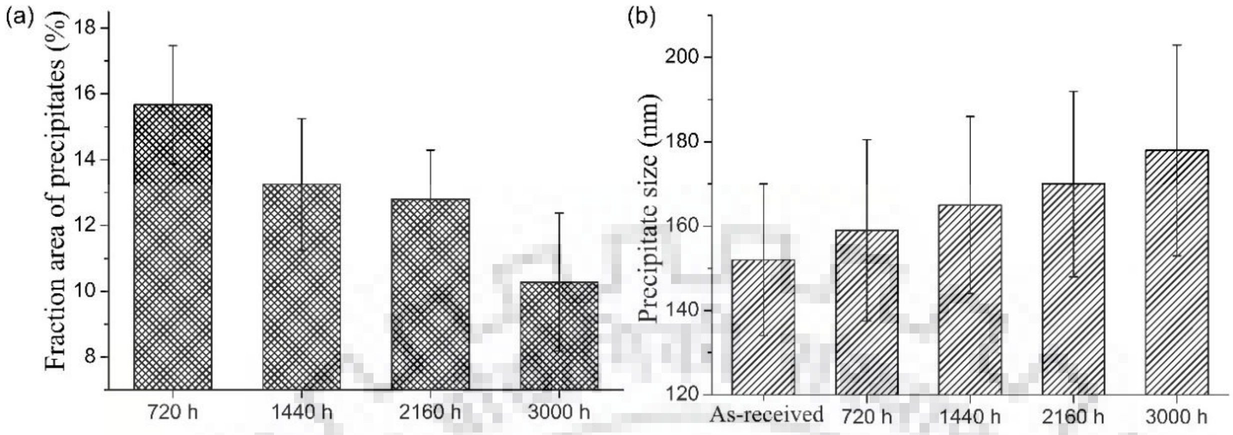

Figure 3.22 Effect of ageing time on (a) fraction area of precipitates and (b) precipitates size

The fraction area of precipitates has observed a great influence on the mechanical properties of material because it governs both solution strengthening and precipitation strengthening. The average diameter of precipitates was increased with increase in ageing time (Fig. 3.22(b)). Heterogeneity was observed in the size of precipitate precipitated along PAGBs and in the matrix region. The average precipitate size increased from 152 ± 22 nm to 178 ± 40 nm after 3000 hrs of ageing. $M_{23}C_6$ precipitates (150 to 200 nm) were observed most effective in pinning the grain boundaries and resulted in higher creep strength (Dimmler et al., 2003). As the size of precipitates increased, they lost their pinning effect that results in poor creep strength. In this study, the $M_{23}C_6$ precipitate size increased with increase in ageing time (but less than 220 nm). However, Laves phase size increased form 180 ± 20 nm (ageing at 720 hrs) to 300 ± 35 nm (ageing at 3000 hrs). The higher size of Laves phase might be the cause of poor tensile strength and creep rupture strength because it acts as the stress raise cites for the crack nucleation.

In order to confirm the formation of Laves phase, EDS spectra was also performed at different ageing time, as shown in Fig. 3.23. In as-received condition, low content of W and Mo was observed, as shown in Fig. 3.23(a). Both W and Mo lead the formation of Laves phase in P92 steel. After thermal ageing, the weight percentage of W and Mo elements were found to be increased continuously which might be the cause of evolution of Laves phase. During long-term service, the formation of Laves phase consumes both Mo and W elements from the matrix. The formation of Laves leads to reduction in impact toughness, strength and hardness by weakening the solid solution. To confirm the presence of Laves phase Mo to Fe and W to Fe ratios were calculated. The values of these ratios were found to be increased with increase in ageing duration (Fig. 3.23(f)). These increased ratios confirm the formation of Laves phase which should be the reason for degradation of mechanical properties after long-term ageing of P92 steel. After the ageing of 3000 hrs, the W and Mo weight percentage were 15.25 and 3.75 %, respectively.

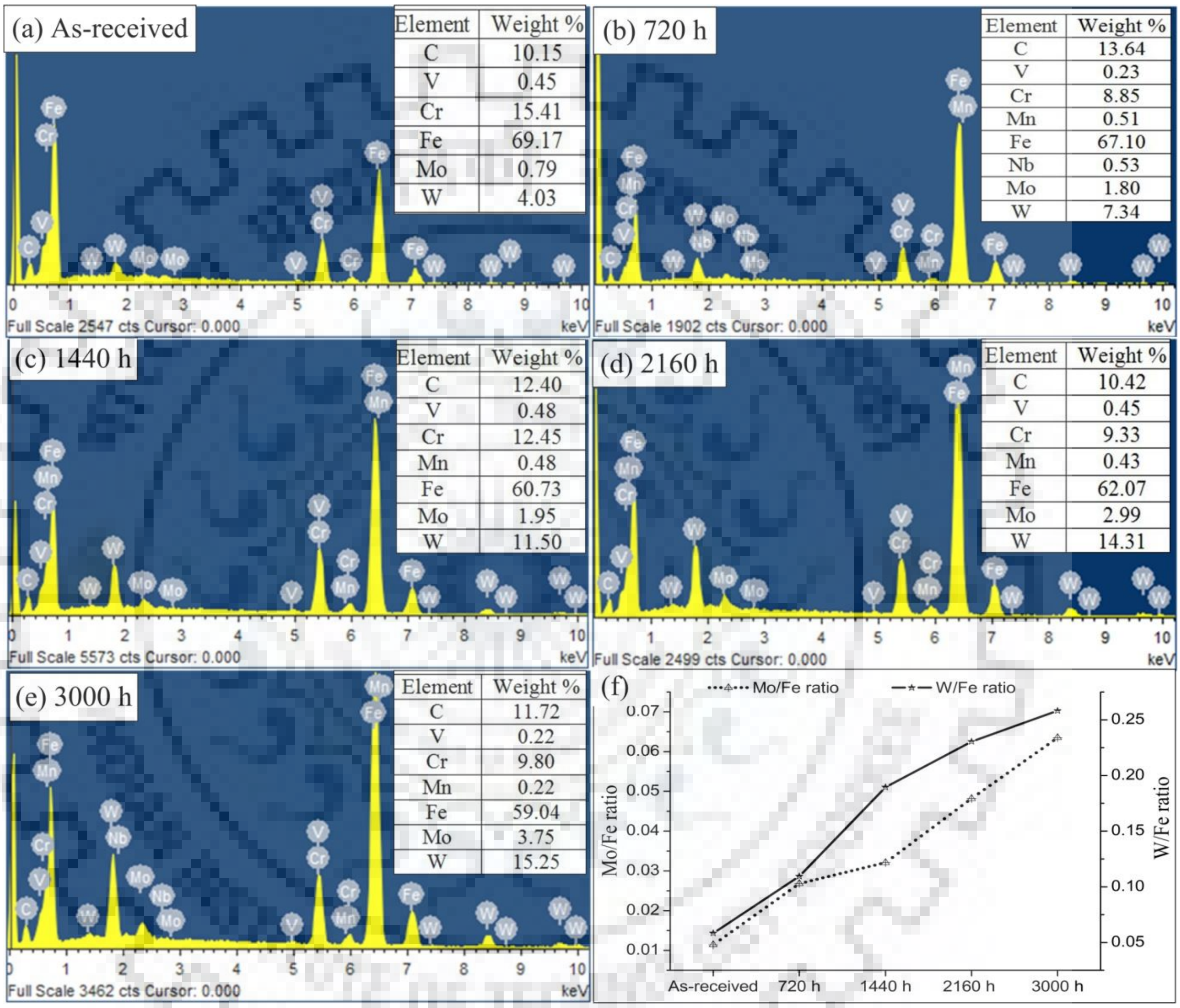

(a) As-received

Element	Weight %
C	10.15
V	0.45
Cr	15.41
Fe	69.17
Mo	0.79
W	4.03

(b) 720 h

Element	Weight %
C	13.64
V	0.23
Cr	8.85
Mn	0.51
Fe	67.10
Nb	0.53
Mo	1.80
W	7.34

(c) 1440 h

Element	Weight %
C	12.40
V	0.48
Cr	12.45
Mn	0.48
Fe	60.73
Mo	1.95
W	11.50

(d) 2160 h

Element	Weight %
C	10.42
V	0.45
Cr	9.33
Mn	0.43
Fe	62.07
Mo	2.99
W	14.31

(e) 3000 h

Element	Weight %
C	11.72
V	0.22
Cr	9.80
Mn	0.22
Fe	59.04
Mo	3.75
W	15.25

Figure 3.23 EDS of particles present at PAGBs for ageing duration of (a) as-received, (b) 720 hrs, (c) 1440 hrs, (d) 2160 hrs, (e) 3000 hrs and (f) variation in Mo/Fe and W/Fe ratio with ageing time at 650 ^{o}C

3.2.3.4 Laves phase characterization

In order to characterize the Laves phase formation during the ageing of P92 steel, line and elemental mapping was also performed. The elemental mapping for as-received and thermal aged sample (720 hrs and 3000 hrs) is shown in Fig. 3.24(a-c). In as-received condition, elemental mapping shows the uniform distribution of Cr, Fe and Mo (Fig. 3.24(a)).

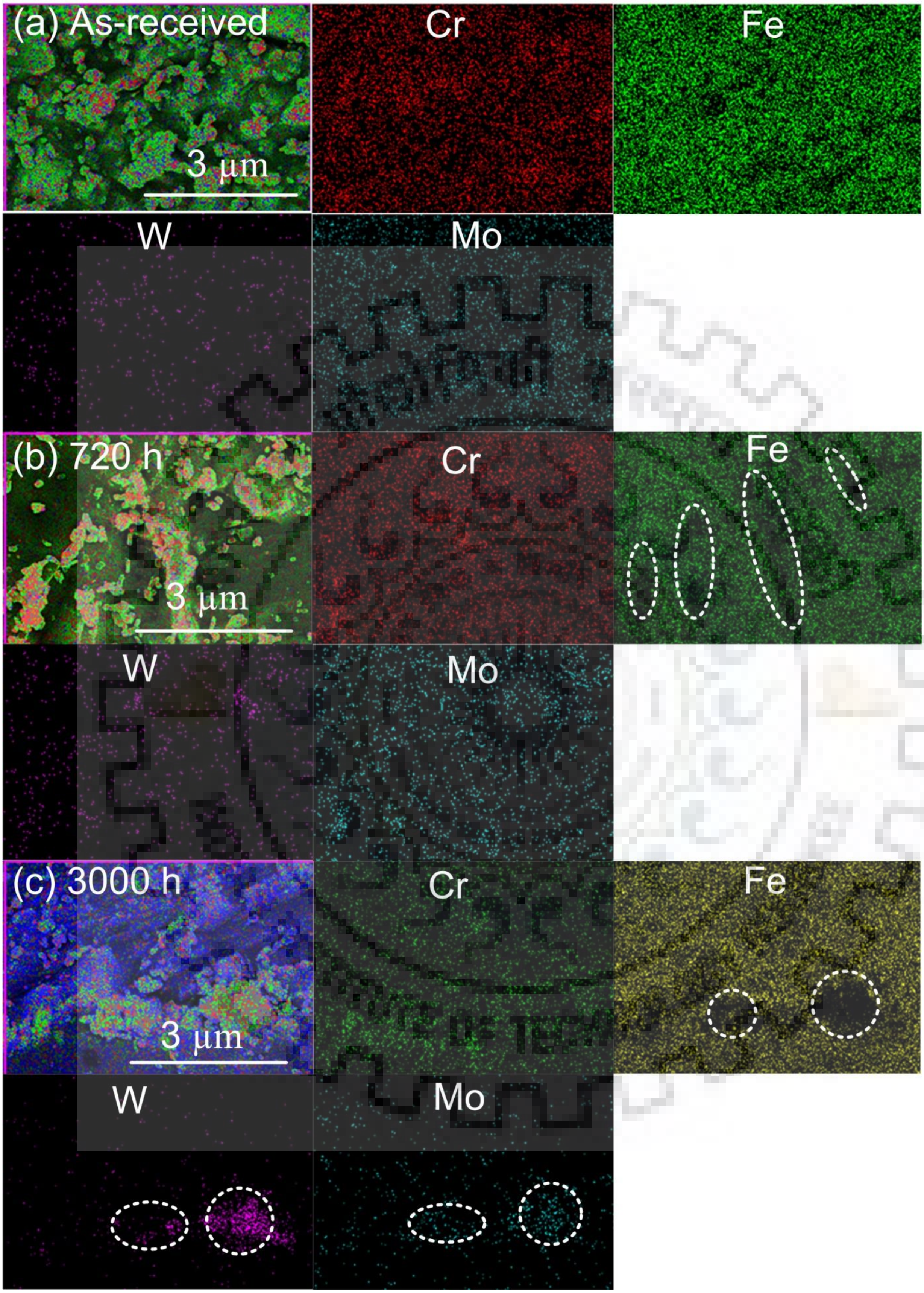

Figure 3.24 Elemental mapping of P92 steel (a) as-received condition, (b) after ageing at 720 hrs, (c) after ageing at 3000 hrs

However, the W was mainly observed along the lath and grain boundaries. The higher concentration of W and Mo along the lath and PAGBs make it preferential sites for the nucleation of Laves phase. After the ageing of 720 hrs, Cr shows the uniform distribution, but Fe is completely removed from the PAGBs. The concentration of W and Mo was observed to be increased along the boundaries and confirmed the nucleation of Laves phase at $M_{23}C_6$ along the boundaries (Fig. 3.24(b)). With further increase in ageing time from 720 hrs to 1440 hrs, the Laves phase formation is clearly observed, as shown in Fig. 3.24(c).

The higher concentration of W and Mo and lower concentration of Fe at coarse precipitates confirmed it as Laves phase. For sample aged at 3000 hrs, line mapping was performed, as shown in Fig. 3.25. The EDS spectra point 1 (Fig. 3.25(c)) shows the higher weight percentage W and Mo. The line mapping is shown in Fig. 3.25(b). The decrease in Fe content and simultaneous increase in W and Mo content at point 1, confirm the formation of Laves phase at point 1. The decrease in Fe and increase in W and Mo content are also shown in Fig. 3.25(e) and 3.25(f-g), respectively. From Fig. 3.25(a), it is confirmed that the Laves phase form near the surrounding area of $M_{23}C_6$ precipitates.

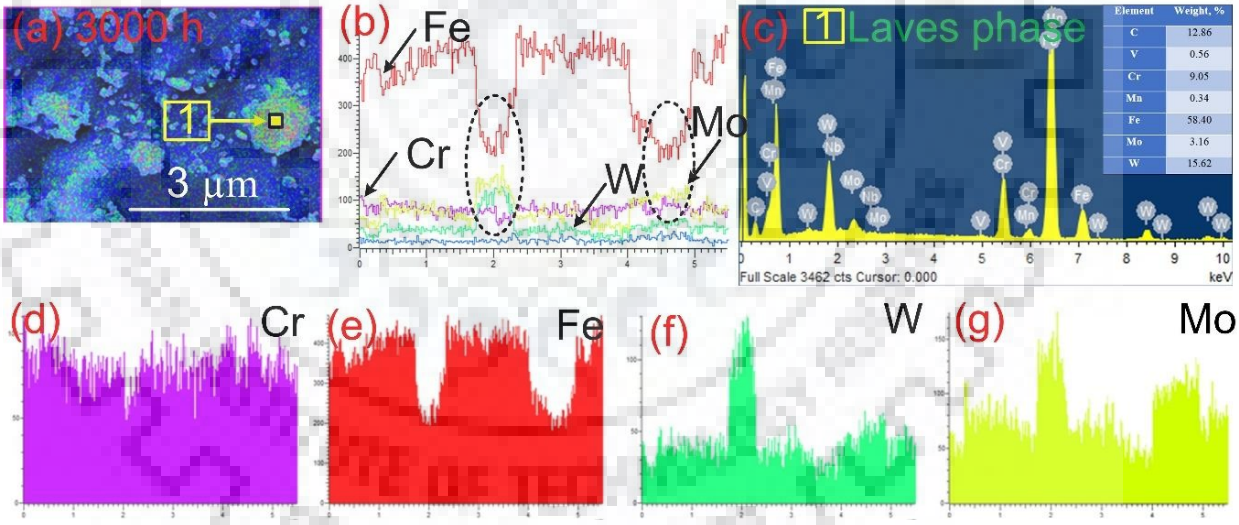

Element	Weight, %
C	12.86
V	0.56
Cr	9.05
Mn	0.34
Fe	58.40
Mo	3.16
W	15.62

Figure 3.25 (a) Mixed microstructure after thermal ageing of 3000 h, (b) line mapping of the precipitates, (c) EDS spectra of the area 1, (d), (e), (f) and (g) area maps for elements Cr, Fe, W, and Mo, respectively

3.2.3.5 XRD analysis and phase determination

Diffractogram of P92 steel samples (as received and aged) is shown in Fig. 3.26. The Precipitates identified by XRD analysis were Fe-rich M_2C and M_3C, Nb and V-rich MX particles, Cr-rich $Cr_{23}C_6$ and W-rich Fe_2W (Laves phase). The as-received specimens were revealed the presence of $M_{23}C_6$ and MX type precipitates. The XRD analysis of aged specimens confirms the presence of Laves phase after ageing of 720 hrs. The nucleation and growth of Laves phase will increase the interfaces mobility and reduce the solid solution strengthening by taking away the strengthening elements (Mo and W) from the matrix. The higher intensity peak of the Laves phase was also observed after the ageing of 3000 hrs, as shown in Fig. 3.26. However, the peak of Mo-rich Laves phase was not observed.

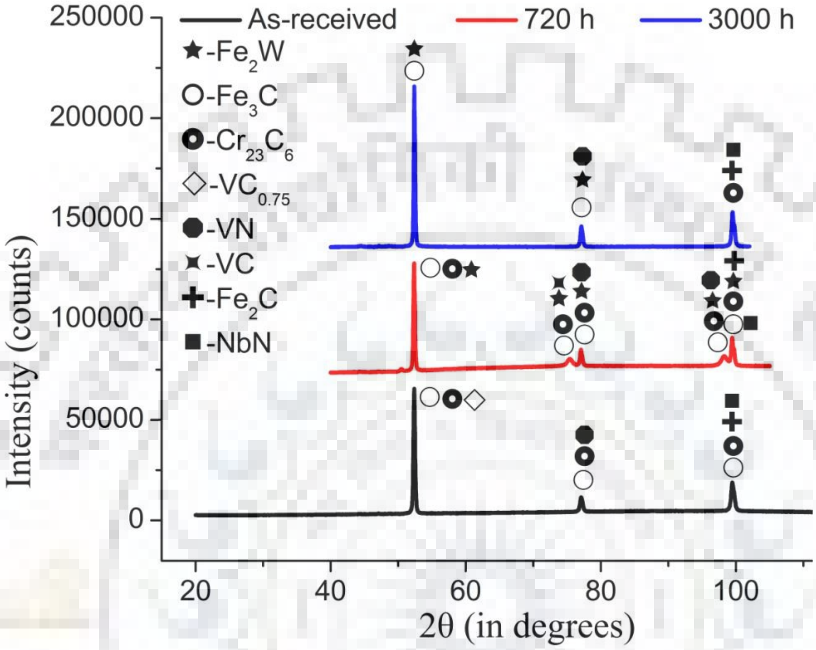

Figure 3.26 Diffractogram of P92 steel in as-received and aging condition

3.2.3.6 Room temperature tensile properties

Figure 3.27(a) shows the stress-strain curve for P92 steel for different stage of thermal ageing. The variation in tensile properties is shown in Fig. 3.27(b-c). The yield strength (YS) of P92 steel (as-received) was measured 530 ± 10 MPa. It was observed that the YS of aged samples were decreased to 520 ± 6 MPa after 720 hrs of ageing. During short ageing time (shorter than 800 hrs), the YS decreased due to Laves phase precipitates and growth into adjacent lath. After ageing of 3000 hrs, the YS decreased to 495 ± 7 MPa. It was observed that drop in ultimate tensile strength (UTS) was higher than YS after 3000 h of ageing. The UTS of P92 steel in as-received condition was measured 678 ± 10 MPa which reduced rapidly to 645 ± 7 MPa after 3000 hrs of exposure. After 720 hrs to 3000 hrs of exposure, Laves-phase coarsening resulted in a continuous reduction in strength of P92 steel. The % elongation and reduction in area versus ageing time plot was plotted (Fig. 3.27(c)). The % elongation and % reduction in area of as-received P92 steel was measured to be 23 ± 2 and 64 ± 2.5 %, respectively. It was observed that these values decreased continuously with increase in exposure duration. The ageing results in growth and coarsening of Laves phase which will increase the mobility and take away the solid solution strengthening elements from the matrix. This phenomenon results in reduced strngth and ductility of the P92 steel.

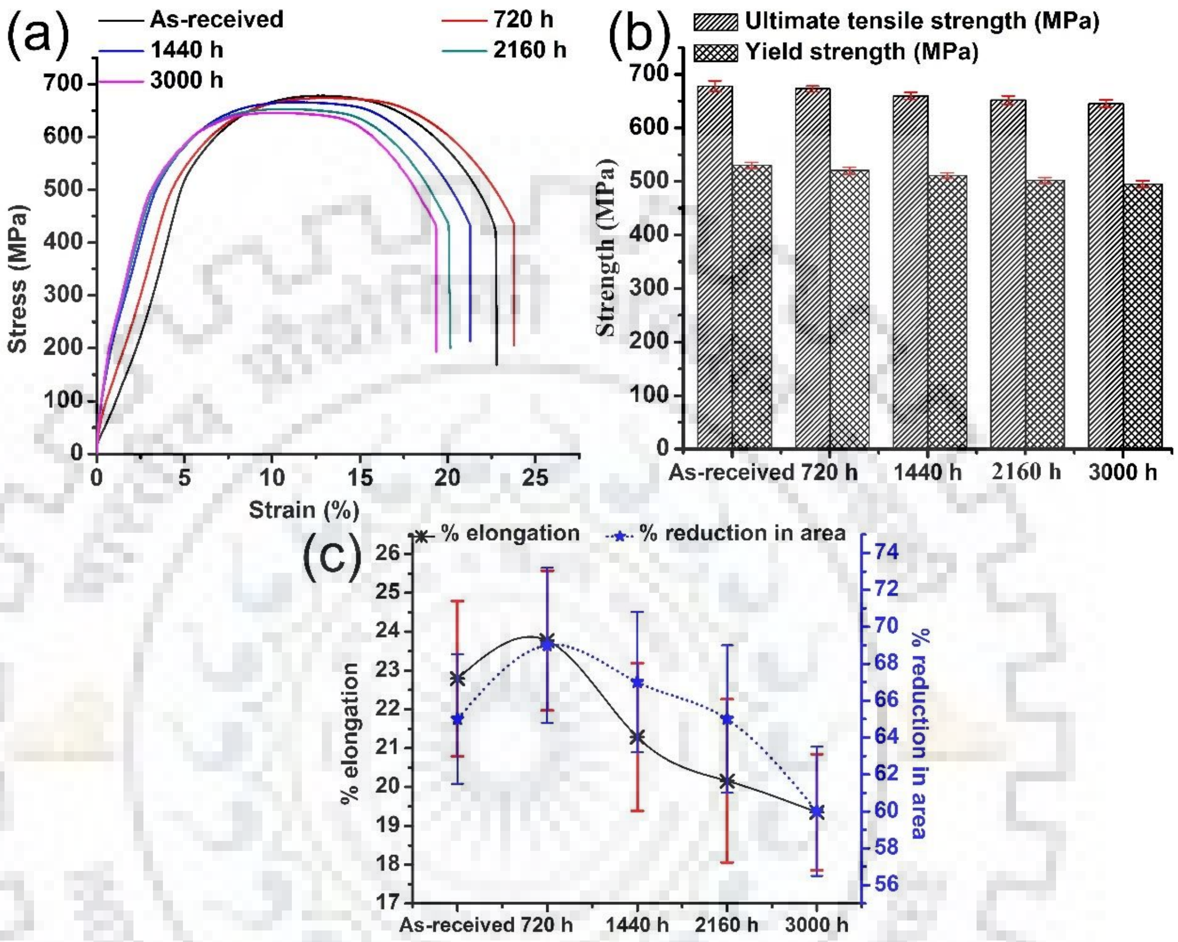

Figure 3.27 (a) Engineering stress-strain curve for various aged specimens, (b) variation of yield and ultimate tensile strength and (c) variation of % elongation and % reduction in area for various ageing time

The variation in room temperature tensuile properties of P92 steel during the thermal ageing is attributed to the complex microstructure evolution at different ageing time. The as-received condition microstructure is associated with the tempered martensite with $M_{23}C_6$ and fine MX preicpitates that stabalize the tempered martensitic microstructure. During the initial stage of the ageing (720 hrs), the nucleation of Laves phase was observed having size is very less and in order of size of coarse $M_{23}C_6$ precipitates. The $M_{23}C_6$ and MX precipitates does not show any considerable change in the size. Hence, nucleation of Laves phase after the ageing of 720 hrs resulted in small change in UTS and YS of P92 steel. A lot of studies have been published in the recent years related to the formation of Laves phase and their influence on the creep strengh of 9-12% Cr steels. Hald (Hald, 2008) reported a positive influence of Laves phase precipitation on long-term creep rupture behaviour of the 9-12% Cr steels inspite of formation of Laves phase reduced the solid solution strengthening due to consumption of W and Mo from the matrix. A lot of research have been published that report a negative influence of the Laves formation on creep rupture behaviour of 9-12% Cr steels (Lee et al., 2006; C. G. Panait et al., 2010a).

However, it is clear form the present study that Laves phase play an key role in deciding the mechanical properties of the P92 steel. AT the initial stage of the precipitation it shows the precipitation hardening effect but it observed to be loss earlier due to its high coarseining rate. The dramatic decrease in the creep strength was observed after the ageing of 720 hrs. the similar results was also reported by the Lee et al. (Lee et al., 2006). The Laves phase formed as a result of the reduction of W and Mo in solid solution matrix, i.e. loss of solid solution hardening. The higher coarseining rate of the Laves phase can not compensate the the loss of solid solution hardenmg. A continious decrease in YS and UTS was observed with increase in ageing time, as shown in Fig. 3.27(b). With increase in ageing time, the number and size of Laves phase increased continiously but coarseining rate decreased and reached to a stable stage after the 2160 hrs. Hence, the varying strength of P92 steel during ageing is mainly depends on the stabality of the microstructure.

The ductility and % reduction in area are relativilty complex during ageing althougth it does not show much variation and shows the similar trend as the strength. At the initial stage of the ageing, the ductility and % reduction in area was observed to be increased. This might be due to dominating softening effect as comapred to formation of he Laves phase. However, after 720 hrs, a continiou decrease was observed. The decrease in the ductility and % redreduction in area are attributed to the formation and coarseining of the Laves phase. The similar results was also reported by the Sun et al.(Sun et al., 2017). The coarse Laves phase might also act the crack nucleation sites that results in poor ductility of the P92 steel.

3.2.3.7 Fracture surface analysis

Figure 3.28 represents the fracture surface morphology of tensile tested samples. The as-received P92 steel tensile fracture surface consists of ductile dimples with some transgranular cleavage facets (Fig. 3.28(a)). After 720 hrs of ageing, the size and amount of dimples were found to be reduced due to the Laves phase evolution. The surface also consists of some amount of tear ridges and cleavage facets (Fig. 3.28(b)). The area fractions of tear ridges and cleavage facets continuously increased with ageing duration (Fig. 3.28(b-e)). After 3000 hrs of ageing, size of tear ridges increased extensively, and the number of ductile dimples reduced to a minimum (Fig. 3.28(e)). The site of Laves phase precipitation at the grain boundaries is considered the potential site for crack nucleation and it makes steel susceptible to inter-granular cracking (Thomas Paul et al., 2008). Hence, P92 steel can fail due to brittle intergranular fracture due to excessive precipitation and coarsening of Laves phase.

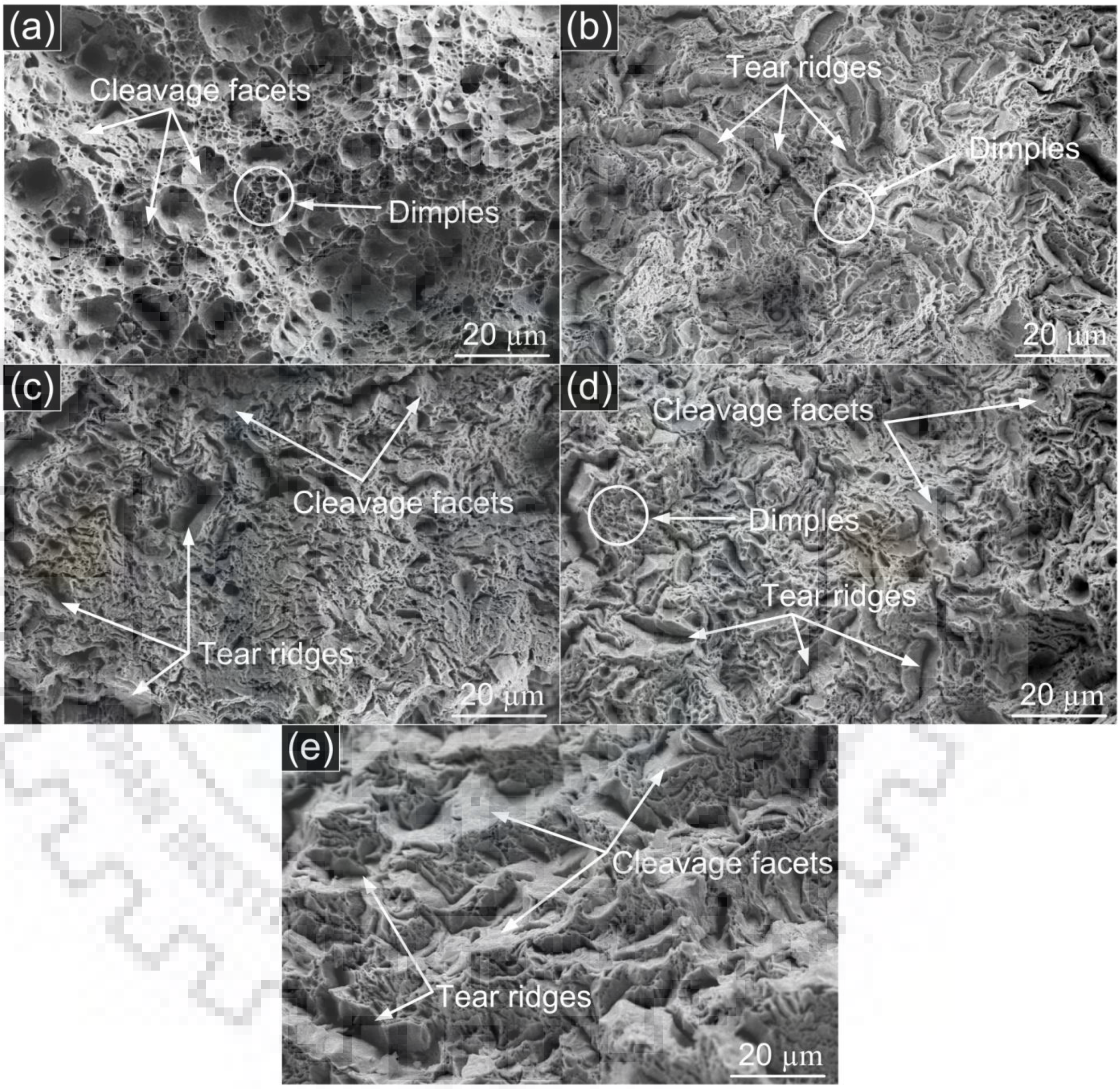

Figure 3.28 Fracture surface morphology of tensile tested specimens after different ageing conditions (a) as-received, (b) 720 hrs, (c) 1440 hrs, (d) 2160 hrs and (e) 3000 hrs

3.2.3.8 Microhardness and Charpy toughness

The microhardness variation with ageing time also showed similar trend as the strength (Fig. 3.29(a)). The hardness of as-received P92 steel was measured to be 227 ± 4 HV. It was observed that the microhardness value decreased gradually as the ageing time prolonged. After ageing of 3000 hrs, the microhardness was measured to be 205 ± 4 HV. The decrease in microhardness with ageing is attributed to reduction in solid solution strengthening and softening of the tempered martensite.

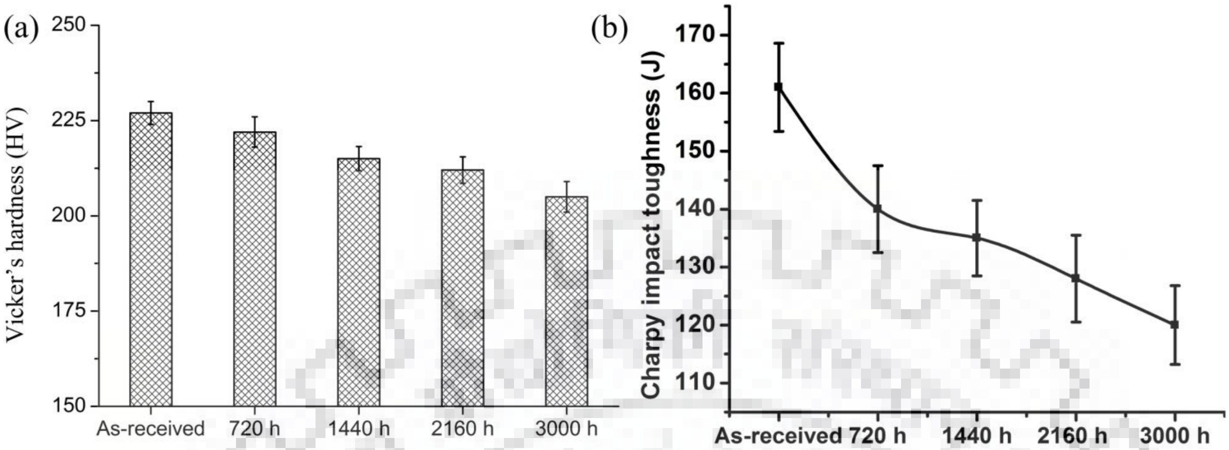

Figure 3.29 (a) Variation in hardness and (b) variation in Charpy toughness with ageing time

The Charpy toughness of P92 steel in as-received state was measured to be 161 ± 5 J. The Charpy toughness showed a decreasing trend with increase in ageing time as shown in Fig. 3.29(b). The Charpy toughness was decreased dramatically to 140 ± 7.5 J after the ageing of 720 hrs. The decrease in Charpy toughness was observed to be relatively slow with further increase in ageing time from 720 hrs to 3000 hrs. The Charpy toughness was measured to be 120 ± 6.8 J, after the ageing of 3000 hrs. The Charpy toughness of samples after 3000 hrs of ageing was noted to be 25 % of as-received P92 steel. The coarsening rate of Laves phase was observed to be higher in ageing time range of 720 to 1440 hrs. After the ageing of 1440 hrs, the rate of coarsening tends to decrease and the evolution of Laves phase become saturated that resulted Charpy toughness reduces in slower rate after the ageing of 1440 hrs. The sudden decrement in Charpy toughness after the 720 hrs of ageing is attributed to cracking of secondary phase particles during thermal straining, formation of Laves phase and decohesion between precipitates and matrix interface (Blach et al., 2009).

3.2.4 *Effect of normalizing and tempering on the dissolution of Laves phase*

The long-term ageing treatment was conducted in a furnace at 620 ^{0}C for 4560 hrs ageing time. After long-term ageing, the normalizing was performed at 1050 ^{o}C for 60 min. the tempering was performed at 760 ^{o}C for varying tempering time from 2 hrs to 4 hrs for microstructure, growth and coarsening of Laves phase. The heat treatment matrix is depicted in Table 3.3.

3.2.4.1 Effect of normalizing and tempering on grain size

Figure 3.30(a-d) presents the optical micrographs of the as-received, Aged, Aged+N&T2 and Aged+N&T4 samples. Figure 3.30(a) shows the prior austenite grain boundaries (PAGBs), lath blocks, martensitic matrix, precipitates along PAGBs as well as in the matrix in the as-received condition of P92 steel. After long term aging as shown in Fig. 3.30(b), the lath morphology disappeared and PAGBs were also straightened. The grains and their grain boundaries were seen in the case of aged+N&T2 as shown in Fig. 3.30(c). The grain boundaries and precipitates at PAGBs were seen more clearly after 4 hrs of tempering as shown in Fig. 3.30(d).

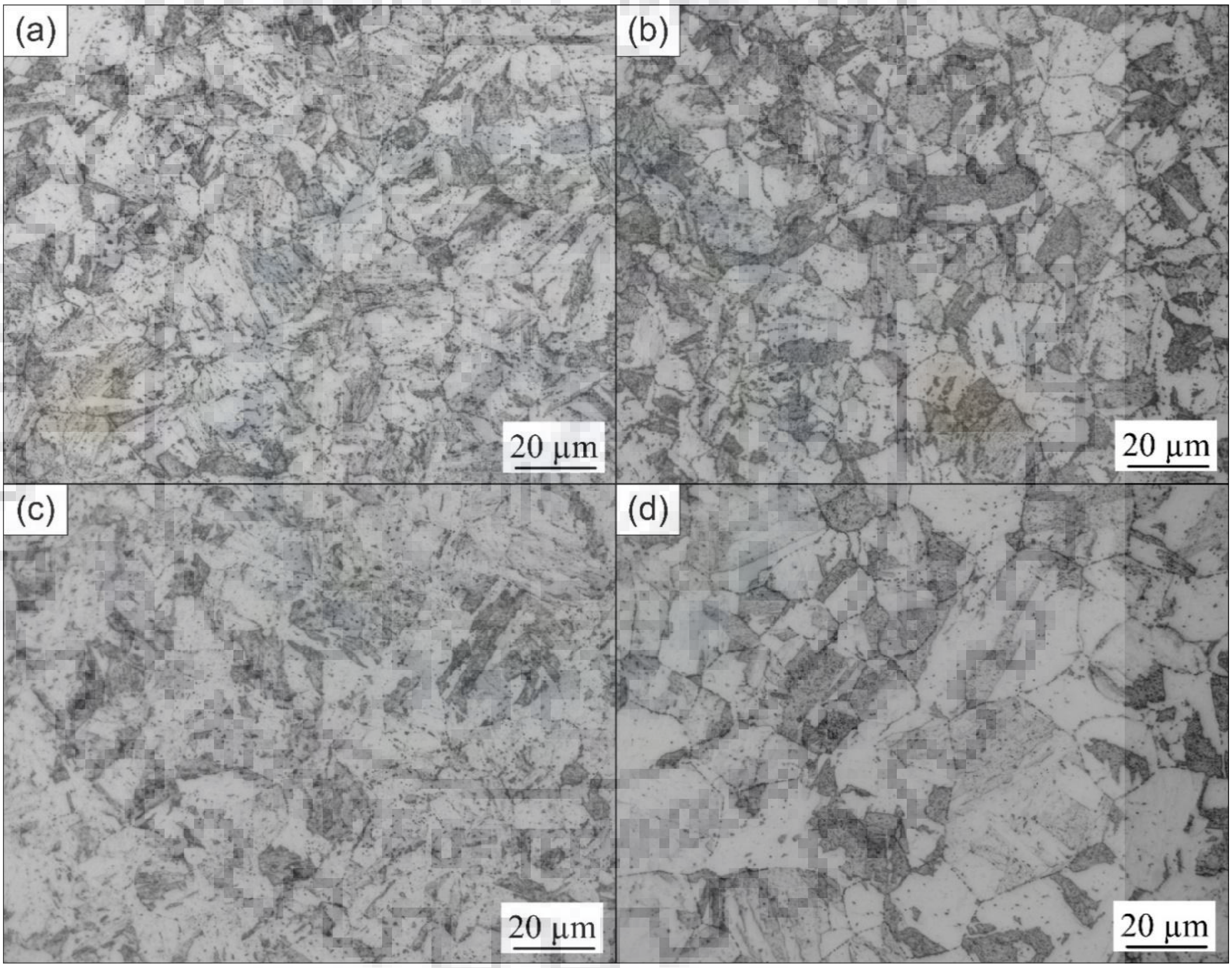

Figure 3.30 Optical micrograph of (a) as-received P92 steel, (b) Aged at 620 ^{o}C for 4560 hrs, (c) Aged + normalized at 1040 ^{o}C for 1 hr + tempered ^{o}C at 760 ^{o}C for 2 hrs and (d) Aged + normalized at 1040 ^{o}C for 1 hr + tempered ^{o}C at 760 ^{o}C for 4 hrs

The optical micrographs were processed using Image J software to see better features of grains and for measurements of grain size. The variation in grain size was plotted as shown in Fig. 3.31(a). The average grain size was measured 16 ± 3 µm for the as-received condition. The average grain size was measured 17 ± 4 μm for the Aged condition. The average grain sizes were measured 15 ± 4 μm and 16 ± 4 μm for Aged+N&T2 and Aged+N&T4 condition, respectively. The variation in microhardness for different aging conditions is shown in Fig. 3.31(b). The as-received P92 steel microhardness was measured at 232 ± 6 HV. After 4560 hrs of tempering, a decrease in microhardness was observed. After aging, the microhardness was measured at 218 ± 2 HV. The microhardness was found increased after normalizing and followed by 2 hrs of tempering. Further 2 hrs of tempering resulted in a small decrease in hardness, possibly due to the softening of further tempering of martensite. The hardness was measured at 222 ± 6 HV after Aged+N&T4 condition. However, no significant change was observed in the microhardness of all heat-treated specimens.

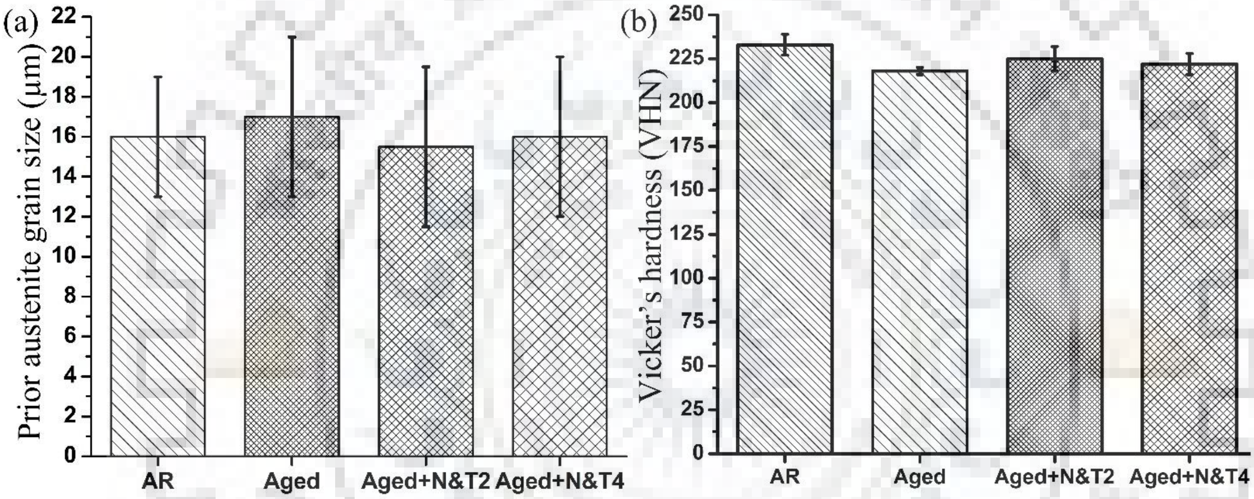

Figure 3.31 (a) Variation in grain size and (b) variation in microhardness for different heat treatment conditions

3.2.4.2 Effect of long-term aging on the nucleation of Laves phase and the effect of N&T on the evanesce of Laves phase

The secondary electron micrographs (SEMs) of the as-received, Aged, Aged+N&T2 and Aged+N&T4 conditions are presented in Fig. 3.32(a-d). Fig. 3.32(a) shows the fine distribution of precipitates at PAGBs and sub-grain boundaries inside a PAG. After aging, the grain boundaries are observed to be straightened as compared to the as-received material. The number of precipitates has increased at sub-grain boundaries and PAGBs, as shown in Fig. 3.32(b). After normalizing and 2 hrs of tempering, finer precipitates were visible at grain boundaries and PAGBs, as shown in Fig. 3.32(c). Additional 2hrs of tempering resulted in more nucleation of precipitates at boundaries. The precipitates and PAGBs were clearly visible while sub-grain boundaries were not visible, as shown in Fig. 3.32(d). The normalization resulted in the dissolution of fine $M_{23}C_6$ precipitates and the formation of martensite structure while tempering resulted in the evolution of precipitates and formation of tempered martensite. The number of precipitates also decreased after the Aged+N&T2 condition.

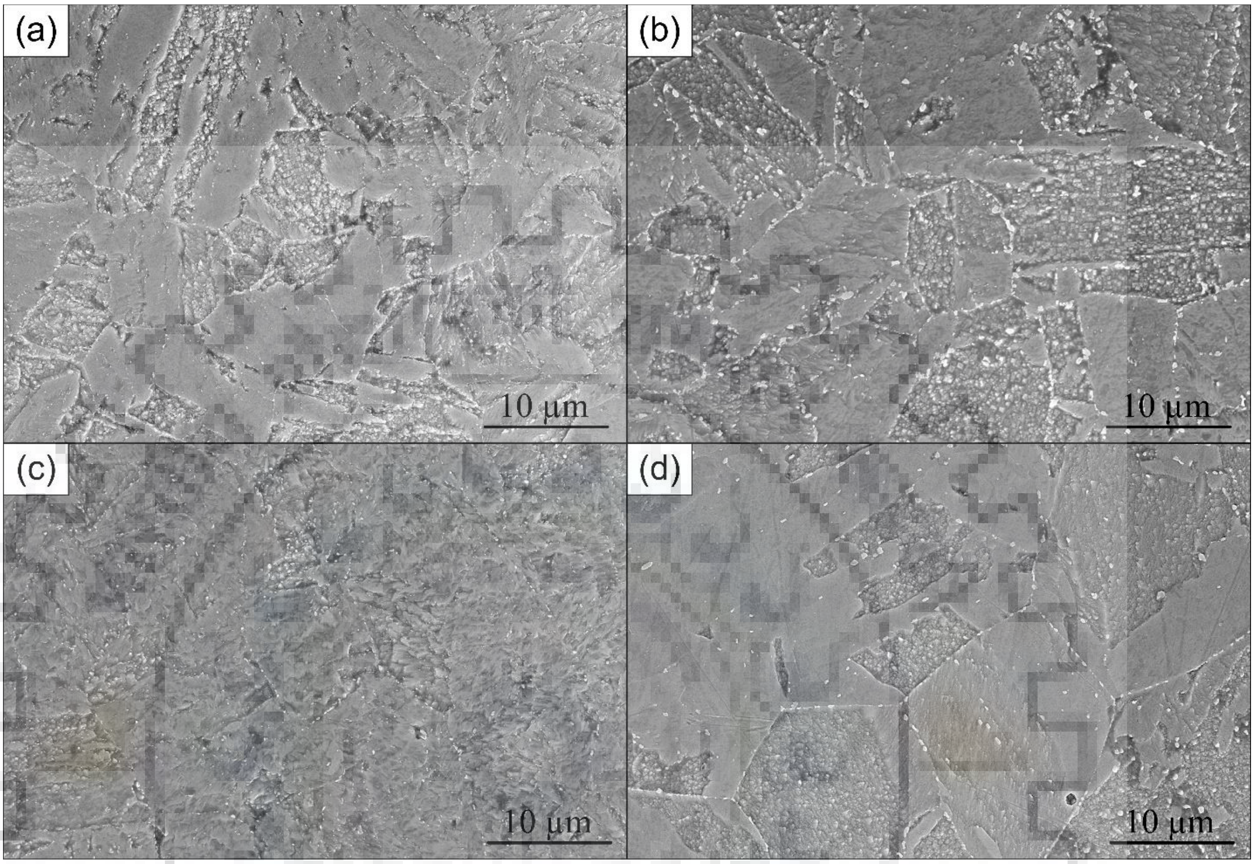

Figure 3.32 Secondary electron micrographs (SEMs) of (a) as-received P92 steel, (b) Aged at 620 ^oC for 4560 hrs, (c) Aged + normalized at 1040 ^oC for 1 hr + tempered ^oC at 760 ^oC for 2 hrs and (d) Aged + normalized at 1040 ^oC for 1 hr + tempered ^oC at 760 ^oC for 4 hrs

Figure 3.33 demonstrates the SEM of the aged specimen at 620 ^oC for 4560 hrs and their line scan results for marked locations. The SEM shows coarse white precipitates with their locations (Fig. 3.33(a)). Two locations were selected to perform line-scan as marked by the yellow lines. The white coarse precipitate present at location 1 was suggested as W and Mo rich Laves phase and second fine precipitate suggested as Cr-rich $M_{23}C_6$ precipitate, as shown in Fig. 3.33(b). The two white precipitates present at location 2 were also suggested as W and Mo rich Laves phase, as shown in Fig. 3.33(c). A precipitate present between these two Laves phase particles was suggested as Cr-rich $M_{23}C_6$ precipitate. The Cr peak in scan results was used as $M_{23}C_6$ carbide signature while W or Mo peaks were used as Laves phase chemical signature.

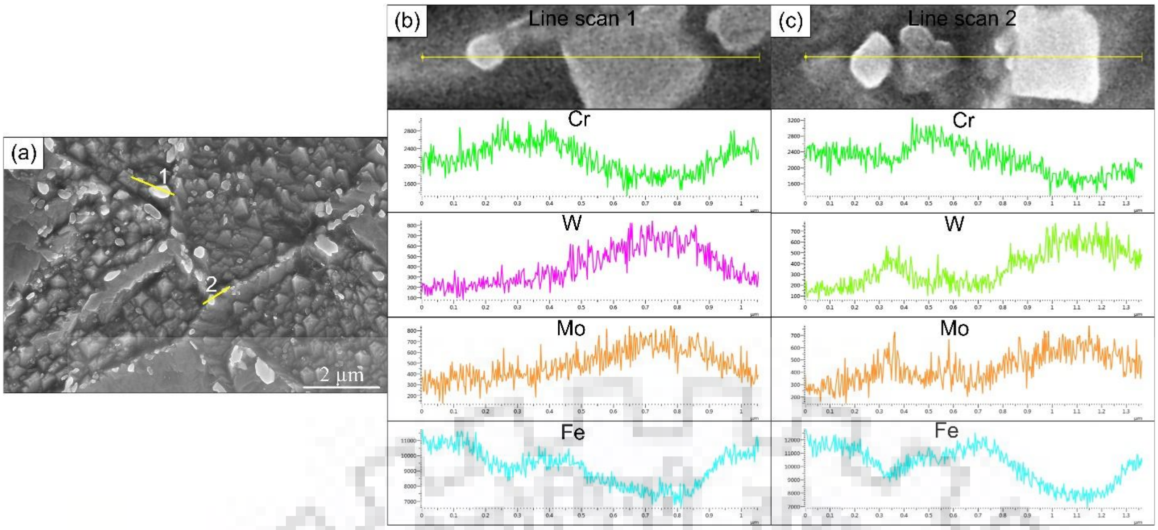

Figure 3.33 (a) SEM of aged specimen at 620 ^{o}C for 4560 hrs, (b) line scans for different elements at point 1 and (c) line scans for different elements at point 2

Figure 3.34 demonstrates the SEM of Aged+N&T4 condition and corresponding line scan results. After N&T4, the micrograph showing coarse white precipitates with two marked locations, as shown in Fig. 3.34(a). The biggest white particle present at location 1 is suggested as $M_{23}C_6$ precipitate, as shown in Fig. 3.34(b). Because the Cr indicates for $M_{23}C_6$ carbide and Laves does not contain enriched Cr. The other two particles present at location 2 are also suggested as Cr-rich M23C6 type carbides, as shown in Fig. 3.34(c). After N&T, Laves phase was not detected at any location. Hence, the dissolution of Laves phase may have been achieved after the N&T treatment of aged specimens.

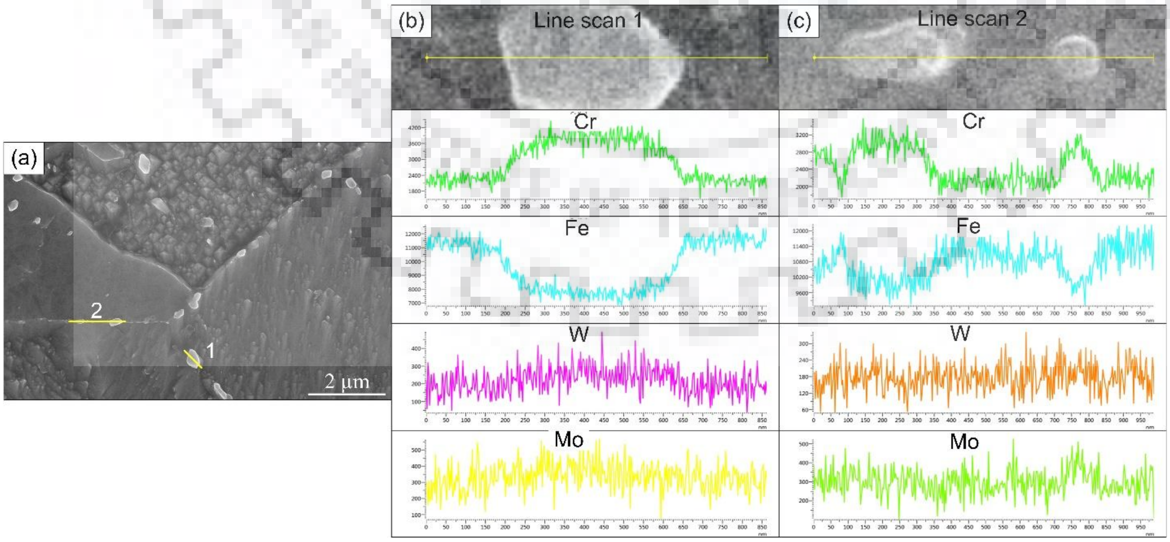

Figure 3.34 (a) SEM of specimen (Aged + normalized at 1040 ^{o}C for 1 hr + tempered ^{o}C at 760 ^{o}C for 4 hrs), (b) and (c) line scans for different elements at point 1 and point 2

The elemental mapping for the as-received, Aged and Aged+N&T4 conditions are presented in Fig. 3.35(a-c). The elemental mapping results confirm the uniform distribution of Fe and Cr on the grain boundaries and other elements in the matrix of the as-received specimen, as shown in Fig. 3.35(a). In aged samples, Fe was found depleted from PAGBs and uniform distribution of Cr was observed, as shown in Fig. 3.35(b). After the aging of 4560 hrs, the Mo and W concentration was observed to be enhanced along the sub-grain boundaries and PAGBs, which is in association with the nucleation of Laves phase near the $M_{23}C_6$ phase.

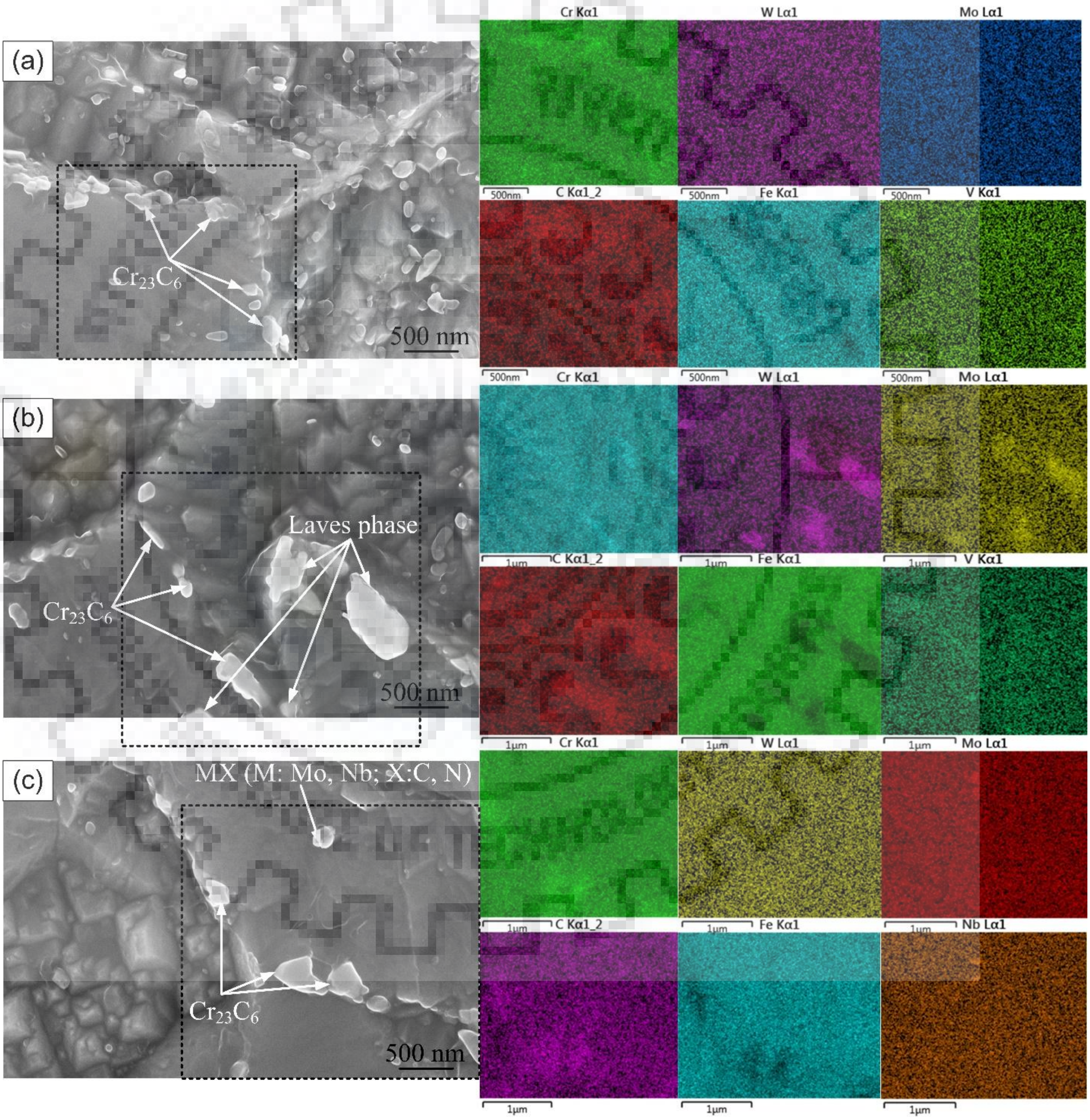

Figure 3.35 Mapping of precipitates present in (a) as-received P92 steel, (b) Aged at 620 °C for 4560 hrs and (c) Aged + normalized at 1040 °C for 1 hr + tempered °C at 760 °C for 4 hrs

The lower concentration of Fe and the higher concentration of Mo and W at white coarse precipitates confirmed it as Laves phase. After re-austenitization followed by tempering of aged specimens, the uniform distribution of Mo and W were observed which indicates the dissolution of Laves phase, as shown in Fig. 3.35(c). The element maps were observed to be similar to the base material. So, the recovery to original microstructure was achieved after normalizing and tempering of aged specimens. The Laves phase is absent but the size of $M_{23}C_6$ precipitates was found to be increased as compared to the as-received base material.

3.2.4.3 Effect of aging and N&T on the fraction of Laves phase

After the Rietveld refinement, the XRD patterns of the as-received, Aging and Aging+N&T4 specimens are shown in Fig. 3.36(a-f). In all three XRD specimens, the higher intensity peaks were clearly identified as BCC, i.e., α-ferrite, which indicates the tempered martensite microstructure. Additionally, some small intensity peaks were identified as $M_{23}C_6$, i.e., $Cr_{23}C_6$, Laves phase, and retained austenite. In the as-received material, only BCC peaks were observed, i.e., α-ferrite, as shown in Fig. 3.36(a). No $Cr_{23}C_6$ precipitates were detected in the as-received material probably due to its small size and fraction. After aging, BCC, $M_{23}C_6$, Laves phase and retained austenite peaks were detected, as shown in Fig. 3.36(b). After aging, the coarsening of $Cr_{23}C_6$ precipitates occurred, indicated by an increase in precipitate size.

The nucleation of Laves phase was also confirmed by the XRD peaks. BCC, $M_{23}C_6$, and retained austenite peaks were detected in Aging+N&T4 specimen, as shown in Fig. 3.36(c). Laves phase was not detected after normalizing of aged specimens. The Laves phases were dissolved during normalizing and unable to re-nucleate at the time of tempering. But $Cr_{23}C_6$ precipitates were detected due to coarsening/increased precipitate size during aging. The phase fractions were calculated using Rietveld refinement of the raw XRD data for different aging conditions are tabulated in Table. 3.8. In the as-received material, 100% BCC ferrite was detected but precipitates were not detected due to their small size which was confirmed from SEM results. After 4560 hrs of aging, 1.3 % Laves phase was detected and a small amount of retained austenite was also detected. But after normalizing and tempering, no Laves phase was detected. To see small intensity peaks, the highest intensity peaks were zoomed, as shown in Fig. 3.36(d-f). In the as-received material, the $Cr_{23}C_6$ precipitate and Laves phase peaks were not seen, as shown in Fig. 3.36(d). But after 4560 hrs of aging, the $Cr_{23}C_6$ precipitate and Laves phase peaks were clearly seen, as shown in Fig. 3.36(e).

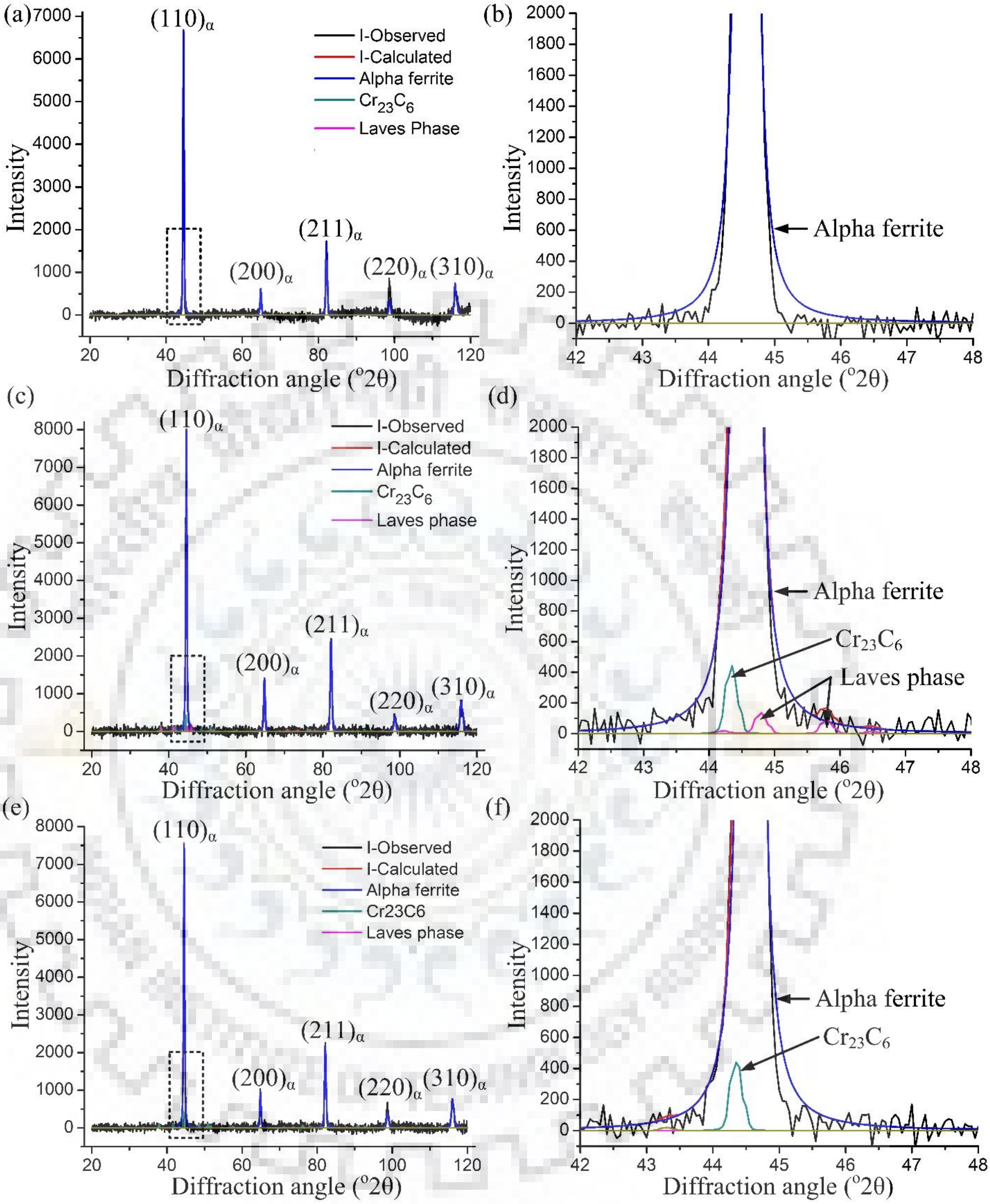

Figure 3.36 XRD profiles after Rietveld refinement for the: (a) & (b) as-received, (c) & (d) Aged and (e) & (f) Aged+N&T4

After normalizing followed by 4 hrs of tempering, only $Cr_{23}C_6$ precipitate peak was seen inside the bigger BCC peak while no Laves phase peaks were seen, as shown in Fig. 3.36(f).

Table 3.8 Phase fractions calculated using Rietveld refinement of the raw XRD data for different aging conditions

Conditions	f_{α}	f_{Cr23C6}	$f_{Laves\ phase}$
As-received	1.0	0.0	0.0
Aging	0.95	0.042	0.013
Aging+N&T4	0.95	0.049	0.0

To see the effect of normalizing and tempering on Laves phase, the Laves phase, and $Cr_{23}C_6$ peaks were plotted separately for Aging and Aging+N&T4 conditions, as shown in Fig. 3.37(a-b). After 4560 hrs of aging, the highest peak of $Cr_{23}C_6$ precipitate was identified at 44.3° and Laves phase peak was confirmed at 44.8°, as shown in Fig. 3.37(a). After 4560 hrs of aging, the phase fractions were calculated after Rietveld refinement as 4.16 and 1.32 % for $Cr_{23}C_6$ and Laves phase, respectively. After normalizing and tempering, no Laves phase peaks are identified, as shown in Fig. 3.37(b). After normalizing followed by 4 hrs of tempering, the phase fraction of $Cr_{23}C_6$ precipitates was increased from 4.2 % to 4.9 %.

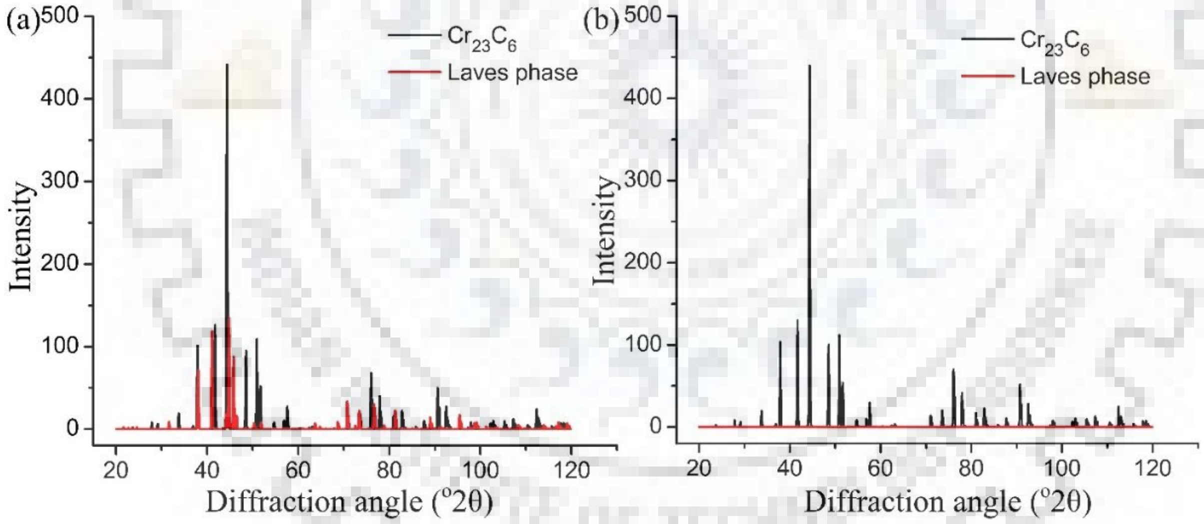

Figure 3.37 XRD peaks of NaCl structure of $Cr_{23}C_6$ and hexagonal structure of Laves phase (a) Aging and (b) Aging+N&T4

Figure 3.38(a-b) shows the EBSD phase map of P92 steel in Aged and Aged+N&T4 conditions. The Laves phase (Fe_2W+Fe_2Mo) was clearly identified only in aged condition, as shown in Fig. 3.38(a). After 4560 hrs of aging, the Laves phase (Fe_2W+Fe_2Mo) and $Cr_{23}C_6$ phase were measured as 1.00 and 26.15 %, respectively. After normalizing followed by 4 hrs of tempering, the dissolution of Laves phase is identified from the EBSD phase map as shown in Fig. 3.38(b). The regions appearing black (zero solutions or non indexable region) are very likely some of the grain boundaries.

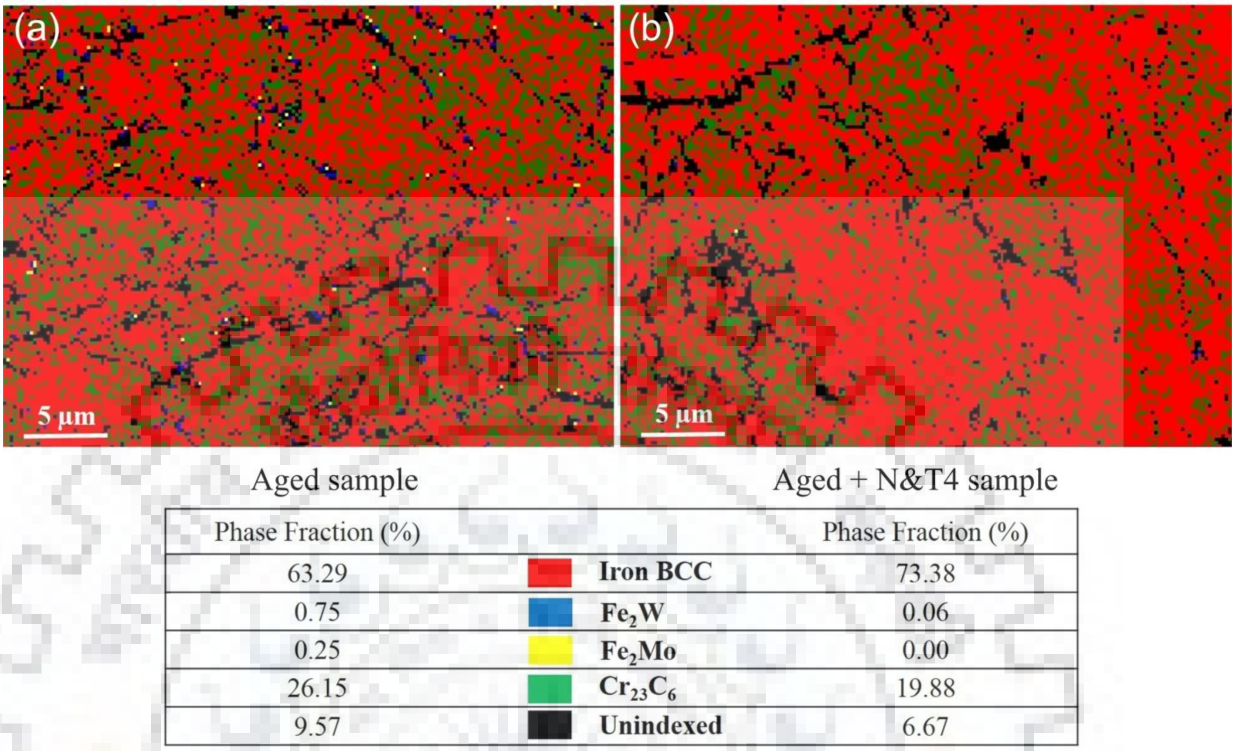

Phase Fraction (%)			Phase Fraction (%)
63.29	🟥	**Iron BCC**	73.38
0.75	🟦	**Fe_2W**	0.06
0.25	🟨	**Fe_2Mo**	0.00
26.15	🟩	**$Cr_{23}C_6$**	19.88
9.57	⬛	**Unindexed**	6.67

Figure 3.38 EBSD phase map of P92 steel (a) 1% Laves phase (Fe_2W+Fe_2Mo) in Aged and (b) no Laves phase in Aged+N&T4 condition

3.2.4.4 Effect of aging and N&T on precipitate size

The SEMs of the as-received, Aged and Aged+N&T4 conditions at higher magnification are presented in Fig. 3.39(a-c). The SEMs demonstrate the morphology evolution of the Laves phase, coarsening of $M_{23}C_6$-type precipitates and dissolution of the Laves phase. Only $M_{23}C_6$ precipitates are detected at the PAGBs in the as-received material, as shown in Fig. 3.39(a). Prior to long term aging, no Laves phase was detected in the as-received material. In aged specimens, Mo and W rich Laves phases were detected on the grain boundaries and martensitic lath boundaries, as shown in Fig. 3.38(b). The coarse intergranular $M_{23}C_6$ precipitates attributed to higher strength by impeding the movement of the sub-grain boundaries while MX precipitates acted as dislocation movement barrier during aging. During aging, the coarsening of coarse intergranular $M_{23}C_6$ precipitates and nucleation of Laves phase at sub-grain boundaries were observed.

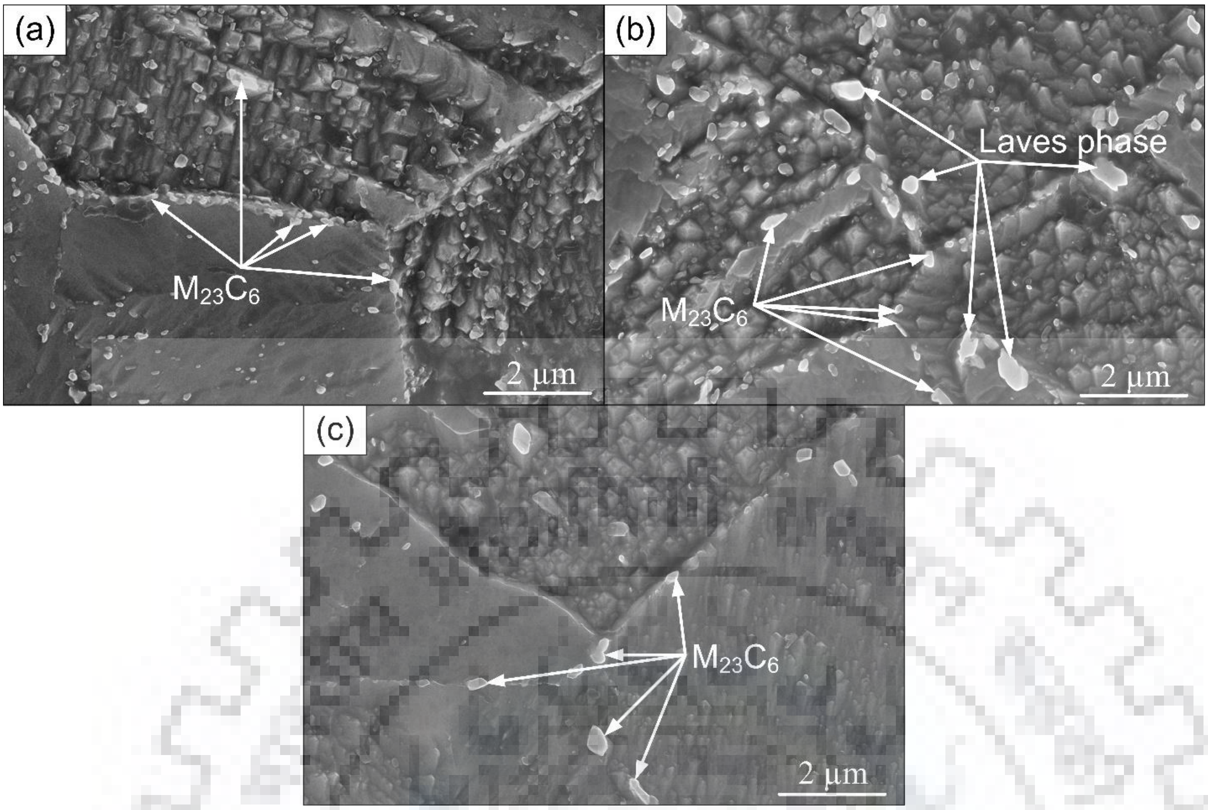

Figure 3.39 SEM of (a) as-received P92 steel, (b) Aged at 620 ^{o}C for 4560 hrs and (c) Aged + normalized at 1040 ^{o}C for 1 hr + tempered ^{o}C at 760 ^{o}C for 4 hrs

The coarsening of precipitates resulted in the reduction of pinning effect while nucleation of Laves phase resulted in the reduction of MX precipitates. Hence, the formation of coarse grains during tempering governed by the loss of pinning effect due to reduction in precipitates presented along the sub-grain boundaries. After aging, the coarsening of $M_{23}C_6$-type precipitates was also observed. But the coarsening of $M_{23}C_6$-type precipitates was observed higher than the coarsening of Laves phase after 4560 hrs of aging. The nucleation and coarsening mechanism will be discussed later. In Aged+N&T4 specimens, the disappearance of Laves phases were observed, as shown in Fig. 3.39(c).

The normalizing at 1040 °C resulted in dissolution of Laves phase and dissolution of fine $M_{23}C_6$ precipitates while fine MX precipitates remained undissolved. The tempering at 760 °C for 2 hrs and 4 hrs resulted in the nucleation of fine $M_{23}C_6$ precipitates and MX precipitates.

The precipitate sizes were measured using Image-J software and plotted on the same scale for all conditions. The mean size of $M_{23}C_6$-type precipitates was reported in the range of 80 nm to 100 nm while the mean size of MX-type precipitates was reported in the range of 20-40 nm (Fedoseeva et al., 2017; Maddi et al., 2016). The precipitates having a size less than 20 nm were not counted due to the limited resolution of the images. Figure 3.40 demonstrates the corresponding average precipitate size distributions with respect to Fig. 3.39. The average precipitate size was measured 116 ± 20 nm for the as-received specimens. This precipitate size corresponds to only $M_{23}C_6$-type precipitates, because there is no Laves phase in the as-received condition.

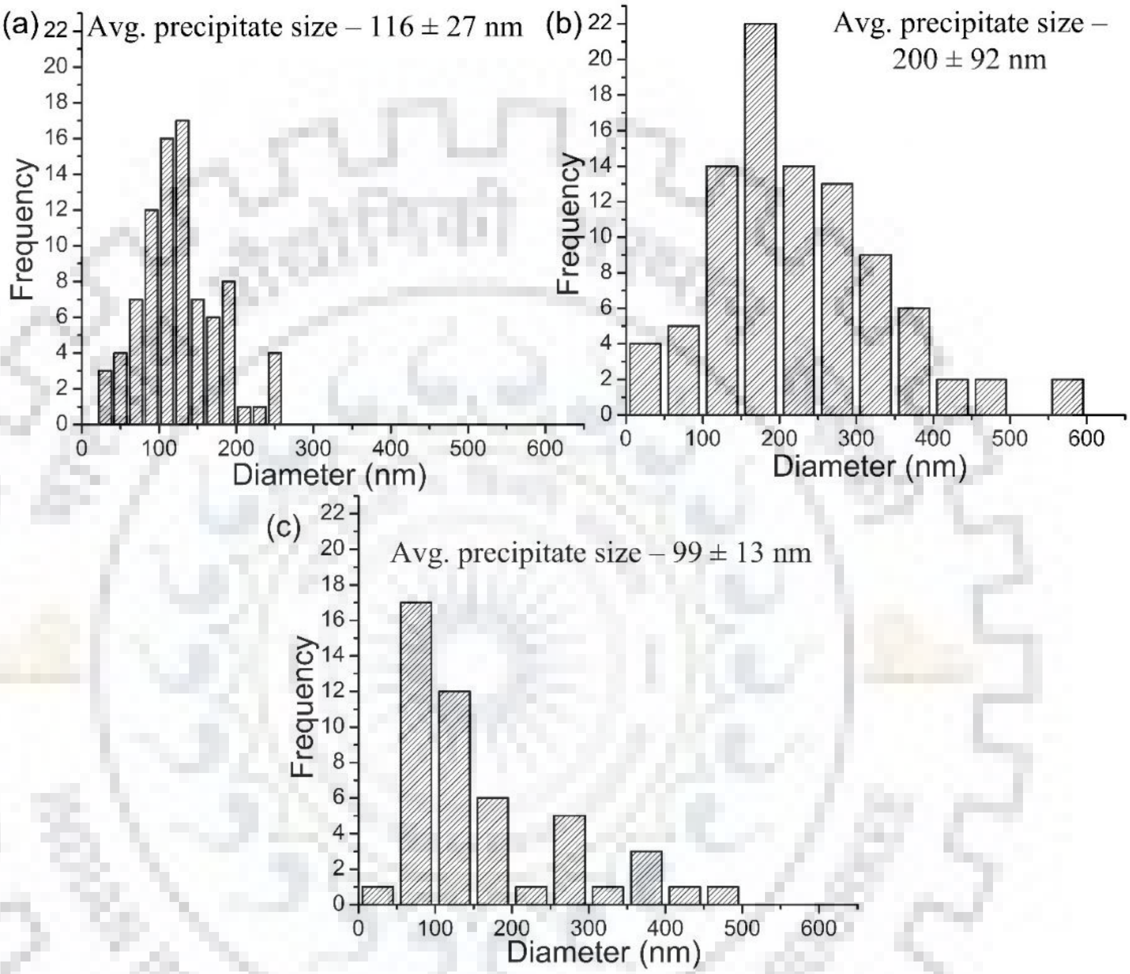

Figure 3.40 Particle size of Laves phase and $M_{23}C_6$ precipitates measured from SEM images (a) as-received P92 steel, (b) Aged at 620 ^{o}C for 4560 hrs and (c) Aged + normalized at 1040 ^{o}C for 1 hr + tempered ^{o}C at 760 ^{o}C for 4 hrs

The Laves phase evolution and coarsening of $M_{23}C_6$ precipitates were observed during aging and average precipitate size was measured 200 ± 92 nm for Aged specimens. This precipitate size was the average of both Laves phase and $M_{23}C_6$-type precipitates. But the average precipitate size was found to be reduced from 200 ± 92 nm to 99 ± 13 nm after aging followed by re-austenitization and tempering. This reduction in precipitate size may be due to the dissolution of Laves phase, and this measured size corresponds to only $M_{23}C_6$-type precipitates.

3.2.4.5 Dissolution of Laves phase

Thermo-Calc is used for calculating the mole fraction of phases as a function of temperature with the TCFE6 database for the alloy composition (given in Table 1), as shown in Fig. 3.41. BCC (austenite), FCC (ferrite), $M_{23}C_6$, MX, Laves phase and Z-phase are the main phases predicted in the temperature range 500-1200 ^{o}C. When the temperature is increased beyond maximum operating temperature (620 ^{o}C) for the P92 boiler steel, the phase fractions of $M_{23}C_6$ and Laves phase will decrease, while the fraction of MX-type precipitates will remain constant up to the temperature 900 ^{o}C.

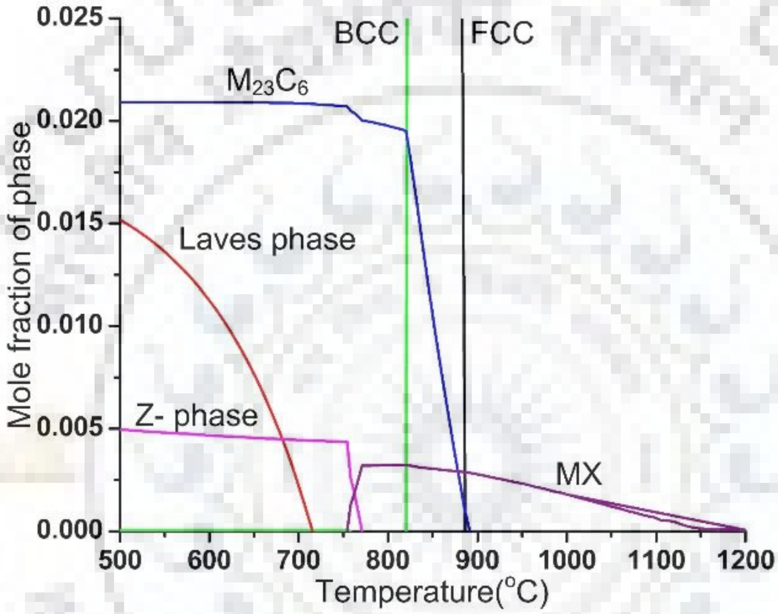

Figure 3.41 Mole fraction of phases as a function of temperature calculated using Thermo-Calc for the temperature range of 500-1200 ^{o}C

The precipitate composition changes with respect to temperature are also calculated using Thermo-Calc software. The calculated $M_{23}C_6$ phase is rich in chromium (Cr), iron (Fe), tungsten (W) and molybdenum (Mo), as shown in Fig. 4.42(a). This model suggests that the $M_{23}C_6$ phase has a drastic change in Cr, W, and Mo composition with an increase in temperature. In the $M_{23}C_6$ phase, the Cr content decreases while the content of W and Fe increase with an increasing temperature. The calculated Laves phase was rich in W, Fe, and Mo, as shown in Fig. 4.42(b). The effect of temperature on the composition of Laves phase is also observed. The W content is slightly decreased while Fe and Mo content are slightly increased with increased temperature. The overall composition of Laves phase shows a smaller degree of change as compared to the $M_{23}C_6$ phase.

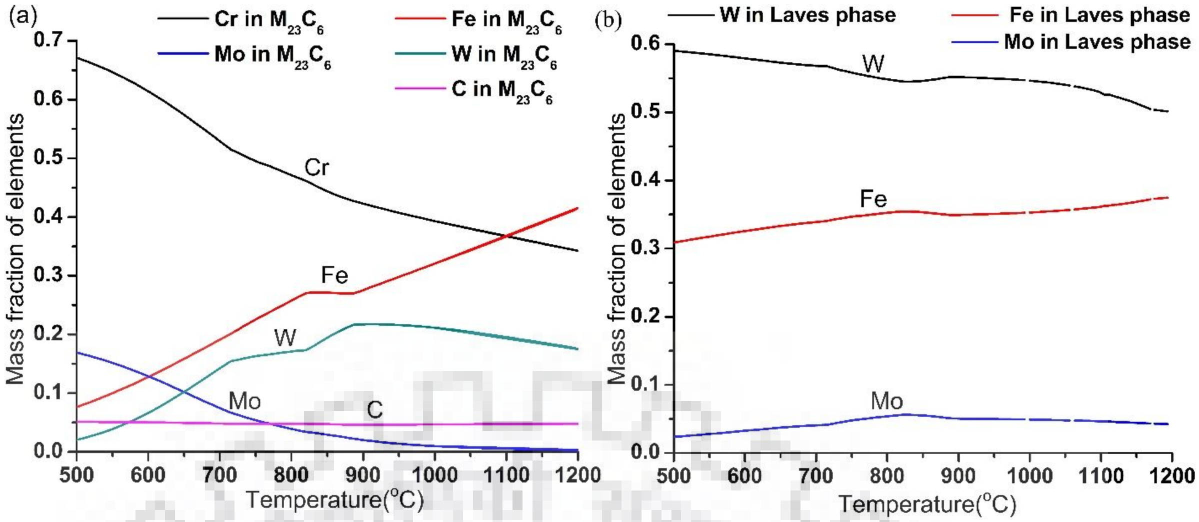

Figure 3.42 Mass fraction of elements in a phase with temperature calculated using Thermo-calc for: (a) $M_{23}C_6$ and (b) Laves phase

Thermodynamically, Fig. 4.41 shows the Laves phases start dissolving above 720 ^{o}C while the dissolving temperature for $M_{23}C_6$ precipitates is near to upper critical temperature (Ac_3) of P92 steel. The austenitization temperature of P92 steel is suggested in the range of 950-1150 ^{o}C. So, we have taken normalizing temperature 1050 ^{o}C to dissolve $M_{23}C_6$ and Laves phase completely. Re-austenitization resulted in martensitic microstructure with high dislocation density while tempering resulted in the evolution of precipitates and tempering of martensite. The dissolution of coarse $M_{23}C_6$ and Laves phase precipitates is observed during normalizing of P92 steel while fine V and Nb-rich precipitates were undissolved. The tempering temperature for P92 steel is suggested in the range of 740-780 ^{o}C for 2 hrs.

A Schematic showing microstructure evolution during aging, after aging, after normalizing and after normalizing and tempering are presented in Fig. 4.43. The as-received microstructure having tempered martensitic microstructure, coarse $M_{23}C_6$, fine MX precipitates, laths, packets, lath boundaries and packet boundaries. During Aging, the nucleation and coarsening of Laves phase at sub-grain boundaries and PAGBS are observed and shown by yellow color, as shown in Fig. 4.43. The coarsening of $M_{23}C_6$ type precipitates is also observed. During normalizing, dissolution of precipitates is observed except some fine V and Nb-rich MX-type precipitates. After tempering, only M23C6-type precipitates nucleate at PAGBs. Because nucleation of Laves phase is a time-dependent process that depends on the time of tempering. Hence, after aging normalizing is performed at 1050 ^{o}C and followed by tempering at 760 ^{o}C which avoids the Laves phase.

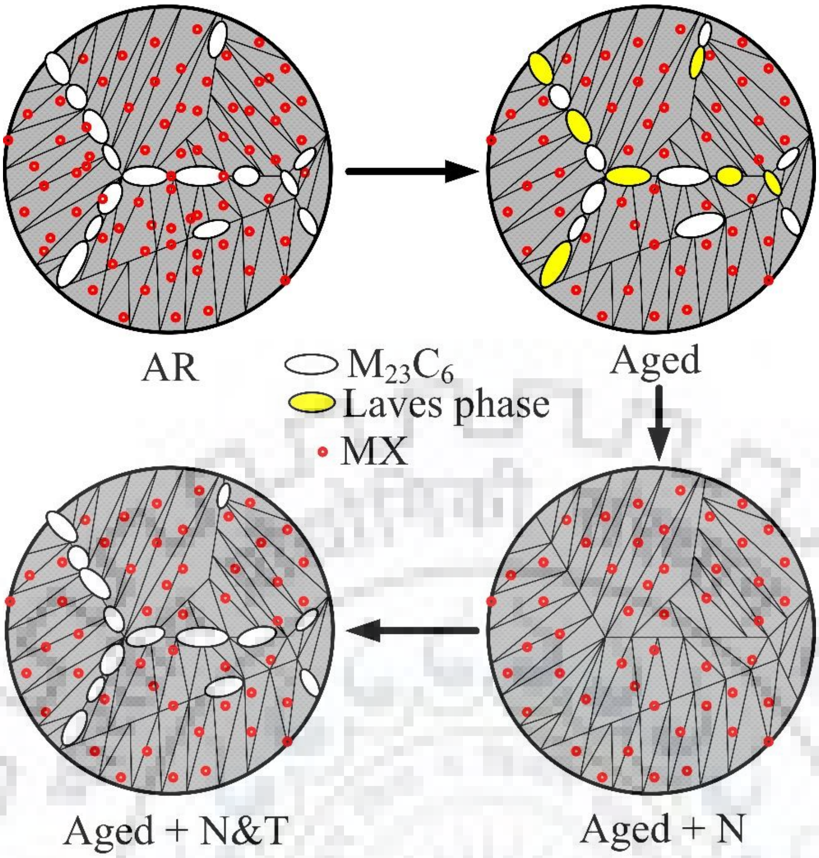

Figure 3.43 Schematic evolution of microstructure and precipitates during aging followed by normalizing and tempering process

Domerus (Doremus, 1985) has found the radius of a dissolved spherical particle as a function of time. To predict the time of re-austenitization at which Laves phase particles will dissolve completely, the following equation is used.

$$R^2 - R_o^2 = 2\frac{(C_i - C_e)Dt}{(C_p - C_e)}\left[1 + \frac{2R_o}{\sqrt{\pi D t}}\right] \qquad (3.2)$$

where R is final radius of precipitate after t time of re-austenitization, R_o is initial radius of precipitate, D is diffusion coefficient of elements (W) in precipitate (Laves phase) at re-austenitization temperature, t is time of re-austenitization, C_i is initial concentration of elements in the matrix, C_e is concentration at the interface of precipitate and matrix, and C_p is the concentration of elements in the precipitate.

Figure 4.44 (a) shows a schematic for modeling the dissolution of a spherical particle. The above eq (2) and this model is used to calculate the precipitate (Laves phase) radius with increasing time of re-austenitization. The calculation is done only for W containing Laves phase because W has lower diffusion coefficient as compared to Mo.

The diffusion coefficient for W is calculated as 1.67 × 10^{-16} m^2/sec from DICTRA. The concentration of W in Laves phase is also measured from EDX. The value of C_p, C_e, and C_i is measured as 25, 5, and 2 respectively. The maximum diameter of Laves phase is also calculated as 600 nm from FESEM micrograph. The complete dissolution is suggested from model after 16 min of time (Fig. 4.44(b)). Additional time of re-austenitization may allow W and Mo to diffuse in the matrix.

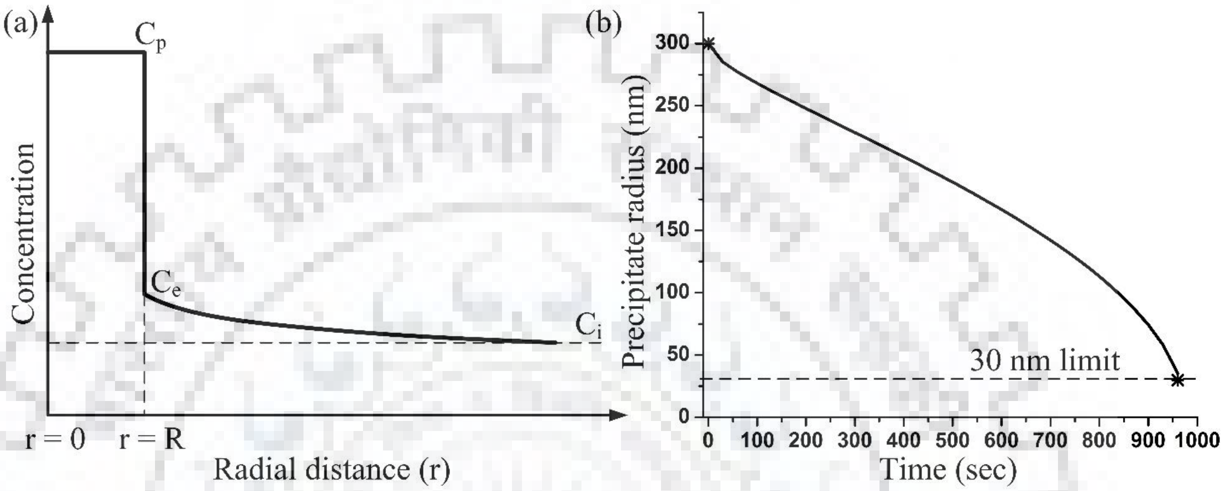

Figure 3.44 Schematic for modeling the dissolution of a spherical particle, and (b) calculated particle radius of Laves phase as a function of time.

Thermo-Calc is also used for calculating the driving force map to precipitate $M_{23}C_6$ and Laves phase at 620 ^oC with varying compositions of Cr & Mn and W & Mo, respectively. In any natural process, the free energy of a closed assembly in thermal contact with its surroundings decreases. The difference in initial and final free energies provides driving energy or thermodynamic potential for the change. This is defined as a driving force. Figure 4.45(a) represents the driving force map for $M_{23}C_6$ with varying compositions of Cr and Mn. The precipitation of $M_{23}C_6$ at 620 ^oC can be increased by designing the chemical composition of steel which should contain less than 8.7 % Cr and less than 0.12 weight % Mn.

The driving force for Laves phase with varying compositions of W and Mo is presented, in Fig. 4.45(b). The precipitation of laves phase at 620 ^oC was mainly governed by W percentage in P92 steel. To avoid precipitation of Laves phase at 620 ^oC, the chemical composition of P92 steel should not contain W more than 0.4 %. But W weight percentage in P92 steel is designed to increase solid solution strengthening and to avoid δ-ferrite formation.

The weight percentage of W is depending on other austenite and ferrite stabilizers in P92 steel to avoid δ-ferrite. The W and Mo have also increased the lower critical temperature (Ac_1) and reduce the martensitic start temperature (M_s).

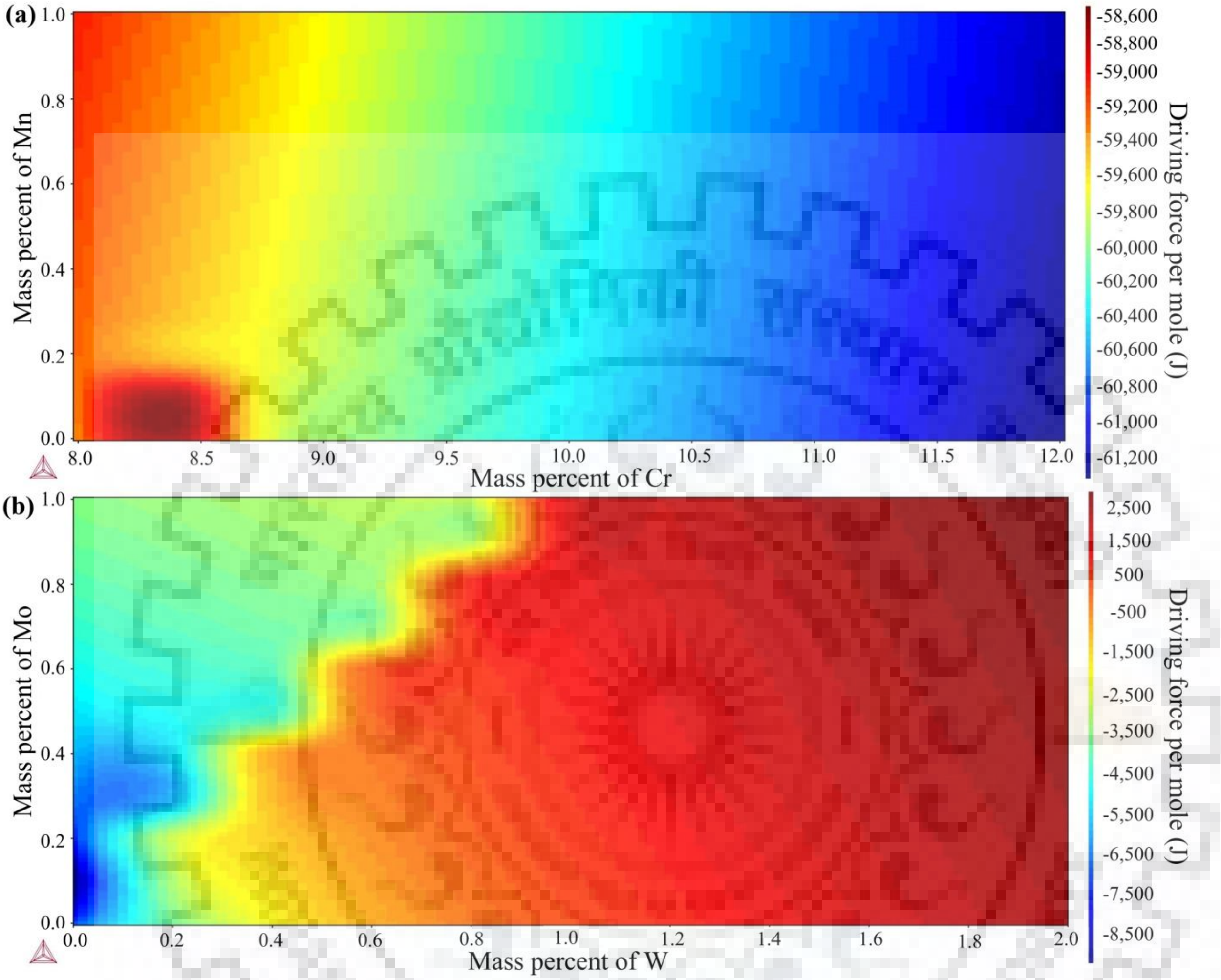

Figure 3.45 Driving force for precipitation simulated using Thermo-Calc at 620 °C for (a) $M_{23}C_6$ with varying mass percent of Cr & Mn and (b) Laves Phase with varying mass percent of W and Mo

The driving force map with varying temperature and mass percent of W for precipitating Laves phase is also predicted using Thermo-Calc, as shown in Fig. 4.46. It is clearly seen from the calculation that the driving force for precipitating Laves phase decreases with an increase in temperature. The precipitation of Laves phase beyond 500 °C was mainly governed by W percentage in P92 steel.

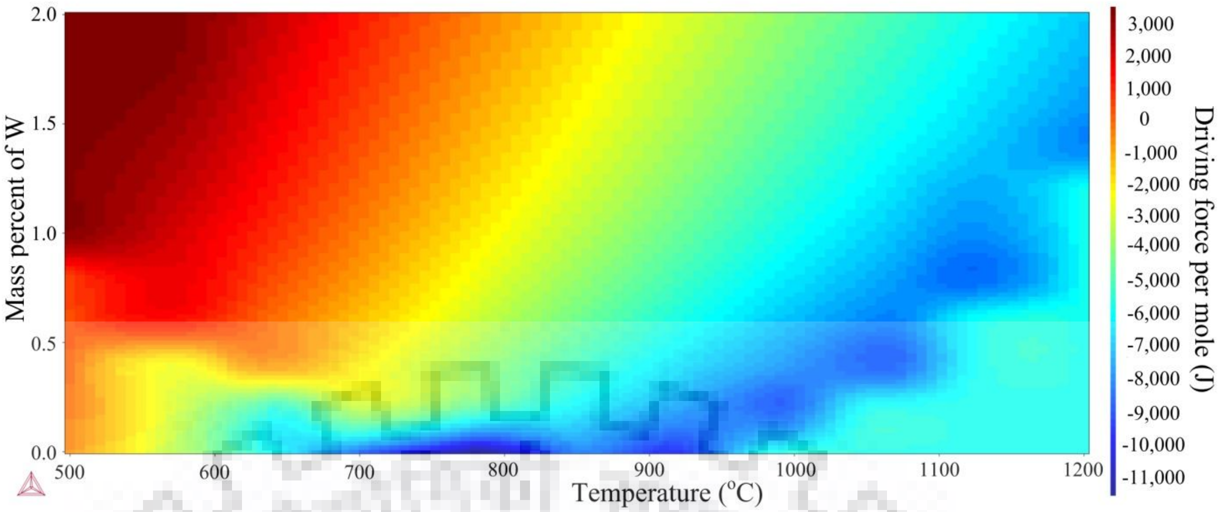

Figure 3.46 Driving force with respect to temperature for Laves phase precipitation simulated using Thermo-Calc

The driving force with varying mass percent of W was also calculated at 620 °C and at 700 °C using Thermo-Calc, as shown in Fig. 4.47(a). It is evident that driving force for Laves phase precipitation decreases at 700 °C as compared to 620 °C. Figure 4.47(b) shows that the driving force changes more rapidly with an increase in Mo as compared to W. A sudden drop in the driving force is also observed at 700 °C. Hence, service temperature and composition of alloy affect the driving force for precipitation of the Laves phase. In P92 steel, solid-solution strengthening is one of the strengthening mechanisms. Solid solution strengthening in P92 steel provided by W and Mo super-saturated solute in the matrix. But the nucleation and coarsening of Laves phase during aging resulted in a decrease of W and Mo elements in the matrix.

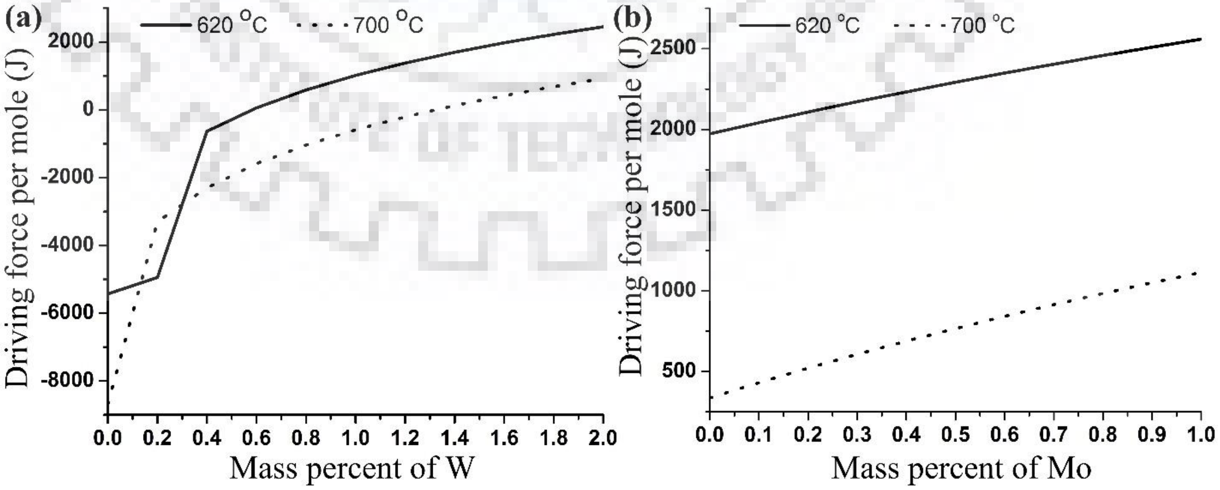

Figure 3.47 Driving force for Laves phase precipitation simulated using Thermo-Calc at 620 °C and 700 °C (a) for varying mass percent of W and (b) for varying mass percent of Mo

The decrease in creep strength may be due to decrease of solute atoms in the matrix. After re-austenitization, the dissolution of Laves phase resulted in disperse of W and Mo solute atoms in the matrix which may help to regain its creep strength. The loss in microhardness during aging is attributed to reduced solid-solution hardening due to precipitation of Laves phase. After re-austenitization, a small increase in microhardness may be attributed due to the dispersion of W and Mo solute in the matrix. Hence, we can say that re-austenitization and tempering helps in regaining the strength of P92 steel.

The implications of current results for CSEF steels can be apply in two ways. First, to increase precipitation strengthening effect, the steel composition should be designed in such a way to allow homogenous precipitation of the Laves phase. Second, the re-austenitization and tempering treatment must be designed in order to delay the coarsening of the Laves phase which helps in maintaining the solid solution strengthening effect during long term service.

3.2.5 *Effect of double austenitization on the microstructural evolution and mechanical properties*

For double austenitization treatment, the samples were subjected to different heating and cooling conditions as per heat treatment matrix given in Table 3.5. The effect of double austenitization was studied on microstructure evolution and mechanical properties of P92 steel.

3.2.5.1 Effect of conventional normalizing and tempering treatment on microstructure evolution

Typical optical micrograph of P92 steel after the conventional normalizing and tempering (CNT) treatment is shown in Fig. 3.48(a). The microstructure confirms the formation of tempered martensite with distinct PAGBs. The different martensite lath direction inside the lath packets is also shown in Fig. 3.48(a). The precipitates inside the lath region and along the boundaries are also observed in black dotted form. Typical SEM micrograph at low magnification (1000x) is shown in Fig. 3.48(b). The heterogeneous grain structure is clearly observed form the micrograph. The microstructure reveals the presence of both coarse and fine PAGs with triple points. The lath blocks decorated with precipitates are observed inside the PAGBs. The higher magnification micrograph (10000x) confirms the presence of coarse precipitates along the PAGBs and lath blocks while fine precipitates inside the intra-lath region. The micrograph also confirms the higher density of the precipitates along the PAGBs and lath blocks, as shown in Fig. 3.48(c).

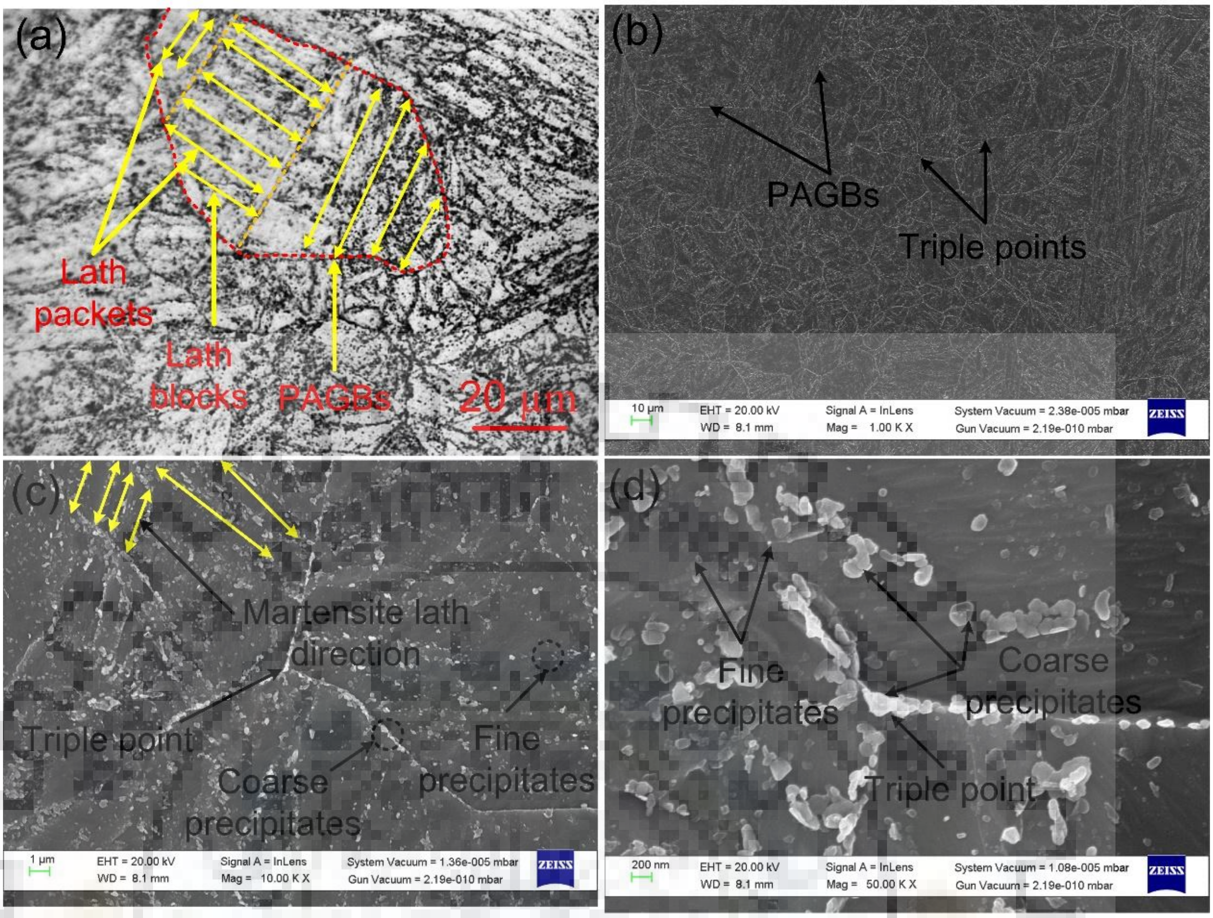

Figure 3.48 Typical micrograph of P92 steel after the conventional normalizing and tempering treatment (a) optical micrograph at 500x, (b) SEM micrograph at 1000x, (c) SEM micrograph at 10000x and (d) SEM micrograph at 50000x

The direction of laths is clearly observed in the micrograph. In order to measure the precipitates size and define the morphology of the precipitates, a micrograph is taken at 50000x, as shown in Fig. 3.48(d). The micrograph shows the globular and spherical shape particles along the PAGBs while fine spherical shape particles and some needle shape particle inside the intra-lath region. A great heterogeneity is observed in size of precipitates located at the PAGBs and inside the intra-lath region. The area fraction of the precipitates was measured 16.56 % using the Image J software.

For the particle size measurement, it is required to generate the map of the matrix, as shown in Fig. 3.49(a). The colors in the analysis figures have been inverted to match the original micrograph. The precipitates are shown in black dotted form along the PAGBs and inside the intra-lath region. The large number of particles in the range of 100 to 200 nm falls in higher frequency, as shown in Fig. 3.49(b). Very few particles of size 400 nm are also observed. The average particle was measured to be 102 nm.

The particle observed along the PAGBs are observed in the range of 100 to 300 nm. The particle inside the intra-lath region is measured in the range of 15 to 100 nm. The particles having a size below than 40 nm was reported as the V and Nb-rich MX type (C. G. Panait et al., 2010c).

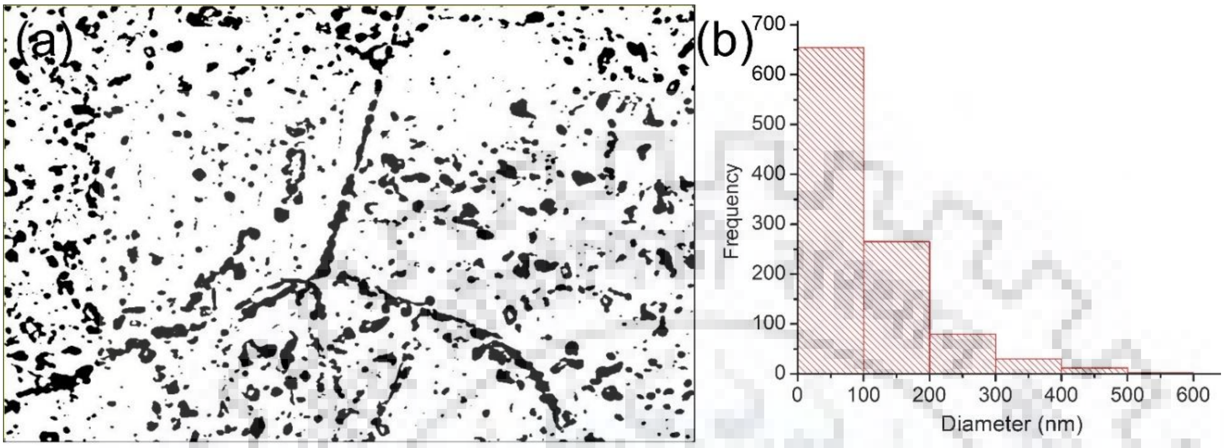

Figure 3.49 (a) Processed image and (b) variation in particle size

The optical micrographs after different DNT treatments of P92 steel are given in Fig. 3.50. In all three cases, complete martensitic microstructure was obtained. In low carbon steels (such as P92 steel), martensitic structure (lath type) is formed and contains several interfaces such as packet boundaries, block, lath, block boundaries and lath boundaries. The refinement of the grains is clearly observed form the optical micrograph. As move away from the DNT 1 to DNT 3 treatment, the number density of PAGBs are observed to be increased. The coarse grain boundaries are observed for the DNT 2 treatment. The size of prior austenite grain is depicted in Table 3.9.

Table 3.9 Grain size for different heat-treated conditions

S. No.	Condition(s)	Grain Size (μm)
1	CNT	32.76
2	DNT 1	26.8
3	DNT 2	27.1
4	DNT 3	18.7234

For the CNT treatment, the grain size was measured about 33 μm. The DNT treatments result in drastic reduction in the grain size and it was measured 27 μm and 28 μm for DNT 1 and DNT 2 treatment, respectively. The reduction in grain size is also confirmed form the optical micrograph, as shown in the Fig. 3.50. For the DNT 3, the grain size was measured to be 18 μm, which was much lower than the CNT and other DNT treatment.

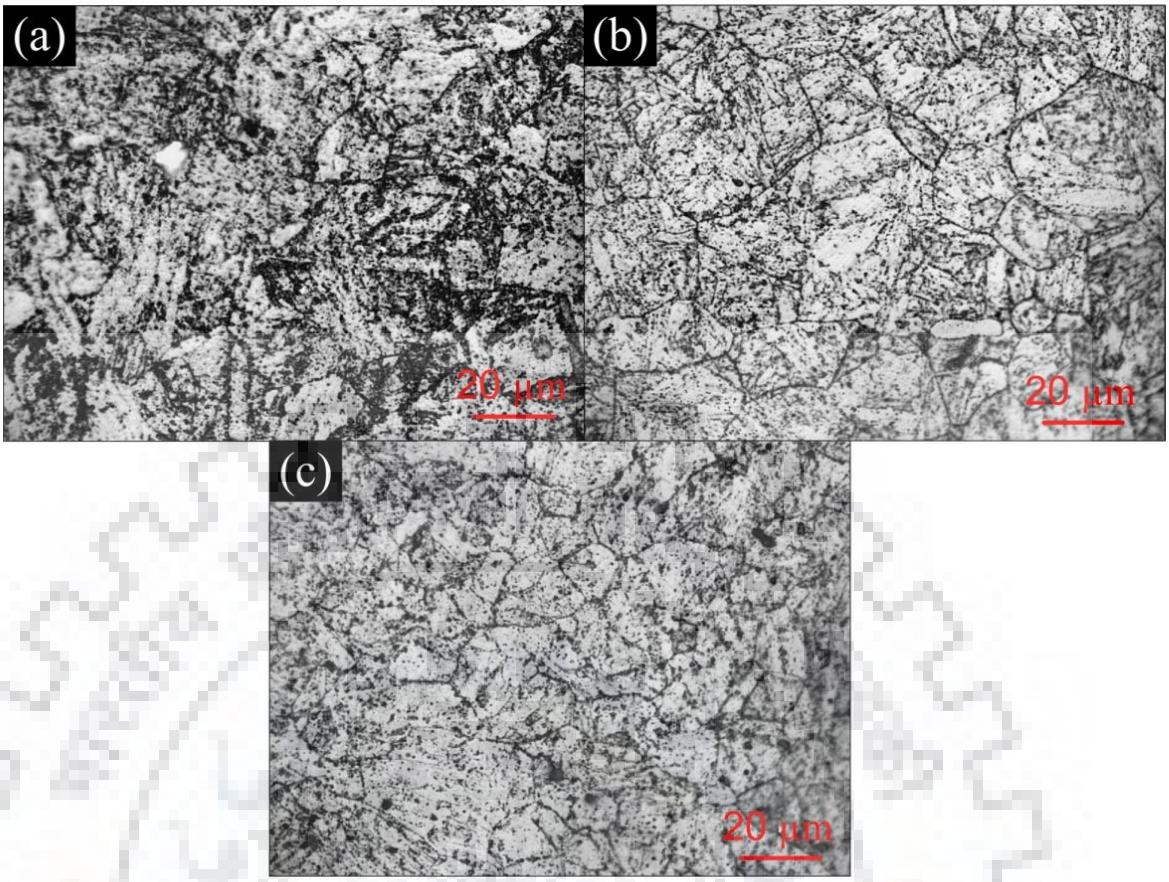

Figure 3.50 Optical micrograph of P92 steel in (a) DNT 1, (b) DNT 2 and (c) DNT 3 condition

The SEM micrograph for the different heat treatments is depicted in Fig. 3.51. The density of fine grains is observed to decrease with increase in normalizing temperature of DNT treatment. The microstructure shows the tempered lath martensite with fine and coarse prior austenite grains. The different martensite lath direction within lath packets are also shown in Fig. 3.51. For the CNT treatment, the number density of grain boundaries is observed to be higher as shown in Fig. 3.51(a). For DNT 2 and DNT 3 treatment the density of PAGBs is observed to be low as compared to CNT treatment as a result of coarsening of grains which are confirmed form the grain size.

For the DNT 3 treatment, a further increase in the number density of PAGBs is observed, as shown in Fig. 3.51(d). Both PAGBs and lath blocks are observed to decorate with the precipitates. With the increase in normalizing temperature, the precipitates of $M_{23}C_6$ type get dissolved but at the same time coarsening of the MX, precipitates are reported (Yoshino et al., 2005). The dissolution of precipitates during the initial normalizing results in the formation of coarse grain boundaries. The dissolution of the precipitates makes the boundaries free form their pinning effect and results in the formation of the bulge and coarse boundary.

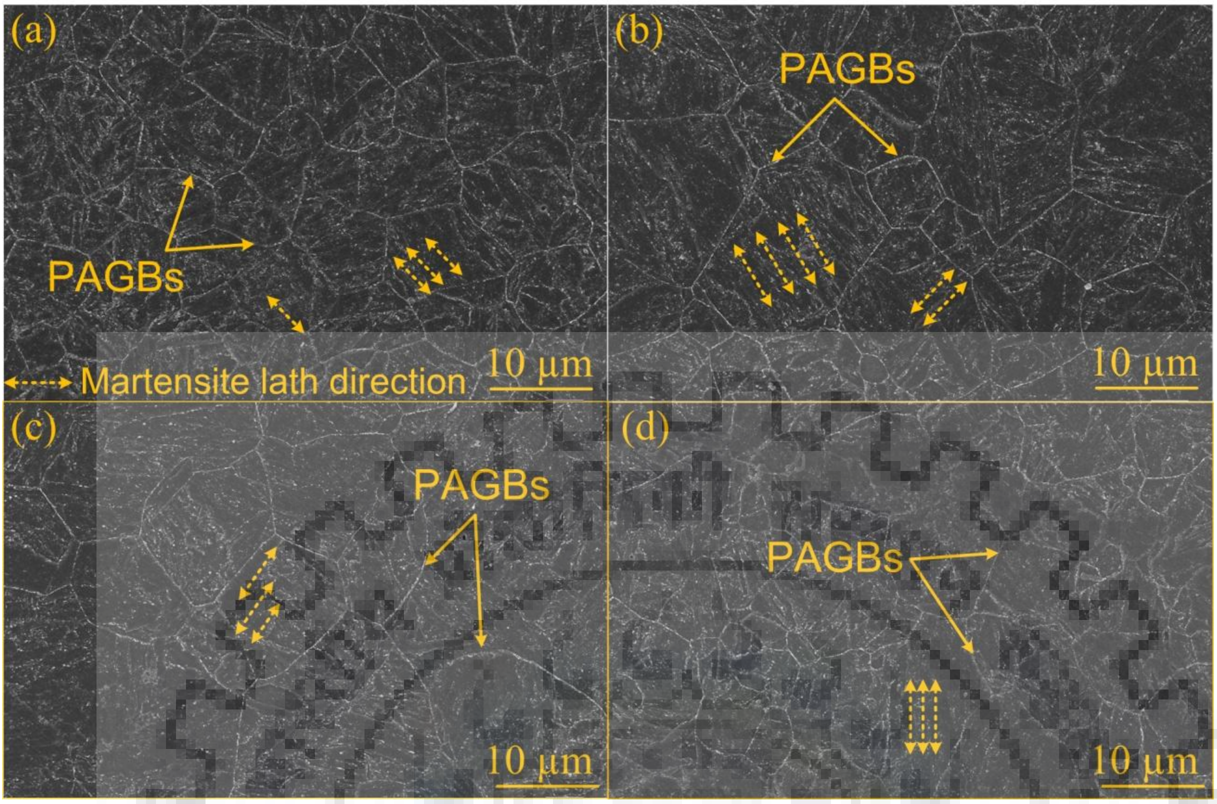

Figure 3.51 Secondary electron micrograph of P92 steel in (a) CNT, (b) DNT 1, (c) DNT 2 and (d) DNT 3 condition

However, increase in normalizing temperature also led to the precipitate coarsening. Yoshino et al. (Yoshino et al., 2005) had reported that the size of MX precipitates increased from 35 to 315 nm with increase in temperature from the 1050 ^{o}C to 1200 ^{o}C. The coarse precipitates provide the pinning effect to the grain boundaries as compared to the fine precipitates of the MX in order of 35-40 nm. That results in the formation of fine grains for DNT 3.

The higher magnification micrograph for the CNT and DNT treatment is shown in Fig. 3.52(a-b). The micrograph shows the decoration of the precipitates along the PAGBS and higher density of the precipitates along the triple points. For the CNT treatment, the precipitates are observed in spherical and needle shape. For the DNT 2 treatment, the coarse precipitate is observed along the boundaries and having globular, spherical and needle shape. The precipitates inside the lath region are observed in a spherical shape. The EDS spectra of the white particle show the higher weight percentage of Cr, Fe, and W in the particles that confirms the formation of Cr, Fe, and W-rich $M_{23}C_6$ type secondary particles. The EDS spectra also show the composition of the matrix. The similar results have also been reported by the Wang et al.(Y. Wang et al., 2016a).

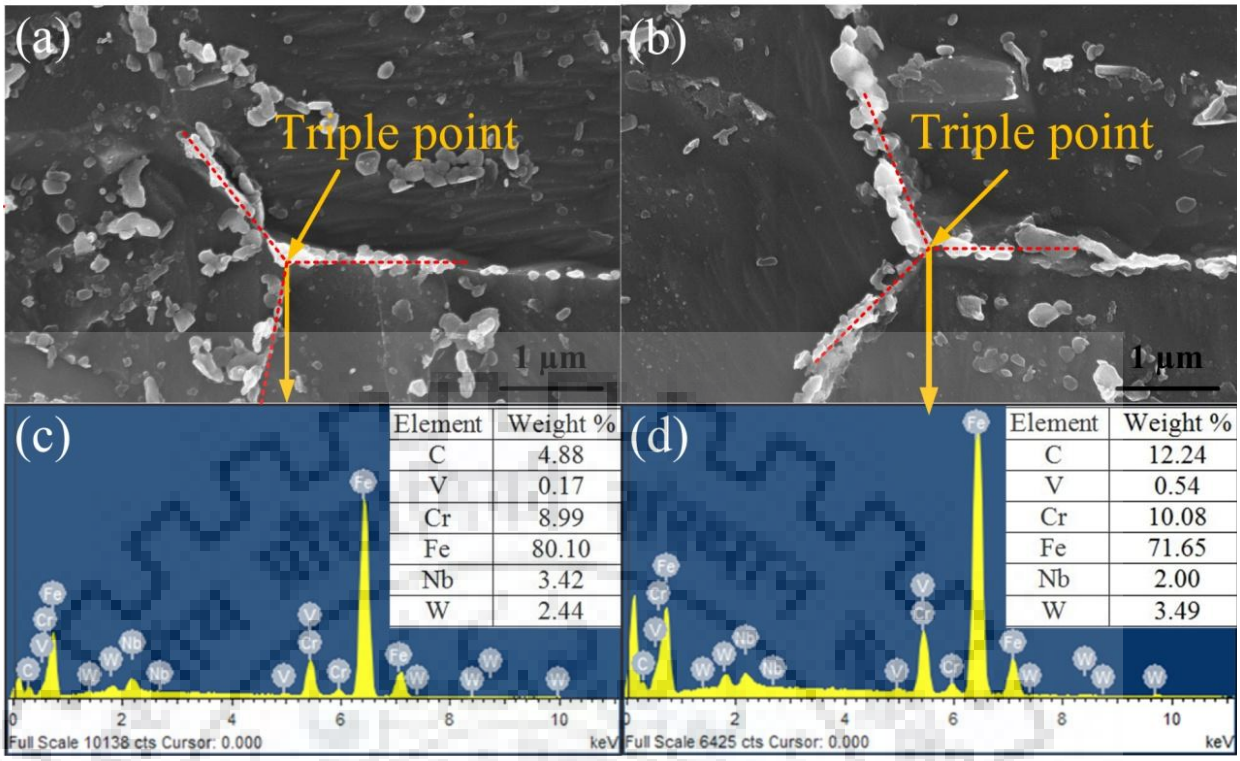

(c)

Element	Weight %
C	4.88
V	0.17
Cr	8.99
Fe	80.10
Nb	3.42
W	2.44

(d)

Element	Weight %
C	12.24
V	0.54
Cr	10.08
Fe	71.65
Nb	2.00
W	3.49

Figure 3.52 Higher magnification micrograph for the CNT and DNT 2 treatment (a) and (b), respectively; EDS of white particles present at the triple point for (c) CNT and (d) DNT 2 condition

Table 3.10 Fraction area of precipitates and precipitate diameter for different heat treatments

Heat treatment	Fraction area of precipitates (%)	Average precipitate diameter (nm)	The range of precipitate diameter (nm)
CNT	10.95	101	13-521
DNT1	11.13	98	13-508
DNT2	12.21	90	13-613
DNT3	13.45	97	13-650

The fraction area of the precipitates and an average diameter in different heat treatment conditions are measured using the Image J software and shown in Table 3.10. The fraction area of the precipitates mainly governs the precipitate hardening and it also affects the solid solution hardening indirectly. The precipitate nucleation mainly occurs at the grain and lath boundaries. It means the higher availability of the grain and lath boundaries leads to the higher area fraction of the precipitates. The minimum area fraction of the precipitates was measured 10.95 % for the CNT treatment and it was attributed to the lower availability of the grain boundaries (coarse grain size) per unit area for the CNT treatment. For DNT 1 and DNT 2 treatment, the area fraction of the precipitates was measured to similar.

The maximum area fraction of the precipitates was measured for the DNT 3 treatment and it was 13.45%. The higher area fraction of precipitates is attributed to the higher availability of grain boundaries per unit area as a result of fine grain size. The CNT and DNT heat treatment have found a minute effect on the average precipitate diameter. The average precipitate diameter was measured 101 nm for the CNT and 97 nm for the DNT 3 treatment. The precipitate of size less than 40 nm was also observed in the SEM micrograph and considered as the V and Nb-rich MX type precipitates (C. G. Panait et al., 2010a). The coarse precipitates size in the range of 80-130 nm are also observed inside the intra-lath region and confirmed as the Cr, Fe and W-rich $M_{23}C_6$ type. The coarse precipitate having size more than 150 nm are mainly evolved at the PAGBs and lath boundaries. The decoration of coarse carbide precipitates along the PAGBs is also shown in Fig. 3.52(a) and (b).

3.2.5.2 Effect of different heat treatments on mechanical properties

The room temperature tensile stress-strain curve for the different CNT and DNT treatments is shown in Fig. 3.53. The ultimate tensile strength (UTS) and % elongation for different heat treatment condition are shown in Fig. 3.54(a). For the CNT treatment, the UTS was measured to be 672 ± 5 MPa. The grain refinement at initial stage leads to increase in strength value and it was measured to be 689 ± 5 MPa for the DNT 1 treatment. With further increase in normalizing temperature from 950 ^{o}C to 1050 ^{o}C (DNT 1 to DNT 2), a drastic reduction in the UTS value was obtained. The UTS was measured about 660 ± 4.5 MPa for the DNT 2 treatment. The minimum UTS was measured to be 657 MPa for the DNT 3 treatment.

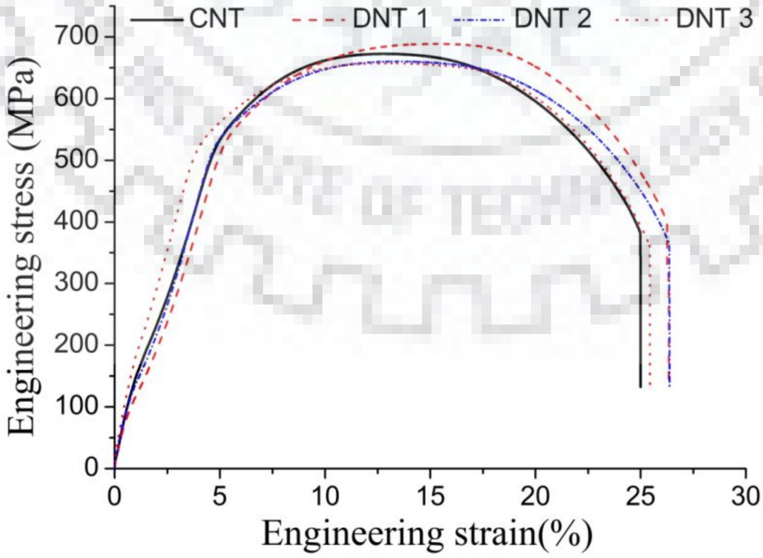

Figure 3.53 Engineering stress-strain curve for different heat treatments

The variation in greatly affected by the grain size that governs the area fraction of the precipitates. In CNT treatment, coarse grain leads to the lower availability of the grain boundaries per unit area and lower availability of the precipitates. That leads to the higher weight percentage of C and N in solid solution matrix and results in higher strength for the CNT specimen. After the DNT treatment, initially, fine grain formation leads to the higher strength of the material for DNT 1. Further fine grain formation in DNT 2 and DNT 3 specimen leads to poor strength as a result of higher fraction area of the precipitates and lower availability of C and N in the solid solution matrix. The variation in % elongation for varying heat treatment is also shown in Fig. 3.54(a). The minimum was measured for the CNT and DNT 3 treatment. However, it remains the stable for DNT 2 and DNT 3 treatment.

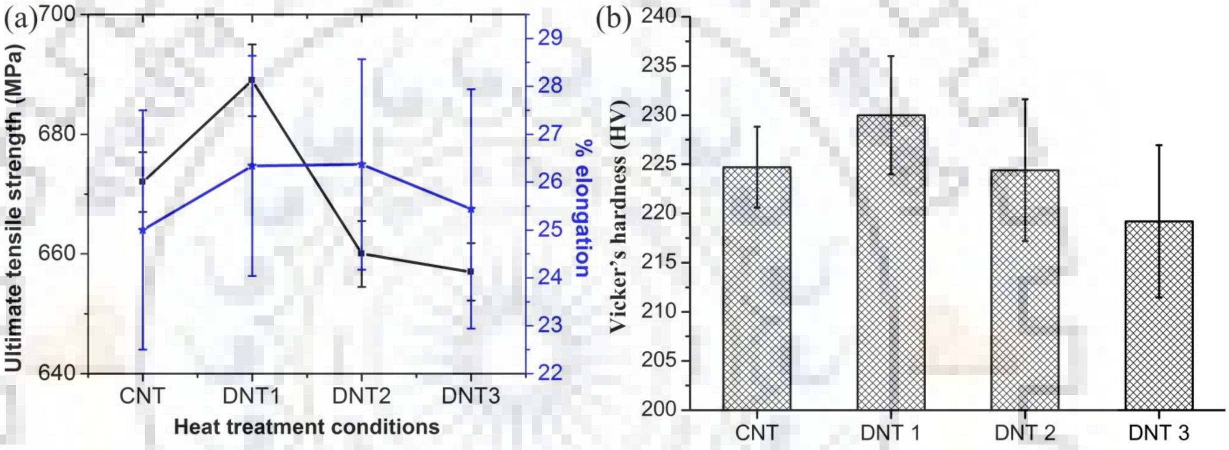

Figure 3.54 (a) Variation in ultimate tensile strength and % elongation and (b) variation in hardness for varying heat treatments

The hardness of the P92 steel for the different heat treatments follows the similar pattern as UTS. The hardness mainly governed by the solid solution strengthening and precipitate strengthening. The hardness of the P92 steel for the different heat treatments is depicted in Fig. 3.54(b). The as-received hardness of the material was measured as 283 HV. The hardness after the CNT treatment was measured 225 HC which clearly confirmed the softening of the material after the CNT treatment as compared to the as-received material. The softening occurs mainly in the form of tempering of the martensite and evolution of the precipitates. After the DNT 1 treatment, a noticeable increase in hardness was measured and it was 230 HV. For DNT 2 and DNT 3 treatment, hardness was measured to be 224 and 219 HV. The lowering of the hardness value for the DNT 2 and DNT 3 treatment is attributed to the poor solid solution strengthening.

However, fine grain formation in DNT 2 and DNT 3 treatment results in the higher availability of the precipitates that leads to the precipitation hardening but at the same time, lower availability of C and N in solid solution matrix leads to poor solid solution strengthening. The reduction in solid solution strengthening has observed to be a more dominating effect over the precipitation strengthening.

3.2.5.3 Effect of conventional normalizing and tempering on microstructure evolution

For different heat treatment conditions, top and detailed view of the fractured tensile tested specimens are depicted in Fig. 3.55. The top view of the fracture surface confirms the presence of both primary crack and secondary cracks. However, the DNT fractured specimen shows the lesser number of the major cracks (primary cracks). The detailed view of the fractured specimen shows the mixed mode of the fracture.

The fracture surface shows the presence of the ductile dimples of fine and deep size, cleavage factors, shear lip and tear ridges. For the CNT specimen, the cleavage facets are observed besides the area of the fine dimples. The number density of deep dimples is observed to be less. The formation of the deep dimples is mainly associated with the presence of coarse carbide precipitates. The coarse carbide precipitates density is observed to be much higher at the triple point. The coarse particles show the brittle nature and act as the crack nucleation sites during the loading and lead to the formation of deep dimples. For the DNT 1, the deep dimples size and density are observed to be higher as compared to the CNT treatment.

The number density of fine dimples is also observed to be higher as compared to CNT sample. the area of cleavage facets is also observed to be reduced. For DNT 2 treatment, the fracture morphology remains same except the higher availability of deep dimples at the fracture surface. The shear lip formation is also observed near the deep dimples that are associated with the plastic deformation. For DNT 3 treatment, the area of cleavage facets is observed to be higher. The number density of deep dimples is also observed to be less as compared to other DNT fractured sample. the tear ridges are found to be more pronounced in the DNT 3 sample.

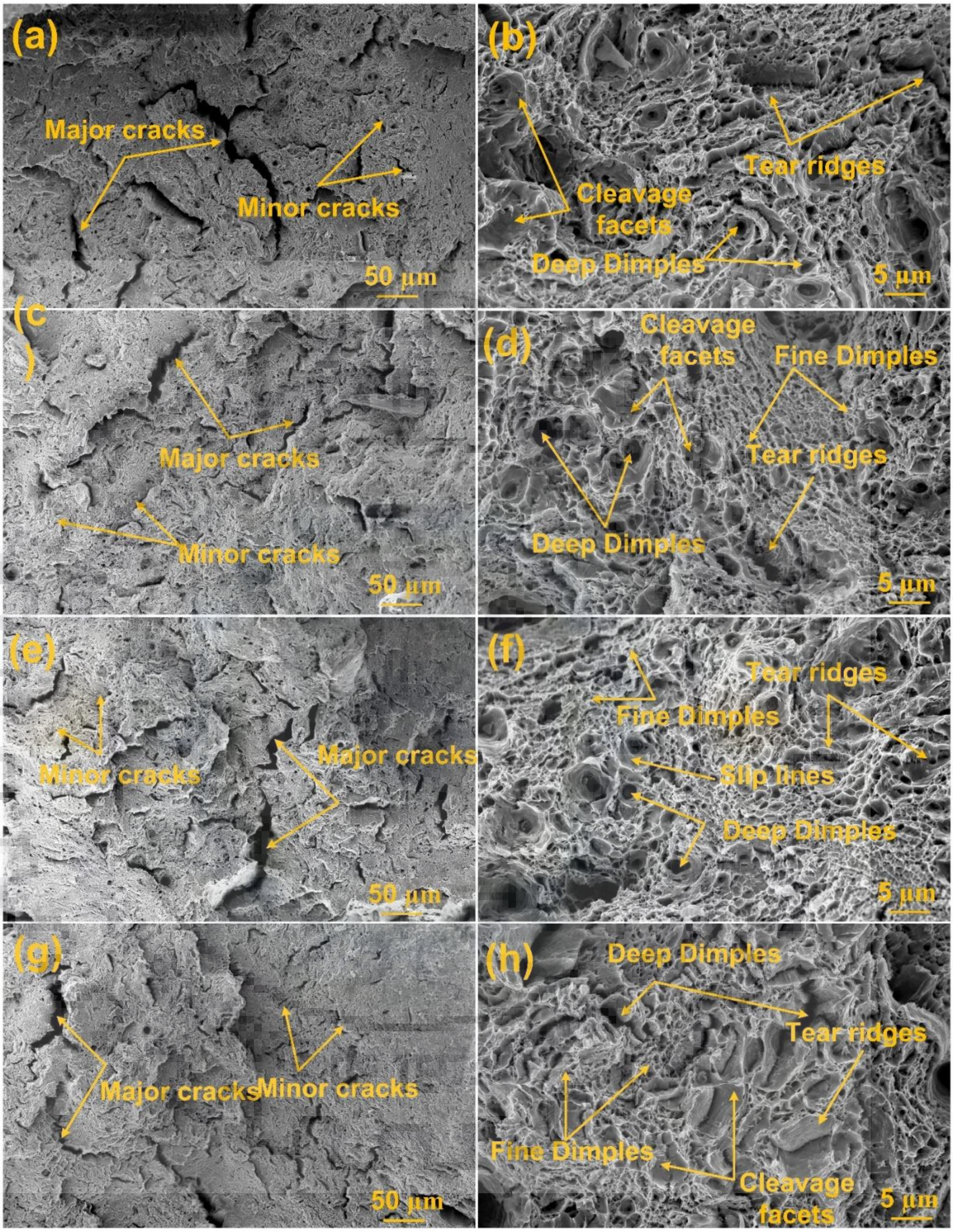

Figure 3.55 Top view and detailed view of the tensile tested fracture specimen, (a) and (b) CNT, (c) and (d) DNT 1, (e) and (f) DNT 2, (g) and (h) DNT 3

3.3 Conclusions

- Based on the observation of an optimum combination of strength, ductility and toughness, the maximum normalizing temperature upto 1050 ^{o}C has been suggested for cast and forged (C&F) P92 steel.
- During ageing, the evolution of Laves phase was found to have pronounced effect on mechanical properties of CSEF P92 steel. The strength and ductility and Charpy toughness were decreased after 720 h of ageing and this is attributed due to a loss in solid solution strengthening and formation of Laves phase.
- The rate of decrement was faster at the initial stage of ageing (720 h) and after that it become stable due to slow coarsening rate of Laves phase.
- After 4560 hrs of aging, the volume fraction of Laves phase was measured around 1.32 %. The dissolution of Laves phase confirmed using mormalizing and tempering process.
- A model is suggested to predict dissolution time for Laves phase. The driving force for Laves phase precipitation decreases with increasing temperature above 620 ^{o}C. The precipitation map for the Laves phase suggested that the steel composition can be designed to avoid precipitation of Laves phase.
- The optimum microstructure stability and mechanical properties were obtained for the treatment (1150^{o}C/1 h//water quench, 1040 ^{o}C/1 h/air cool' and'760 ^{o}C/2 h/air cool') as a result of the grain refinement.

CHAPTER 4. SIMILAR WELDED JOINTS OF P92 STEEL

In this chapter, effect of preheating temperatures (200-300 ^{o}C) on the weld geometry in autogenous-TIG welds have been studied and a model is suggested to predict a preheating temperature for a given plate using Rosenthal equation. The dissolution of δ-ferrite using post-weld normalizing and tempering in the autogenous TIG welds of P92 steel has been studied and their effect on mechanical properties have also been studied. The effect of different filler compositions on the microstructure evolution and mechanical properties of P92 steel weldments welded using SMAW have been studied.

4.1 Experimental procedure

4.1.1 *As-received material*

The plates of the as-received P92 steel were in normalized and tempered condition with dimension of 300 mm × 120 mm × 12 mm. The normalized temperature was 1000 ^{o}C for 1 hr and tempering temperature was 760^{o}C for 2 hrs. The chemical composition of as-received P92 steel, P92 filler, P911 filler, weld using P92 filler and weld using P911 filler is given in Table 4.1. The mechanical properties of P92 steel in normalized and tempered condition is given in Table 4.2.

Table 4.1Chemical compositions of base metal, fillers and weld joints

Element	Chemical composition (wt. %)												
	C	Cr	Mo	W	Nb	V	Mn	Al	Si	N	Ni	Cu	Fe
P92 steel	0.09	8.7	0.41	1.81	0.04	0.19	0.51	0.01	0.22	0.04	0.11	0.01	balance
P92 filler	0.11	8.9	1.01	1.82	0.06	0.22	0.61	-	0.19	0.06	0.66	0.04	balance
P911 filler	0.11	9.5	1.0	1.0	0.05	-	0.80	-	0.25	0.05	0.50	-	balance
P92 filler weld	0.10	8.8	0.97	1.75	0.06	0.21	0.71	-	0.20	0.05	0.51	0.04	balance
P911 filler weld	0.13	9.4	0.84	1.2	0.05	0.08	0.75	-	0.25	0.04	0.45	0.01	balance

Table 4.2 Mechanical properties of P92 steel in normalized and tempered condition

P92 steel	Yield strength (MPa)	Tensile strength (MPa)	Elongation (%)	Hardness (VHN)	Toughness (J)
	520±11	678 ± 10	23 ± 2	227 ± 4	198 ± 8

4.1.2 *Optimization of preheating temperature and prediction of preheating temperature for thin plates in autogenous TIG welds by using Rosenthal equation*

4.1.2.1 Optimization of preheating temperature

To make butt weld joints, the plates were machined with a dimension of 150 mm × 50 mm × 6 mm. The plates were surface ground and cleaned using acetone for making the proper intimate contact during welding. Autogenous tungsten inert gas welding (GTAW) process with fully automation welding setup was used to prepare the welded joints of P92 steel. The welding process parameters used for GTAW process are tabulated in Table 4.3. Before the welding, the plates are subjected to the preheating conditions. The four different welded joints were prepared with different preheating conditions of plates. The first welded joint was prepared without preheating of plates. The other joints were made with different preheating temperature of 200 ^{o}C, 250 ^{o}C and 300 ^{o}C for 40 min. The other welding process parameters were kept as constant (Table 4.3).

Table 4.3 Welding process parameters used for GTAW process

Parameters	GTAW process
Electrode	EWTh-2 (2% Thoriated)
Electrode tip angle	60^{o}
Polarity	DCEN, water cooled torch
Shielding gas	Commercially pure argon (99.9%)
Arc gap	3 mm
Weld groove	No
Welding current	185 Amp
Welding speed	80 mm/min

To see the effect of preheating temperature on the weld bead geometry, the welded plates were sectioned normal to the welding direction. To contrast grain boundaries, samples were polished followed by etching with vilella’s reagent for 85 sec. The stereo microscope was used to carry out macro examination of specimens. The weld geometry shape was characterized by using depth of penetration (DOP), bead width (BW) and ratio of DOP to BW.

4.1.2.2 Prediction of preheating temperature for thin plates using Rosenthal equation

An analytical method first developed by Rosenthal to predict temperature distribution as a function of time in arc welding. The Rosenthal's equation was derived by assuming no convention in the weld pool, no heat losses from welded plate surface, steady-state heat flow, constant thermal properties and point heat source. A schematic of two-dimensional (2-D) heat flow during welding of thin sheets is shown in Fig. 4.1 (Kou, 2002). The heat flow was assumed 2-D only due to thin sheets.

The following equation was derived by Rosenthal during the welding of thin plates of infinite width for 2-D heat flow (Kou, 2002; Rosenthal, 1946):

$$\frac{2\pi(T-T_o)kg}{Q} = exp\left(\frac{Vx}{2\alpha}\right)K_o\left(\frac{Vr}{2\alpha}\right) \tag{4.1}$$

Where, T is temperature at a location (x,y), Q is heat transferred from heat source to workpiece, k is thermal conductivity of workpiece, g is thickness of workpiece, T_o is initial temperature of workpiece before welding, α is thermal diffusivity of workpiece (k/ρC, where C and ρ are specific heat and density of workpiece), V is welding speed, r is radial distance from origin($\sqrt{x^2+y^2}$) and K_o is modified Bessel's function of zero-order and second kind.

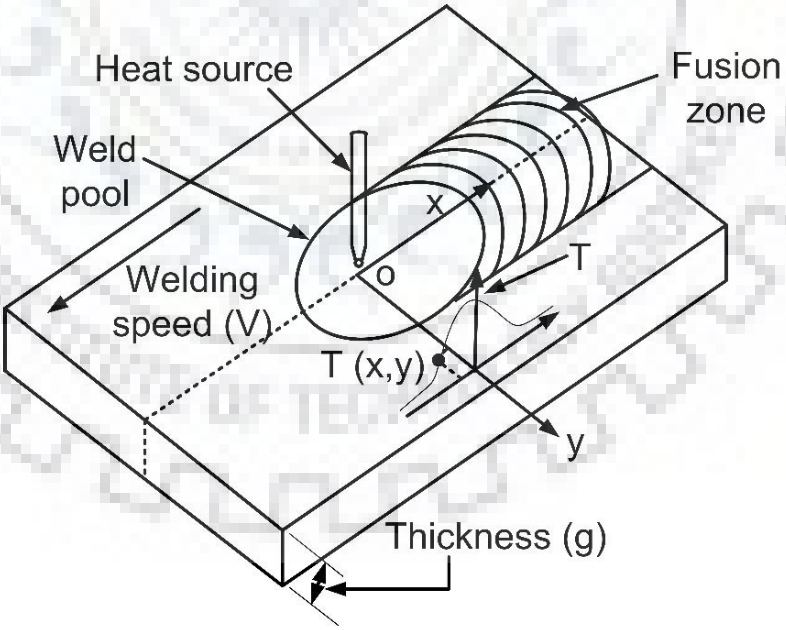

Figure 4.1 Two-dimensional heat flow during welding of thin sheets (Kou, 2002)

4.1.3 *Dissolution of δ-ferrite using post-weld heat treatments*

The plates machined with dimension of 150 mm × 50 mm × 6 mm to make butt weld joints. To make similar double-sided welded joints, an autogeous GTAW process was used.

The constant voltage welding machine with welding current of 180 Amp was used. Commercially pure argon (99.9%) gas was used for shielding purposes. A water-cooled welding torch having EWTh-2 (2% Thoriated) electrode was used with DCEN polarity. A fully automated setup of GTAW welding was used to maintain the welding speed of 80 mm/min for all welded joints. Before welding, the machined plates were subjected to a fixed preheating temperature of 300 ^{o}C for 30 min. Other welding parameters were kept constant for all welded plates except post-weld heat treatments. After welding, the welded joints were subjected to three different post-weld conditions.

The first double-sided welded joint was cooled in air up to room temperature. This welded plate named as-welded plate for this study. The second welded joint was subjected to conventional post-weld heat treatment (PWHT). The third welded plate was subjected to normalizing temperature of 1050 ^{o}C for 1 hr and then cooled in air up to room temperature. After normalizing the third plate was subjected to tempering of 760 ^{o}C for 2 hrs and then cooled in air. The third plate was named as post-weld normalized and tempered (PWNT).

In each condition, the hardness measurement was taken from the weld center to across the welded joint of second pass at 2 mm below the weld reinforcement outer surface. A matrix of measurement (3 rows * 60 columns) was taken in each specimen. Transverse sub-size tensile test specimens (flat) were prepared from different post-weld heat-treated plates as per ASTM A370-14. The gauge length, width and total length of tensile specimens were 25, 6 and 100 mm, respectively. The standard sub-size specimens for impact toughness were prepared as per ASTM A370 with dimensions 55 mm × 5 mm × 5 mm. The V-notch was prepared at the center of all weld samples.

4.1.4 *Effect of different filler on microstructure evolution and mechanical properties of SMAW welded joints of P92 steel*

The plates of size 150 mm x 60 mm x 12 mm were machined for the weld joints from the as-received P92 steel plate. A conventional V-groove design was prepared for making the weld joint with groove angle and root height of 37.5^{o} and 1.5 mm, respectively, as shown in Fig. 4.2(a). The welding process parameters for root and filler pass are given in Table 4.4. Shielded metal arc welding (SMAW) was carried out to prepare 92 steel weld joints using 4 mm diameter flux-coated E911 and P92 fillers. Before welding, the preheating of plates was performed in the range of 280-300 ^{o}C. The complete weld joints of P92 steel are shown in Fig. 4.2(c). After welding, the first plate was allowed to cool in the air up to room temperature.

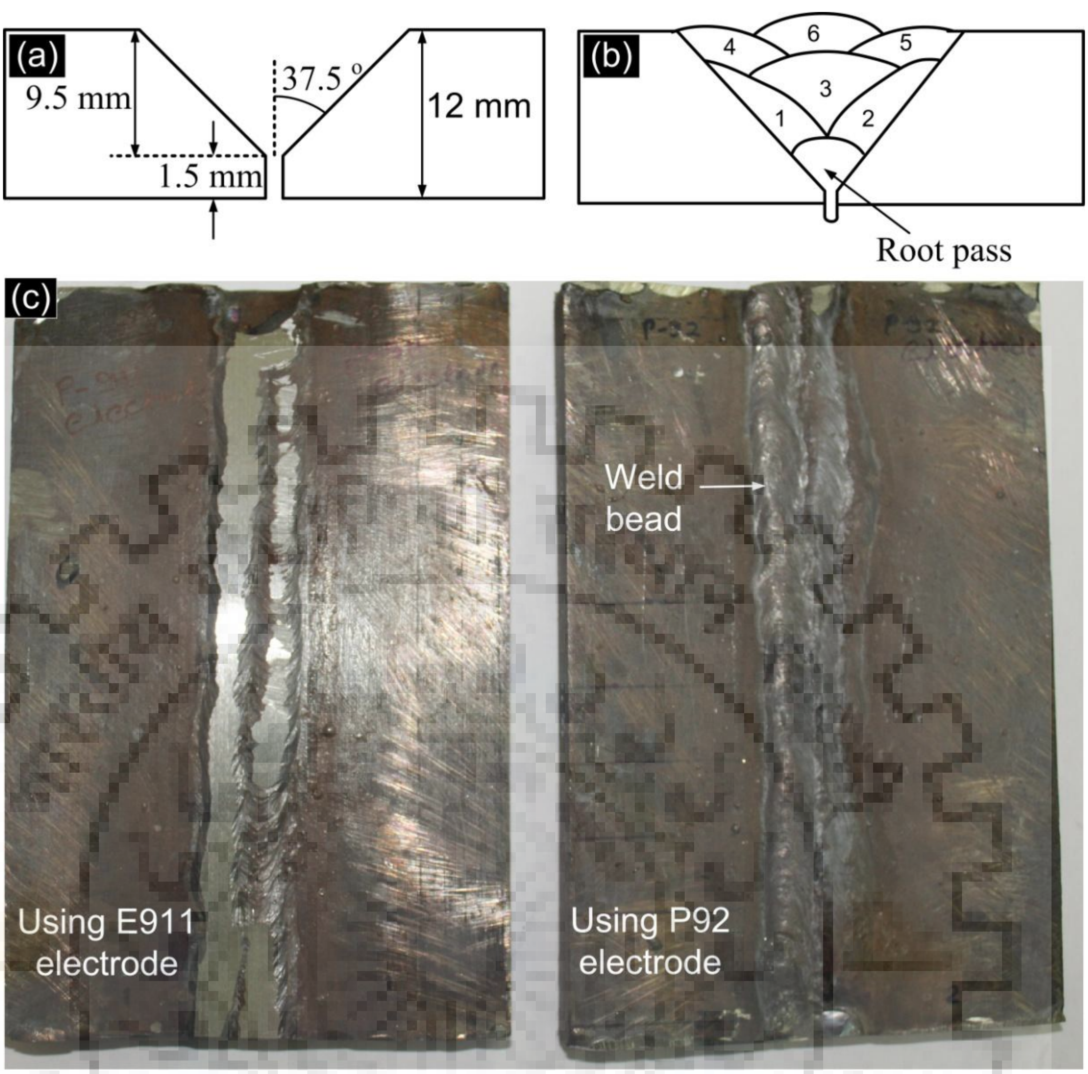

Figure 4.2 (a) Schematic of groove design, (b) schematic of the weld passes and (c) complete weld joints

Table 4.4 Welding process parameters for root pass and filler pass

Passes	Process	Current (I) amps	Voltage (V) volts	Travel speed (T) (mm/min)	Arc efficiency	Avg. heat input (kJ/mm)
Root pass	GTAW	115-120	14-15	130	0.75	0.079
Filler pass 1	SMAW	140	22-23	150	0.75	0.126
Filler pass 2	SMAW	140	21-23	145	0.75	0.127
Filler pass 3	SMAW	140	22-24	148	0.75	0.130
Filler pass 4	SMAW	140	21-24	140	0.75	0.135
Filler pass 5	SMAW	140	23-25	145	0.75	0.139
Filler pass 6	SMAW	140	22-26	140	0.75	0.144

To find the influence of PWHT on the weld and heat affected zone (HAZ) microstructure, after welding plates were subjected to post weld heating at 250 ^{o}C for 40 min and then air cooling up to 100 ^{o}C and followed by PWHT at 760 ^{o}C for 2 h and then air-cooled up to room temperature. The inter-pass temperature during welding was maintained in the range of 250-300 ^{o}C.

To determine the tensile properties of P92 steel weldment, longitudinal and transverse tensile specimens were prepared as per ASTM E8/E8M (ASTM_A370-17, 2017). The schematic shows the location and dimension of Charpy toughness and tensile test specimens removed from the welded plates, as shown in Fig. 4.3. The gauge length and width of transverse tensile specimens were taken as 25 and 6 mm, respectively. For longitudinal specimens, the width and gauge length were taken as 10 and 15 mm, respectively. To determine the Charpy toughness of P92 steel weld fusion zone and heat affected zone (HAZ), standard size V-notch samples were prepared with dimensions of 55mm × 10mm × 10mm according to ASTM A370. To study the fracture surface morphology of tensile tested specimens, Field-emission scanning electron microscope (FESEM) was utilized.

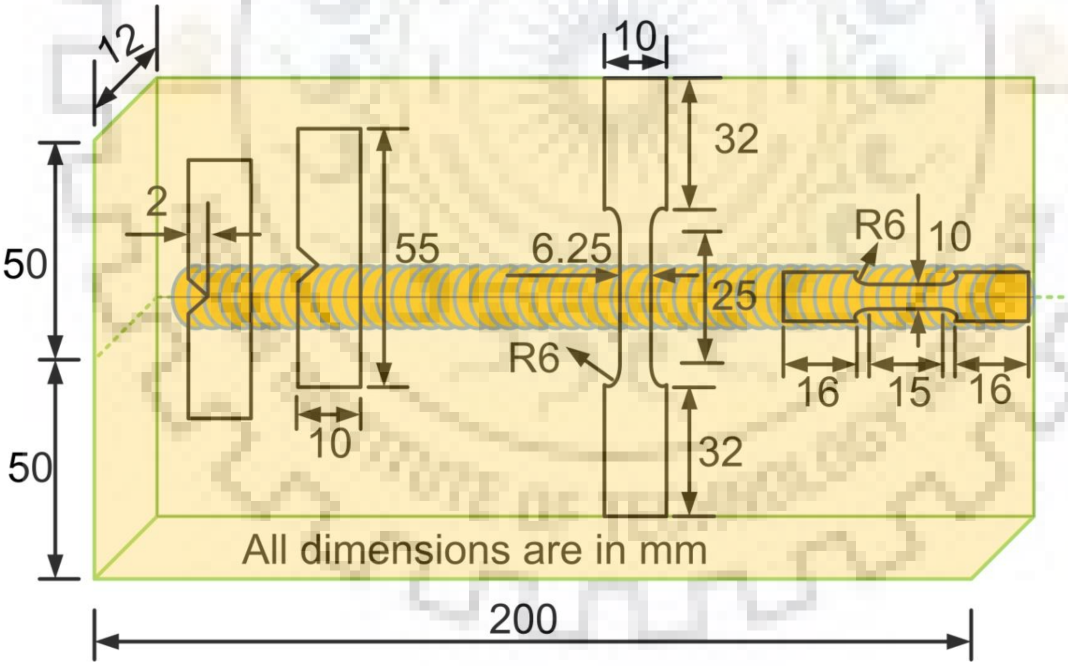

Figure 4.3 Schematic of the welded plate showing locations and dimensions of Charpy toughness and tensile test specimens

4.1.5 *Material characterization and testing*

For microstructural characterization, all welded joints were sectioned normal to the welding direction. The specimens were mount, ground and polished with SiC sand-papers (Grit

120, 300, 600 and 1200) and cloth polished. The welded specimens were etched using Vilella's reagent for 85 to 90 s. Optical microscope (OM) and FESEM was utilized for microstructural characterization. The operating parameters of FESEM were 8 mm working distance, 60 μm objective aperture and 20 kV accelerated voltage. To calculate percentage area fraction of δ-ferrite in the weld fusion zone, Image-J software was used. The average of ten micrographs was reported to calculate average volume fraction of δ-ferrite.

X-ray diffraction (XRD) was used to detect the phases present after different post-weld heat treatments. Profex software was used for Rietveld refinement of measured data to confirm the presence of δ-ferrite. All XRD measurements were performed within the scan range of 20-120^{o} and scan rate of 2^{o} per minute. The microhardness measurement of all-welded specimens was carried with Vickers hardness tester at the load of 0.5 kgf and dwell time of 10 s. The room temperature tensile test was performed on vertical tensile testing machine (Instron-5982) with crosshead speed of 1mm/min. The room temperature Charpy toughness test was performed for all specimens. The average of three tested specimens was reported in each case.

4.2 Results and discussion

4.2.1 *As-received material*

The secondary electron micrograph (SEM) of as-received material is shown in Fig. 4.4(a). The microstructure of P92 steel consists of prior austenite grain boundaries (PAGBs), PAGs, martensitic laths, packet boundaries, packets, block boundaries, blocks, precipitates, and sub-grains. A schematic of a prior austenite grain showing laths, packets, blocks, block boundaries, and lath boundaries, is shown in Fig. 4.4(b) The equiaxed tempered martensite microstructure having precipitates along PAGBs and inside the intra-lath regions was also confirmed by the in-lens micrograph, as shown in Fig. 4.4(c).

No δ-ferrite patches were observed in the as-received P92 steel. Energy dispersive X-ray spectra (EDS) of white particle present at triple point (Point 1) and present at PAGB (Point 2) were shown in Fig. 4.4(d) and 4.4(e), respectively. EDS spectra of particles present at Point 1 and Point 2 indicate that the precipitates present at the PAGBs are enriched in Cr, W, V, and Nb. EDS spectra of Point 3 (a point present in the matrix region) indicates the nominal composition of P92 steel, as shown in Fig. 4.4(f). The precipitates decorated along the lath boundaries and PAGBs were identified as coarse $M_{23}C_6$ (M: Cr, Mo, and Fe) (C. Pandey et al., 2018). The precipitates inside the matrix were identified as fine MX (M: Nb, V, Ti, and X: C, N).

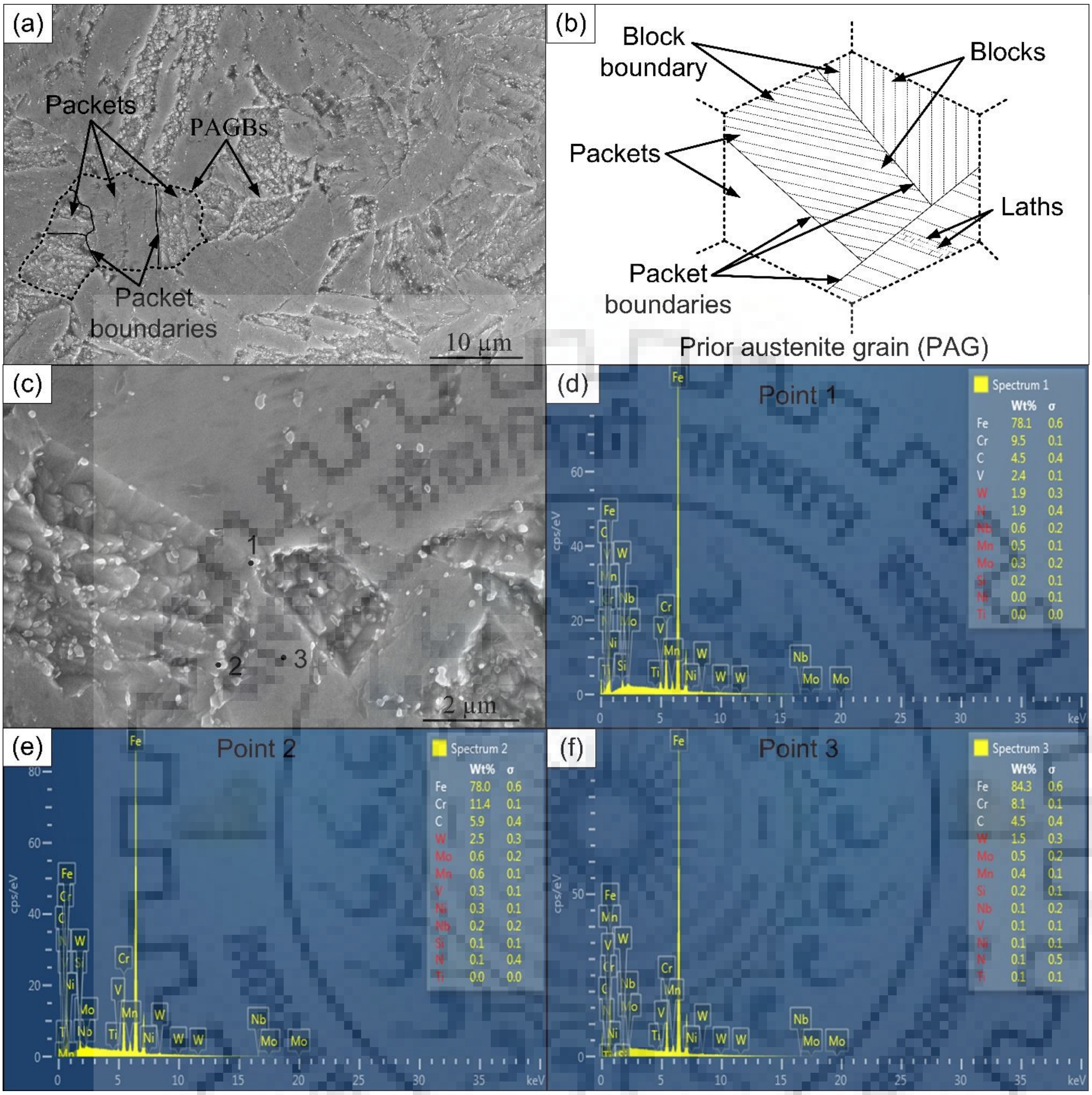

Figure 4.4 (a) Secondary electron micrograph (SEM) of as-received P92 steel, (b) schematic of a prior austenite grain, (c) in-lens micrograph of as received P92 steel, (d) energy-dispersive X-ray spectra (EDS) of a white particle present at triple point, (e) EDS of a white particle present at PAGB and (f) EDS of a point present in the matrix

4.2.2 *Optimization of preheating temperature and prediction of preheating temperature for thin plates in autogenous TIG welds by using Rosenthal equation*

4.2.2.1 Effect of preheating temperature on weld bead geometry

The top and backside of four different weld joints prepared with different preheating temperature are shown in Fig. 4.5. The backside of weld joint confirmed that the full penetration was achieved for last weld joint, which was welded with 300 ^{o}C preheating temperature (Fig. 4.5(b)). The surface appearance of weld bead was observed to be good for without preheating weld joint, but DOP was quite low.

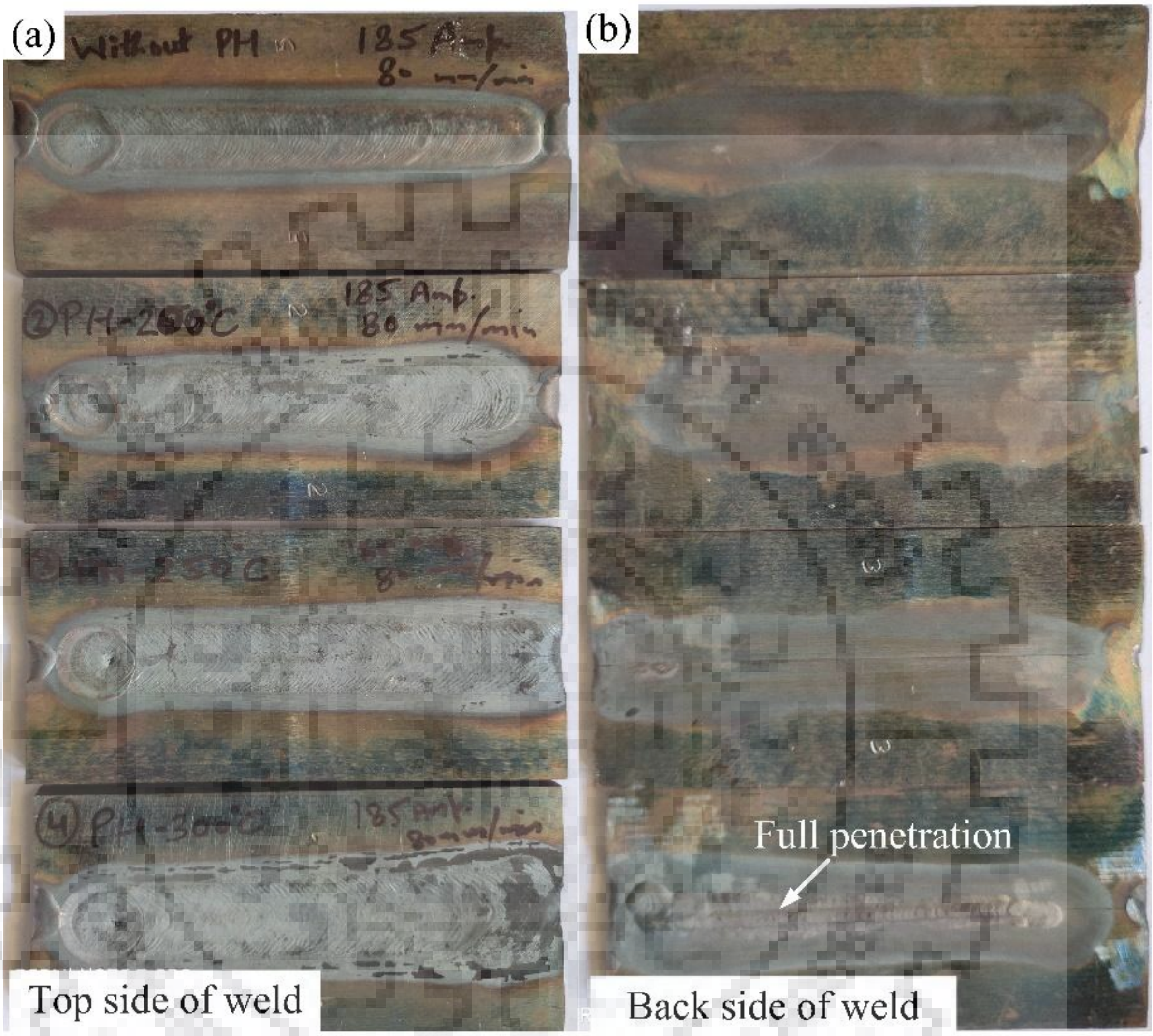

Figure 4.5 (a) Top and (b) backside of weld joint welded at different preheat temperatures

The macrographs of weld cross-section made by GTAW process under different preheat conditions are represented in Fig. 4.6(a-d). The DOP, BW and DOP to BW ratio of the weld cross-section under different preheating condition, were measured. Proper fusion without any defects was observed in all four welds, but the DOP was observed to be increased as preheating temperature increases. The DOP was measured about 3.4 mm for welded joint using without preheating of plates, as shown in Fig. 4.6(a). An abrupt change in DOP from 3.4 mm to 4.3 mm at a preheat temperature of 200 ^{o}C was observed, as shown in Fig. 4.6(b). Further, it was observed that the increase in preheating temperature also increased the width of weld bead. The DOP was measured around 5 mm for preheat temperature of 250 ^{o}C, as shown in Fig. 4.6(c).

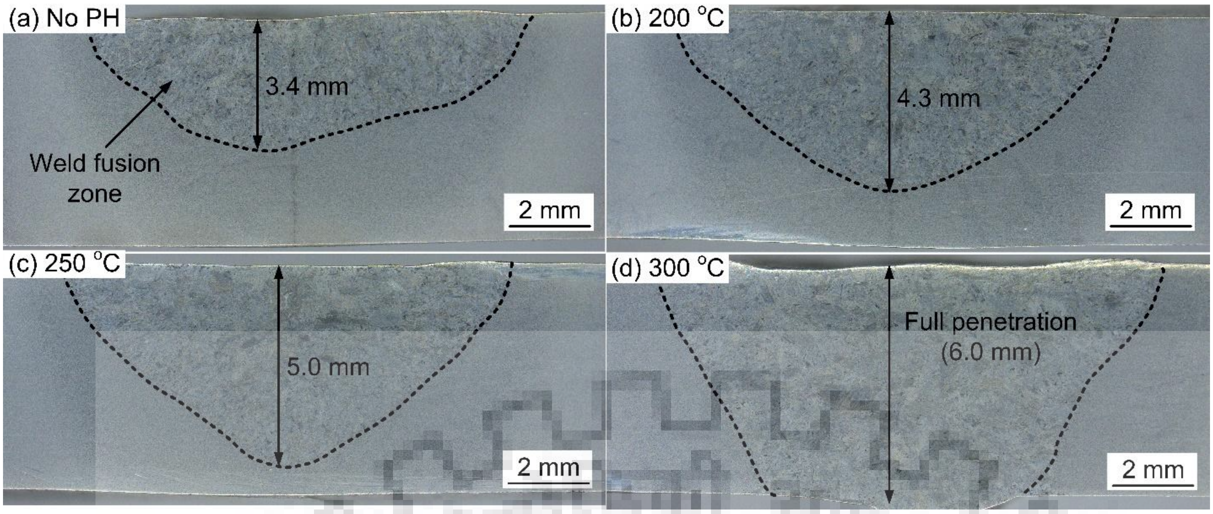

Figure 4.6 Cross-sectional macrographs of welded joints with preheating temperature of (a) No PH, (b) 200 °C, (c) 250 °C and (d) 300 °C

The full penetration (DOP - 6 mm) was achieved for welded joint made using preheat temperature of 300 °C, as confirmed by the cross-sectional macrograph, as shown in Fig. 4.6(d). A graph was plotted to see the effect of preheating temperature on the DOP and on the ratio of DOP to BW, as shown in Fig. 4.7. Both DOP and ratio of DOP to BW was found to be increased with preheating temperature.

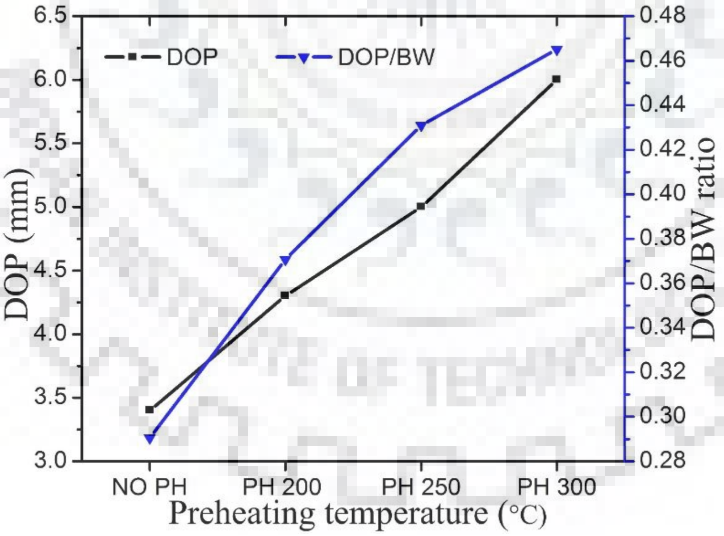

Figure 4.7 Effect of preheating temperature on DOP and DOP/BW ratio

Further, it was observed that the increase in preheating temperature also increased the area of the weld bead which might affect the retention of δ-ferrite in the microstructure of welded joint. The change in DOP was observed higher with increases in preheat temperature as compared to change in BW. The minimum and maximum ratio of DOP to BW were measured 0.29 and 0.47 for without preheated and with preheat temperature of 300 ^{o}C, respectively.

4.2.2.2 Prediction of preheating temperature for thin plates by using Rosenthal equation

The modified Bessel function of zero-order and second kind is given in Fig. 4.8 (Kou, 2002). The function was fitted in a small range for the accuracy of the system. The fitted equation of modified Bessel ($K_o(z)$) is given by:

$$K_o(z) = 1.5253(z)^6 - 10.132(z)^5 + 26.976(z)^4 - 36.988(z)^3 + 28.228(z)^2 - 12.63(z) + 3.385 \qquad (4.2)$$

Where, $z = \frac{Vr}{2\alpha}$, V is welding speed, α is thermal diffusivity of workpiece and r is radial distance from the origin.

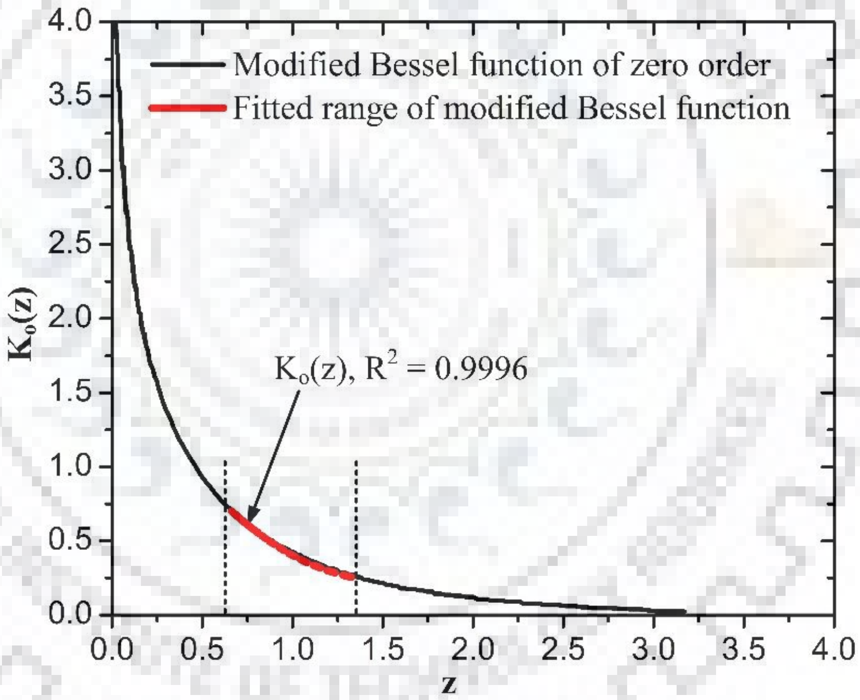

Figure 4.8 Plot of modified Bessel function of zero-order

To predict a preheat temperature for a given thin plate, the eq (4.1) is solved by putting $T = T_m$ (melting point) that means all temperature locations which lies on the periphery of the weld pool. To solve for a single value of x and y, the unknown coefficient y was taken as zero (refer to the coordinates in Fig. 4.1), which lead to a single point on the periphery of the weld pool, where $T = T_m$. The following equation was modified from eq (4.1) by putting $T = T_m$, $y = 0$ and $r = \sqrt{x^2 + y^2} = x$.

$$\frac{2\pi(T_m-T_o)kg}{Q} = \exp\left(\frac{Vx}{2\alpha}\right)K_o\left(\frac{Vx}{2\alpha}\right) \qquad (4.3)$$

The melting point of P92 steel was considered as 1505 ^{o}C, which is calculated by using Thermo-Calc. The other material properties such as thermal conductivity and thermal diffusivity were taken from previous works (Richardot et al., 2000; Yaghi et al., 2012). Now, putting materials properties (T_m = 1505 ^{o}C, k = 0.028 ^{o}C w/mm.k, α= 8.59 mm^2/sec) and welding process parameters (V = 1.333 mm/sec, Q = 3552 J) in the eq (4.3), which lead to the following equation:

$$T_o = 1505 - \frac{20189.9}{g}\exp(0.078x)\,K_o(0.078x) \qquad (4.4)$$

To develop a relationship between the thickness of plate (g) and x, the values of DOP considered as thickness of plate for different values of preheating temperatures. The unknown values of x were obtained from eq (4.4) for the different values g, T_o and K_o(z) (from eq (4.2)), as given in Table 4.5.

Table 4.5 Values of x calculated for different g and T_o

T_o (^{o}C)	g (mm)	x (mm)
25	3.4	10.378
200	4.3	9.845
250	5	9.286
300	6	8.580

Now, the values of x plotted corresponds to the values of g and a curve was obtained by extrapolating, which lead to the following equation with $R^2 = 1$:

$$x = 0.0705(g)^3 - 1.0249(g)^2 + 4.1483(g) + 5.3491 \qquad (4.5)$$

The following equation was obtained from eq (4.4) by putting the value of x in terms of g from eq (4.5):

$$T_o = 1505 - \{\frac{20189.9}{g}\exp\,[0.078\{0.0705(g)^3 - 1.0249(g)^2 + 4.1483(g) + 5.3491\}] \times$$

$$Ko[0.078\{0.0705(g)3-1.0249(g)2+4.1483(g)+5.3491\}]\} \qquad (4.6)$$

The extrapolated fitting equation of T_o in terms of g from experimental results with R^2 = 1is given by the following equation:

$$T_o = 24.723(g)^3 - 390.87(g)^2 + 2099.7(g) + 3567.4 \quad (4.7)$$

A curve between preheating temperature and thickness of thin plates has been plotted by using eq (4.6) and eq (4.2) simultaneously, as shown in Fig. 4.9. The experiment values and extrapolated curve from experiment results (using eq (4.7)) also clubbed in this graph, as shown in Fig. 4.9. The predicted preheat temperature curve has some following constraints:

- Valid only for thin plates due to limitation of Rosenthal 2-D equation.
- Valid only for P92 steel, if you want to use for different materials then use their material properties.
- The predicted preheating temperature is valid for fixed heat input.

The predicted and experimental results of preheating temperature were matched completely in the thickness range of 3.4 to 7.0 mm. After a thickness of 7.0 mm, the predicted and experimental curves started to separate that means we cannot use this equation further. So, this proposed method is valid only for thin plates up to 7.0 mm for the good accuracy of predicted preheating temperature.

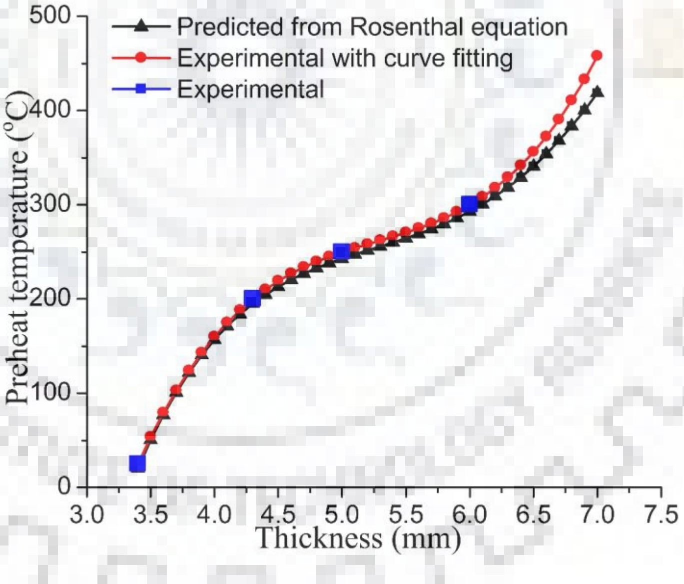

Figure 4.9 Predicted preheating temperature curve with a thickness of thin plates

4.2.2.3 Effect of cooling rates on retained δ-ferrite

To predict δ-ferrite in the weld fusion zone, several empirical formulas available in literature such as Schaeffler, Schneider, Kaltenhauser and Newhouse were used which works on the chemical composition of the weld metal.

The weighted effects of austenite and ferrite forming elements were calculated by calculating chromium equivalent (Cr_{eq}) and nickel equivalent (Ni_{eq}). The ferrite factor (FF = Cr_{eq} - Ni_{eq}) was also calculated for different empirical formulas, which was used as a parameter that can predict the presence of δ-ferrite in the weld fusion zone. The calculated values of Cr_{eq}, Ni_{eq} and FF were given in Table 4.6. The FF and their resulting statements showed that based on chemical composition the probability of having δ-ferrite in the weld fusion zone is low.

Table 4.6 Calculated values of Cr_{eq}, Ni_{eq} and FF for various empirical formulas

Alloy	Schaeffler		Schneider		Kaltenhauser		Newhouse	
	Cr_{eq}	Ni_{eq}	Cr_{eq}	Ni_{eq}	Cr_{eq}	Ni_{eq}	Cr_{eq}	Ni_{eq}
P92 steel	9.46	3.06	12.13	4.06	11.85	6.66	16.8	6.3
Ferrite factor	6.4		8.07		5.19		10.5	
δ-ferrite prediction	No		May be		No		Yes	

Though based on composition, the probability of having δ-ferrite in the weld fusion zone is low, the δ-ferrite patches were observed throughout the weld fusion zone in all welded joints. So, we can say that other factors also affect the evolution and retention of δ-ferrite in the weld fusion zone. The liquidus temperature of P92 steel is calculated using Thermo-Calc about 1505 °C. Then the liquid starts to solidify as δ-ferrite at 1505 ^{o}C. δ-ferrite to austenite transformation starts at 1436 ^{o}C and completes at 1193 ^{o}C. So, below this temperature, if any delta-ferrite does not transform to austenite will be present in the weld. Similar results of phase transformation have been reported in previously published work (Sam et al., 2014).

During slow cooling, δ-ferrite transformed completely into austenite as compared to fast cooling. So, we can say that the δ-ferrite retention in weld fusion zone depends upon chemical composition, heat input and cooling rate. The main reason for δ-ferrite in the weld fusion zone is that during cooling δ-ferrite was not transformed completely to austenite. Hence, cooling rate plays critical role in retention of δ-ferrite.

The optical micrographs of weld fusion zone with different preheating temperature are represented as shown in Fig. 4.10(a-d). The cooling rate decreases as preheating temperate increases (Sam et al., 2014). So, we can see the effect of cooling rate on the volume fraction of δ-ferrite in the weld fusion zone by changing the preheating conditions of welded joint. Figure 4.10(a) represents the microstructure of weld fusion zone which was welded with preheating the welded plates, having δ-ferrite and martensitic structure.

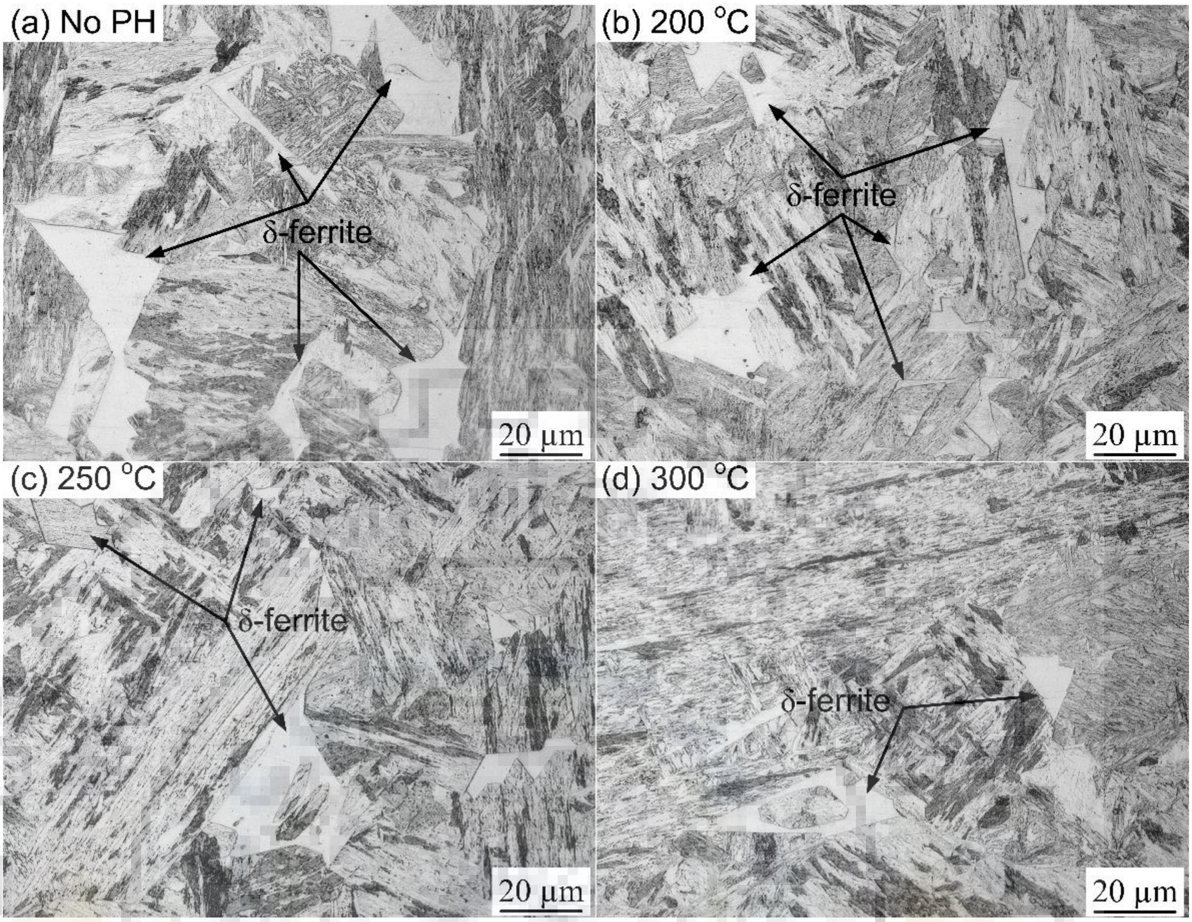

Figure 4.10 Optical micrographs of the weld fusion zone with different preheating temperatures

The retention of δ-ferrite was observed in welded joint which prepared by without preheating due to higher cooling rate. The lesser retention of δ-ferrite was observed in the weld fusion zone of welded plates which was welded with preheat temperature of 200 ^{o}C, as shown in Fig. 4.10(b). A reduction in the average size of δ-ferrite was also observed. The δ-ferrite patches were decreased from the above two conditions due to slow cooling rate with preheat temperature of 250 ^{o}C, as shown in Fig. 4.10(c). Figure 4.10(d) shows the microstructure of weld fusion zone welded with preheat temperature of 300 °C. Least retention of δ-ferrite was observed with 300 °C preheat temperature due to slowest cooling rate as compared to other welded joints.

The optical micrographs were processed using Image J software to see the better features of δ-ferrite and used in the volume fraction calculation of δ-ferrite. The volume fraction of δ-ferrite was measured manually by measuring the area of δ-ferrite patches present in one micrograph from Image J processed micrographs. To calculate total volume fraction of δ-ferrite, the average of ten micrographs were taken.

The variation of volume fraction of δ-ferrite with different preheating conditions is represented in Fig. 4.11. As the preheating temperature is increased from 200 ^{o}C to 300 ^{o}C, the volume fraction of δ-ferrite was decreased from 9±4 to 5±2. The minimum and maximum volume fraction of δ-ferrite were measured for 300 ^{o}C preheat temperature and without preheat, respectively. Hence, a decrease in cooling rate resulted in reduced volume fraction of δ-ferrite in the weld fusion zone. So, we can say that even highest preheat temperature (slowest cooling rate) in the current study is not slow enough to complete the phase transformation process from δ-ferrite to austenite.

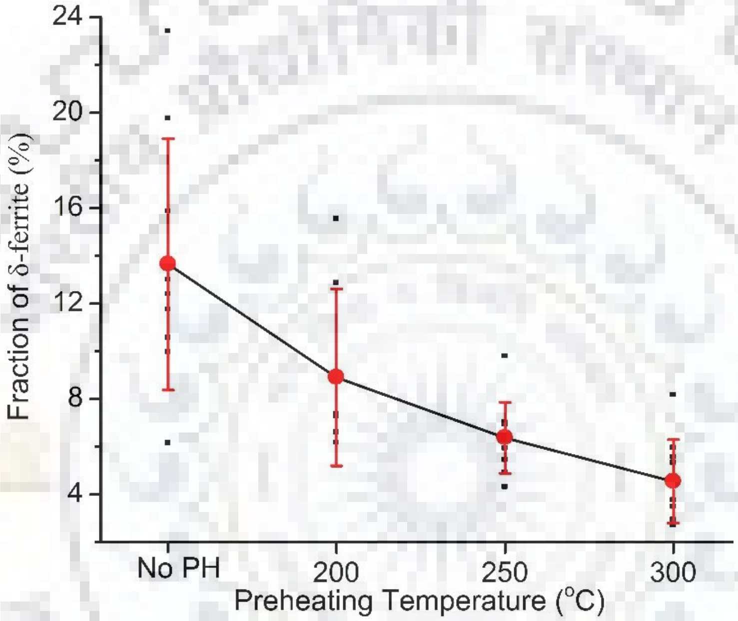

Figure 4.111 Effect of cooling rate on the fraction of δ-ferrite in the weld fusion zone

4.2.3 *Dissolution of δ-ferrite using post-weld normalizing and tempering*

A double-sided autogenous GTAW weld was designed, as shown in Fig. 4.12(a). The top side of the welded joint after 1st pass of GTAW welding is shown in Fig. 4.12(b). The smooth weld bead with almost zero reinforcement was observed. No surface open defect was observed after welding. The cross-sectional view of double-sided GTAW weld is shown in Fig. 4.12(c). Full penetration is confirmed from the cross-sectional macrograph.

Figure 4.13(a-c) shows the optical micrographs of the weld fusion zone of second pass weld in the as-welded, PWHT, and PWNT condition. In the as-welded condition, fresh martensite microstructure with some δ-ferrite patches was observed in the weld fusion zone of the second pass (Fig. 4.13(a)). After PWHT, the fresh martensite microstructure was tempered but the δ-ferrite patches were unchanged (Fig. 4.13(b)). After PWNT, no δ-ferrite patches were detected, as shown in Fig. 4.13(c).

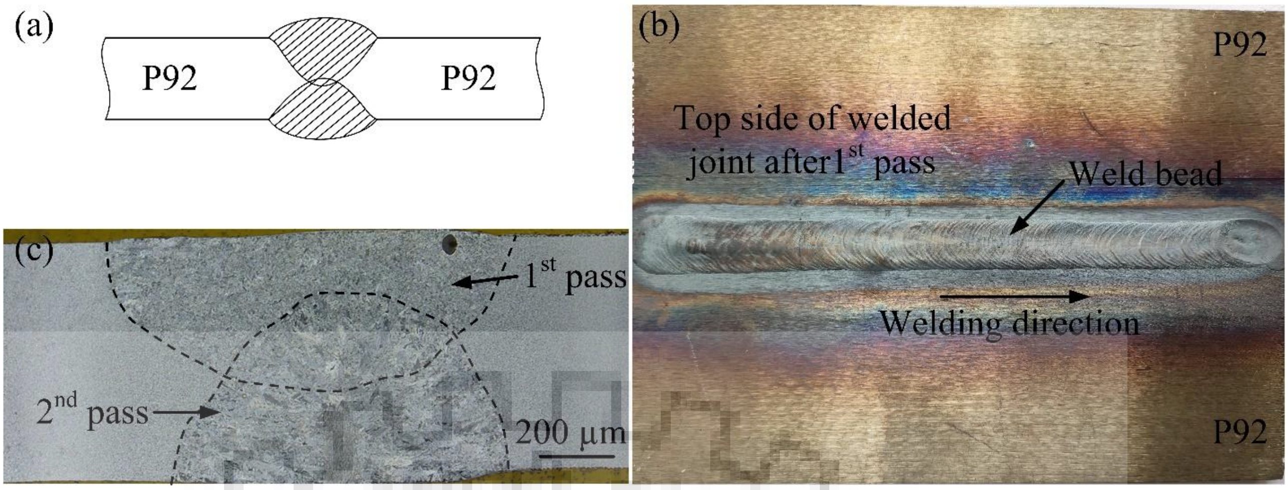

Figure 4.122 (a) Weld design of double-sided GTAW weld, (b) complete welded joint after 1st pass and (c) cross-sectional view of the weld

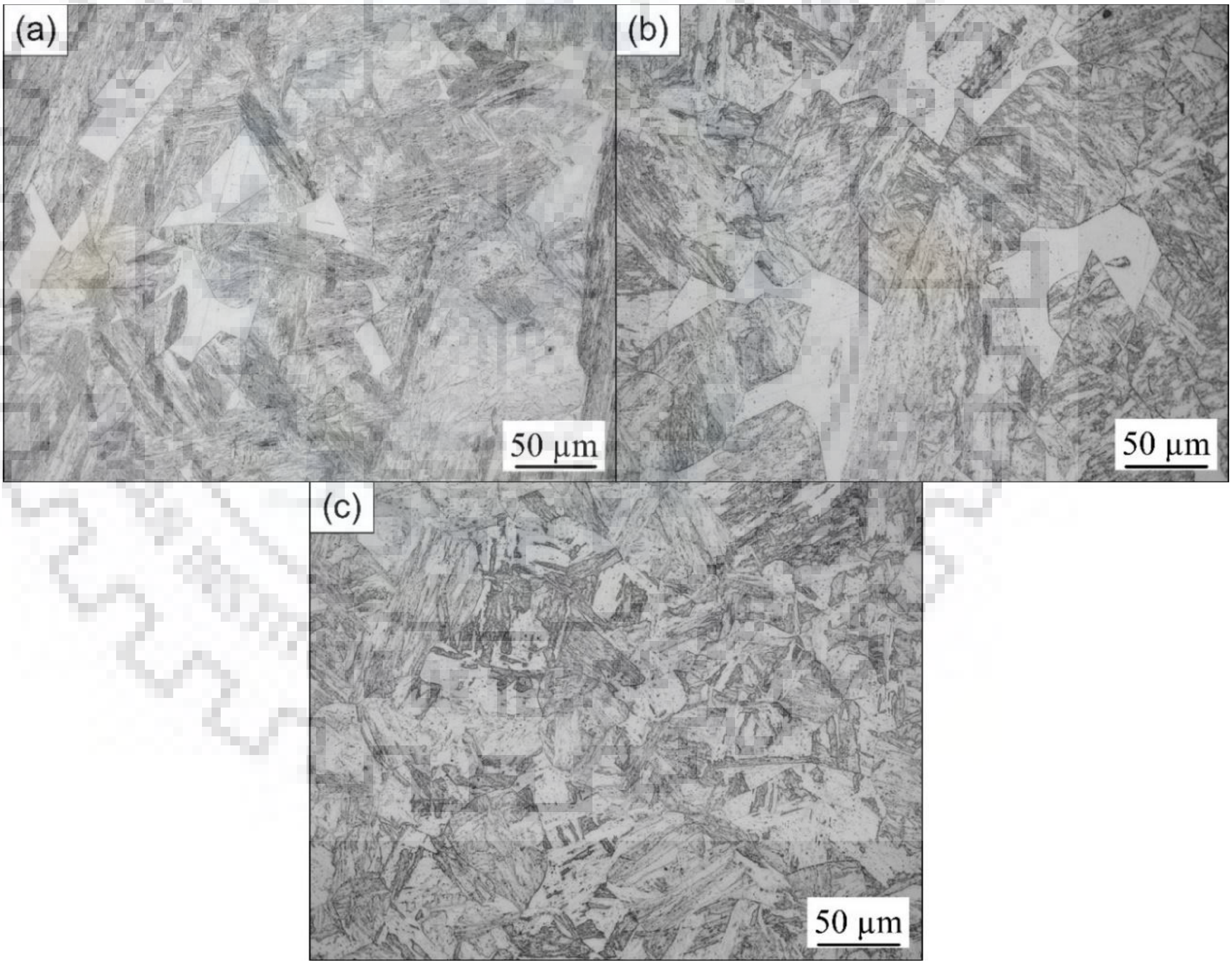

Figure 4.133 Optical micrographs of weld fusion zone of second pass weld in (a) the as-welded, (b) PWHT, and (c) PWNT condition

The SEMs of weld fusion zone of both first and second passes in the as-welded, PWHT and PWNT conditions are presented in Fig. 4.14(a-f). The retention of large δ-ferrite patches in the weld fusion zone of the second pass is observed (Fig. 4.14(a)). The morphology shows patches of smooth δ-ferrite grains surrounded by lath martensitic regions. In the as-welded condition, the high cooling rate may be the reason for the retention of δ-ferrite that did not allow δ-ferrite to transform into austenite. The first pass weld fusion zone has smaller and remnants patches of δ-ferrite because it undergoes post-weld heating (auto-tempering) during the second pass of welding which may allow δ-ferrite to transform into austenite (Fig. 4.14(b)).

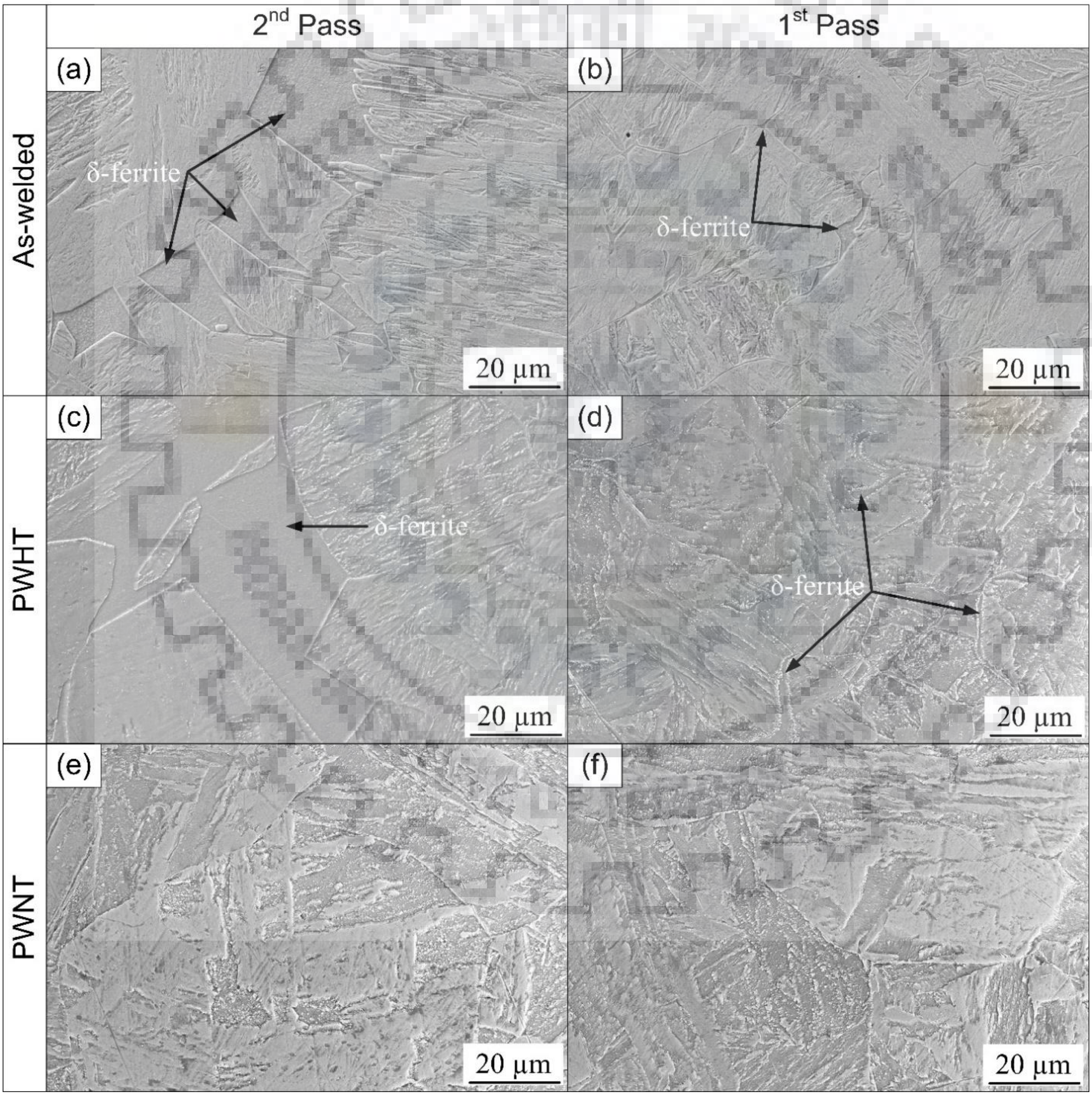

Figure 4.144 Secondary electron micrographs of weld fusion zone of the second and first pass in (a) and (b) the as-welded, (c) and (d) PWHT, (e) and (f) PWNT condition, respectively

In the as-welded condition, no precipitates were detected in weld fusion zone of both the passes. After PWHT, the precipitates were present at the boundary of δ-ferrite and martensitic microstructure as well as in the matrix while the δ-ferrite region was free of precipitates as shown in Fig. 4.14(c) and 4.14(d). After PWHT, no effect on δ-ferrite content was observed in the weld fusion zone of both the passes as compared to the as-welded condition. In PWNT condition, the weld fusion zone microstructures of second and first pass are presented in Fig. 4.14(e) and 4.14(f), respectively. After PWNT, both the passes were free from the δ-ferrite patches. The dissolution of δ-ferrite is suggested from the microstructure of the weld fusion zone in both the passes.

In the as-welded condition, Fig. 4.15(a) shows the micrograph of weld fusion zone (second pass) showing δ-ferrite and matrix interface. The EDX spectra of area 1 located in the δ-ferrite region is presented in Fig. 4.15(b). The higher weight percentage of ferrite stabilizers, Cr, and Mo were suggested in the δ-ferrite region. The EDX spectra of area 2 located in the matrix region shows lower weight percentage of ferrite stabilizers in the matrix region as compared to δ-ferrite region (Fig. 4.15(c)). The EDX spectra results are used as chemical verification of δ-ferrite in the weld fusion zone.

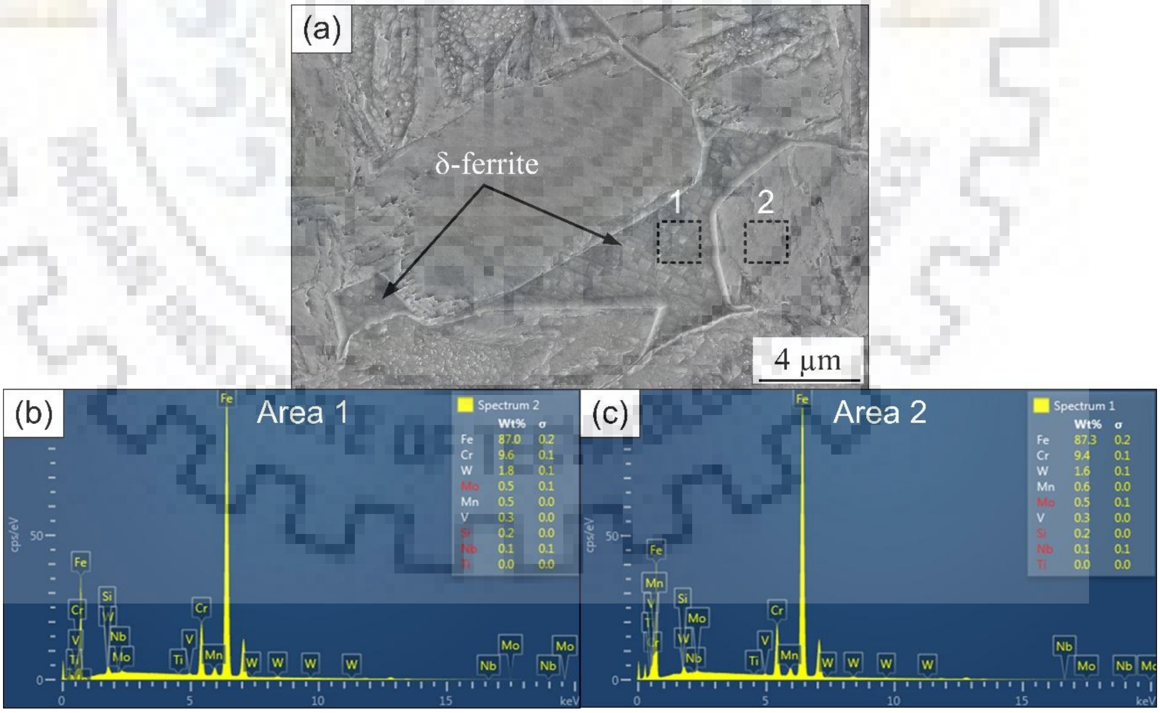

Spectrum 2

	Wt%	σ
Fe	87.0	0.2
Cr	9.6	0.1
W	1.8	0.1
Mo	0.5	0.1
Mn	0.5	0.0
V	0.3	0.0
Si	0.2	0.0
Nb	0.1	0.1
Ti	0.0	0.0

Spectrum 1

	Wt%	σ
Fe	87.3	0.2
Cr	9.4	0.1
W	1.6	0.1
Mn	0.6	0.0
Mo	0.5	0.1
V	0.3	0.0
Si	0.2	0.0
Nb	0.1	0.1
Ti	0.0	0.0

Figure 4.15 (a) Micrographs of weld fusion zone (second pass) in as-welded condition showing δ-ferrite and matrix region with their boundary, (b) EDX of area 1 present in the δ-ferrite, and (c) EdX of area 2 present in the matrix region.

The XRD patterns are used for the structural verification of δ-ferrite. Figure 4.16(a-c) shows the XRD patterns of the weld fusion zone after the Rietveld refinement in as-welded, PWHT, and PWNT conditions. In all three conditions, the highest intensity peaks were clearly identified as BCT, i.e., α’-martensite. Additionally, some small intensity peaks were identified as ferrite (δ-ferrite) and retained austenite. In the as-welded condition, BCT, ferrite and retained austenite peaks were observed (Fig. 4.16(a)).

After PWHT, all peaks were similar to the as-welded condition probably due to low tempering temperature (below Ac$_1$) that did not allow any fractional change in ferrite and martensite percentage (Fig. 4.16(c)). In PWNT condition, BCT peaks were observed, but no ferrite peaks were observed (Fig. 4.16(c)). The phase fractions were calculated using Rietveld refinement of the raw XRD data for different post-weld heat treating conditions are tabulated in Table. 4.7. In the as-welded condition, around 15 % δ-ferrite phase fraction was detected while the content was 17 % in PWHT condition.

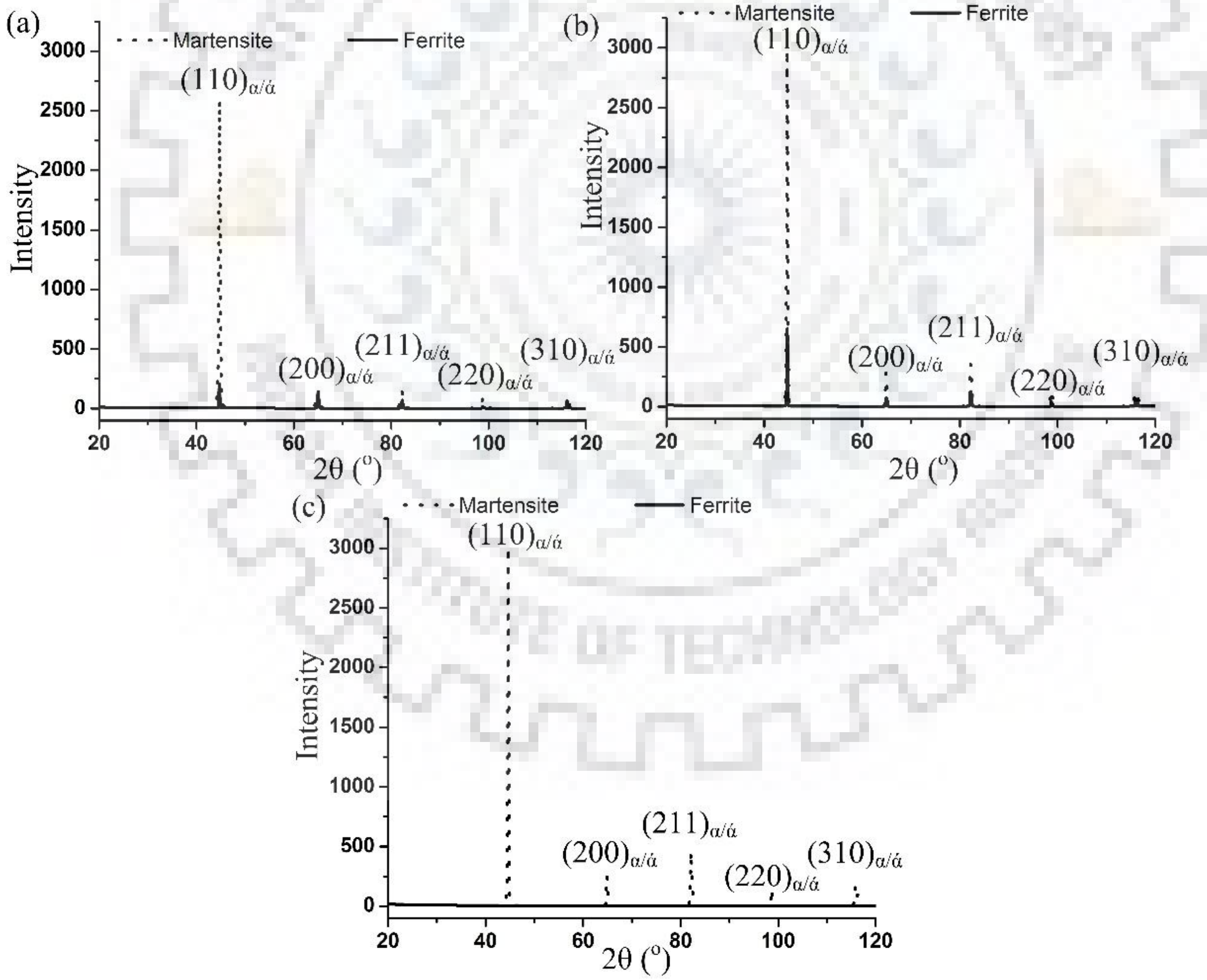

Figure 4.166 XRD profiles after Rietveld refinement for (a) as-welded, (b) PWHT, and (c) PWNT

After PWNT, no δ-ferrite content was detected in the weld fusion zone. Since the martensite and ferrite phases have similar lattice parameters and the same crystal structure, this leads to the overlapping of their XRD peaks. However, (110)$_{\alpha/\acute{\alpha}}$ peaks of all three conditions for martensite and ferrite are plotted (Fig. 4.17). Figure 4.17(a) is used to see any peak shift of martensite phase during temper towards ferrite. After PWHT and PWNT, (110)$_{\alpha/\acute{\alpha}}$ peak shifts towards left i.e., change in 2θ position of the peak.

The c/a ratio for martensite phase is presented in Table 4.10. The c/a ratio of martensite for PWNT condition was reduced probably due to formation of carbides during tempering. To verify the location of ferrite peak, ferrite phase peaks are plotted in Fig. 4.17(b). In as-welded condition, the ferrite peak location is identified as 44.6^{o} while 44.65^{o} for martensite phase.

Table 4.7 Phase fractions calculated using Rietveld refinement of the raw XRD data for different post-weld heat treating conditions

Conditions	Fraction of ferrite (f_{α})	Fraction of martensite ($f_{\acute{\alpha}}$)	Fraction of austenite (f_{γ})
as-welded	0.146±0.02	0.80±0.01	0.05±0.004
PWHT	0.166±0.03	0.83±0.03	0.05±0.003
PWNT	0.0±0.0	0.997±0.002	0.003±0.002

Table 4.8 c/a ratios for martensite phase after different post-weld conditions

Conditions	Lattice parameter (c)	Lattice parameter (a)	c/a ratio
as-welded	0.288882	0.285143	1.013
PWHT	0.287180	0.287712	0.998
PWNT	0.287322	0.287569	0.999

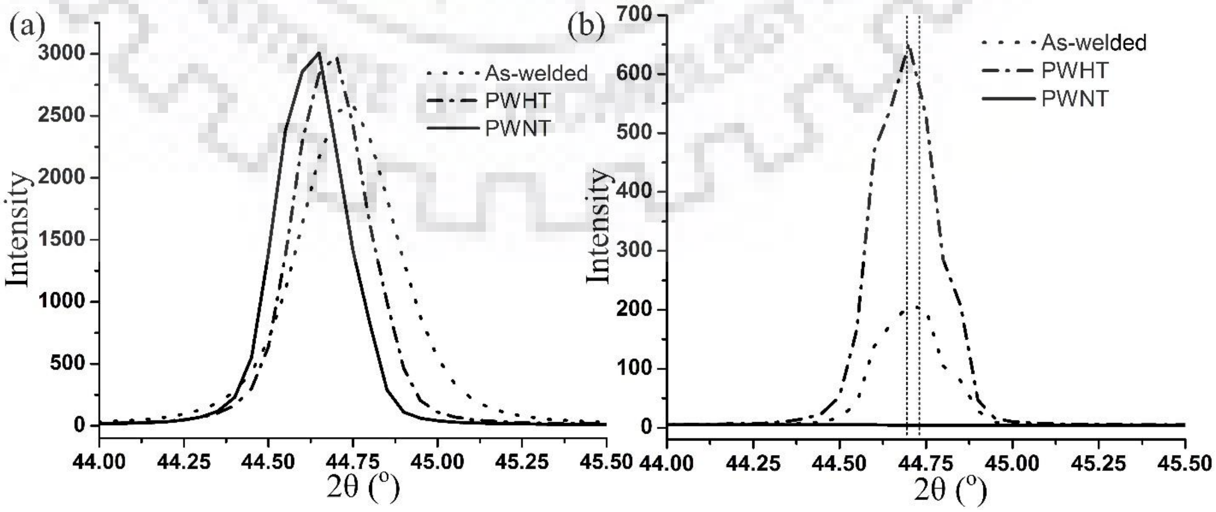

Figure 4.17 (a) peak shift in martensitic phase and (b) peak confirmation of ferrite phase

Figure 4.18 shows a change in the volume fraction of δ-ferrite with different post-weld conditions. The δ-ferrite fraction was measured using optical micrographs and using XRD Rietveld refinement. In the as-welded condition, the δ-ferrite fraction was measured as 12 ± 3 %and 14.5 ± 3 % from optical micrographs and from XRD Rietveld refinement, respectively. After PWHT, similar fraction of δ-ferrite was measured as 13 ± 4 %and 16.5 ± 2 % from optical micrographs and from XRD Rietveld refinement, respectively. In PWNT condition, no δ-ferrite fraction was detected from XRD Rietveld refinement while δ-ferrite was not seen in optical micrographs.

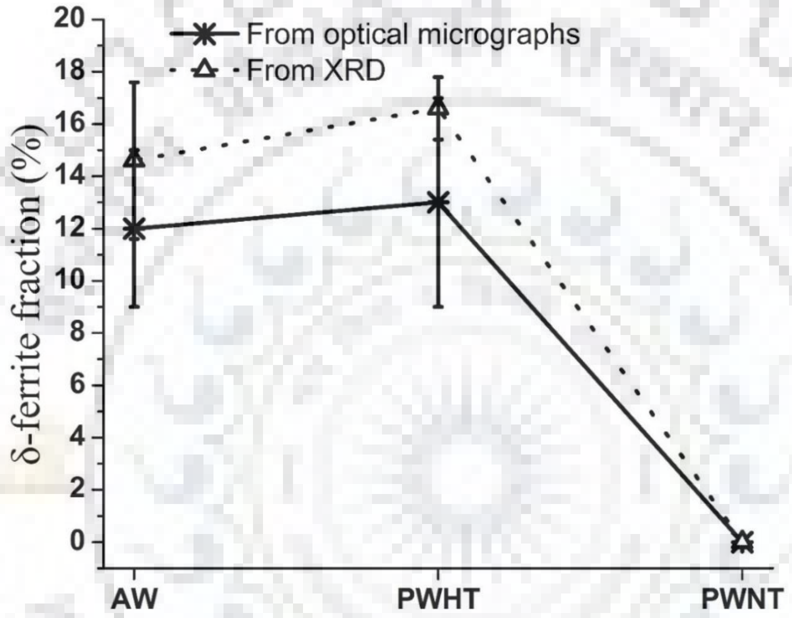

Figure 4.18 Fraction of δ-ferrite measured for different post-weld conditions from optical micrographs and from XRD Rietveld refinement

The hardness of δ-ferrite is also compared with the martensite phase (Figure 4.19(a)) shows an optical micrograph of hardness indentations in the δ-ferrite and matrix region. The hardness value for the δ-ferrite region was measured as 225 HV while 439 HV for martensitic matrix redundant. The microhardness value of another δ-ferrite region was measured as 190 HV, as shown in Fig. 4.19(b). The average microhardness of the δ-ferrite region was measured in the range of 190-250 HV. However, the microhardness of matrix region (un-tempered lath martensite) was measured in the range of 420-469 HV. In as-welded condition, microhardness variation across the welded joint is shown in Fig. 4.20(a). The weld fusion zone microhardness varies in the range of 310–469 HV probably due to the presence of soft δ-ferrite patches. The δ-ferrite regions were seen only in the weld fusion zone as suggested by the optical micrographs.

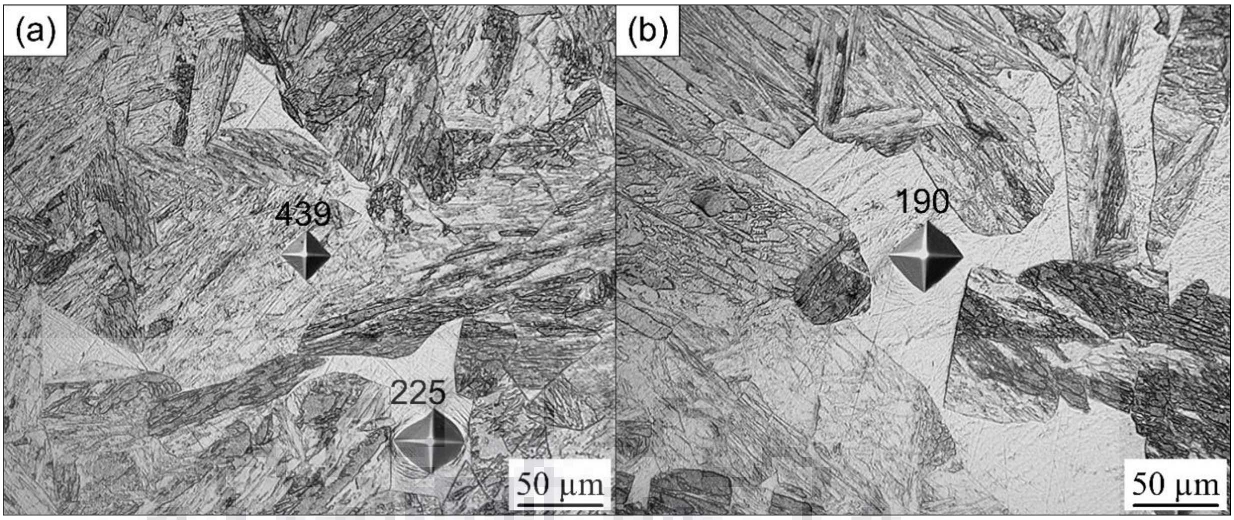

Figure 4.19 Optical micrographs of hardness indentation in (a) δ-ferrite and matrix region and (b) δ-ferrite region

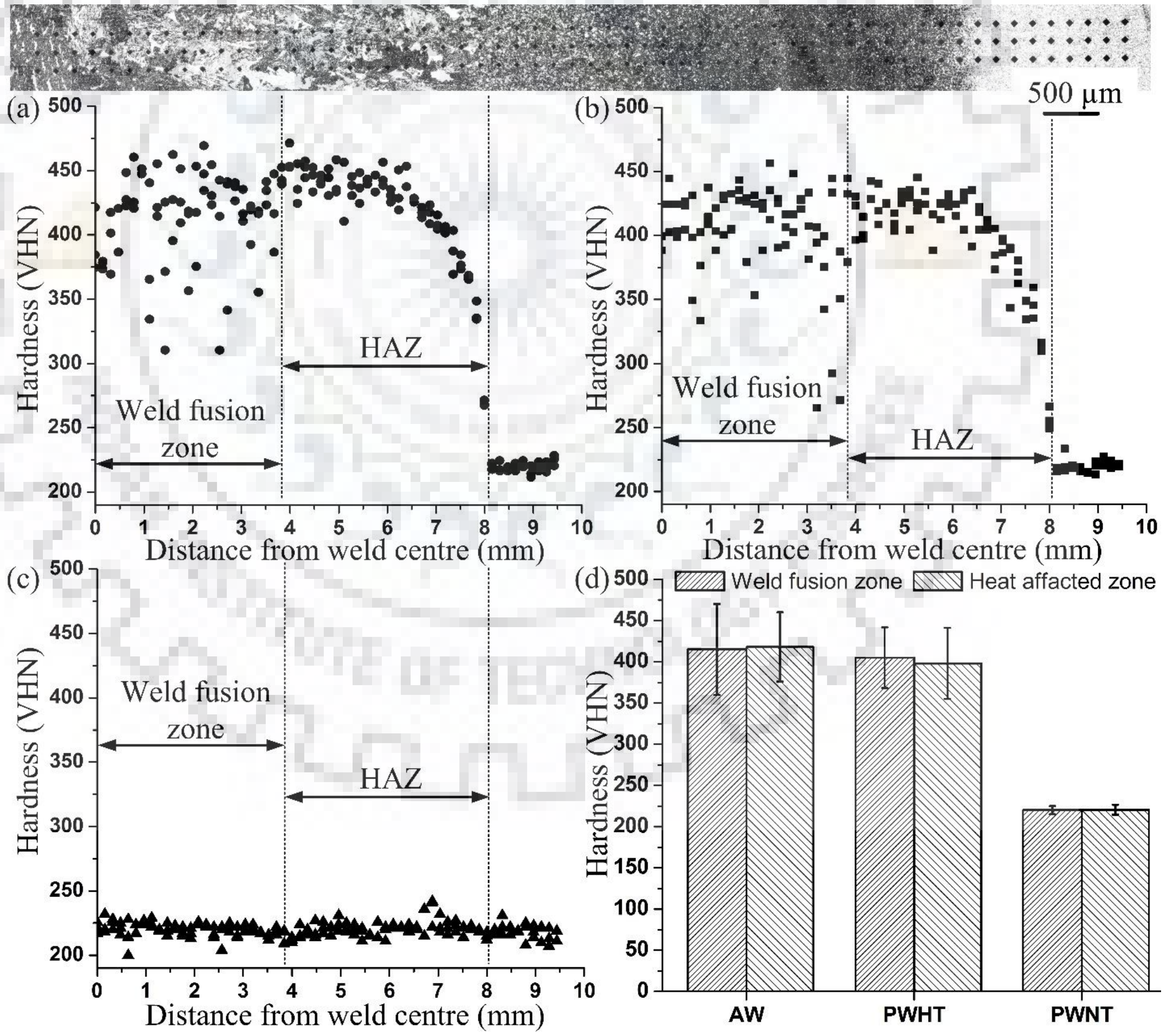

Figure 4.20 Hardness variation across the welded joint in (a) as-welded, (b) PWHT, (c) PWNT condition, and (d) average microhardness of weld fusion zone and HAZ in all three conditions

The same is confirmed by the microhardness plots because the variation in microhardness is more in weld fusion zone as compared to HAZ. A continuous reduction in microhardness was measured in all three conditions as a move away from the fusion boundary i.e., HAZ. The similar results of microhardness were also observed in the PWHT condition except small decrease in the average microhardness of HAZ (Fig. 4.20(b)). In PWHT condition, the average microhardness of weld fusion zone lies in the range of 265–456 HV while HAZ microhardness lies in the range of 249–445 HV. However, the microhardness of the weld fusion zone after PWNT varies in the range of 200–232 HV which was similar to as-received base material hardness (Fig. 4.20(c)). The average microhardness values of weld fusion zone and HAZ are plotted in Fig. 4.20(d). The heterogeneity in the microhardness removed after PWNT as compared to as-welded and PWHT conditions.

The tensile samples before and after fracture that show the fracture location within the gauge length are shown in Fig. 4.21(a). The fracture location is confirmed as over tempered base metal in as-welded and PWHT conditions while the center of the weld fusion zone in PWNT condition. Figure 4.21(b) shows an engineering stress-strain curve for all three post-weld conditions. The minimum ductility was measured in the as-welded condition while maximum in PWNT condition. The tensile strengths were measured as 771 ± 15, 702 ± 14 and 748 ± 14 MPa in the as-welded, PWHT and PWNT conditions, respectively. However, there is not much difference found in tensile strength because two of samples were actually testing the base metal, while the third was testing the annealed fusion zone (just like base metal).

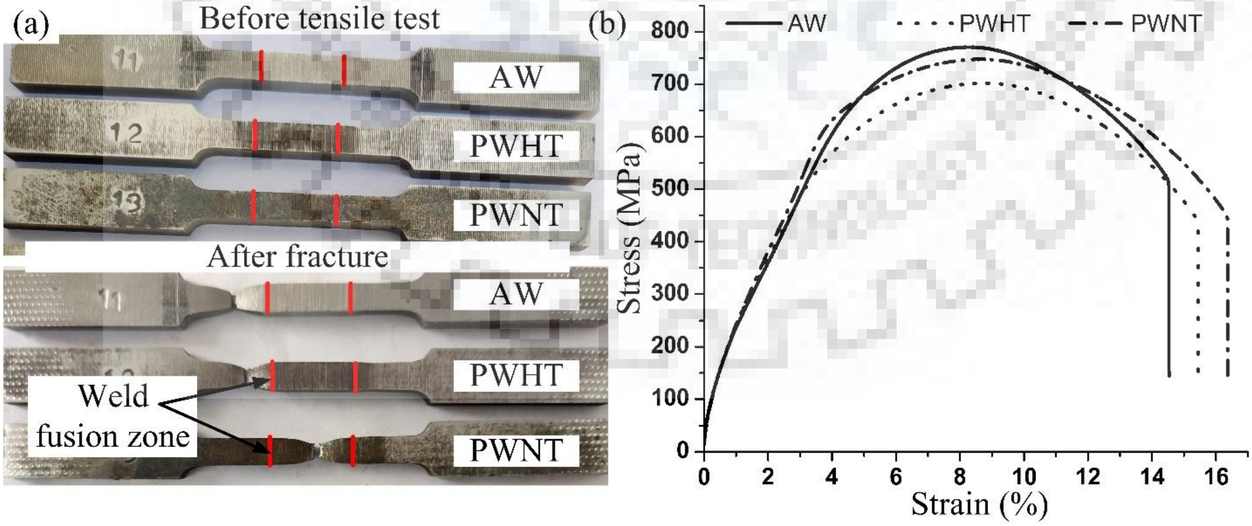

Figure 4.21 (a) Tensile specimens before and after fracture, and (b) engineering stress-strain curves for welded joints welded with different post-weld conditions

In all three conditions, sub-size samples (55 mm × 10 mm × 5 mm) having V-notch at the weld center were tested for Charpy toughness. The Charpy toughness of as-received P92 steel was measured as 69 ± 3 J. Figure 4.22 shows the variation in Charpy impact toughness of weld fusion zone in different post-weld conditions. In the as-welded condition, the average Charpy toughness was measured as 8 ± 2 J.

The poor Charpy toughness may be due to presence of δ-ferrite and brittle fresh martensitic microstructure. Schafer (Schafer, 1998a) reported that the presence of δ-ferrite may be the reason for poor Charpy toughness of the weld fusion zone. After PWHT, an increase in Charpy toughness is observed may be due to tempering of fresh lath martensite. The value of average Charpy toughness was 26 ± 3 J in PWHT condition. After PWNT, the average value of Charpy toughness is increased more and reaches approx. to as received base material. This increased in Charpy toughness may be achieved due dissolution of δ-ferrite and due to tempering of martensitic microstructure.

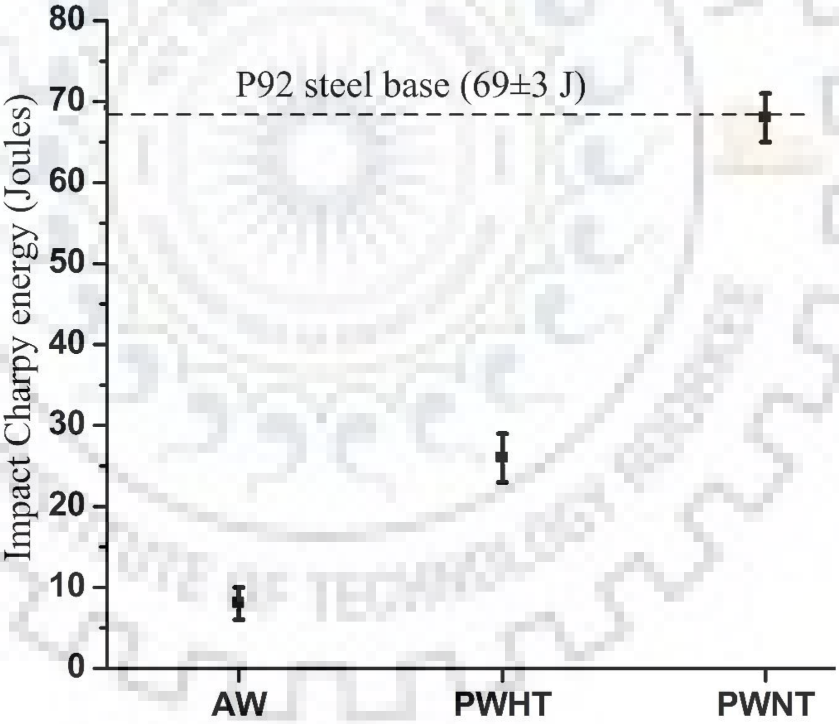

Figure 4.22 Variation in Charpy impact toughness of weld fusion zone in different post-weld conditions

Figure 4.23(a-f) shows the optical micrographs of the weld fusion zone of first pass in as-welded, PWHT, and PWNT conditions. The multi-pass effect was observed in the weld fusion of first pass. Lower δ-ferrite content was seen in the weld fusion zone of first pass (Fig.

4.23(a)). At higher magnification, the long narrow needle-like δ-ferrite patches were clearly observed, as shown in Fig. 4.23(b). During second pass, the first pass has more time at temperature above Ac_1 or below its melting point that allows δ-ferrite to transform into austenite (γ) which further changes into ferrite and on cooling to martensite. The same concept has been used for the dissolution of δ-ferrite.

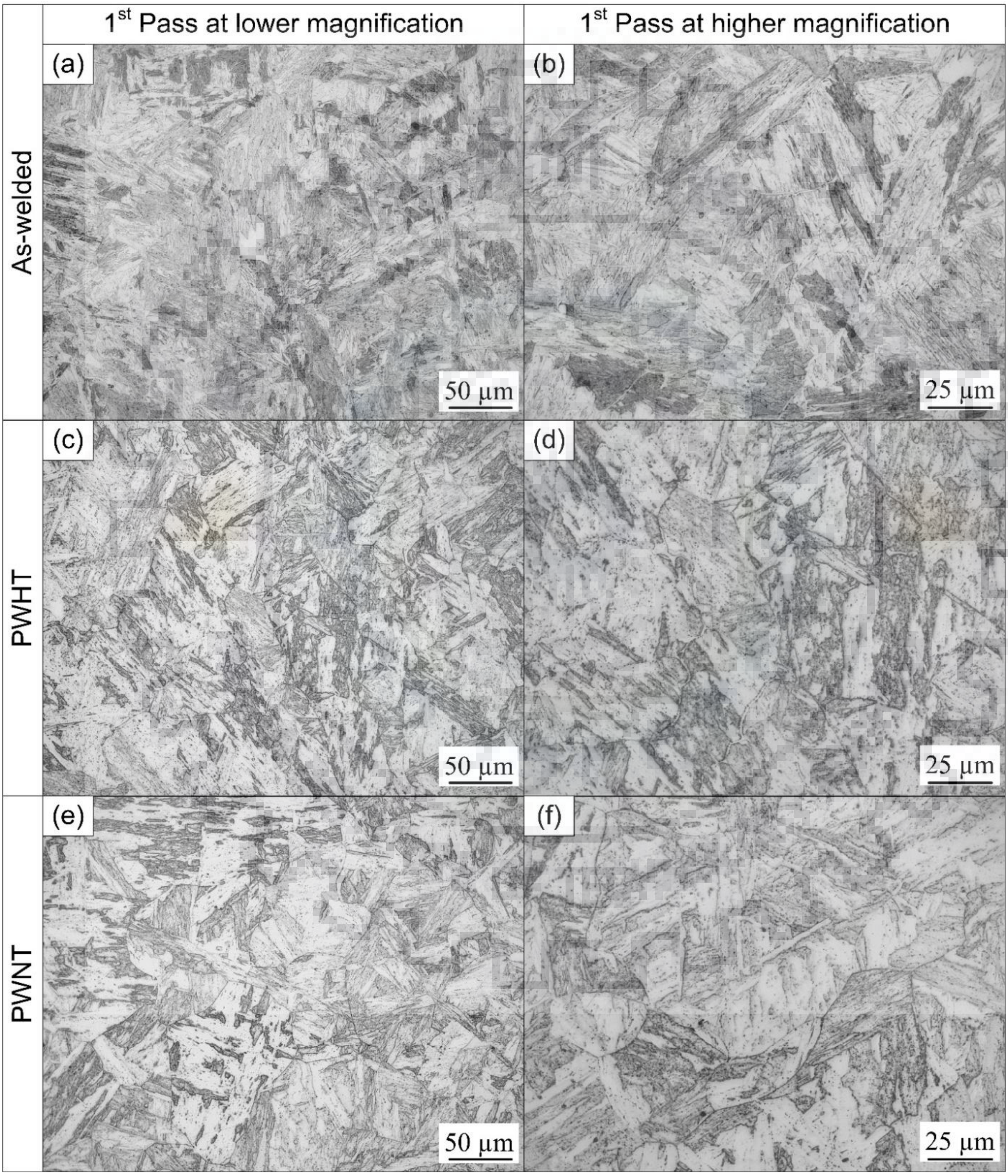

Figure 4.23 Optical micrographs of weld fusion zone of the first-pass weld at lower and higher magnification in (a) and (b) as-welded, (c) and (d) PWHT, (e) and (f) PWNT condition

Similar long narrow needle-like tunnels of δ-ferrite were also observed from the microstructure of weld fusion of first-pass after PWHT, as shown in Fig. 4.23(c) and 4.23(d), respectively. After PWNT, no δ-ferrite patches were observed from weld fusion zone microstructure of first pass at lower and higher magnification is shown in Fig. 4.23(e) and 4.23(f), respectively.

Fig. 2.8(a) shows that the δ-ferrite is not stable below 1250 ^{o}C. If we placed the welded joint below this temperature and above 887 ^{o}C (Ac$_3$ of P92 steel), then dissolution of δ-ferrite may start by diffusion of ferrite stabilizers (Cr and W). The holding time during PWNT may diffuse the Cr and W enriched δ-ferrite into austenite. An analytical solution for dissolution of δ-ferrite in austenite is obtained by assuming initial compositions of austenite and δ-ferrite are constant, and the matrix (austenite) is infinite in dimension (Kim et al., 2003; Vitek et al., 1995).

$$Cr^{\delta} - Cr^{\delta/\gamma} = \frac{(Cr^{m} - Cr^{\delta/\gamma})\exp\{(K_{Cr}^{\gamma})^{2}\}}{K_{Cr}^{\gamma}(\pi^{1/2})\{1-\mathrm{erf}(K_{Cr}^{\gamma})\}} \tag{4.9}$$

$$W^{\delta} - W^{\delta/\gamma} = \frac{(W^{m} - W^{\delta/\gamma})\exp\{(K_{W}^{\gamma})^{2}\}}{K_{W}^{\gamma}(\pi^{1/2})\{1-\mathrm{erf}(K_{W}^{\gamma})\}} \tag{4.10}$$

$$\Delta f/f_{o} = \frac{x - x_{o}}{x_{o}} = \frac{K_{Cr}^{\gamma}}{x_{o}}\{2 * \sqrt{(D_{Cr}^{\gamma}t)}\} \tag{4.11}$$

$$\Delta f/f_{o} = \frac{x - x_{o}}{x_{o}} = \frac{K_{W}^{\gamma}}{x_{o}}\{2 * \sqrt{(D_{W}^{\gamma}t)}\} \tag{4.12}$$

where Cr^{δ} and W^{δ} are Cr and W concentration in δ-ferrite phase, $Cr^{\delta/\gamma}$ and $W^{\delta/\gamma}$ are Cr and W concentration at δ-ferrite and austenite interface, Cr^{m} and W^{m} are Cr and W concentration in the matrix (austenite phase), K_{Cr}^{γ} and K_{W}^{γ} are dimensionless dissolution parameters for Cr and W in austenite, x is half-width of δ-ferrite and $\Delta f/f_{o}$ is dissolved δ-ferrite fraction. D_{Cr}^{γ} and D_{W}^{γ} are diffusion coefficients of Cr and W in the austenite phase. t is normalizing temperature.

The above analytical solution is used with experiment data at 1050 ^{o}C. The average size of δ-ferrite is measured as 100 μm from optical micrographs. The Cr and W concentration values are measured as 9.45 and 1.65, 9.6 and 1.8, 9.4 and 1.6 at δ-ferrite/austenite boundary interface, in the δ-ferrite and in the matrix (austenite) from SEM-EDX. The diffusion coefficients of Cr and W in austenite at 1050 ^{o}C is calculated as 8×10^{-14} and 2.5×10^{-14} m^{2}/sec, using DICTRA.

The dimensionless dissolution parameters K_{Cr}^{γ} and K_{W}^{γ} are calculated as -0.16 and -0.125 using eq (4.9) and eq (4.10). The dissolved δ-ferrite fraction is plotted with PWNT holding time (Fig. 4.24), which shows the dissolution of δ-ferrite completes after 27 min of PWNT. The experimental results seem to agree with this analytical model prediction for dissolution kinetics of δ-ferrite in the weldments of P92 steel.

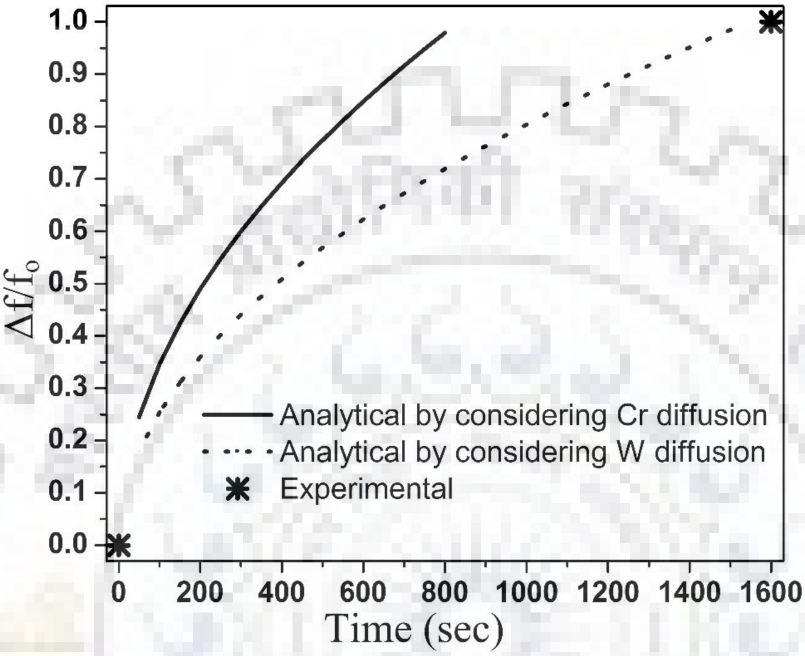

Figure 4.24 Analytical solution with experimental data for dissolution kinetics of δ-ferrite at 1050 ^{o}C.

4.2.4 *Effect of different filler compositions on the microstructure evolution and mechanical properties of SMAW welded joints of P92 steel*

4.2.4.1 Microstructure evolution in as-welded condition

The micrograph of weld fusion zone of P92 steel for E911 filler is shown in Fig. 4.25(a). The weld fusion zone in as-welded state consisted of columnar lath martensitic structure with different martensite lath directions. In FGHAZ, the tempered martensite of base metal transformed to austenite during weld thermal cycle. Some undissolved precipitates were also observed in the FGHAZ, as shown in Fig. 4.25(b) and (d). These un-dissolved precipitates obstruct the growth of austenite grains by pinning it, which resulted in fine grains of austenite in FGHAZ. In FGHAZ of P92 steel, the lath martensite was formed within the PAGBs with a low length to width ratio.

In P92 steel, Schneider formula is utilized to predict the tendency of the δ-ferrite formation. Schneider formula is given by Onoro (Onoro, 2006) as Ferrite factor (FF) which is difference of Cr_{eq} and Ni_{eq} [$\{Ni_{eq} = Ni + 0.5Mn + 30C + 25N + 0.3Cu\}$ and $\{Cr_{eq} = Cr + 2Si +5V+1.5Mo + 1.75Nb + 0.75 W\}$]. If FF ≥ 8.5, weld shows the high tendency of the δ-ferrite formation. Onoro et al. reported that complete absence of δ-ferrite was found in weld fusion zone with low FF (Onoro, 2006). In case of multi-pass welding, the complete transformation of δ-ferrite to austenite occurs due to additional time for diffusion (Chandan Pandey et al., 2018b).

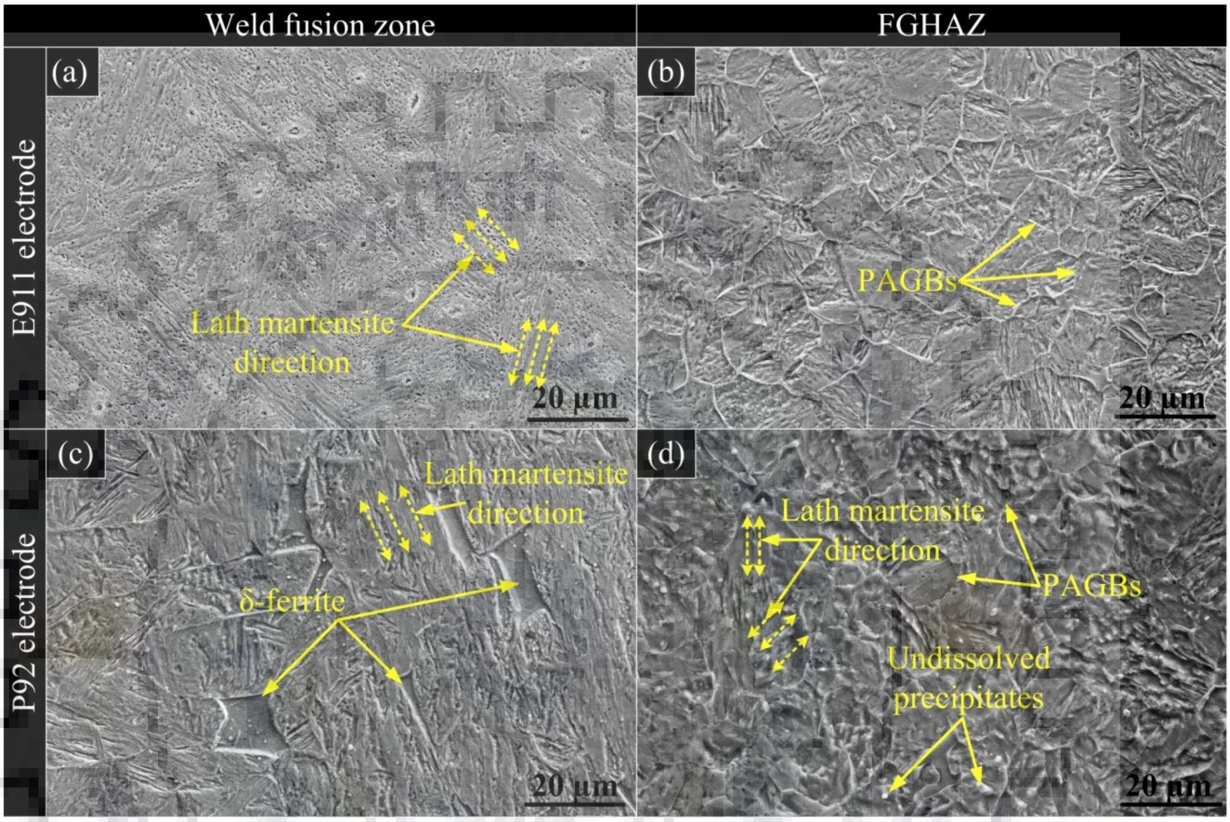

Figure 4.25 Secondary electron micrograph in as-welded condition (a) weld fusion zone for E911 filler, (b) FGHAZ for E911 filler, (c) weld fusion zone for P92 filler and (d) FGHAZ for P92 filler

The FF was calculated from weld compositions (Table 4.1) for E911 and P92 filler as 6.5 and 6.2, respectively. In spite of the low value of FF, some δ-ferrite patches were observed in the weld fusion zone of P92 steel weldments as a result of higher weight percentage of the ferrite stabilizer in the filler metal. Although multi-pass welding and FF is near to limited value for the δ-ferrite evolution, the presence of δ-ferrite was confirmed in the weld fusion zone of P92 steel weldments welded with P92 filler, as shown in Fig. 4.25(c). The distribution of δ-ferrite ferrite patches was clearly observed in several local areas of the microstructure, which might have been due to the higher weight percentage of ferrite stabilizers like W, Mo, V, and Nb in the P92 weld fusion zone as compared to E911 filler weld fusion zone, as given in Table 4.1.

4.2.4.2 Microstructure evolution of weldments after PWHT

In P92 steel, post weld heat treatment (PWHT) resulted in coarsening of existing precipitates as well as nucleation of new precipitates along the PAGBS and lath blocks and also inside the intra-lath region. PWHT of P92 steel welds for different fillers revealed evidence of microstructural changes, as shown in Fig. 4.26. After subsequent PWHT, tempered martensite with $M_{23}C_6$ and MX precipitates that beautify the PAGBs and lath packet boundaries were observed for both filler in weld fusion zone and HAZs microstructure. Due to higher availability of chromium (Cr) along the boundaries and higher diffusion coefficient of carbon(C), the Cr-rich $M_{23}C_6$ type precipitates formed preferentially along the PAGBs.

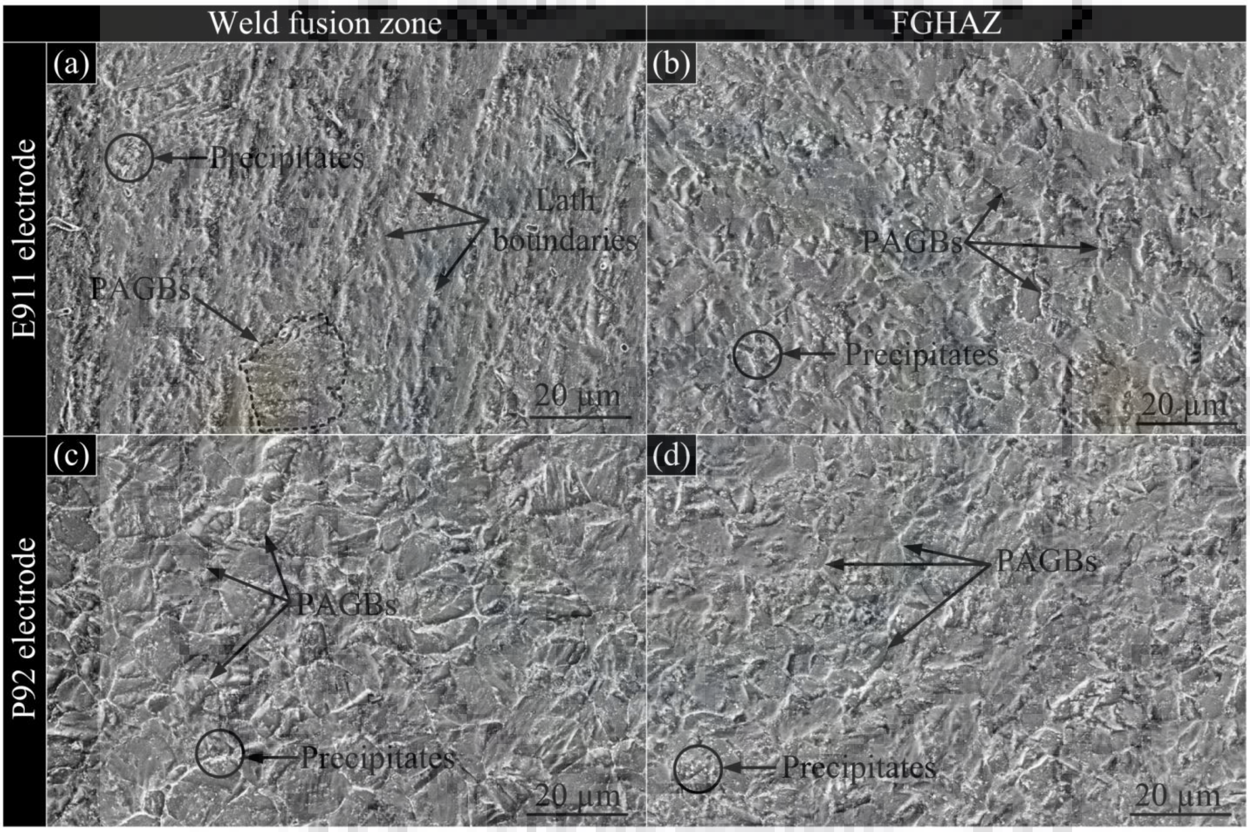

Figure 4.26 Secondary electron micrograph in PWHT condition (a) weld fusion zone for E911 filler, (b) FGHAZ for E911 filler, (c) weld fusion zone for P92 filler and (d) FGHAZ for P92 filler

The typical microstructure of weld fusion zone having tempered lath martensitic microstructure for E911 filler condition is shown in Fig. 4.26(a). It was characterized by PAGBs, lath boundaries, tempered lath martensite, $M_{23}C_6$ type precipitates and fine MX type precipitates. The secondary electron micrograph of FGHAZ is shown in Fig. 4.26(b), which clearly reveals the presence of PAGBs, $M_{23}C_6$ and MX precipitate (Wang et al., 2013).

In weld fusion zone of E911 filler, the columnar lath morphology is still observed after the PWHT while in the P92 filler, PWHT results in the transformation of laths from columnar to equiaxed morphology, as shown in Fig. 4.26(c). In FGHAZ, equiaxed tempered lath is formed for both the fillers, as shown in Fig. 4.26(b) and (d).

A schematic of carbide evolution based on as-received, welding using filler and PWHT conditions is presented in Fig. 4.27(a) (Chandan Pandey et al., 2018c). In as-received condition, $M_{23}C_6$ are located along PAGBs, packet boundaries, martensite block and $M_{23}C_6$ is in a near-equilibrium condition, as shown in Fig. 4.27(b). In as-received condition, the distribution of the precipitates and their morphology is shown in Fig. 4.27(e). To prevent movement of boundaries, it is important to have $M_{23}C_6$ type precipitates on the grain boundaries because $M_{23}C_6$ resulted in four times more pinning pressure than MX type precipitates. Inside martensite blocks and at martensite block boundaries, MX type precipitates are also presented.

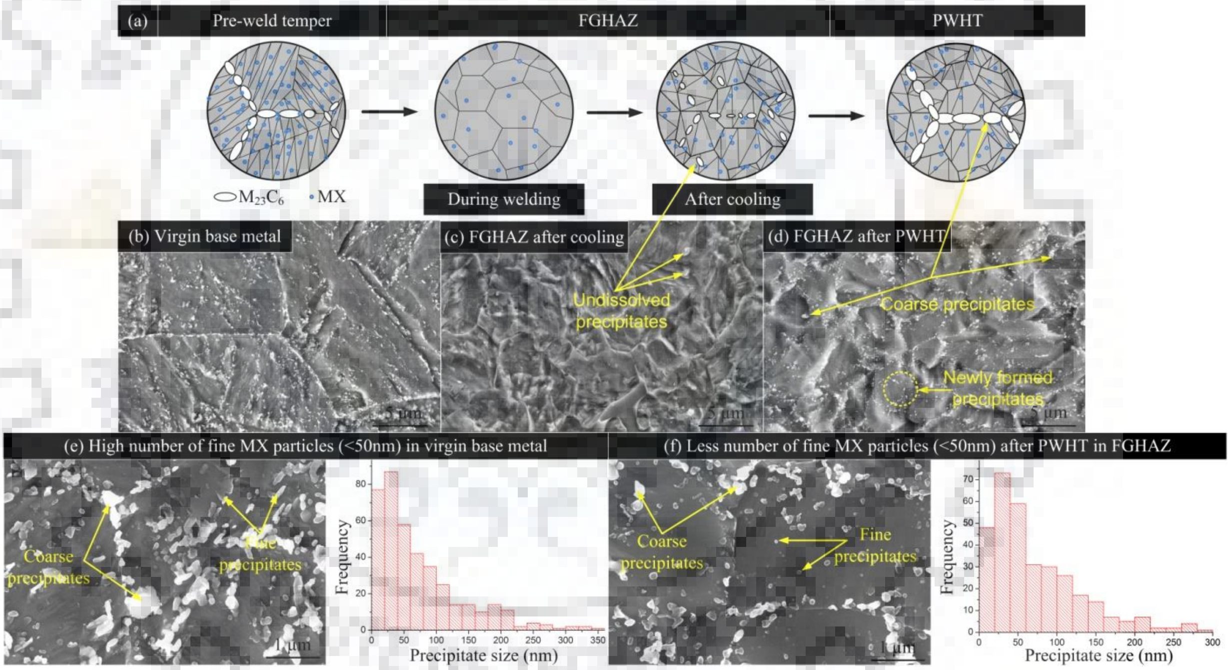

Figure 4.277 (a) Schematic showing microstructure evolutions after welding and PWHT, (b), (c), (d) micrographs of base metal, FGHAZ after welding, FGHAZ after PWHT, respectively, (e) fine MX particles in base material and (f) fine MX particles in FGHAZ after PWHT

After welding, some coarse $M_{23}C_6$ precipitates were observed but the MX remains unchanged due to higher thermal stability, as shown in Fig. 4.27(c) and also confirmed form the schematic diagram of FGHAZ in the as-welded state. After PWHT, supersaturated carbon in the martensite matrix of FGHAZ will support the growth of un-dissolved $M_{23}C_6$ instead of the formation of new $M_{23}C_6$ precipitates. For the same reason, the amount of newly formed MX precipitates will be less as compared to the as-received material condition, as shown in Fig. 4.27(d-f). The secondary electron micrographs showing the precipitate evolution in the FGHAZ after PWHT for E911 and P92 filler are given in Fig. 4.28(a) and 4.28(b), respectively. The precipitate size present at PAGBs in FGHAZ was measured using Image J software as 107 ± 36 and 115 ± 32 nm for E911 and P92 filler, respectively.

The size of precipitates present in the matrix region was measured to be 60 ± 16 and 62 ± 12 nm for E911 and P92 filler, respectively. For both the fillers, a negligible change was observed in the size of precipitates present at PAGBs and in the matrix area, as shown in Fig. 4.28(c). Some precipitates having size less than 40 nm was also seen in higher magnification micrograph that is confirmed as fine MX precipitates (C. G. Panait et al., 2010b).

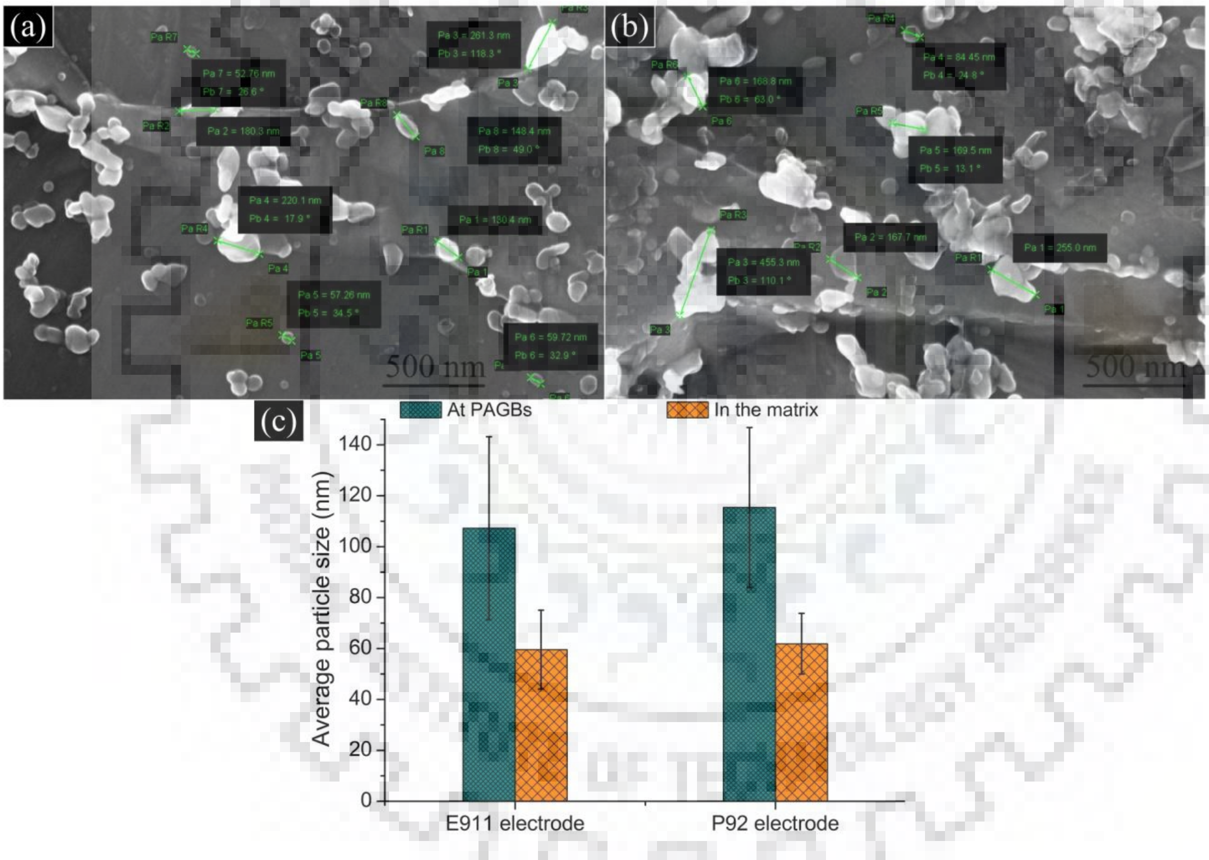

Figure 4.28 Secondary electron micrograph of FGHAZ after PWHT (a) for E911 filler, (b) for P92 filler and (c) average particle size in FGHAZ for different filler

4.2.4.3 Effect of fillers on tensile strength of welded joints

For the transverse tensile test, fractured and un-fractured specimens for the as-welded and PWHT condition are shown in Fig. 4.29. For each result, the averages of three tests are reported.

In as-welded condition, for P92 filler, fracture occurred form FGHAZ, as shown in Fig. 4.29(a). For E911 filler fracture occurs in the ICHAZ, as shown in Fig. 4.29(a). The FGHAZ and ICHAZ are considered as the softest zone in P92 weldments which is also confirmed form the hardness variation. After the PWHT, the fracture location was shifted from FGHAZ/ICHAZ to the over-tempered base metal for all specimens welded with E911 and P92 fillers, as shown in Fig. 4.29(b). In as-welded condition, the un-fractured and fractured longitudinal tensile specimen for E911 and P92 fillers are shown in Fig. 4.30.

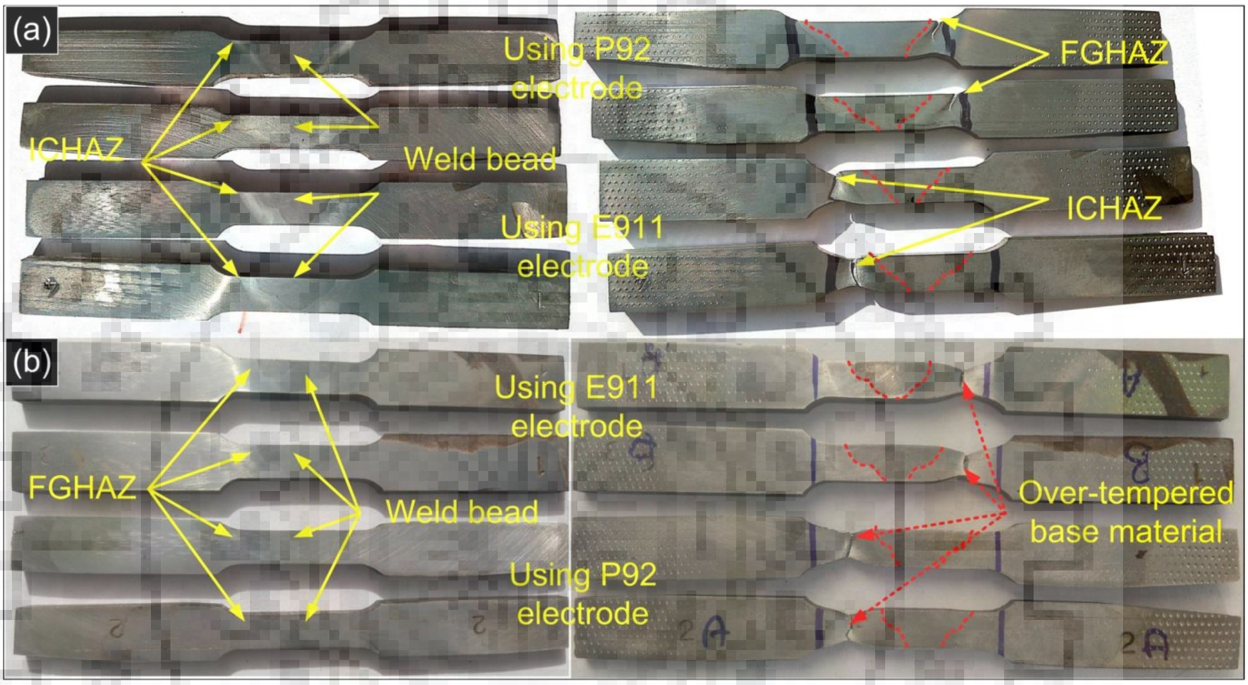

Figure 4.29 Tensile specimens before and after the transverse tensile test in (a) as-welded condition and (b) PWHT condition

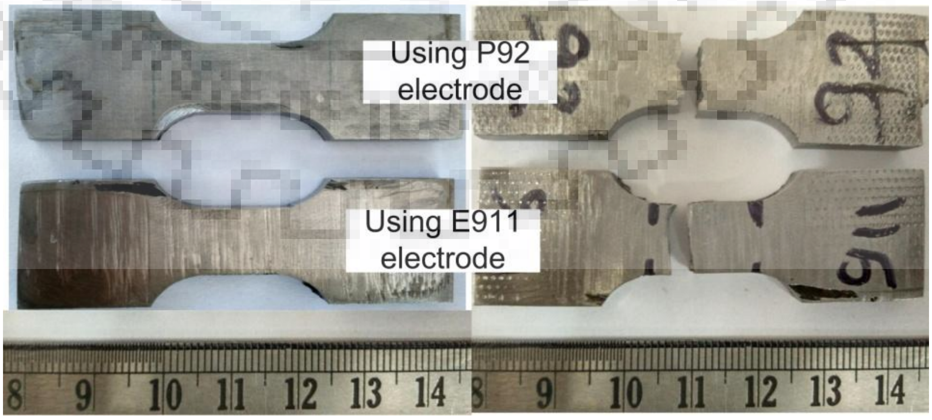

Figure 4.30 Specimens before and after the longitudinal tensile test in as-welded condition

Engineering stress-strain curve for longitudinal tensile tested specimens is shown in Fig. 4.31(a). To find out the effect of different fillers on the tensile behavior of P92 steel weldments, the engineering and true stress-strain curves were imposed in as-welded condition, as shown in Fig. 4.31(b). For both filler welds, the true stress-strain curve was observed on top of engineering stress-strain curve.

The true and engineering stress-strain curves were shifted towards the higher side for P92 steel specimens welded with P92 filler. In as-welded condition, the ultimate tensile strength (UTS) of weld fusion zones of P92 steel weldments were measured to be 958 ± 35 and 1359 ± 38 using E911 and P92 filler, respectively. The % elongations of the weld fusion zone were measured 20 and 25 % for E911 and P92 filler, respectively. In P92 filer, higher strength of weld was attributed to the higher weight percentage of carbon in solution matrix as compared to E911 filler. The higher weight percentages of W and Mo in P92 weld fusion zone also lead to higher strength of P92 filler weld as compared to E911 filler weld.

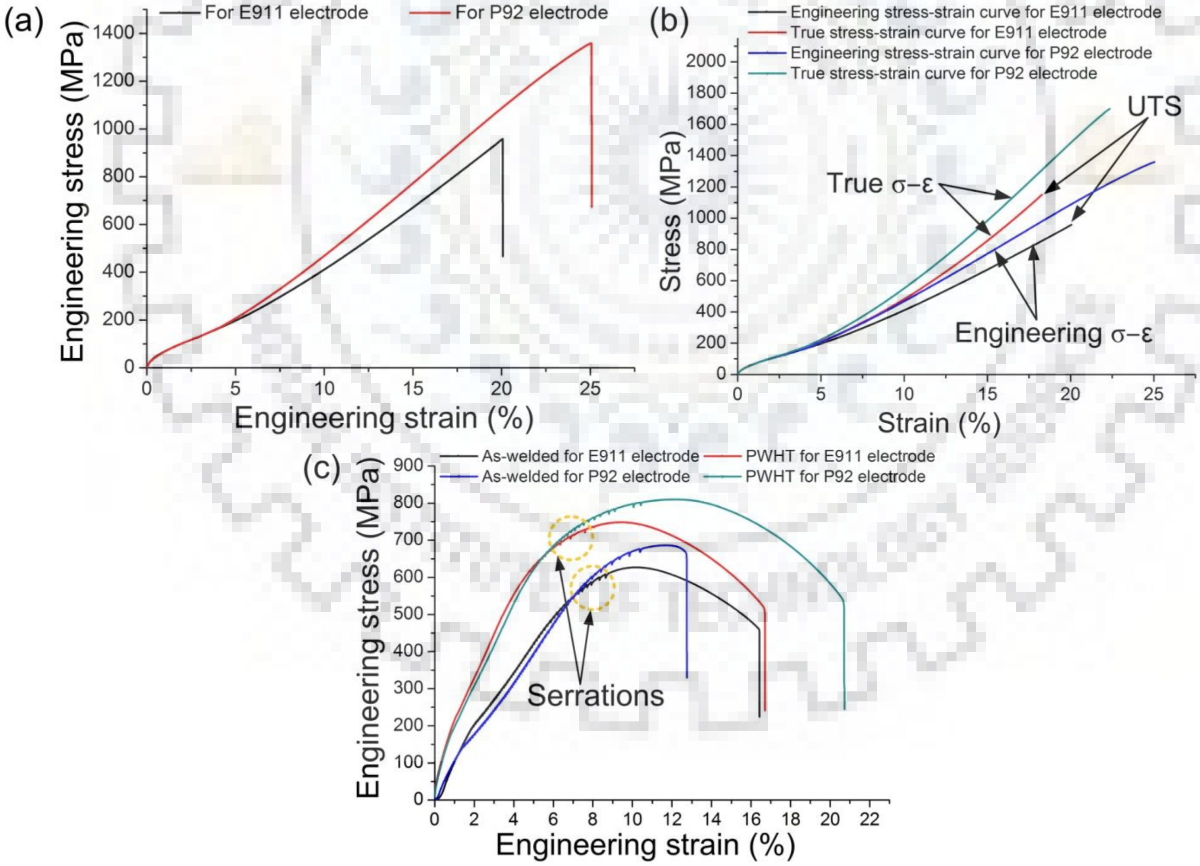

Figure 4.31 (a) Longitudinal engineering stress-strain curve for different fillers, (b) true and engineering stress-strain curve in longitudinal samples with different fillers and (c) transverse engineering stress-strain curve for different fillers and post weld conditions

The higher weight percentage of C, Mo and W in weld fusion zone of P92 filler results in higher solid solution hardening that leads to higher strength. Engineering stress-strain curve for transverse tensile tested specimens welded with E911 and P92 fillers is shown in Fig. 4.31(c). In transverse tensile tested specimens, serrations were also observed in as-welded and PWHT conditions for both the fillers. At low strain rate, serrations are characterized as repeated appearance of discontinuities in the stress-strain curve of deforming alloy. The engineering stress-strain curves were shifted towards the higher side for P92 steel filler weld specimens. After PWHT, engineering stress-strain curves were also shifted towards the higher side for both filler weld specimens, as shown in Fig. 4.31(c).

The UTS variation of P92 steel weldments for different filler and post weld conditions is given in Fig. 4.32(a). In as-welded condition, the UTS were measured to be 644 ± 24 and 674 ± 18 MPa for E911 and P92 filler, respectively. The value of UTS for transverse welded joints was closer to the value of as-received material UTS. In transverse tensile tested specimen, fracture was also occurred in softest FGHAZ and ICHAZ zone. The higher strength of weld for both E911 and P92 filler, results in fracture form softest zone. After PWHT, UTS were measured 760 ± 16 and 786 ± 25 MPa for E911 and P92 filler, respectively which is much higher than the as-received P92 steel UTS.

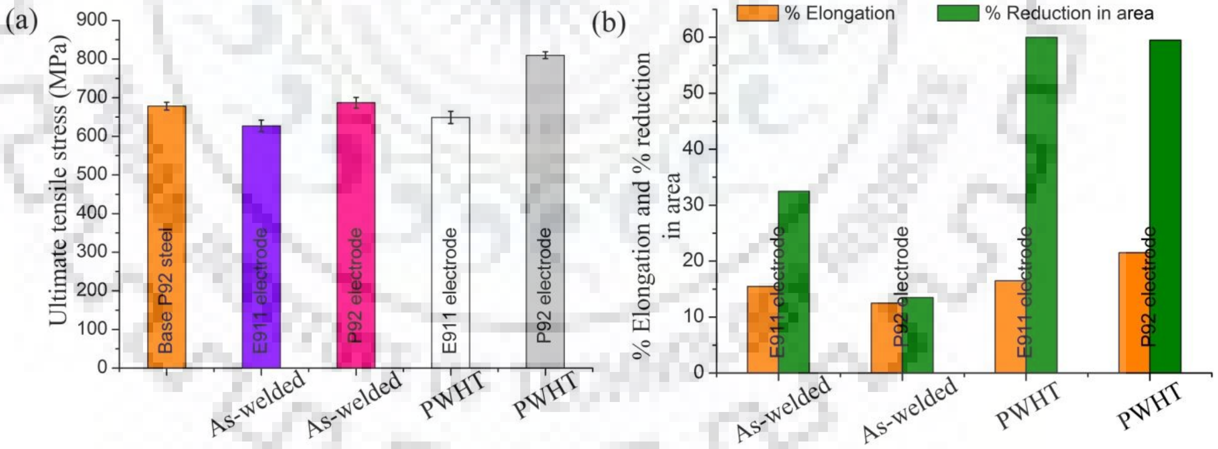

Figure 4.32 For different fillers and post weld conditions: (a) ultimate tensile strength and (b) % elongation and % reduction in area

The increase in strength might be due to precipitation of $M_{23}C_6$ and MX precipitates that leads to precipitation hardening. In as-welded condition, % elongation for transverse welded joints using E911 and P92 fillers were measured 16 ± 3 and 12.5 ± 2.5 %, respectively. The welded specimens have much lowered value of % elongation as compared to as-received P92 steel (23 ± 2 %).

The low value of % elongation in as-welded condition is attributed to formation of untempered lath martensite in weld fusion zone. After PWHT, the % elongation remains same for E911 filler welds, but it was observed to be increased for P92 filler, i.e. from 12.5 ± 2.5 % to 21 ± 4 %. In as-welded state, the % reduction in area was observed to be much high in case of E911 filler welds as compared to P92 filler welds, as shown in Fig. 4.32(b). The % reduction in area was found to be increased after PWHT for both the filler, as shown in Fig. 4.32(b).

Fig. 4.33(a–b) represents the final fracture zones of the longitudinal tensile tested specimen for E911 and P92 fillers, respectively. The fracture surface was characterized with the quasi-cleavage facets and ductile dimples for specimens welded with E911 filler and P92, as shown in Fig. 4.33(a-b). However, In P92 filler percentage area of cleavage facets was observed to be much higher than E911 filler. In case of P92 filler, fewer amount of ductile dimples were observed besides the area of cleavage facets.

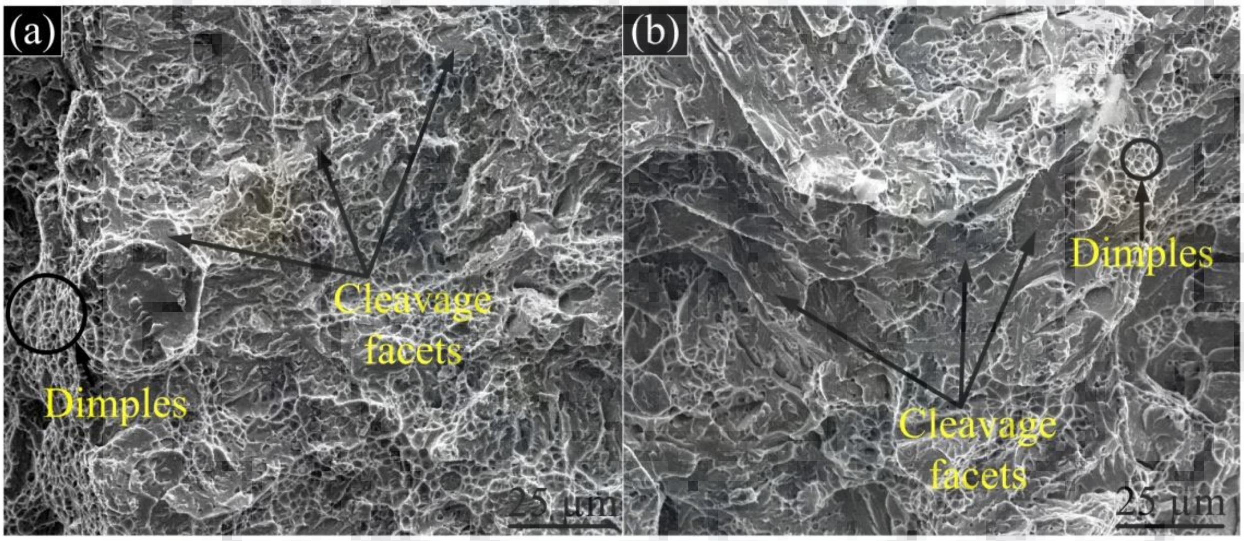

Figure 4.33 Fracture surface morphology of longitudinal tensile specimen (a) using E911 filler (b) using P92 filler

In as-welded condition, the crack initiation zone and final fracture zone of across the weld tensile tested specimens for P92 filler were represented in Fig. 4.34(a) and (c), respectively. The detailed view of final fracture zone was characterized by mixed mode of the fracture. Both ductile dimples and cleavage facets are observed at the fracture surface, as shown in Fig. 4.34(a). However, the area of cleavage facets is observed to be higher than ductile dimples. Microvoid coalescence is the mechanism of ductile transgranular fracture and cleavage is the mechanism of brittle transgranular fracture which occurs through cleaving of the crystals along crystallographic planes (Chandan Pandey et al., 2017c).

The top view of fracture surface for as-welded P92 steel using P92 filler in across the weld direction after the tensile test is shown in Fig. 4.34(b). It represents the presence of secondary cracks in the crack initiation zone and river like pattern in the final fracture zone. The river like pattern is formed when the cleavage fracture is forced to re-initiate at the boundary of a grain in a different orientation. The detailed view of crack initiation zone was characterized by the quasi-cleavage facets and ductile tear ridges, as shown in Fig 4.34(c).

In as-welded condition, the top view of fracture surface for E911 filler after the static tensile test is represented in Fig. 4.34(d). The primary and secondary cracks appeared in the top view fracture surface. The detailed view of final fracture zone was characterized by the by the ductile tear ridges, quasi-cleavage facets and transgranular ductile dimples as shown in Fig. 4.34(e). The percentage area of ductile dimples for E911 filler was higher than the fracture surface for the P92 filler.

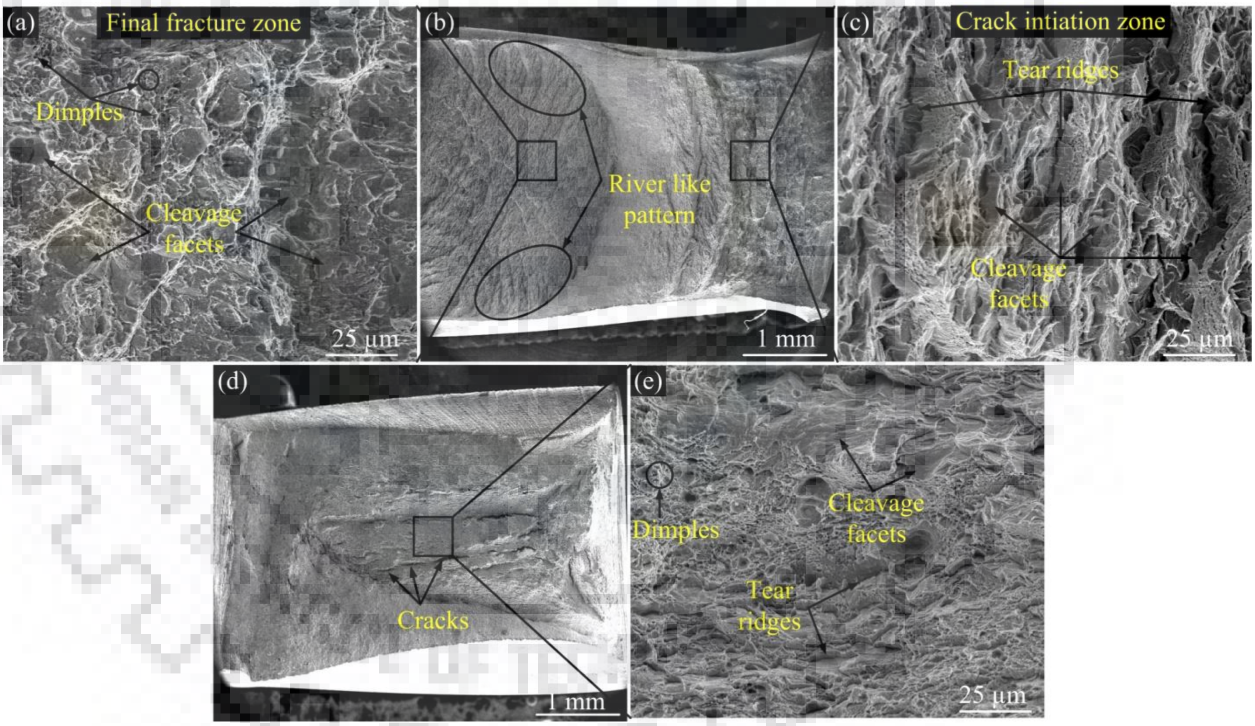

Figure 4.34 Fracture surface appearance across the welded specimen in as-welded condition (a), (b) & (c) using P92 filler and (d) & (e) using E911 filler

After the PWHT, the top view of fracture surfaces for welded using E911 and P92 filler was shown in Fig. 4.35(a) and (c), respectively. After PWHT, the numbers of primary and secondary cracks were decreased as shown in Fig. 4.35(a). The detailed view of final fracture zone for E911 filler was characterized by mainly ductile dimples and quasi-cleavage facets as shown in Fig. 4.35(b).

The percentage area of ductile dimples was enhanced after PWHT for E911 filler. After PWHT, the river like pattern and number of cracks were decreased as compared to as-welded condition for the P92 filler as shown in Fig. 4.35(c). The width of tear ridges and percentage area of cleavage facets were decreased after PWHT in the final fracture zone for the P92 filler as shown in Fig. 4.36(d). After PWHT, the percentage area of ductile dimples was also increased for the P92 filler.

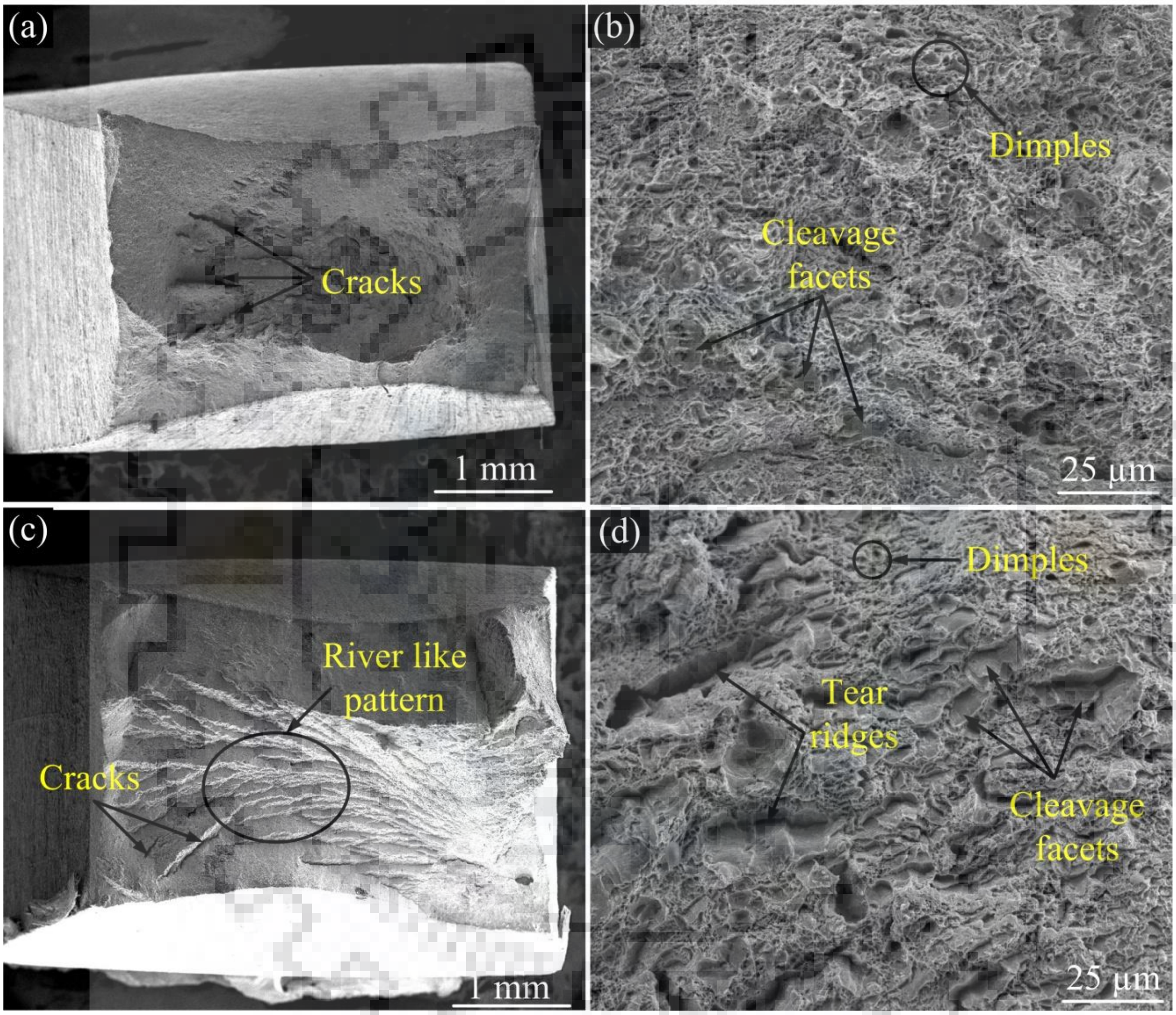

Figure 4.35 Fracture surface appearance across the welded specimen after PWHT (a) & (b) using E911 filler and (c) & (d) using P92 filler

4.2.4.4 Effect of fillers on harness and Charpy toughness of welded joints

The hardness of P92 steel weldments depends on the presence of C and N in the solid solution matrix, precipitates density, presence of fine precipitates of MX (M: V, Nb; X: C, N) and grain size (Chandan Pandey et al., 2017a; Pandey and Mahapatra, 2016b). The variation in hardness for different filler and post weld conditions of P92 steel welds is shown in Fig. 4.36.

In as-welded condition, the average hardness of weld fusion zone was measured to be 451 ± 20 and 571 ± 24 HV for E911 and P92 fillers, respectively. The higher weight percentage of C in weld fusion zone of P92 filler leads to solid solution hardening that result in higher average hardness in P92 weld fusion zone for P92 filler as compared to E911 filler. The hardness was observed to be decreased as move away from the weld fusion zone. The minimum hardness was measured in soft ICHAZ zone.

The ICHAZ hardness was measured to be 214 HV and 220 HV for E911 and P92 filler, respectively. After PWHT, the average hardness of weld fusion zone was measured to be 224 ± 7 and 252 ± 8 HV for E911 and P92 fillers, respectively. The lowering in hardness of P92 weldments after the PWHT is attributed to the tempering of martensite and evolution of new fine MX and coarse $M_{23}C_6$ precipitates. However, PWHT did not affect so much to the hardness value of ICHAZ and the minimum hardness was still measured in soft ICHAZ zone. After the PWHT, the hardness of soft ICHAZ zone was measured to be 196 HV and 180 HV for P92 and E911 filler, respectively.

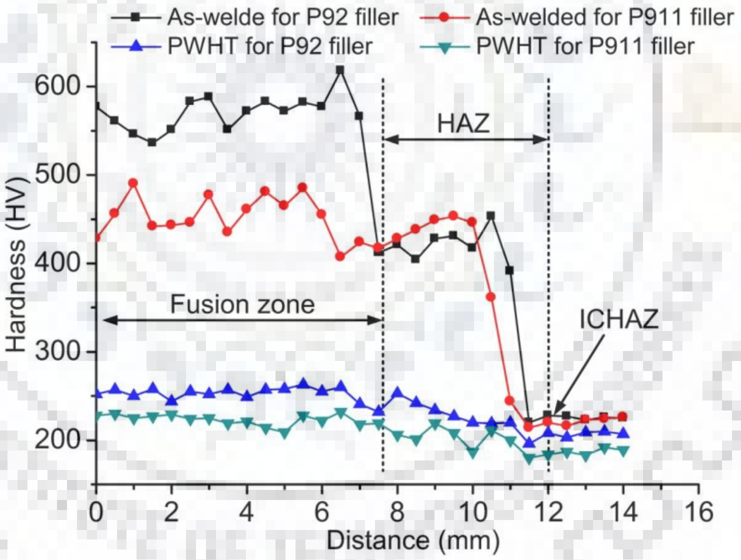

Figure 4.36 Hardness variation for different filler and post weld conditions from center of the weld fusion zone to the base material

To evaluate the HAZ impact toughness of P92 weldments notches were created in the samples. It was difficult to make notches exactly in the CGHAZ and ICHAZ because of small width of zones. Notches were prepared adjacent to weld fusion zone boundaries. Variation in Charpy toughness of weld fusion zone with respect to different filler and post weld conditions is depicted in Fig. 4.37(a).

Three specimens were used to estimate the average impact energy of weld fusion zone. It was observed that, the welds with P92 filler exhibited the poor Charpy toughness in weld fusion zone as compared to E911 filler welds. In as-welded condition, poor Charpy toughness is attributed to untempered lath martensite. P92 steel welds require a minimum of 47 J during the hydro testing of vessels as per the EN1557: 1997 specification. In P92 filler weld fusion zone, higher V and Nb content (V-0.23 % and Nb-0.06 %) than E911 filler weld fusion zone (V-0.08 % and Nb-0.05 %).

In P92 filler, higher content of V and Nb in weld fusion zone is the responsible for the poor Charpy toughness value of weld fusion zone (Arivazhagan and Vasudevan, 2014). The other facts that affects the Charpy toughness value is the higher weight percentage of C in P92 filler weld fusion zone that leads to formation of brittle untempered martensite. In as-welded condition, the Charpy toughness of weld fusion zone for both P912 and E911 filler does not meet the minimum required Charpy toughness value of 47 Joules. After the PWHT, the Charpy toughness of weld fusion zone was measured to be 66 ± 5 and 80 ± 6 Joules for E911 and P92 filler, as shown in Fig. 4.37(a).

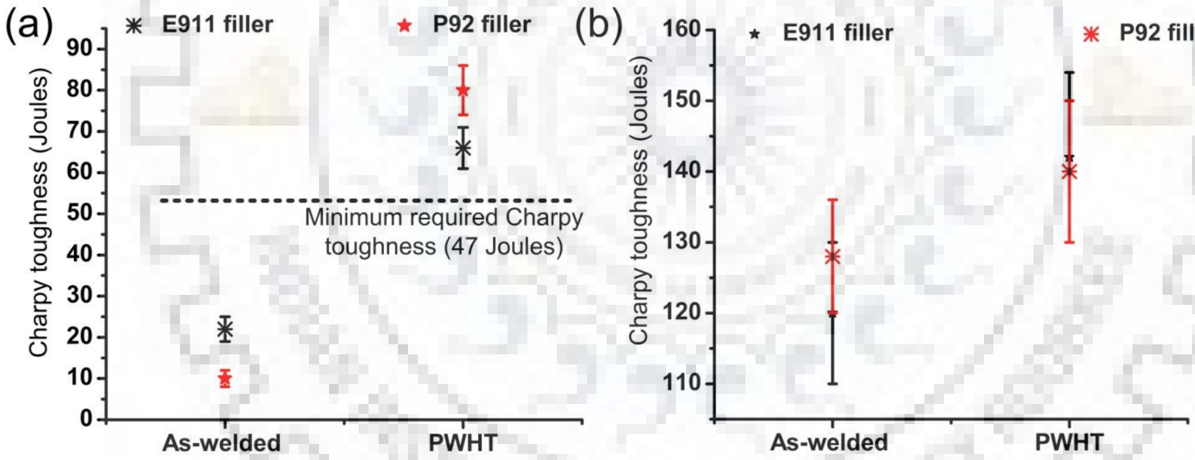

Figure 4.37 Charpy toughness of (a) weld fusion zone (b) HAZ for different filler in as-welded and PWHT condition

After PWHT, welds with both fillers have attained the minimum required Charpy toughness value (47 J, as per EN 1599) to reduce the chances of brittle fracture in weld fusion zone. Although both filler welds in weld fusion zone attained the minimum required Charpy toughness value but still both welds showed the poor Charpy toughness as compared to base metal (198 ± 8 Joules). In as-welded condition, the HAZ Charpy toughness of P92 steel welds was measured to be 120 ± 7 and 128 ± 8 J for E911 and P92 fillers, respectively. After PWHT, HAZ Charpy toughness of P92 steel welds was measured to be 142 ± 8 and 140 ± 5 Joules for

E911 and P92 filler, as shown in Fig. 4.37(b). Hence, PWHT have observed a minute effect on the Charpy toughness of HAZ for both E911 and P92 filler.

4.3 Conclusions

- The depth of penetration was maximum with a preheat temperature of 300 ^{o}C. A relation was successfully developed which can predict a preheat temperature for a given plate thickness of thin plates (maximum of 7.5 mm).
- In the as-welded condition, the presence of δ-ferrite was confirmed. After PWHT, no effect on δ-ferrite was observed. After PWNT, the dissolution of δ-ferrite was confirmed.
- After PWNT, the hardness and Charpy toughness of the weld fusion zone was improved to similar to that of the as-received base metal while the tensile strength did not change significantly.
- A model is used to analyze the dissolution kinematics of δ-ferrite. The model predicts with sufficient accuracy that 27 min is required to hold the welded plates at 1050 ^{o}C to dissolve the δ-ferrite.
- The higher strength in P92 filler was attributed to the higher weight percentage of W and Mo in P92 weld fusion zone as compared to E911 filler welds. In as-welded condition, transverse tensile specimens were fractured from fine grain heat affected zone or inter-critical heat affected zone (FGHAZ/ICHAZ) but after PWHT, the fracture location was shifted to over tempered base metal from FGHAZ/ICHAZ.

CHAPTER 5. DISSIMILAR WELDED JOINTS OF P92 STEEL

This chapter deals with effect of post-weld heat treatments on the microstructure evolution and mechanical properties of dissimilar welded joints of P911 and P92 steel have been studied. The effect of filler compositions on the microstructure evolution and mechanical properties of dissimilar welded joints of P91 and P92 steel have also been studied.

5.1 Experimental procedure

5.1.1 *As-received material*

The plates of the as-received P91, P911 and P92 steel were in normalized and tempered condition with dimension of 300 mm × 120 mm × 12 mm. The normalized temperature was 1040 ^{o}C for 1 hr and tempering temperature was 760^{o}C for 2 hrs. The chemical composition of as-received P92 steel, P92 filler and P911 filler composition were given in Table 4.1 (Chapter 4). The chemical composition of as-received P91, P911 steel, P91 filler, P91 filler weld and P92 filler weld are given in Table 5.1.

Table 5.1 Chemical compositions of base metals, fillers and weld joints

Element	Chemical composition (wt. %)											
	C	Cr	Mo	W	Nb	V	Mn	Si	N	Ni	Cu	Fe
P911 steel	0.3	9.5	1.03	1.01	0.04	0.12	0.54	0.26	0.05	0.57	0.08	balance
P91 steel	0.07	9.4	1.0	-	0.05	0.18	0.38	0.49	0.04	0.13	0.05	balance
P91 filler	0.11	9.5	1.0	-	0.05	-	0.80	0.25	0.05	0.56	-	balance
P91 filler weld	0.10	0.5	0.95	-	0.05	0.15	0.50	0.30	0.05	0.55	0.03	balance
P92 filler weld	0.11	0.6	0.55	1.84	0.07	0.23	0.60	0.32	0.05	0.61	0.04	balance

The mechanical properties of the P911, P91 and P92 steels in N&T condition are depicted in Table 5.2.

Table 5.2 Mechanical properties of the P91 and P92 steel in N&T condition

Material	Yield strength (MPa)	Tensile strength (MPa)	Elongation (%)	Hardness (VHN)
P911	620±7	840±12	19.8±3	245±5
P91 steel	530±8	760±10	20 ± 3	247± 5
P92 steel	520±11	678 ± 8	23 ± 4	227 ± 7

5.1.2 *Effect of post-weld heat treatments on the microstructure evolution and mechanical properties of dissimilar SMAW welded joints of P911 and P92 steel using P911 filler*

Two plates of P911 and P92 steel of size 150 x 50 x 12 mm were machined from N&T plates, as shown in Fig. 5.1(a). A conventional V-groove is prepared for the weld joint as shown in Fig. 5.1(b). The groove angle and root height were 37.5^0 and 1.5 mm, respectively. A 4 mm diameter flux-coated P911consumable electrode rod was used to prepare the dissimilar P911 and P92 weld joint by manual metal arc welding (MMA) procedure. The working voltage and current were 22-25 V and 140 amp, respectively. Before welding, the preheating of N&T plates was performed at 300 ^{o}C. The deposition was performed with weld bead overlap of around 50% and a preheat/inter-pass temperature was maintained between 200-300 °C. The complete weld joint is shown in Fig. 5.1(c). After welding, the welded plates were subjected to following heat treatments; after welding, the first plate is allowed to cool in the air up to room temperature. The second plate was subjected to post weld heating at 250 ^{o}C for 40 min and then air cooling up to 100 ^{o}C and after that subjected to post-weld heat treatment (PWHT) at 760 ^{o}C for 2 h. After welding, the third plate is allowed to cool in the air up to room temperature and then subjected to normalize/tempering (N&T) treatment (normalized-1040 ^{o}C/1 h and tempered-760 ^{o}C/2 h).

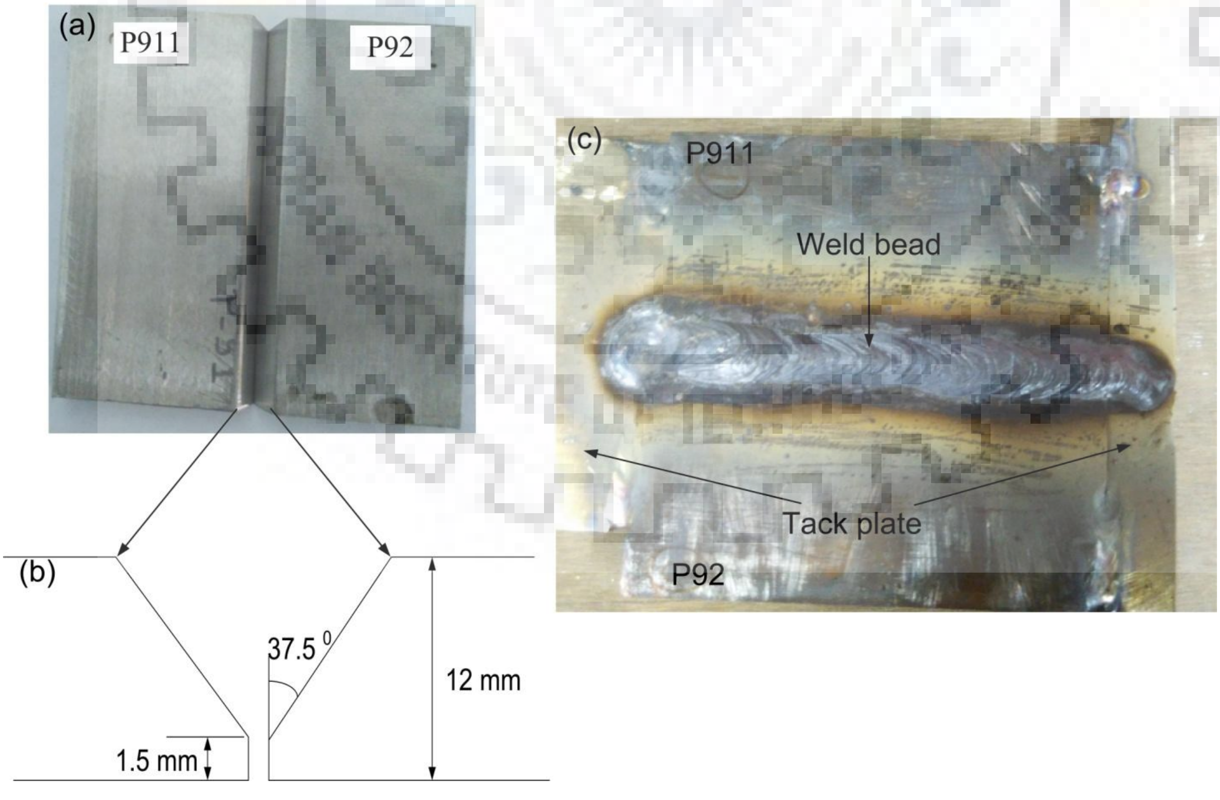

Figure 5.1 (a) Plates before welding, (b) weld groove design, (c) plate after completion of welding

The temperature in heat affected zones (HAZs) lies in the range of just above Ac_1 to melting temperature (T_m) of P911 and P92 steel, during the weld thermal cycle and just after the welding cools down to room temperature within few minutes. The sub-layers exists within the P911 and P92 weldment are divided into weld fusion zone, coarse grained heat affected zone (CGHAZ), inter-critical heat-affect zone (ICHAZ), and fine-grained heat affected zone (FGHAZ) (Y. Wang et al., 2016a). A schematic of peak temperature experienced by the HAZs and their typical microstructure for as-welded P911 and P92 weldment is shown in Fig. 5.2.

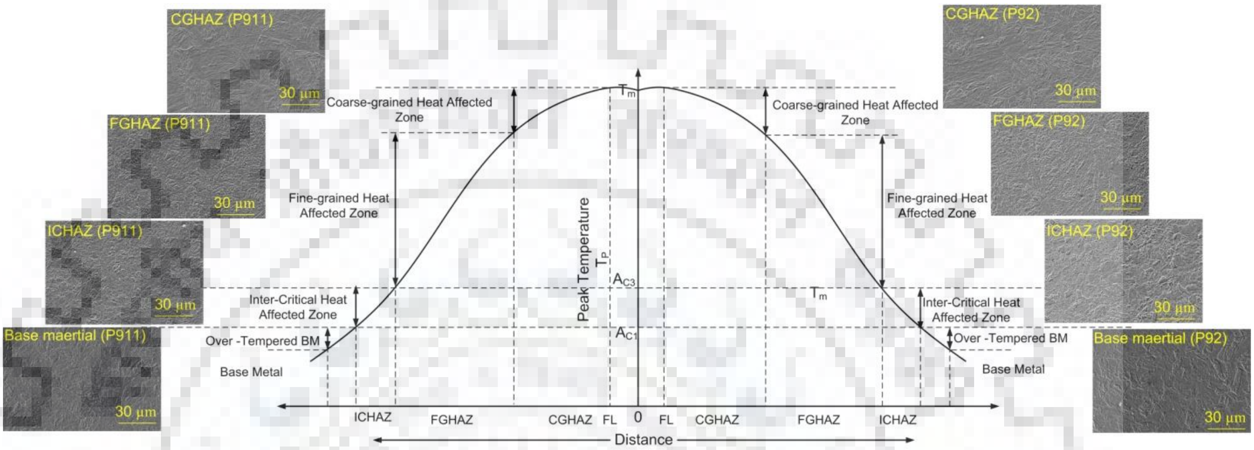

Figure 5.2 A schematic of peak temperature profile and their typical microstructure in the HAZs of as-welded P911 and P92 weldment

5.1.3 *Effect of filler compositions on mechanical properties of dissimilar SMAW welded joints of P91 and P92 steel*

For making dissimilar multi-pass welds joint, the plates were machined from as received materials with dimensions of 200 mm × 60 mm × 12 mm. A conventional V-groove was designed as shown in Fig. 5.3(a). Before the welding, the plates are subjected to the preheating at a temperature of 250 ^{o}C (Jandová et al., 2010; Nisho et al., 1971). The flux coated 4 mm diameter welding consumables with low hydrogen content were used to make the welded joint. The consumables are designated as AWS ER90S-B9 (9Cr–Mo–V–N) for P91 steel and MAILARC–P92 (9Cr–Mo–1.8W–V–N) for P92 steel. The low alloy and high tensile strength MAILARC–P92 consumables were procured from Mailam India Ltd., India. Prior to welding, the fillers were backed in the range of 280-300 ^{o}C for 2 h to remove the moisture content. Two dissimilar welds joint of P91 and P92 steel were welded with different fillers using shielded metal arc welding (SMAW) process. The four different abbreviations were used for various dissimilar P91 and P92 weld joints such as AW–P91 (as-welded condition and P91 filler), AW–P92 (as-welded condition and P92 filler), PWHT–P91 (PWHT condition and P91 filler) and PWHT–P92 (PWHT condition and P92 filler). The sequence of welding passes and complete welded joint with tensile and toughness sample locations are shown in Fig. 5.3(b) and 5.3(c), respectively. The parameters used for the gas tungsten arc welded different passes are tabulated in Table 5.3.

Table 5.3 Process parameters of welding

Passes	Process	Arc voltage (V)	Welding current (amp)	Travel speed (mm/min)
Root pass	GTAW	14– 15	115–120	130
Filler pass 1-9	SMAW	22– 25	140	140 – 150

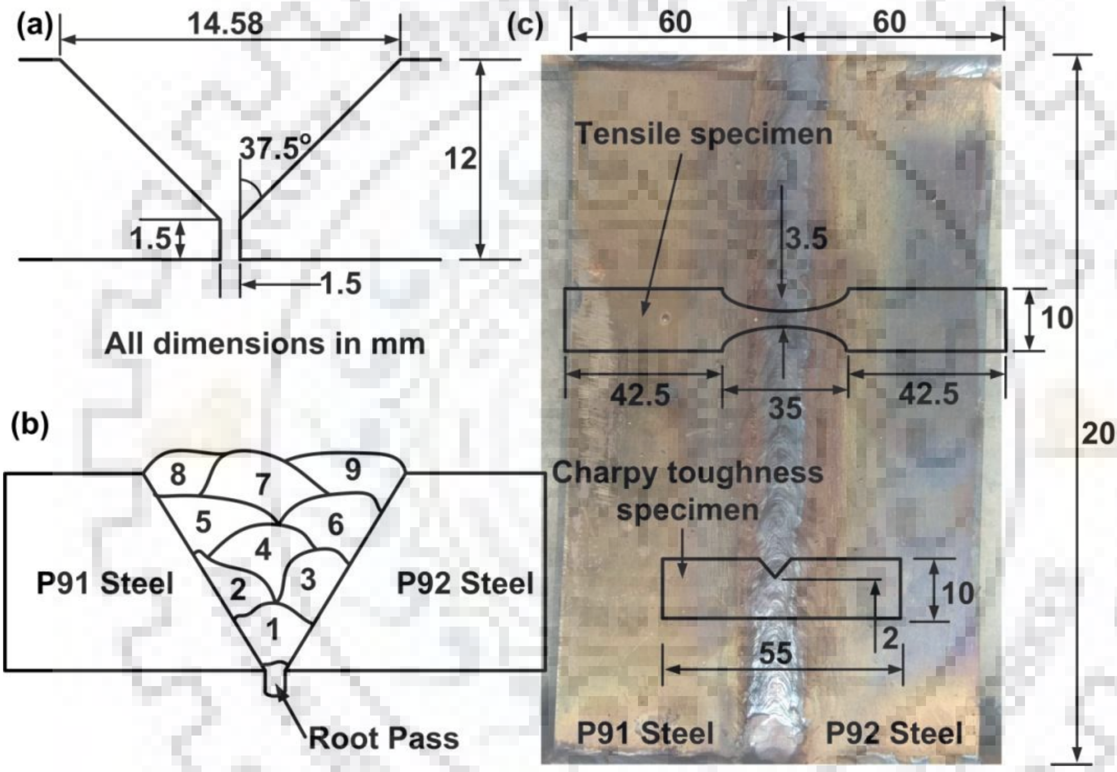

Figure 5.3 (a) Groove design, (b) sequence of welding passes and (c) complete welded joint with tensile and Charpy toughness sample locations.

5.1.4 *Material characterization and testing*

For microstructural characterization, all dissimilar welded joints were sectioned normal to the welding direction. The specimens were mounted, grounded, polished with SiC sand-papers (Grit 120, 300, 600 and 1200) and cloth polished Standard metallographic techniques. Futher, the welded specimens were etched using Vilella’s reagent for 85-90 s. Optical microscope (OM) and Field-emission scanning electron microscope (FESEM) was utilized for microstructural characterization. The operating parameters of FESEM were 8 mm working distance, 30 μm objective aperture and 20 kV accelerated voltage. To compare the effect of

N&T heat treatment and subsequent PWHT on tensile properties of weld fusion zone of P911 and P92 steels, standard flat sub-size specimens were prepared according to ASTM E8 (ASTM: E8/E8M, 2009) with gauge length and width of 30 mm and 6 mm, respectively. The tensile specimens were prepared in the transverse direction. The room temperature tensile tests were performed on Vertical Tensile Testing Machine (Instron 5982) with a constant strain rate of 5.56×10^{-4}/s. To study the various phase formed in weld fusion zone of P911 and P92 steel in different condition, X-ray diffraction (XRD) was conducted on D-8 Bruker AXS diffractometer. As per ASTM A370, standard sub-size V-notch specimens were machined with dimensions of 55 mm × 10 mm × 7.5 mm to determine the weld fusion zone Charpy impact toughness. The microhardness measurement of all-welded specimens was carried with Vickers hardness tester at the load of 0.5 kgf and dwell time of 10 s. The room temperature tensile test was performed on vertical tensile testing machine (Instron-5982) with crosshead speed of 1mm/min. The room temperature Charpy toughness test was performed for all specimens. The average of three tested specimens was reported in each case.

5.2 Results and discussion

5.2.1 *As-received material*

Fig. 5.4(a, b) shows the microstructure of ‘as-received’ P911 steel. The low magnification micrograph shows the prior austenite grain boundaries (PAGBs), lath blocks, packets, and packet boundaries. The lath blocks are observed to be oriented in spatial direction inside the lath packets of PAGBs. Fine V and Nb-rich precipitates and coarse Fe, Cr and Mo-rich $M_{23}C_6$ precipitates are shown in higher magnification micrograph. The higher magnification micrograph also shows the morphology and distribution of precipitates. Figure 5.4(b) confirms the higher density of $M_{23}C_6$ precipitates along the PAGBs. The EDS of P911 steel was taken for point-1 at PAGBs and area-1 in the matrix region as shown in Fig. 5.4(c-d), which shows higher weight percentage of Cr and Fe that confirms the presence of $M_{23}C_6$ type precipitates (Y. Wang et al., 2016a). These $M_{23}C_6$ precipitates obstructed the motion of dislocations which resulted in high strength of the material by impending along the boundaries (Abe, 2009).

The typical scanning electron micrograph of P91 steel in N&T condition is shown in Fig. 5.5(a). The microstructure was characterized with tempered lath martensitic microstructure, prior austenite grain boundaries (PAGBs), blocks, lath boundaries, packets, subgrains, and precipitates.

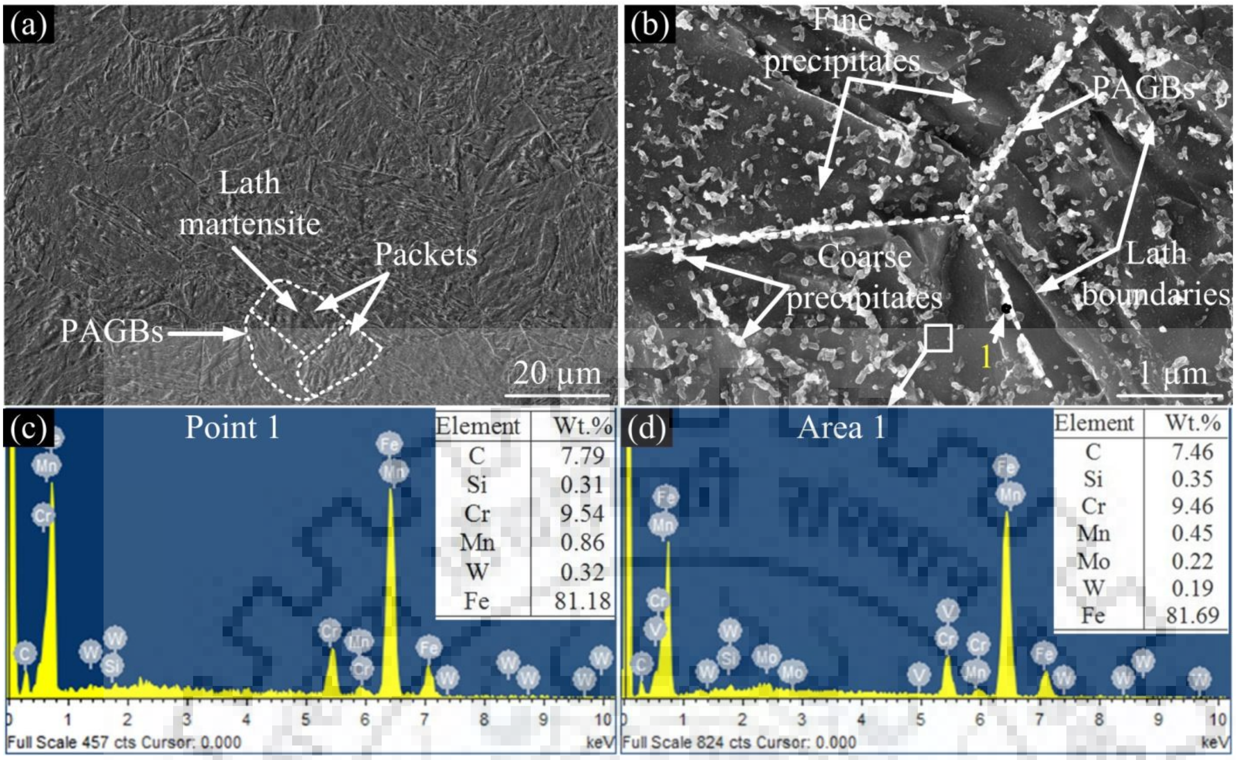

Element	Wt.%
C	7.79
Si	0.31
Cr	9.54
Mn	0.86
W	0.32
Fe	81.18

Element	Wt.%
C	7.46
Si	0.35
Cr	9.46
Mn	0.45
Mo	0.22
W	0.19
Fe	81.69

Figure 5.4 (a) & (b) Micrograph of as-received P911 steel and (c) EDS of precipitates present at PAGB as point-1 and (d) EDS of matrix region as area-1

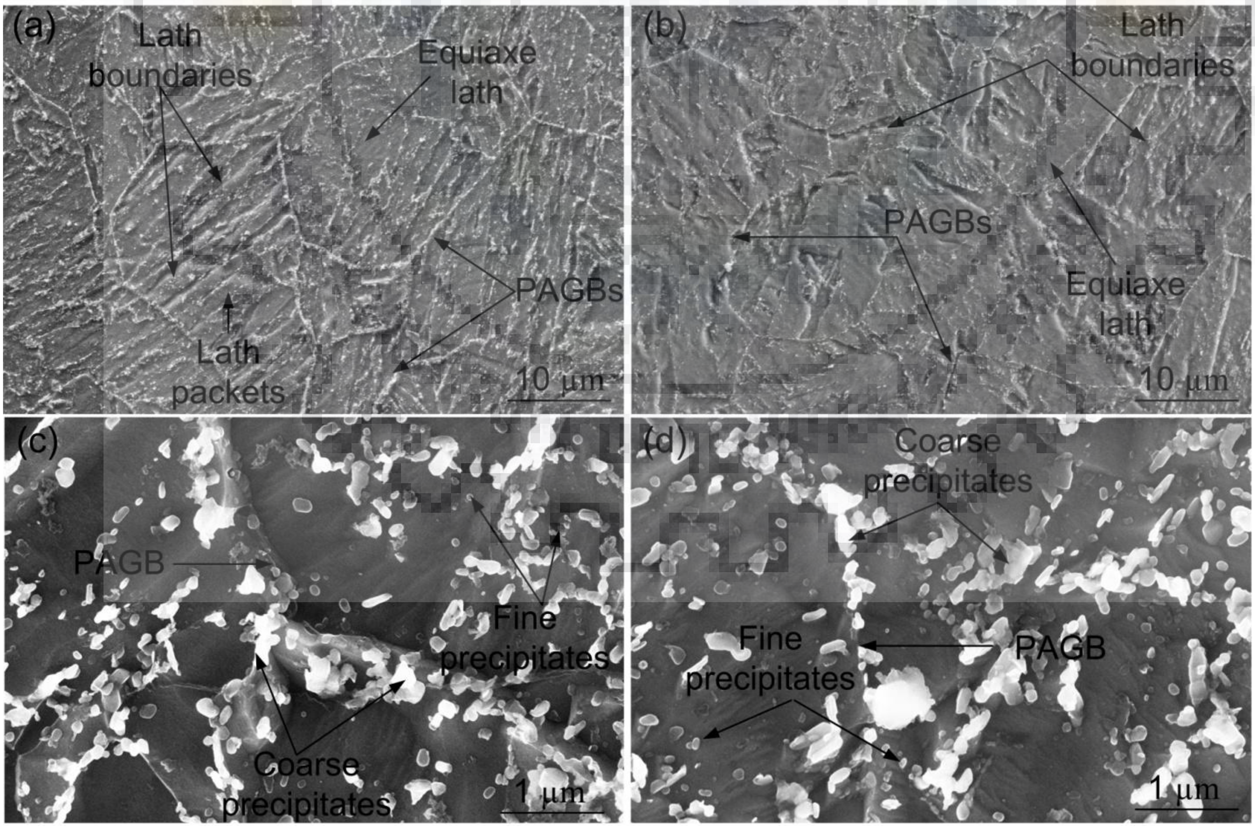

Figure 5.5 Secondary electron micrograph of N&T (a) & (c) P91 steel, (b) & (d) P92 steel

The micrograph of N&T P92 steel was characterized with tempered martensitic microstructure with a large number of coarse precipitates at the PAGBs and fine precipitates within matrix region or subgrain boundaries as shown in Fig. 5.5(b) and 5.5(d). The stability of tempered lath martensitic microstructure is governed by coarse $M_{23}C_{6,}$ fine MX precipitates and high dislocation density. The microstructure of P91 steel and P92 steel at higher magnification is used to show the distribution and shape morphology of precipitates along the grain boundaries and intra-lath region region. $M_{23}C_6$ [M: Cr, Fe, Mn and Mo] type carbide precipitates and fine MX [M: Nb, V; X: C, N] type precipitates that beautify the PAGBs and grain interior region are shown in Fig. 5.5(c). The precipitates located along the boundaries were mainly needle shape while in intra-lath region fine spherical precipitates were observed. The large numbers of coarse precipitates were found along PAGBs and fine precipitates within subgrain boundaries or matrix region.

5.2.2 *Effect of post-weld heat treatments on the microstructure evolution and mechanical properties of dissimilar SMAW welded joints of P911 and P92 steel using P911 filler*

5.2.2.1 Microstructure evolution in the weldments

The weldments consist of over tempered base material, deposited weld metal and HAZs. The HAZ, which started next to weld fusion line, is divided into three sub-zones: CGHAZ, FGHAZ, and ICHAZ. The region adjacent to the fusion line is called CGHAZ or grain growth zone that experienced the temperature much above then the transformation temperature Ac_3. The approximate width of CGHAZ was 1 mm. In CGHAZ region, the dissolution of precipitates increased the solid solution strengthening because of the presence of C and N in solution which resulted in the formation of lath martensite with negligible grain boundary precipitation. Due to complete dissolutions of precipitates, the CGHAZ shows the high hardness and low toughness as compared to other HAZs (C. Pandey et al., 2017). The CGHAZ region for P911 and P92 steel side is shown in Fig. 5.6(a) and 5.6(b), respectively. In CGHAZ, at high temperature, the precipitates that obstruct the growth of austenite's dissolve completely.

This result in a reduced pinning force applied from the precipitates that help the austenite grains to grow faster. This resulted the formation of coarse austenite grains. After cooling, the CGHAZ was transformed to martensite and delta ferrite. The CGHAZ of P92 is characterized with clearer PAGBs and lath boundaries as compared to CGHAZ of P911. The weld fusion zone is shown in Fig. 5.6(c), characterized with martensitic lath packets and untempered lath martensitic microstructure. In weld fusion zone, the blocks having similar spatial orientation were formed inside the PAGBs. The weld fusion zone is more susceptible towards cracking due to the untempered lath martensitic microstructure. The untempered lath martensitic microstructure is characterized by poor toughness with high strength and hardness. In weld fusion zone, almost no precipitates are seen in as-welded condition and needle shape particles are observed at higher magnification.

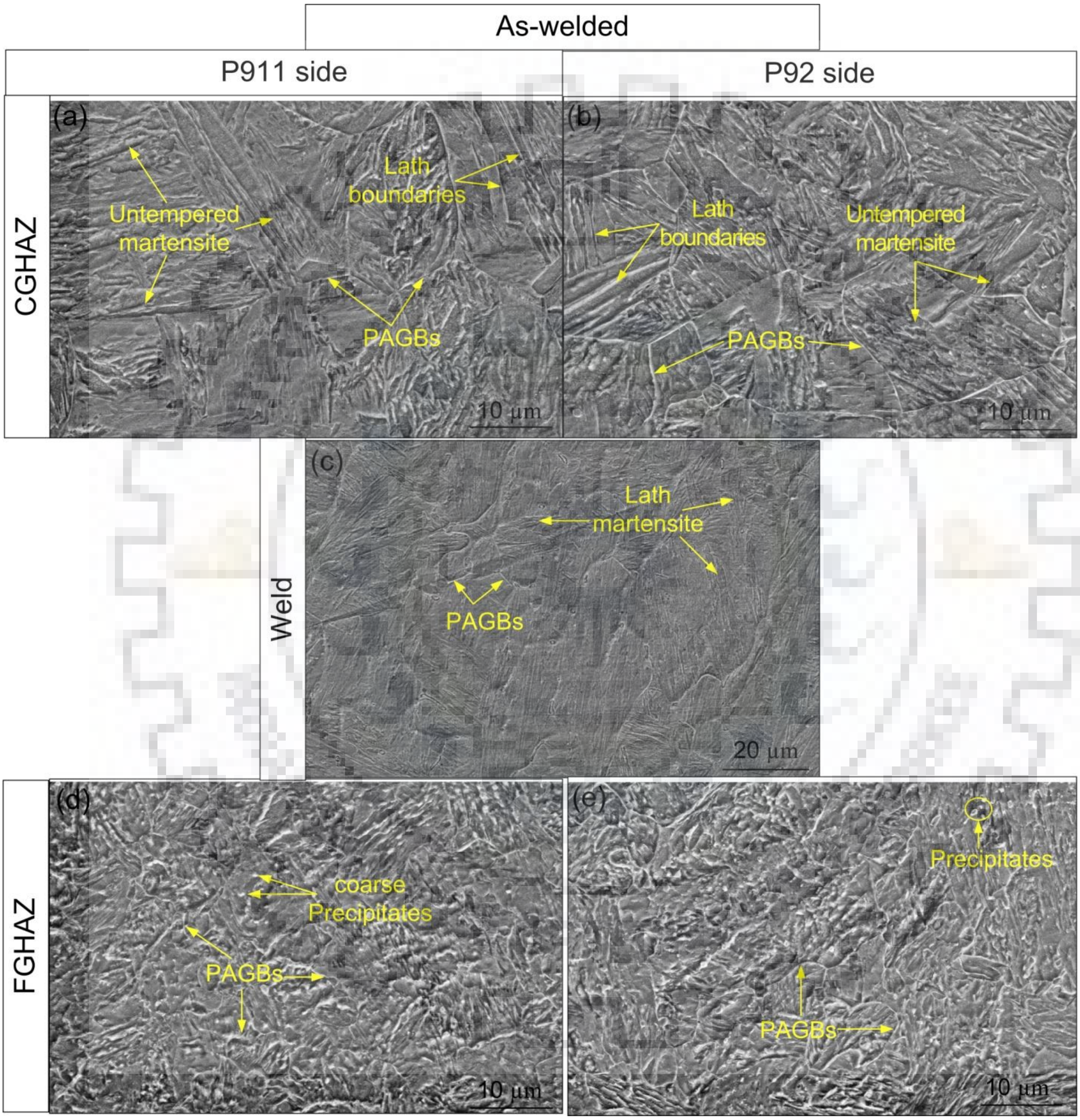

Figure 5.6 Micrograph of sub-zones of dissimilar weldments (a) CGHAZ of P911 (b) CGHAZ of P92 (c) weld fusion zone, (d) FGHAZ of P911, (e) FGHAZ of P92

The FGHAZ region was similar on both sides of weld fusion zone. The FGHAZ is characterized by fine austenite grain boundaries with undissolved precipitates as shown in Fig.

5.6(d) and 5.6(e) for P911 and P92 side, respectively. The lath martensite with a low length/width ratio was formed in FGHAZ, within the PAGBs. The precipitates were observed in the FGHAZ because the temperature is just above the transformation temperature A_{c3} which make difficult the complete dissolution of existing precipitates. These undissolved precipitates are helpful to limit the growth of austenite grains by pinning it. The presence of inhomogeneous microstructure in P911 and P92 weldment leads the variation in mechanical properties. In as-welded condition, the fine grains, coarse existing precipitates and fine newly developed precipitates are the main characteristic feature of FGHAZ. It is characterized by low hardness and moderate toughness. The FGHAZ is treated as weakest portion of weldments because the most common premature type IV cracking generally occurred in the FGHAZ during the long term service condition.

To temper the fresh untempered lath martensite and to reduce the quenching residual stress, the PWHT below the lower transformation temperature was performed (P. Biswas et al., 2011; Pankaj Biswas et al., 2011). The microstructure of weld fusion zone and HAZs (in order of decreasing peak temperature experienced during the welding thermal cycle) after the subsequent PWHT and N&T treatment is presented in Fig. 5.7(a-f). After PWHT, the grain coarsening, precipitates coarsening, recovery and dynamic recrystallization of lath martensite was observed. Fig. 5.7(a) represents the microstructure of the weld fusion zone after PWHT condition which is characterized with lath tempered martensite, lath boundaries, PAGBs, equiaxe laths and precipitates. Both fine and coarse precipitates are observed along the PAGBs and matrix region.

After N&T treatment, the columnar laths become disappear from the weld fusion zone and microstructure is characterized by tempered equiaxe lath martensite with $M_{23}C_6$ precipitates along the PAGBs, lath boundaries, packets, and laths, as shown in Fig. 5.7(b). For N&T treatment, PAGBs present in the weld fusion zone showed the coarse behaviour as compared to subsequent PWHT. In N&T treatment, after the normalizing, the weldments became homogenized. After N&T treatment, each zone present in the weldments can be treated as the virgin material. As the consequence of PWHT, the elements are re-precipitated which dissolve during the weld thermal cycle in the CGHAZ of P92, as shown in Fig. 5.7(c). After N&T treatment, the CGHAZ of P92 steel was found similar to the virgin materials and grains formed in CGHAZ are in elongated shape, as shown in Fig. 5.7(d). After PWHT condition, wide FGHAZ zone of the P92 steel is shown in Fig. 5.7(e).

In the case of PWHT, the FGHAZ of the P92 side is characterized by the fine PAGBs, coarse undissolved precipitates and fine re-precipitated phase. After PWHT, the highest degree of martensite recovery would be possible in FGHAZ because the fewer amounts of precipitates get dissolved during the welding thermal cycle as compared to CGHAZ. While after N&T treatment, the FGHAZ of the P92 side is characterized by coarse PAGBs and it looks similar to weld fusion zone and CGHAZ, as shown in Fig. 5.7(f). Hence, after the PWHT, the microstructure homogenization occurs across the weldments up to a large extent while in N&T condition, complete homogenization of microstructure was observed.

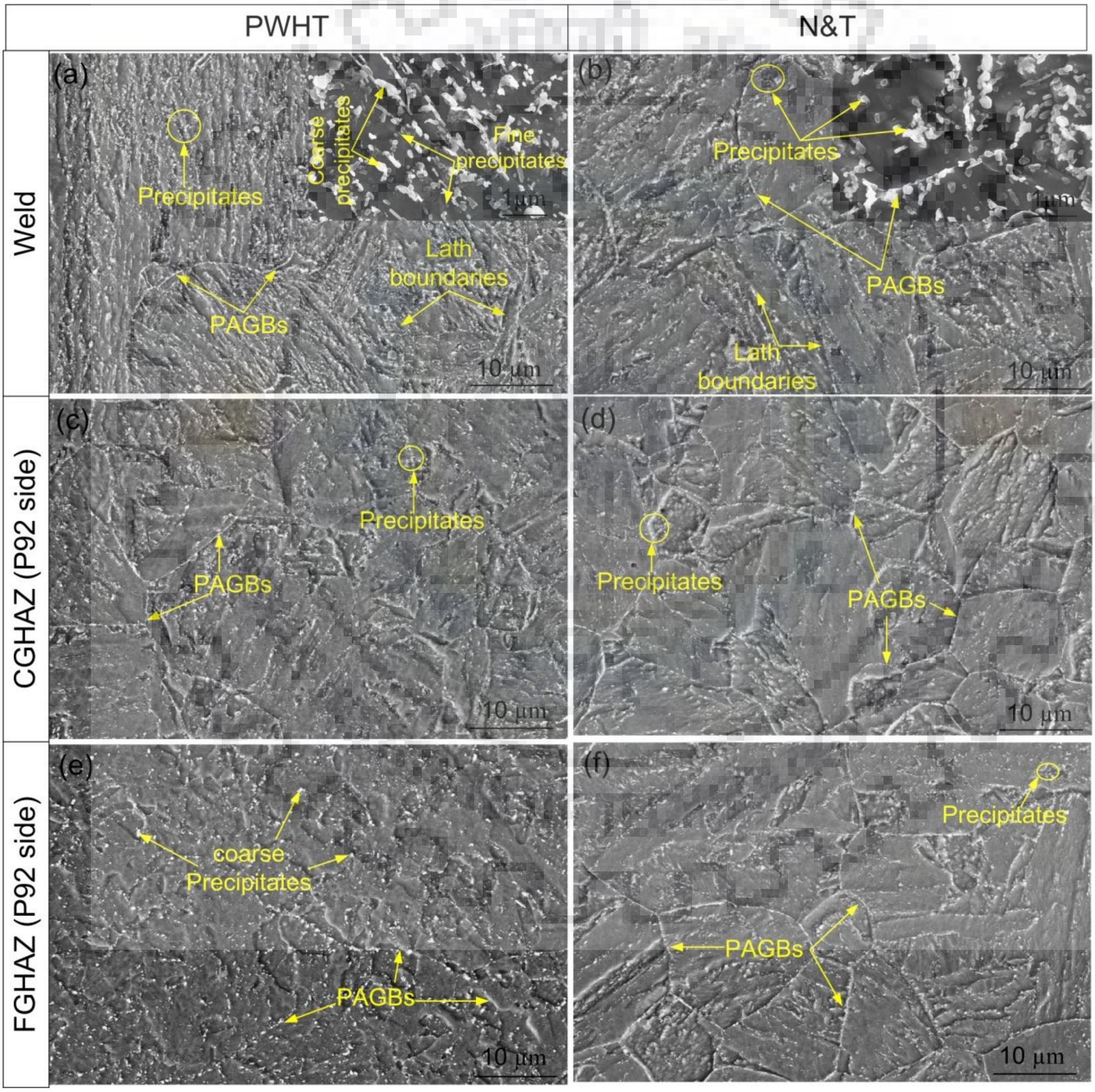

Figure 5.7 Micrograph of sub-zones of dissimilar weldments after PWHT and N&T treatment, respectively; (a), (b) weld fusion zone; (c), (d) CGHAZ; (e), (f) FGHAZ

After the PWHT, the CGHAZ of the P911 side is shown in Fig. 5.8(a). The CGHAZ of the P911 side is characterized with coarse PAGBs with precipitates along the boundaries. After N&T condition, the CGHAZ of both sides was found similar to the virgin steel (P911 and P92 steel, respectively), as shown in Fig. 5.8(b). As the result of PWHT, the FGHAZ of the P911 side is characterized with fine PAGBs, as shown in Fig. 5.8(c). In N&T condition, the FGHAZ of the P911 side is behaving like as-received P911 material and looks similar to CGHAZ, as shown in Fig. 5.8(d). Hence, N&T provide the complete homogenization of microstructure across the dis-similar weldments. The fraction area of precipitates observed in the sub-zones of weldments for N&T treatment was found to be less compared to subsequent PWHT.

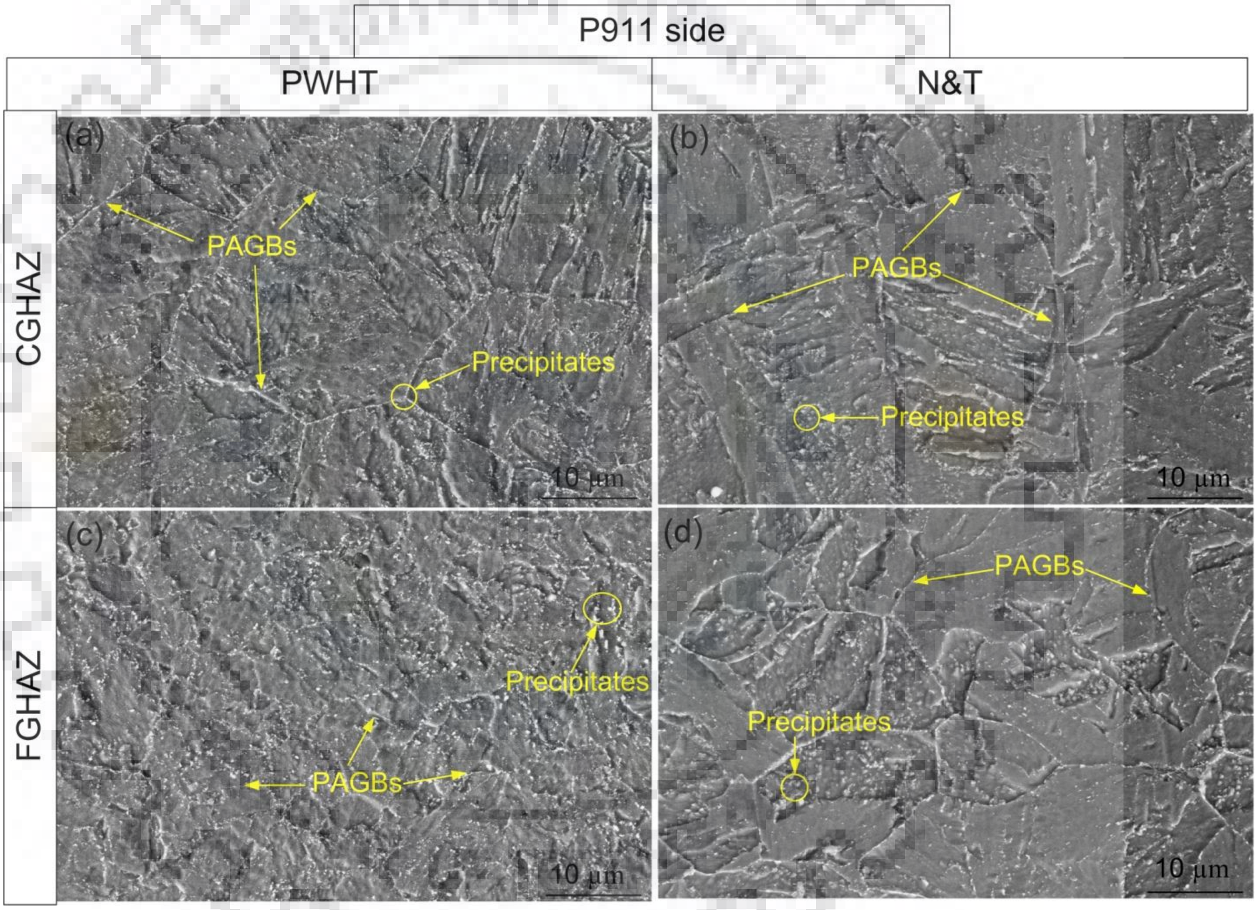

Figure 5.8 Microstructure of HAZs of dissimilar weldments on P911 side (a) CGHAZ after PWHT, (b) CGHAZ after N&T, (c) FGHAZ after PWHT, (d) FGHAZ after N&T

The diffractogram of dissimilar weld fusion zone in as-welded, PWHT and N&T condition is shown in Fig. 5.9. The phases identified in as-welded condition are Cr-rich $M_{23}C_6$, V-rich MX, Cr-rich M_7C_3, Cr and Fe-rich M_2X and W-rich M_7X_6 type. After the PWHT, the number of peaks was reduced, as shown in Fig. 5.9. After N&T condition, mainly M_7C_3,

$M_{23}C_6$, M_3C and W-rich M_7X_6 type phase was observed in weld fusion zone. The structure and lattice parameter of various phase formed in a different state are given in Table 5.4.

Table 5.4 XRD analysis report for the structure and lattice parameter of phases present in weld fusion zone in different conditions

S.No.	Phase identified	Structure	Lattice parameter (A^o) [a, b, c]	Weld fusion zone		
				As-welded	PWHT	N&T
1	$Cr_{23}C_6$	Cubic	10.66, 10.66, 10.66	✓	✓	✓
2	Cr_7C_3	Orthorhombic	7.015, 12.15, 4.53	✓	✓	✓
3	Cr_2N	Hexagonal	4.75, 4.75, 4.43	✓	–	–
4	NbN	Hexagonal	2.96, 2.96, 5.53	✓	–	–
5	VC	Cubic	4.165, 4.165, 4.165	✓	–	–
6	VN	Tetragonal	8.11, 8.11, 8.11	–	–	✓
7	Fe_3C	Orthorhombic	4.51, 5.04, 6.73	✓	✓	✓
8	Fe_2C	Hexagonal	2.75, 2.75, 4.35	✓	–	–
9	Fe_7W_6	Rhombohedral	4.76, 4.76, 25.91	✓	✓	✓

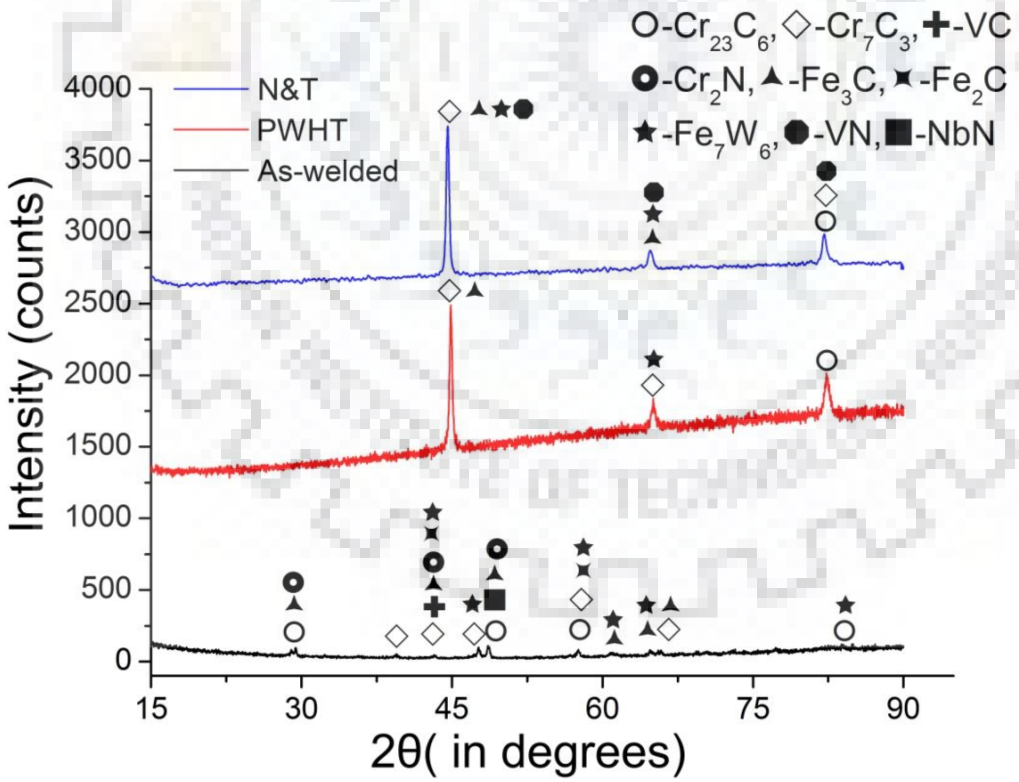

Figure 5.9 XRD peaks for weld fusion zone in different operating condition

5.2.2.2 Mechanical properties of weld fusion zone

The tensile fracture specimens in different heat treatment condition are shown in Fig. 5.10(a). The lower ultimate tensile strength (UTS) and yield strength (YS) in the over-tempered base metal zone may also be due to the presence of coarse grains resulting from the heat treatment. The variation in tensile properties of welded specimens in different heat treatment conditions is shown in Fig. 5.10(b). The UTS and YS were measured in the as-welded condition was to be 608±7 MPa and 420±5 MPa, respectively. In the as-welded condition, the higher volume fraction of untempered lath martensite being associated with these results. In each case, the fracture was observed in over-tempered base metal zone of P92 steel. After the PWHT, The UTS value was found to be increased about 0.33% and after the N&T, the UTS was found to be increased further about 2.72%.

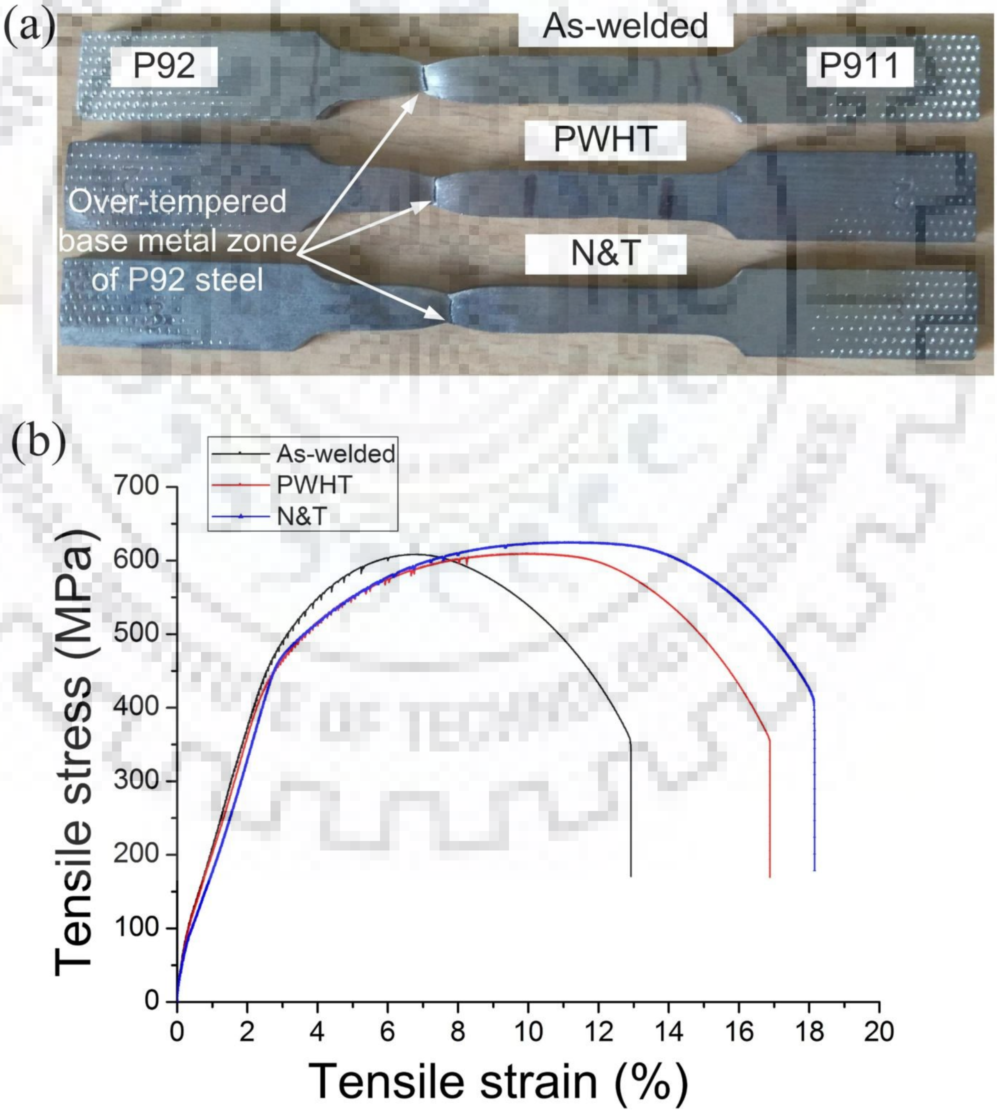

Figure 5.10 (a) Interrupted tensile specimens (b) engineering stress-strain curve

After N&T, a complete homogenization of the microstructure resulted a reduction in the volume fraction of lath martensite that lead to increase in the YS and UTS simultaneously. The variation of YS and UTS is shown in Fig. 5.11(a). The serrations are clearly observed in Fig. 5.10(b) because of low strain rate of 5.56 x 10^{-4}/s. In the low strain rate region, serrations is characterized as repeated appearance of discontinuities in the strain stress curve of deforming alloy and known as Portevin-Le Chatelier (PLC) effect. Serrations are mainly observed at high temperatures and low strain rates. However, sometimes serrated flow with few serrations was observed at room temperature and low strain rate (Qian et al., 2013) . At low strain rate, interaction between solutes atmosphere and dislocations may be dominant. It was presumed that the dislocations are aged by the solutes carbon from initial straining. When number of dislocation reach a critical moving velocity, they can break away from the carbon solutes atmosphere (Ozturk et al., 2011; Picu et al., 2006). This resulted a rapid mobile dislocations and hence the abrupt change in stress and finally lead to serrations.

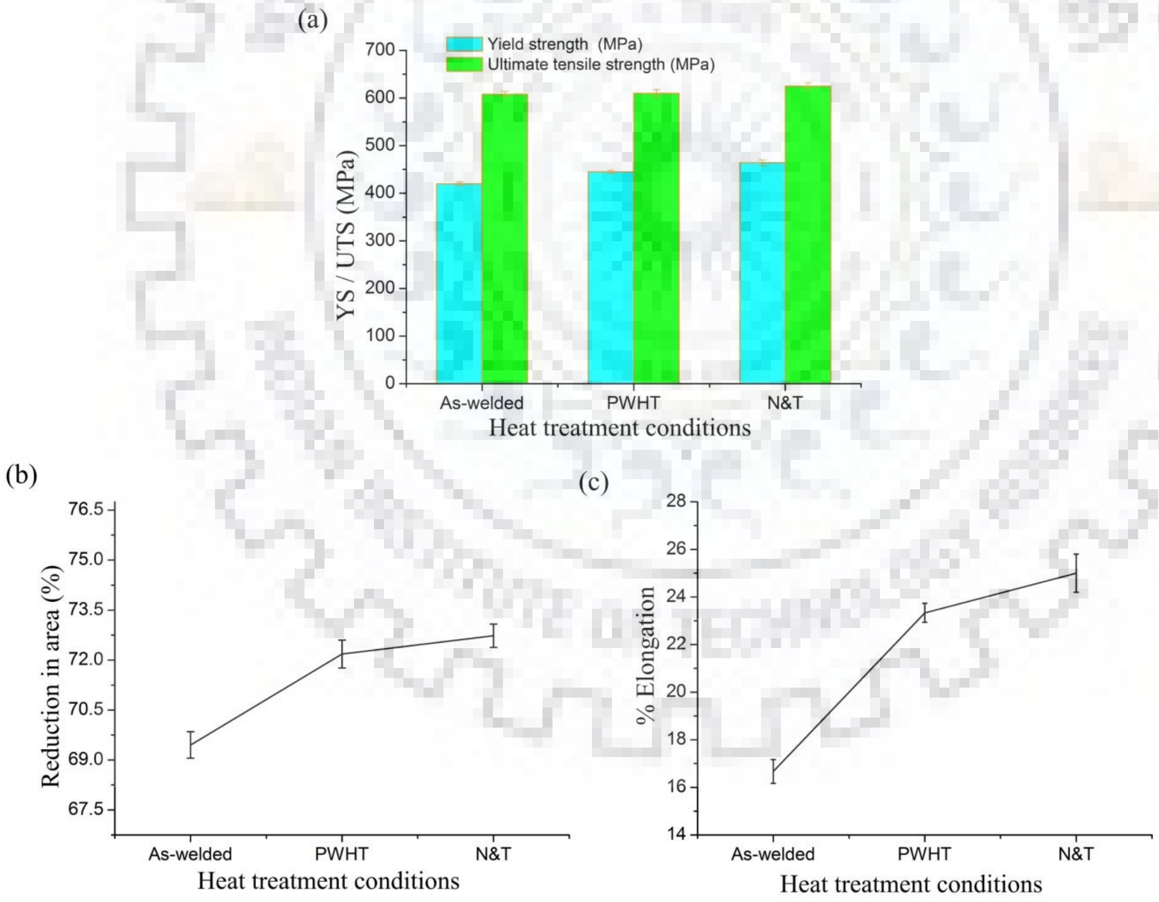

Figure 5.11 Variation in tensile properties for different heat treatment condition (a) YS and UTS, (b) % reduction in area (c) % elongation

The % elongation measured for the as-welded condition was 16.7 ± 2%. After PWHT and N&T, a continuous increase in % elongation was observed as shown in Fig. 5.11(b). The maximum % elongation was measured for N&T treatment, i.e. 25 ± 2.5%. The similar trend of variation was also observed for % reduction in area, as shown in Fig. 5.11(c).

The top view of fracture surface after the room-temperature interrupted tensile test is shown in Fig. 5.12(a-b). The top view of fracture surface revealed the presence of both main crack and secondary cracks of smaller size. The similar fracture surface was observed for as-welded and PWHT condition however in N&T condition, the bigger size cracks are observed rarely. In as-welded and PWHT condition, the top view of fracture surface revealed the 'splitting' nature (Chandan Pandey et al., 2017c).

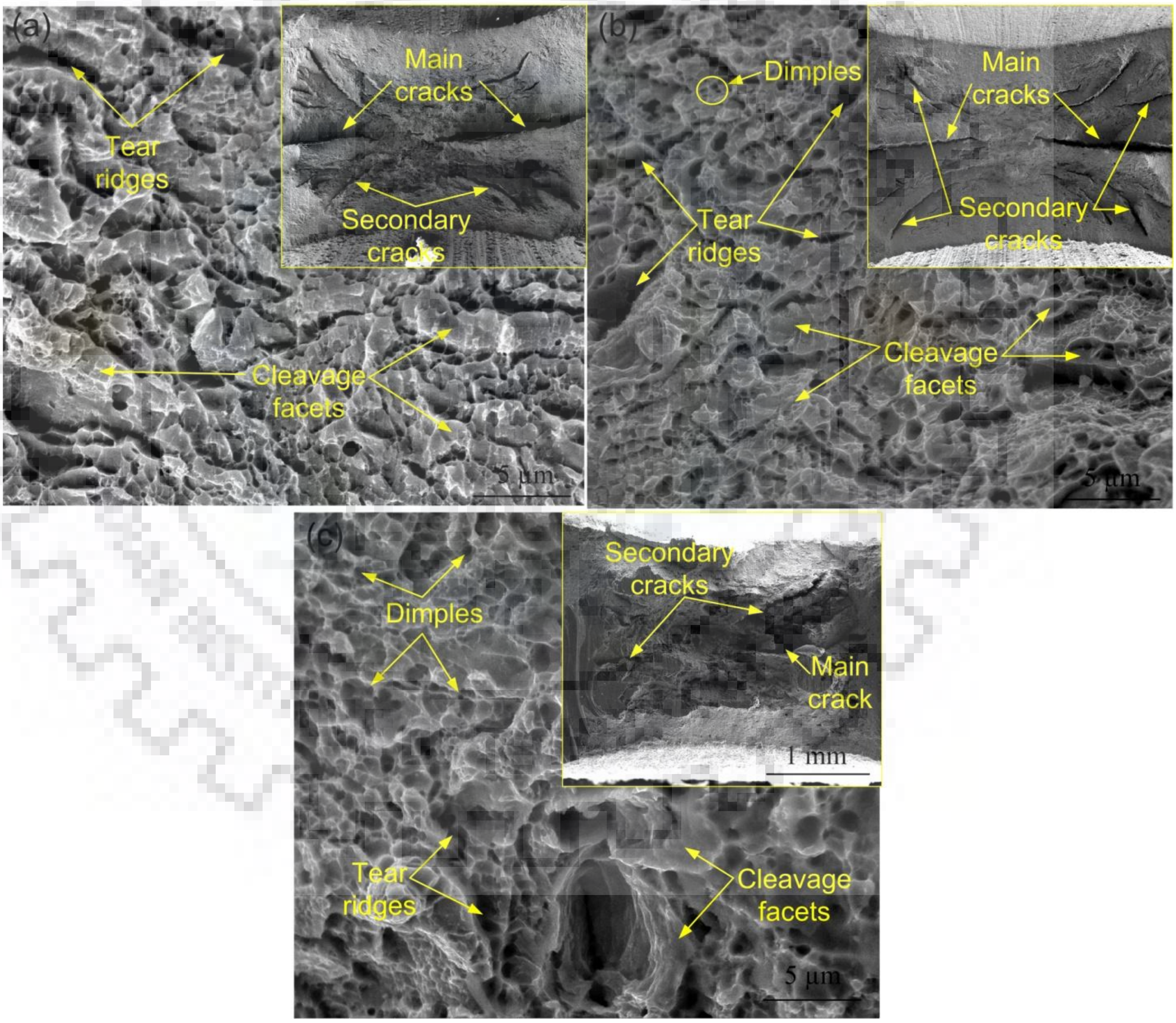

Figure 5.12 Fractographs after room temperature static tensile testing for different condition (a) as-welded, (b) PWHT, (c) N&T

The detailed view of fracture surface for each case is shown at higher magnification (Fig. 5.12(a-b)). The detailed view of fracture surface revealed the presence of ductile tear ridges, transgranular cleavage facets, and ductile dimples. During tensile loading, the coalescence of microvoids results in equiaxed dimples and spherical dimples on tensile fracture surface normal to the loading axis. The detailed view indicates the mixed mode of the fracture for all the cases. In as-welded condition and PWHT condition, the similar fractographs are found. The higher percentage of ductile tear ridges were observed for the as-welded condition while in N&T and PWHT state, less percentage of tear ridges are found. In N&T condition, the number density of dimples was fond to be increased (Fig. 5.12(c)). The heterogeneity in size of dimples is observed for all the cases.

The hardness variation in different heat treatment conditions is shown in Fig. 5.13. The main factors that govern the variation in hardness along the various regions of weldments are the presence of fine MX precipitates, microstructure, grain size, solid solution strengthening and number density of precipitates (Pandey and Mahapatra, 2016b). In the as-welded state, the average hardness of the weld fusion zone was measured 512 ± 25 HV. The weld fusion zone showed a great hardness variation because of multi-pass welding effect.

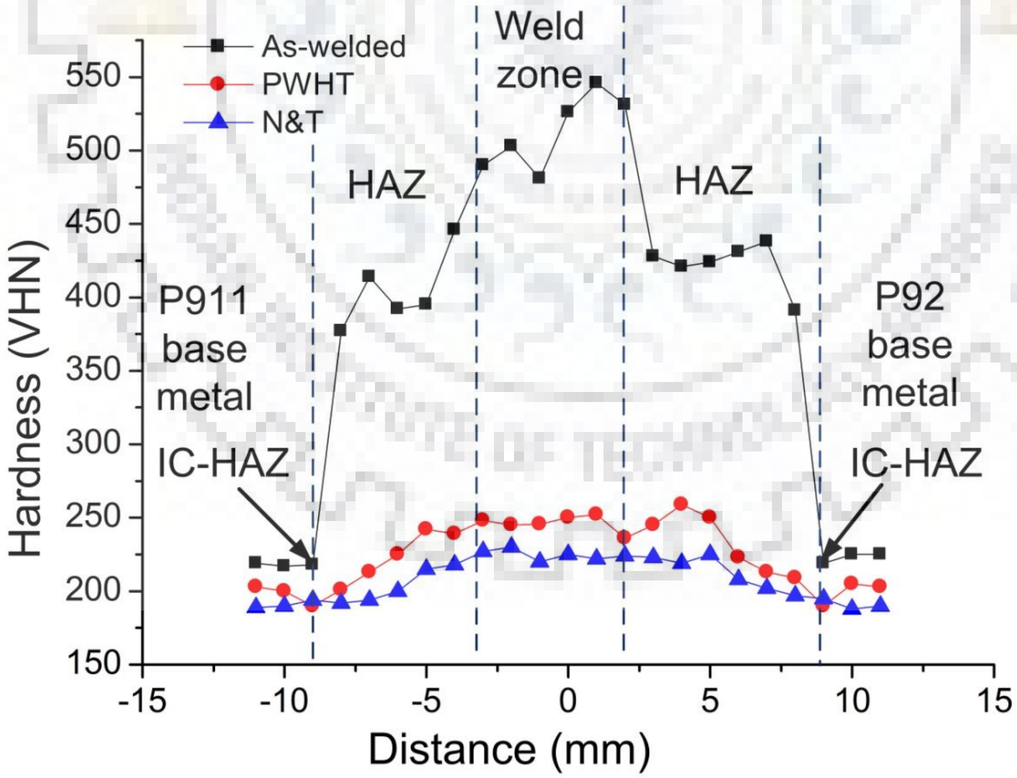

Figure 5.13 Hardness variation across the dissimilar weldments for different operating condition

A gradual decrease in hardness value was observed as move away from the fusion line on both sides of the dissimilar weld. The CGHAZ hardness measured on P92 and P911 side were 531 ± 15 HV and 490 ± 10 HV, respectively. FGHAZ on both the sides exhibited gradually decrease hardness value of 422 ± 16 HV and 400 ± 20 HV for P92 and P911 side, respectively. After the FGHZA, a sudden dip in hardness value was observed at the base-HAZ boundary. The region is identified as the soft region of dis-similar weldments. The hardness measured in soft-zone was 219 HV with respect to the P92 steel side.

In PWHT condition, a considerable softening occurred throughout the weldments. The tempering reaction causes the tempering of lath martensite and re-precipitation of phases along the boundaries and inside the matrix region. The average hardness value of weld fusion zone was measured to be 246 ± 7 HV. The PWHT resulted, 52 % of reduction in hardness value of weld fusion zone. The formation of carbide and carbonitride precipitates during the PWHT causes the weakening of the solution that lead to decrease in hardness value. Tempering reaction also lead to coarsening of existing precipitates and reduction of dislocation density in FGHAZ, IC-HAZ and over tempered base metal of P911 and P92 steel. On P92 side, hardness of CGHAZ and FGHAZ was measured 259 ± 8 HV, 236 ± 10 HV, respectively. On P911 side, hardness of CGHAZ and FGHAZ was measured 242 ± 6 HV, 225 ± 8 HV, respectively.

In N&T condition, a uniform microstructure evolution was observed. After N&T treatment, each zone present in the weldments behave as the nature of virgin material. Aftre N&T treatment, the hardness measured for the weld fusion zone and subzones was found to be less compared to PWHT, as shown in Fig. 5.13. After the N&T treatment, the average hardness of weld fusion zone was 222 ± 12 HV. A negligible variation in hardness was found after N&T treatment of weldments.

The variation in Charpy toughness value of weld fusion zone with respect to the various heat treatment conditions is shown in Fig. 5.14. The Charpy toughness value in as-welded condition was 24 ± 2 J. The presence of untempered columnar laths in weld fusion zone attributed to the lower Charpy toughness value in the as-welded condition. The PWHT resulted in the tempering of martensite and evolution of phases along the grain boundaries and inside the matrix region of weld fusion zone (Pandey and Mahapatra, 2016a). PWHT also included the rejection of C and N from solid solution, i.e. reduction in solid solution strengthening. This resulted in a drastic increase in the Charpy toughness vale of the weld fusion zone after the PWHT. For PWHT condition, the Charpy toughness value of weld fusion zone was measured 68 ± 4 J.

The Charpy toughness of weld fusion zone in N&T condition was measured to be higher as compared to PWHT. After the N&T treatment, the complete weldments is considered as the virgin material (as-received N&T P91 steel). After N&T treatment, the hardness and microstructure gradient are reduced completely across the weld fusion zone and HAZs and the weldments become homogenize. The Charpy toughness value measured after the N&T was 110 ± 7 J which is much higher than the as-welded and PWHT condition. The Charpy toughness valve measured in N&T condition was almost similar to as-received P911 steel (100 ± 6 Joules). Hence, in as-welded, PWHT and N&T condition, the maximum Charpy toughness value of weld fusion zone was measured for the N&T condition because of homogeneous microstructure and tempering.

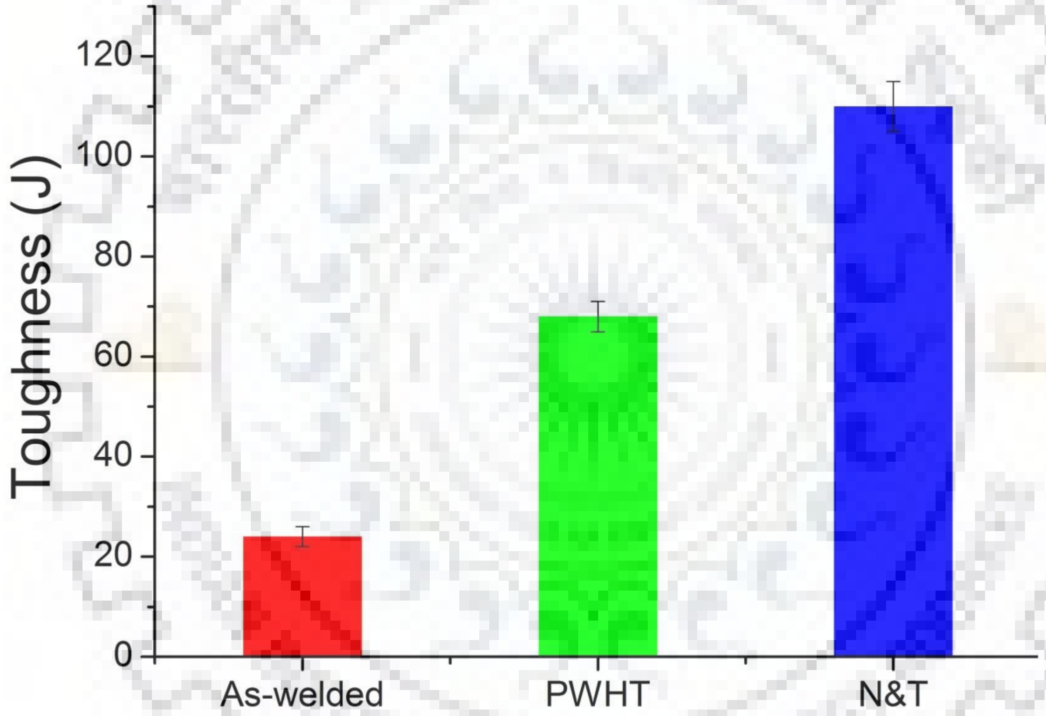

Figure 5.14 Charpy toughness of weld fusion zone in different operating condition

The fracture surface morphology of impact tested specimen was studied by using the FESM, as shown in Fig. 5.15(a-c). In as-welded condition, the fracture surface revealed the presence of quasi-cleavage with a negligible amount of dimples. The presence of smooth intercrystalline area denotes the embrittling effect that occurs due to coarsening of precipitates. After PWHT, the mode of fracture remains same as in as-welded condition. The smooth intercrystalline area indicates the brittle mode of fracture, as shown in Fig. 5.15(b). In N&T condition, the fracture is characterized by tear ridges and cleavage facets as shown in Fig. 5.15(c). The small area of dimples is seen besides the smooth inter-crystalline area.

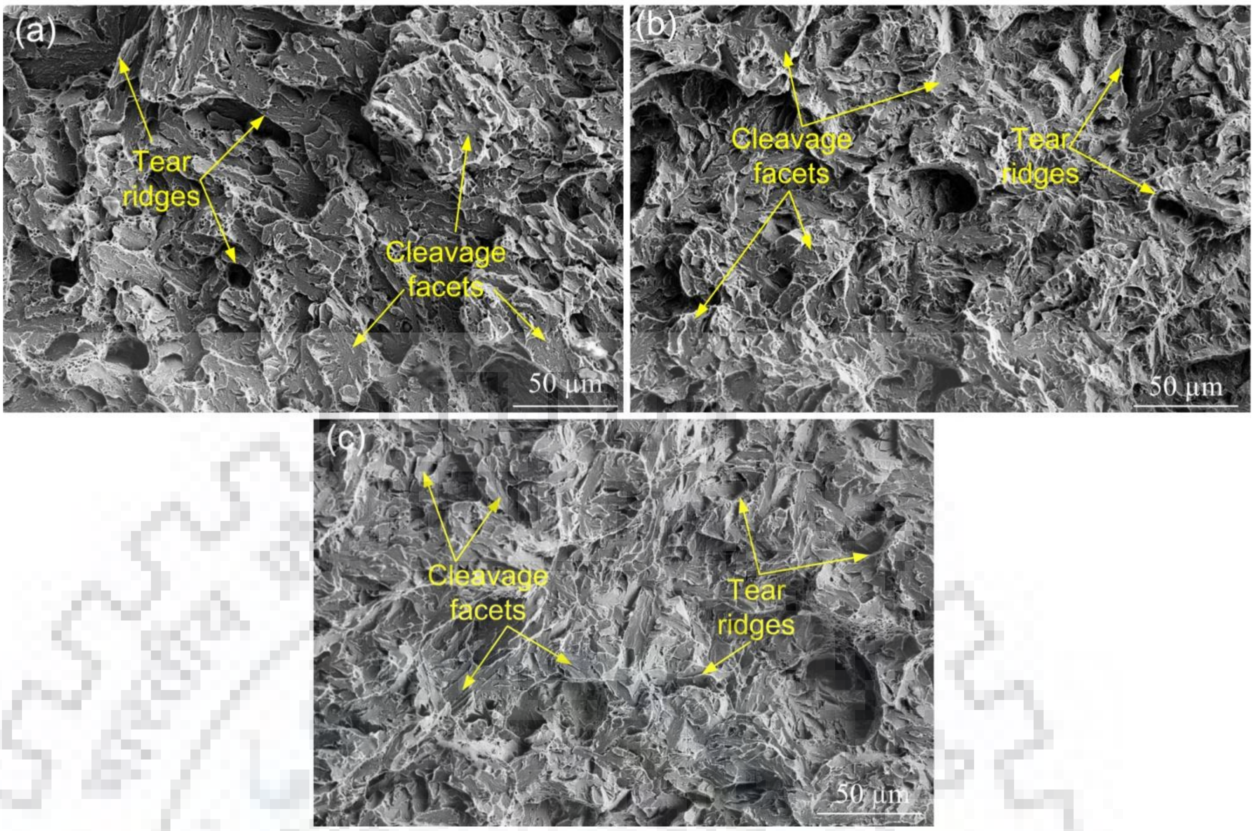

Figure 5.15 Fracture surface morphology after Charpy toughness tests (a) as-welded, (b) PWHT, (c) N&T

5.2.3 *Effect of filler compositions on mechanical properties of dissimilar SMAW welded joints of P91 and P92 steel*

5.2.3.1 Microstructure evolution in the weldments

The weld fusion zone micrographs for different filler rod and after PWHT are represented in Fig. 5.16. The welding cycle leads to the formation of the untempered martensite as well as a high weight percentage of C and N in the solution matrix. The martensite lath blocks with different orientation are shown in Fig. 5.16(a) and 5.16(b). The micrograph of the welds joint after the PWHT is shown in Fig. 5.16(c) and 5.16(d) for PWHT–P91 and PWHT–P92 welded joint. The tempering results in the evolution of the precipitates along the PAGBs and lath boundaries and also inside the intra-lath region, as shown in Fig. 5.16(c). The microstructure revealed the presence of the tempered lath martensite with precipitates for both P91 and P92 filler rod except the formation of the δ ferrite in the P92 filler rod, as shown in Fig. 5.16(d). The δ−ferrite was present in the as-welded condition which did not respond to the PWHT (Chandan Pandey et al., 2018d). The δ−ferrite boundaries are observed to be surrounded with the precipitates with higher density.

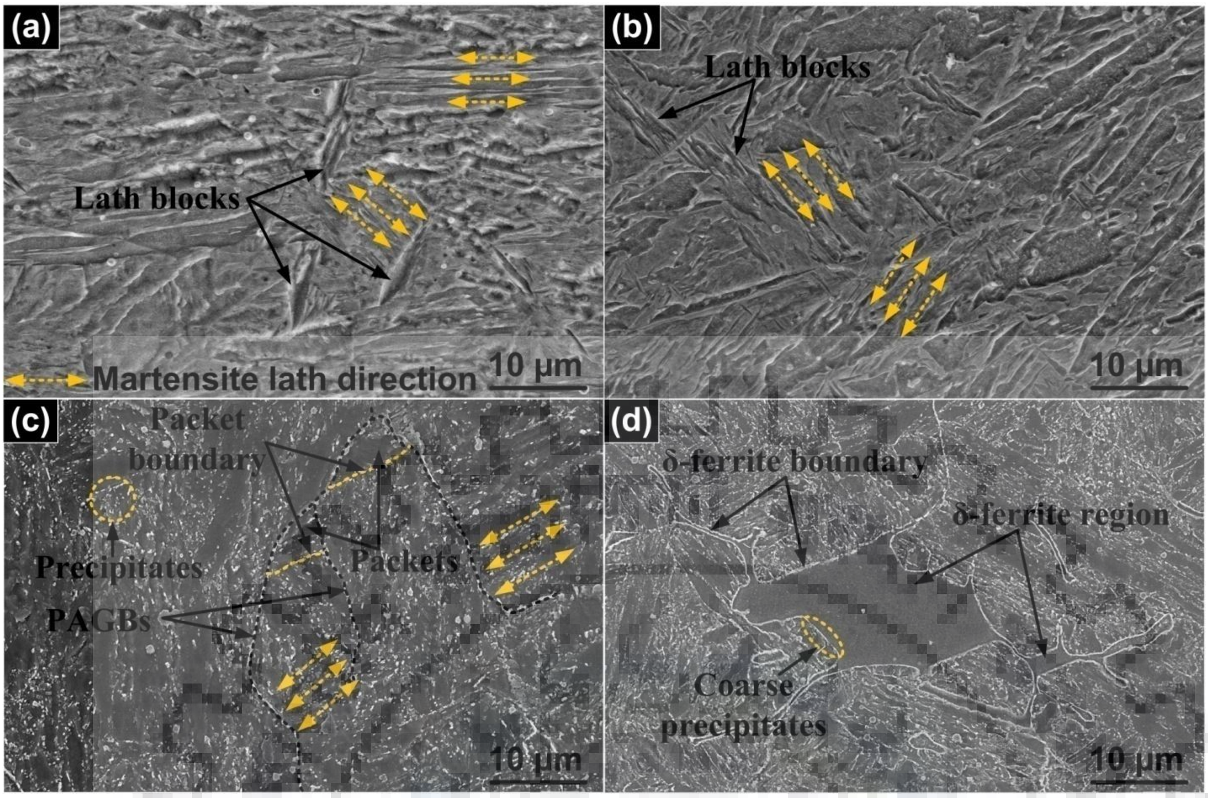

Figure 5.16 Secondary electron micrograph of weld fusion zone of the weld joints for (a) AW–P91, (b) AW–P92, (c) PWHT–P91 and (d) PWHT–P92

The formation of the δ ferrite ejects the austenite stabilizer like C and N from the region. The C and N get combine with the ferrite stabilizer present along the boundaries and leads to the formation of the carbide precipitates. In P92 filler rod, the higher weight percentage of the ferrite stabilizer like V, Nb and W might be responsible for the δ ferrite formation. The change in the chemistry of the base metal due to the weld thermal cycle is represented in Fig. 5.17. During the welding cycle, high heat input results in the dissolution of the fine MX and coarse $M_{23}C_6$ precipitates. However, some MX precipitates mainly Nb-rich particles still remain undissolved and after the cooling, a complex structure of coarse PAGBs, packet boundaries and lath blocks are formed. During PWHT, the initial stage of the tampering leads to the evolution of the both $M_{23}C_6$ and MX precipitates. After the PWHT, the tempered lath martensitic microstructure with precipitates are formed which are also confirmed from the Fig. 5.16(c) and 5.16(d).

After the PWHT, micrographs of the subzones of the dissimilar welds joint for P91 filler is depicted in Fig. 5.18. After the PWHT, the dissolve precipitates comes out and get decorated along the lath boundaries and PAGBs. The micrograph of the weld fusion zone (Fig. 5.15(b)) shows the lath blocks, lath packets, packet boundaries, PAGBs and precipitates both along the boundaries and inside the intra-lath region. The weld fusion zone micrograph at higher magnification (Fig. 5.18(e)) represents the orientation of lath blocks along with higher density of the coarse precipitates. The energy dispersive X-ray spectroscopy (EDS) spectra of the precipitates (Fig. 5.18(h)) confirms the formation of secondary phase carbide precipitates.

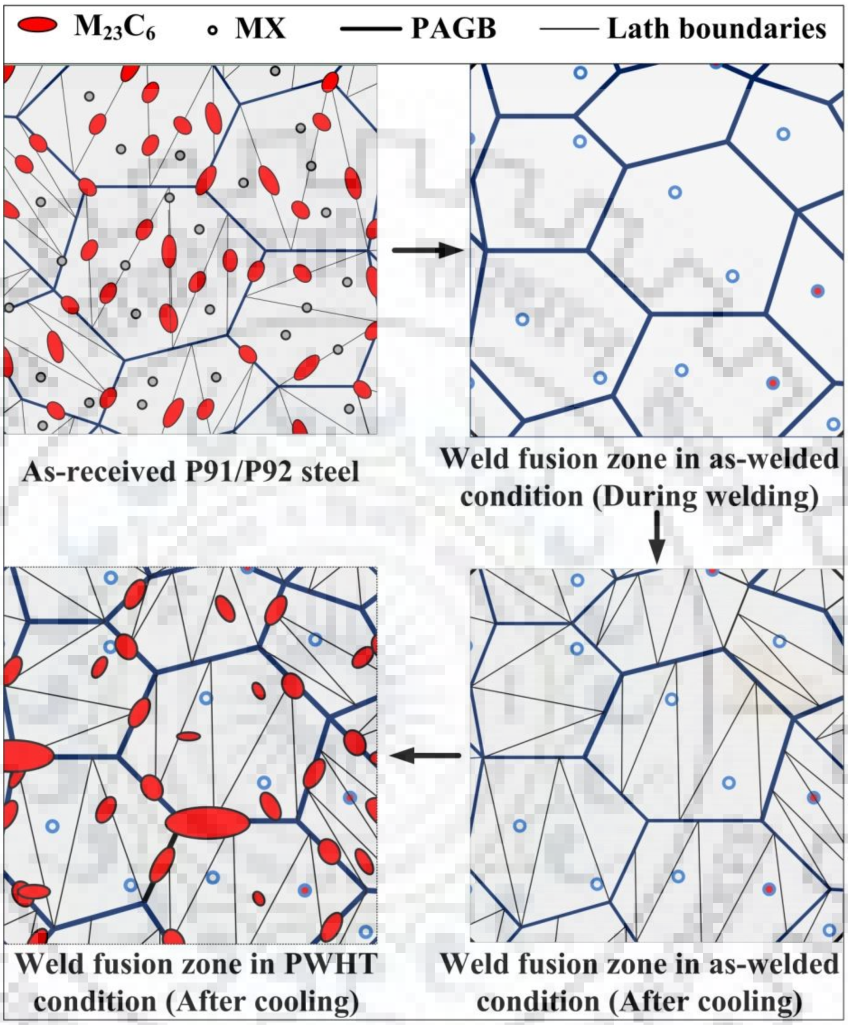

Figure 5.17 Schematic of transformation behavior in weld fusion zone after different weld thermal cycles

The coarse-grained HAZ (CGHAZ) for both the side shows the similar microstructure. For the P91 side, CGHAZ microstructure reveals the PAGBs and different orientation of lath blocks. The precipitate also comes out as a result of the tempering reaction. The lath morphology still remains in the microstructure, as shown in Fig. 5.18(a) and 5.18(b). In fine-grained HAZ (FGHAZ), the pinning effect of the precipitates results in the formation of the fine PAGs. In FGHAZ, the precipitates get partially dissolved during the welding and remain in the microstructure after the tempering.

The FGHAZ for both P91 and P92 side is shown in Fig. 5.18(d) and 5.18(f), respectively. These coarse precipitates also lead to the cracking during creep as a result of their brittle nature. The most interesting region in the dissimilar welded joint is inter-critical HAZ (ICHAZ) that facilitates the Type IV cracking. The weld thermal cycle results in the partial dissolution of the precipitates and partial tempering of the martensite and at the same time formation of new untempered lath martensite near the boundary of HAZ and base material.

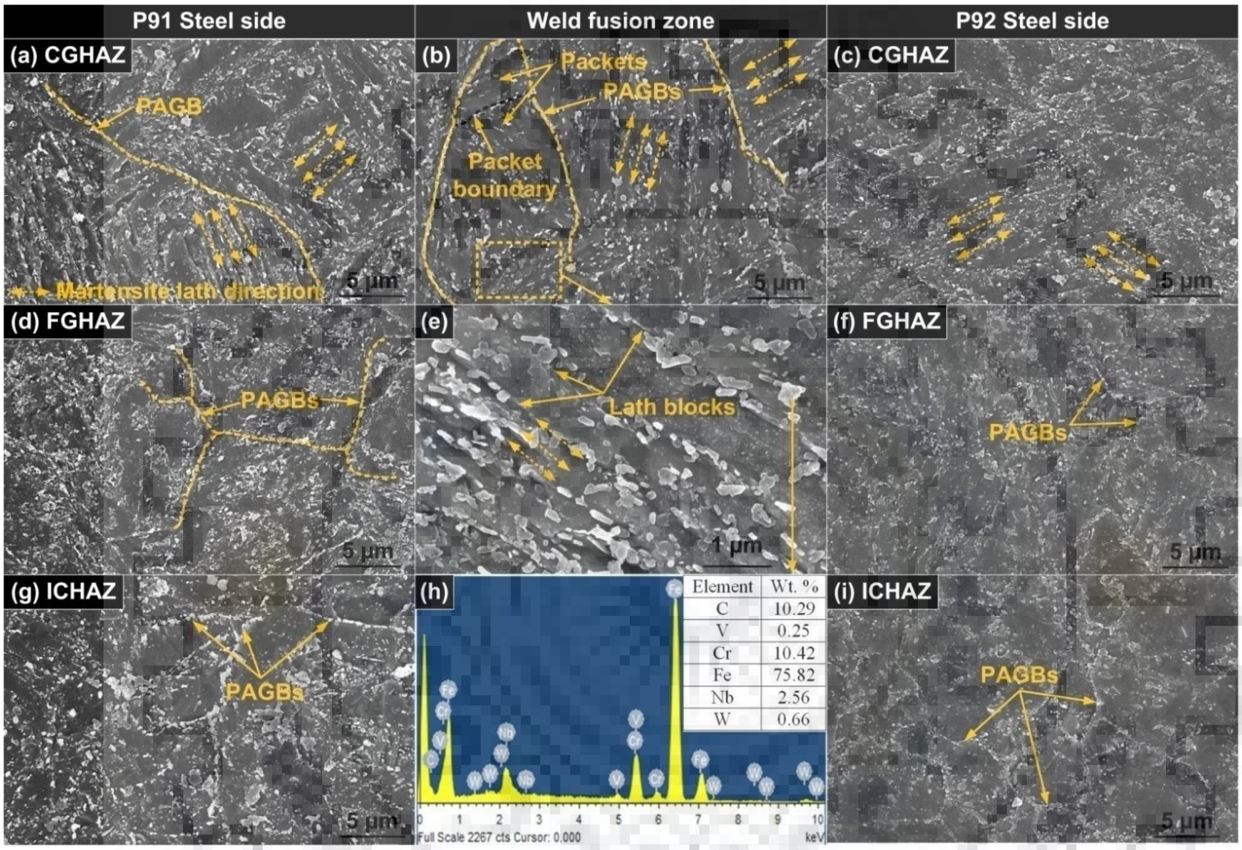

Figure 5.18 Secondary electron micrograph of PWHT-P91 weldment: (a) CGHAZ P91 side, (b) weld fusion zone at lower magnification, (c) CGHAZ P92 side, (d) FGHAZ P91 side, (e) weld fusion zone at higher magnification, (f) FGHAZ P92 side, (g) ICHAZ P91 side (h) EDS spectra of particles present in the weld fusion zone and (i) ICHAZ P92 side

All the reaction leads to the formation of the complex structure and referred as ICHAZ. After the PWHT, the evolution of new precipitates occurs in the ICHAZ as well as both over tempering of the martensite and formation of the newly tempered martensite also occurs simultaneously. Fig. 5.18(g) shows the undissolved coarse precipitates in the ICHAZ of P91 side. The microstructure on P92 side ICHAZ (Fig. 5.18(i)) looks similar as P91 side except the number density of coarse undissolved precipitates.

The micrographs of P91 and P92 dissimilar weldments for the P92 filler are shown in Fig. 5.19. For P92 filler, weld fusion zone shows soft δ ferrite patches having hardness was reported in the range of 195-250 HV for the P91 and P92 welds (Chandan Pandey et al., 2018d). This soft zone formation is attributed to the higher amount of ferrite stabilizer in the P92 filler. The region is also considered as the carbide precipitate free region. The austenite stabilizer elements get ejected from and collected near the boundary. The higher density of the austenitizing element (C, N) at the grain boundaries leads to the formation of Cr, Mo and W-rich $M_{23}C_6$ precipitates.

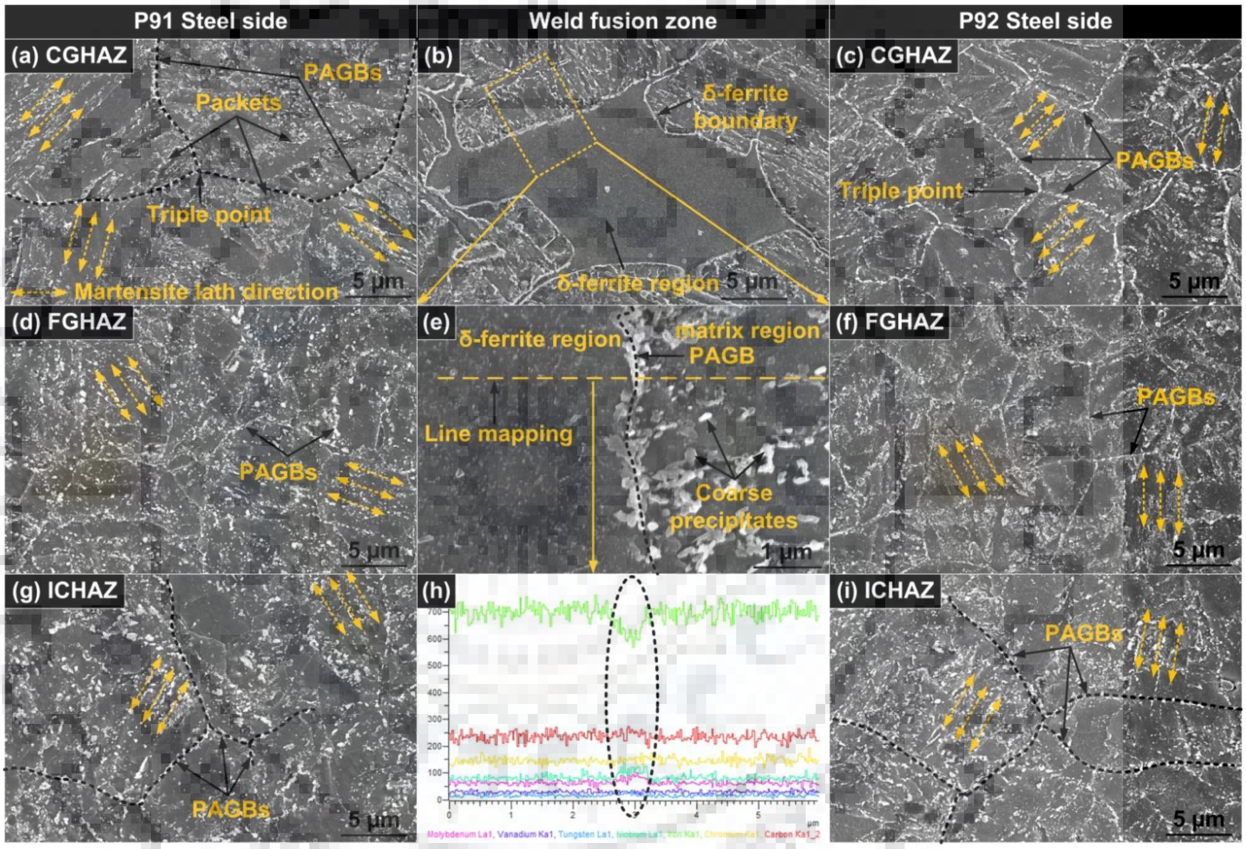

Figure 5.19 Micrograph of PWHT-P92 weldment: (a) CGHAZ P91 side, (b) weld fusion zone showing δ ferrite, (c) CGHAZ P92 side, (d) FGHAZ P91 side, (e) weld fusion zone at higher magnification showing δ ferrite boundary, (f) FGHAZ P92 side, (g) ICHAZ P91 side, (h) line mapping of the δ ferrite boundary and (i) ICHAZ P92 side

Fig. 5.19(a) also confirms the higher density secondary phase precipitates along the δ ferrite boundaries. The precipitates free δ ferrite region is further characterized at higher magnification using the line mapping (Fig. 5.19(e)). The line mapping also confirms the high amount of the precipitates enriched in Cr, Mo and W. The peak intensity of the Fe also gets reduced near the δ ferrite boundary as shown in Fig. 7(h). The CGHAZ for both side base material looks similar. The PAGBs get highlighted with the black dotted line (Fig. 5.19(a)). The PAGS along P91 side CGHAZ looks coarse as compared to P92 CGHAZ. The martensite lath direction shows different orientation inside the lath packets. The FGHAZ and ICHAZ for both the side of are also shown in Fig. 5.19. Some undissolved coarse precipitates of size in the range of 250-300 nm are also observed in the FGHAZ and ICHAZ.

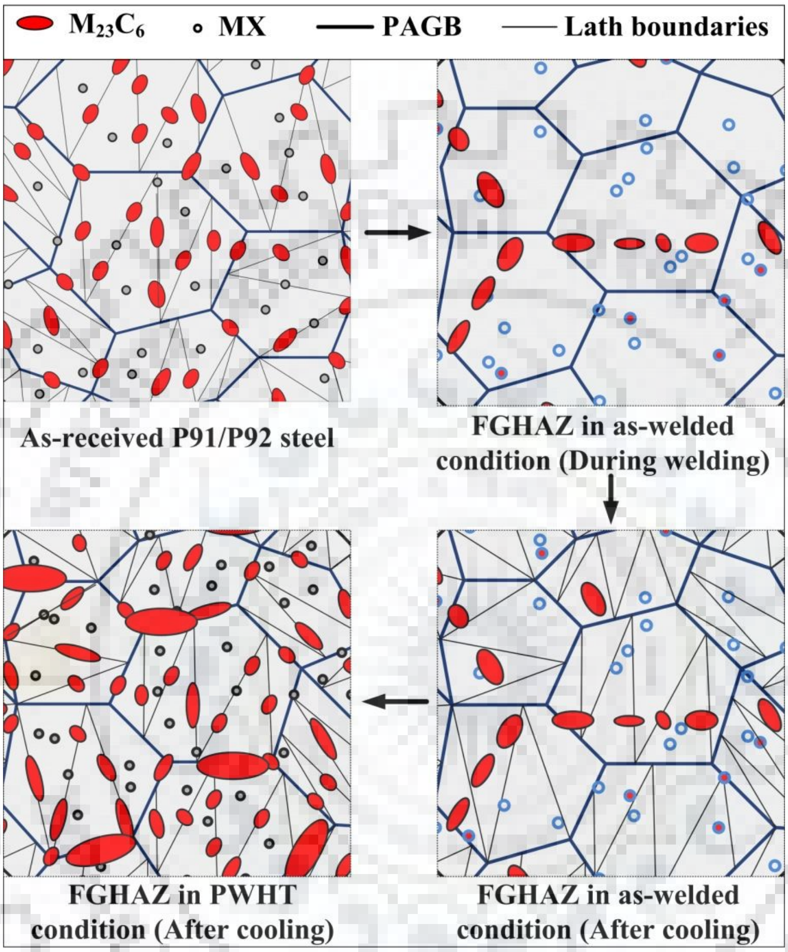

Figure 5.20 Schematic of transformation behavior in FGHAZ after different weld thermal cycles

The schematic diagram showing the microstructural change in the FGHAz during the weld thermal cycle is represented in Fig. 5.20. During this cycle, the peak temperature experienced about A_{c3} that result in the complete dissolution of fine $M_{23}C_6$ precipitates while some coarse $M_{23}C_6$ precipitates remain undissolved, as shown in Fig. 5.20. However, the fine MX precipitates present in FGHAZ remain unaffected as a result of higher thermal stability. After the cooling, FGHAZ shows the complex structure of untempered martensite with undissolved coarse $M_{23}C_6$ precipitates and fine MX precipitates. The PWHT resulted that the undissolved precipitates get coarsen and further evolution of new $M_{23}C_6$ precipitates The martensite also gets tempered during the PWHT process.

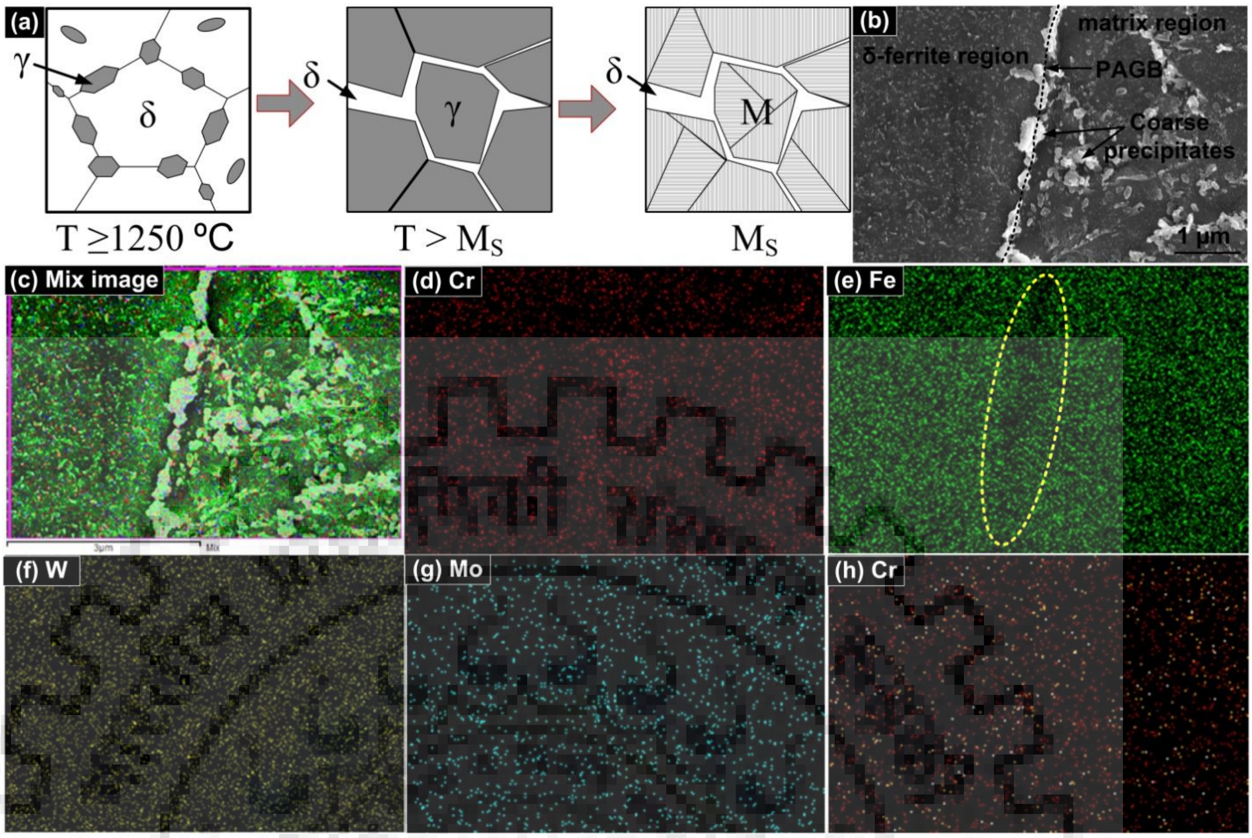

Figure 5.21 (a) Schematic of evolution of δ-ferrite, (b) Micrograph of the weld fusion zone for PWHT joint, (c), (d), (e), (f), (g) and (h) line mapping of the matrix and δ-ferrite boundary region

The schematic evolution of the δ-ferrite during the weld thermal cycle is presented in Fig. 5.21(a). The austenite to ferrite transformation mainly depends on the heating rate. At high cooling rate stripped morphology of δ ferrite was reported. For slow cooling rate sample remain in ϒ/δ phase for larger time. After that, both move their equilibrium stage and promote the formation of δ ferrite from ϒ. After that, both move their equilibrium stage and promote the formation of δ ferrite from ϒ. With the time or growth of austenite, curved δ-ferrite/ϒ-austenite interphase boundaries evolve into finger type morphology that grows at a much faster rate along the δ-ferrite boundaries as compared to the δ-ferrite matrix. This occurred as a result of fast diffusion of solute atoms along the boundaries.

The area mapping of the δ ferrite region was also performed and reported in Fig. 5.21(b-h). The area mapping confirms the homogeneous distribution of the elements inside the ferrite and martensite region. However, at the δ-ferrite boundaries, the depletion of the Fe elements are observed which are also confirmed by the line mapping. The line mapping also shows the elements present in the Fe-matrix.

5.2.3.2 Mechanical properties of weldments

The stress-strain curve for the welded joint is depicted in Fig. 5.22(a). The variation in ultimate tensile strength (UTS) for different filler and heat treatment condition is shown in Fig. 5.22(b). The UTS were measured 1178±16 and 1348±18 MPa for AW-P91 and AW-P92 welded joint, respectively. The higher UTS are attributed to the untempered lath martensite and higher solid solution strengthening. The UTS was measured higher for P92 filler as compared to P91 filler as a result of higher weight percentage of solid solution strengthening element like W. After the PWHT, a drastic reduction in UTS was measured as shown in Fig. 10(b). The reduction is attributed to the tempering reaction that includes the lath breakup, tempering of martensite, evolution of carbide and carbonitride precipitates, reduction in solid solution hardening and removal of quenching stress.

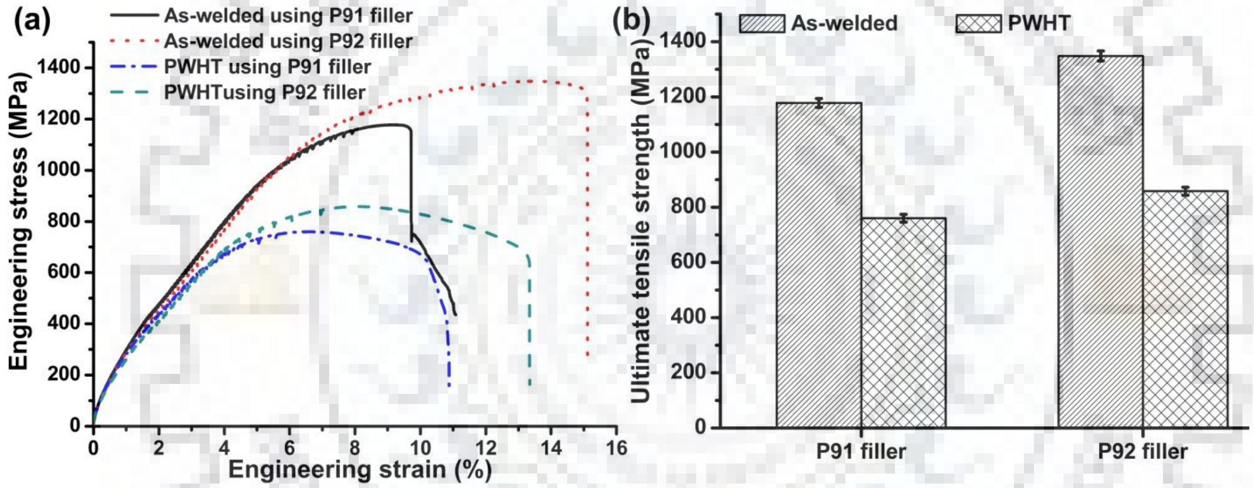

Figure 5.22 (a) Stress-strain curve for various welded specimens and (b) tensile strength

The UTS were measured 760±10 and 858±12 MPa for PWHT-P91 and PWHT-P92 welded joint, respectively. The percentage elongation was measured to be higher about 15±2 % for AW-P92 welded joint. The weld efficiency of dissimilar weld joints was calculated using this equation;

$$Weld\ efficiency = {}^{UTS\ of\ welded\ joint}\Big/_{UTS\ of\ as-received\ base\ material} \qquad (5.1)$$

The maximum and minimum joint efficiency were measured 199 and 174 %, respectively for AW-P91 and AW-P92 welded joint, respectively. After the PWHT, the minimum joint efficiency about 112 % was measured for PWHT-P91 welded joint. The microhardness profile of dissimilar welded joints across the transverse direction is shown in Fig.5.23. The average microhardness of fresh martensite was measured 521 ± 16 and 500 ± 18

HV for AW-P91 and AW-P92 welded joint, respectively. However, a great variation was observed in microhardness of weld fusion zone for both fillers. Whereas, in weld fusion zone, the average hardness for P92 filler was measured lower than the P91 filler as a result of the soft δ-ferrite in P92 weld fusion zone. The average microhardness of FGHAZ in the P91 side was measured 451 ± 26 and 484 ± 24HV for AW-P91 and AW-P92 welded joint, respectively. The higher microhardness of FGHAZ was observed 488 ± 22 and 477 ± 21HV in the P92 side as compared to P91 side with similar conditions. The large heterogeneity in the hardness of the subzones leads to the premature failure of dissimilar welds (Abson and Rothwell, 2013b).

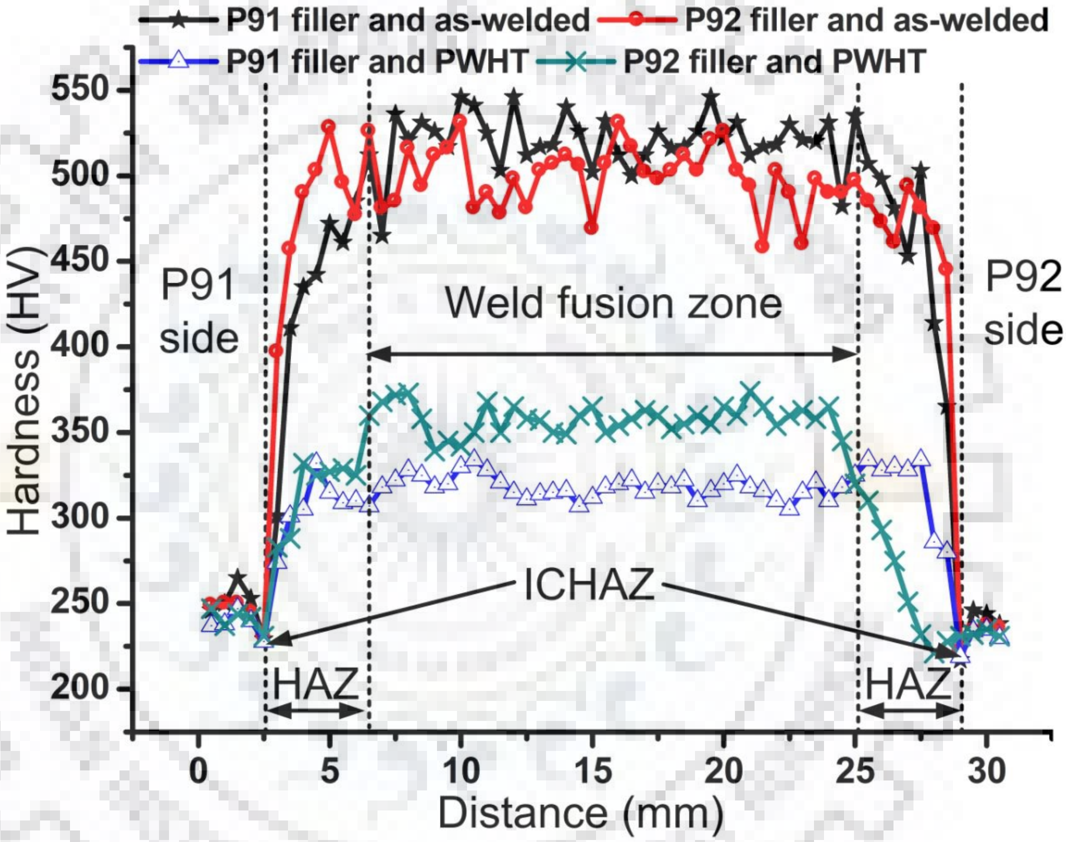

Figure 5.23 Microhardness profile across the welds joints

The PWHT resulted in a substantial drop in microhardness of weld fusion zone and other HAZs of welds joint. This reduction in hardness was attributed to the synergistic effect of softening of martensite and evolution or/and growth of precipitates. After PWHT, the heterogeneity in microhardness still remains. After PWHT, the average microhardness of weld fusion zone was measured 318 ± 7 and 357 ± 10 HV for PWHT-P91 and PWHT-P92 welded joint, respectively. After PWHT, the FGHAZ in P91 and P92 side of weld for P91 filler exhibited microhardness in the range of 312 ± 11 HV, 321 ± 16 HV, respectively whereas for P92 filler the values observed where 323 ± 18 HV and 250 ± 28 HV, respectively.

However, the microhardness of the ICHAZ in the P91 side was observed 228 HV and 231 HV for PWHT-P91 and PWHT-P92 welded joint, respectively. Whereas the ICHAZ in the P92side exhibited a microhardness value of 219HV and 231HV, for PWHT-P91 and PWHT-P92 welded joint, respectively that clearly shows the heterogeneity across the welds joint after the PWHT. For P91 and P92 steel welds joint, the minimum Charpy impact toughness was recommended about 47 J as per EN: 1557:1997 specifications for the hydro testing of vessels. In the present investigation, the Charpy toughness of the weld fusion zone was measured 8 ± 2 and 5 ± 3 J for AW-P91 and AW-P92 welded joint, respectively which were less than the minimum recommended value.

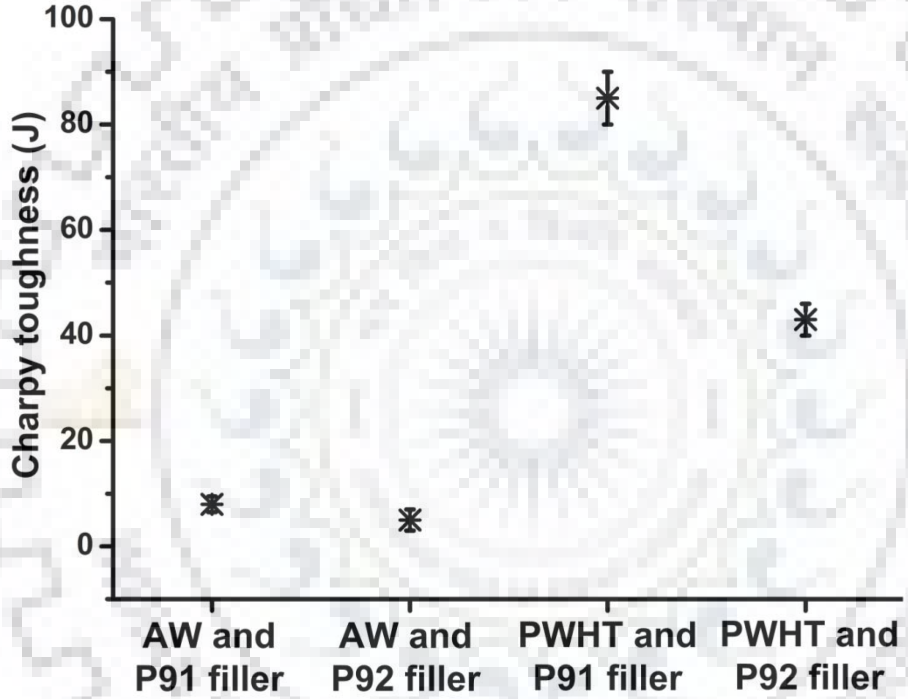

Figure 5.24 Charpy impact toughness of different welded joints

In order to get the minimum required Charpy toughness value, PWHT was recommended by the researchers (Cao et al., 2011; Zhu and Xuan, 2010). The toughness was measured 85 ± 5 and 43 ± 7 J for PWHT-P91 and PWHT-P92 welded joint, respectively. The required toughness value was achieved for the P91 filler as per PWHT reaction. However, it was still less in case of P92 filler. Hence, for the P92 filler PWHT, about 760 ^{o}C for 2 h was recommended and it was suggested to increase the duration of the PWHT to get the desired results. In P92 filler, the higher weight percentage of the ferrite stabilizer might be the possible cause of the poor toughness. The ferrite stabilizer like W and Mo enhance the solid solution hardening that imparts to brittleness in the microstructure.

The effect of the ferrite stabilizer on weld fusion toughness of the welds joint has also been reported by the Arivazhagan et al. (Arivazhagan and Vasudevan, 2014) reported that the Charpy toughness value gets reduced with an increase in the weight percentage of the ferrite stabilizers. The other cause of the poor toughness for the P92 filler can be the presence of the soft δ-ferrite patches in weld fusion zone which is also governed by the ferrite stabilizer. Schafer (Schafer, 1998b) had observed the encapsulation of δ-ferrite and $M_{23}C_6$ carbides, resulting in reduced toughness. The negative influence of the δ ferrite patches on Charpy impact toughness was also reported by the Pandey et al. (Chandan Pandey et al., 2018b). The Charpy toughness value for different filler and heat treatment condition are depicted in Fig. 5.24.

5.3 Conclusions

- In as-welded and PWHT condition, a significant variation was observed in the microstructure of CGHAZ, FGHAZ, IC-HAZ and over tempered base metals for both P92 and P911 side.
- The PWNT resulted in a homogenize microstructure across the dissimilar weldments that lead to improve mechanical properties. For subsequent PWHT, the tensile strength and yield strength was increased as compared to as-welded state. In as-welded condition, considerable hardness gradient was observed across the weldments. PWHT resulted in a considerable lowering in the hardness gradient.
- Minimum hardness gradient across the dissimilar weldments was observed in PWNT condition. The PWNT treatment provides the Charpy toughness value near to the as-received P911 steel.
- The microstructure of weld fusion zone revealed the untempered lath martensite with high solid solution hardening for both as-welded-P91 and as-welded-P92 welded joint. The PWHT resulted in the tempering of the martensite with the evolution of new $M_{23}C_6$ and MX precipitates in the weld fusion zone.
- In P92 filler rod, the higher weight percentage of the ferrite stabilizer resulted in the formation of the soft δ ferrite patches in weld fusion zone that did not respond to the PWHT. The tensile strength was measured 1178 ± 16 and 1348 ± 18 MPa for P91 and P92 filler, respectively in the as-welded condition and reduced drastically after PWHT and was measured 760 ± 10 and 858 ± 12 MPa. The higher strength and weld efficiency for P92 filler was attributed to high W percentage that enhanced the solid solution hardening.

- The required toughness value (minimum value 47 J) was achieved for the P91 filler as per PWHT reaction. However, it was still less in case of P92 filler.

CHAPTER 6. HYDROGEN EMBRITTLEMENT OF P92 STEEL

In this chapter, the effect of filler conditions on the diffusible hydrogen content have been studied and the effect of diffusible hydrogen content on the embrittlement of P92 steel weldments has also been studied. The effect of welding parameters on the diffusible hydrogen content have been studied and implant tests have also been performed to identify the effect of diffusible hydrogen on embrittlement.

6.1 Experimental procedure

6.1.1 *Base Material and weld consumable*

The as-received P92 steel was in normalized and tempered condition with the dimension of 200 mm ×100 mm ×10 mm. The normalizing temperature of the as-received material was 1000 °C for 60 min, and tempering temperature was 760°C for 120 min. To see the effect of filler condition, 4 mm diameter E-911 filler (Metrode: CH12MV-40) was utilized for SMAW process to deposit weld metal. To see the effect of welding process parameters, 4 mm diameter MAILARC–P92 filler was utilized for SMAW process to deposit weld metal. The chemical composition of as-received Grade P92 steel and fillers were given in chapter 4 (Table 4.1). The mechanical properties of the Grade P92 steel in normalized and tempered (N&T) condition are also depicted in Table 4.2 (chapter 4). The as-received microstructure of Grade P92 steel in N&T condition is also given in section 4.2.1 (chapter 4).

6.1.2 *Process variations*

6.1.2.1 Effect of filler conditions on diffusible hydrogen content

The diffusible hydrogen test was conducted under three different conditions of the fillers as shown in Table 6.1.

Table 6.1 Weld filler conditions used for diffusible hydrogen measurement

S.N.	Test case	Filler condition
1	Case I	Filler dried at 300 °C for 2 h
2	Case II	Filler used without drying
3	Case III	Filler dipped in oil (15 W grade) before bead depositing for 10 min

6.1.2.2 Welding process parameters

Different welding process parameters were used to deposited metal for mercury method (Table 6.2). The heat input equation (HI=(η*V*I*60/S)) was used for calculation with 80 % efficiency (η) of process.

Table 6.2 Welding process parameters

S.N.	Sample condition	Welding current (I) (Amps)	Welding voltage (V)	Welding speed (S) (mm/min)	Heat input (kJ/min)
1	condition I	130	22-24	135-150	1.01
2	condition II	150	23-25	135-150	1.21
3	condition III	170	24-25	135-150	1.40

6.1.3 *Mercury method*

For diffusible hydrogen measurement, mercury method was used in this study. In mercury method, the hydrogen measurement is based on the displacement of mercury by hydrogen and the subsequent volumetric measurement of hydrogen. The apparatus, materials, procedures for specimen preparation, the diffusible hydrogen calculation and its analysis by using mercury method is given in details in many standards (American and Standard, 2006; BIS, 1986). In this study, the Indian standard (IS) was utilized for diffusible hydrogen measurement (BIS, 1986). The photograph of the Y-shaped eudiometers used for the collection of diffusible hydrogen is shown in Fig. 6.1. In each test, the preheating of diffusible hydrogen specimens was carried out at 250 ^{o}C for 1 h before the deposition of metal (Albert et al., 2011).

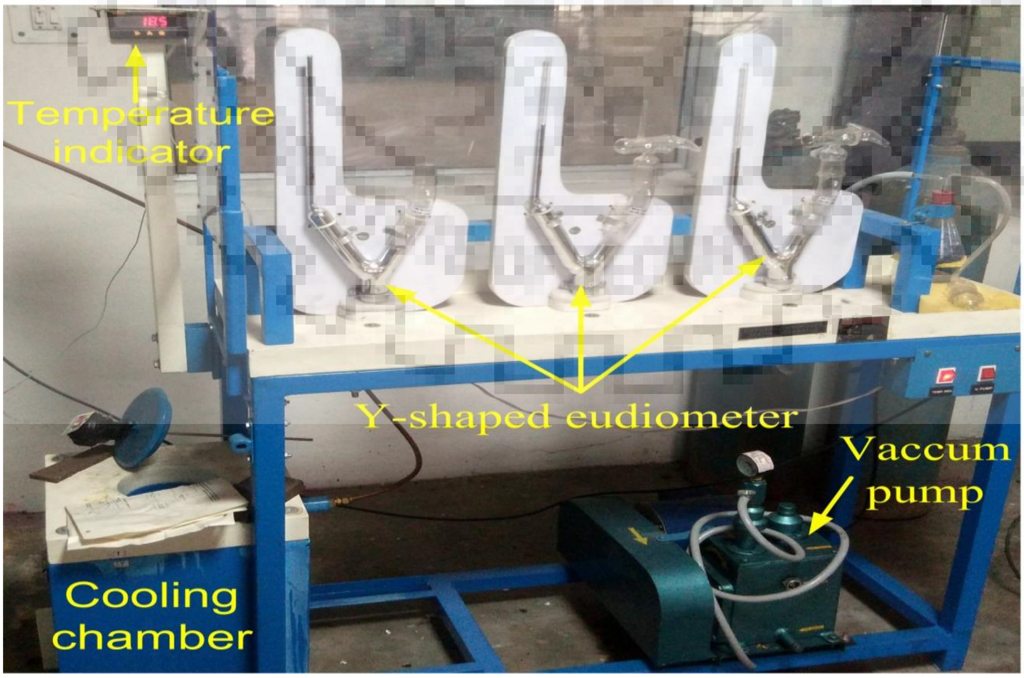

Figure 6.1 Diffusible hydrogen testing apparatus (mercury method)

For each test, the average of two results has been reported. The schematic of mercury method test assembly used for diffusible hydrogen measurement was shown in Fig. 6.2(a). As per IS, the mercury method test assembly consisted of run on piece of dimensions 45 x 15 x 10 mm, hydrogen sample piece of dimensions 30 x 15 x 10 mm and run off piece of dimensions 45 x 15 x 10 mm. To remove the bulk hydrogen, the test assembly was heated at 650 ^{o}C for 1 h just before bead depositing and after cooling cleaned with the emery paper. The run on piece, hydrogen sample and run off piece were placed on a copper jig fixture. After placing on copper jig fixture, metal was deposited by using SMAW process as shown in Fig. 6.2(b). The arc voltage, welding current and travel speed were 22-25 V, 140 A and 3.1 mm/s, respectively. The test assembly was quenched in ice water, within 15 s after the bead depositing. Then run off and run on piece are broken from test assembly using vice and hammer. The hydrogen sample (center-piece) was broken out from the test assembly, as shown in Fig. 6.2(c). The centerpiece (hydrogen sample) was placed at -50^{o}C in the cooling chamber for 3 min after 40 s of welding.

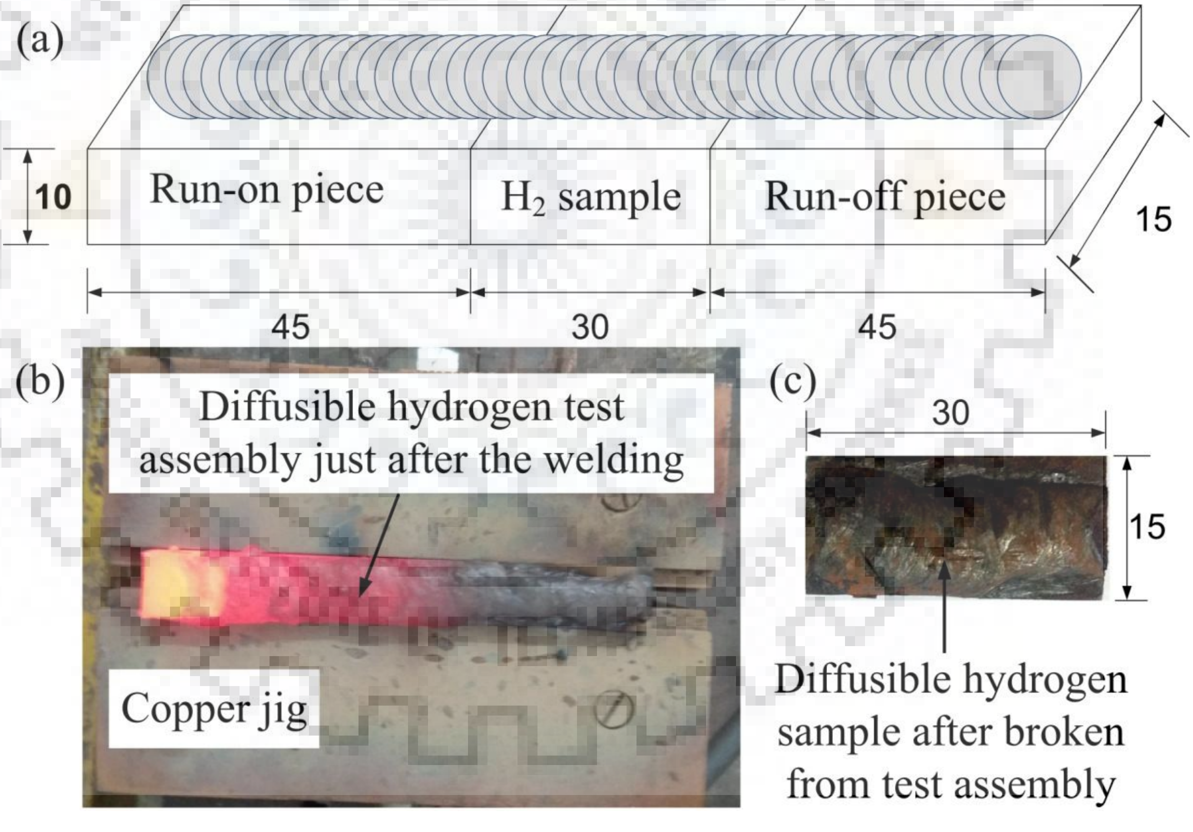

Figure 6.2 (a) Schematic of mercury method test assembly, (b) test assembly fixed on copper jig during after the deposited metal and (c) hydrogen sample after broken out from test assembly

The test specimens were removed from the cooling chamber and washed with alcohol for a period of 3-4 s. Subsequently, the test sample was washed with pure ether for a period between 3 to 5 s and then placed in the glass capsule for drying in a blast of dry nitrogen supplied from a nozzle for 20 to 22 s. The Y-shaped eudiometer was evacuated by a suction/rotary pump, just before the specimen admitted into the eudiometer. After evacuation, the vacuum was released and the initial reading in the graduated limb of the Y-tube was recorded. Then, the specimen was admitted through the open limb into the Y-shaped eudiometer and limb was closed. The weld sample was moved to the graduated close limb of the Y-type eudiometer with the help of a strong magnet. After that, the Y-shaped eudiometer was evacuated again, and the specimen allowed to evolve hydrogen for 72 h at room temperature. After 72 h, the specimen was removed from the apparatus and thoroughly clean and then weighed to an accuracy of 0.01 g. To calculate the diffusible hydrogen content ($H_{mercury}$) in ml/100 g of deposited metal, the expression was given below (Kumar and Yu-ichi, 2013):

$$H_{mercury} = V_g \frac{273}{(273+T)} * \frac{(B-H)}{760} * \frac{100}{(w_1-w_2)} \tag{6.1}$$

where, $H_{mercury}$ is the diffusible hydrogen content at NTP (ml/100 g of deposited metal), V_g (V_F - V_I) is the (final volume of gas - initial volume of gas) in Y-tube burette after 72 h, T is the room temperature when Vg is measured in ^oC, B is barometric pressure in mm of H_g, H is the mercury head in mm, i.e., difference in the heights of mercury levels in the two limbs of Y-tube at the end of measurement, w_1 is the mass of the sample in g before weld deposition and w_2 is mass of the sample in g after removal from the burette.

6.1.4 *Granjon Implant test*

Granjon implant test is the most common method used to evaluate the HAZ HAC susceptibility and used by many researchers (Dix et al., 1974; Magudeeswaran et al., 2008; Vasudevan et al., 1981; Yue, 2014; Yue et al., 2013). In implant test, a cylindrical test specimen is inserted into a hole in the test plate. The schematic of implant test with dimensions is depicted in Fig. 6.3(a-c). The implant test specimens were prepared from P92 steel as per dimensions are given below: Base plate (thickness-9.52 mm, width-50.80 mm, length-66.68 mm and center hole diameter-6.35 mm) and implant specimen (total length-41.27 mm, gripping diameter-9.52 mm, thread type ¼-28 UNF, pitch-0.907 mm, major diameter-6.35 mm, minor diameter-5.24 mm, thread length-9.52 mm, thread angle-60^o and thread root radius-0.1 mm). The cylindrical specimen was affixed with test plate specimen by using a standard weld bead.

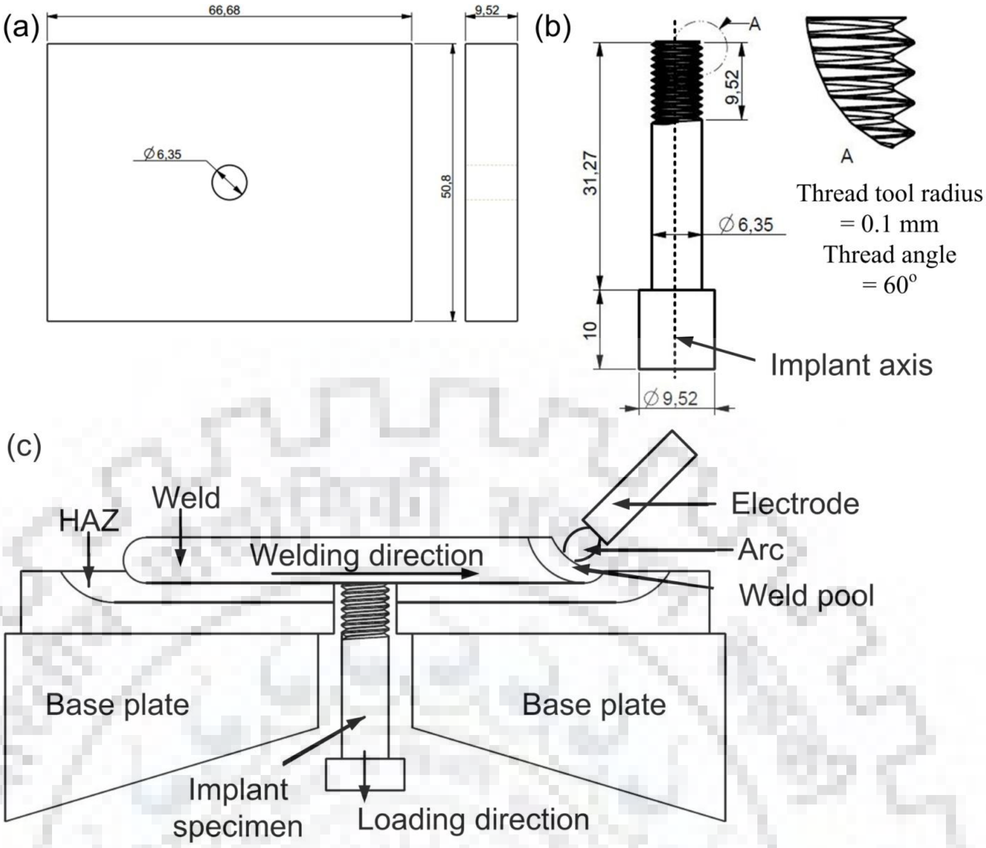

Figure 6.3 The schematic of implant test: (a) base plate, (b) implant specimen, and (c) test assembly

The implant test electrode conditions and welding parameters were similar as used for diffusible hydrogen test. To introduce diffusible hydrogen in deposited metal the three different electrode conditions (with drying, without drying, and dipped in oil) were utilized. In each test, the preheating of implant specimen and base plate was carried out at 250 ^{o}C for 1 h before using in implant test assembly (Albert et al., 2011). In each case, a single pass weld bead was deposited with 4 mm diameter electrode by using the SMAW process. The bead was passed over the hole and thread. After the completion of bead depositing, the implant specimen was quenched in ice water, within 15 s. The implant specimen was subjected to the static tensile load within a minute after bead depositing on the Universal Testing Machine (Instron) as per reference (Bradley, 1981). The selection of tensile stress was taken from the load divided by the cross-section area of the root diameter of the thread. The time required to fail the implant sample for each stress condition was noted. A plot of failure stress versus time was obtained from the Granjon implant test.

6.1.5 *Material characterization and testing*

Standard metallographic techniques were utilized to characterize the microstructural evolution during aging. The specimens were mounted, ground, polished with SiC sand-papers (Grit 120, 300, 600 and 1200) and cloth polished using a Buehler Meta-ServTM-250 grinder polisher. The cloth polished specimens were etched using Vilella's reagent for 85 s. The hardness of fractured and un-fractured samples was measured using Vickers Microhardness Tester (Omnitech-S. Auto). The load was taken as 500 g and dwell time of 10 s for the hardness measurement. Field emission secondary electron microscope (FESEM) was used to study the fracture surface morphology of implant samples.

6.2 Results and discussion

6.2.1 *Effect of electrode conditions on diffusible hydrogen content and their effect on embrittlement of P92 steel*

6.2.1.1 Diffusible hydrogen measurement

At the time of bead depositing, the hydrogen absorbed in deposited metal (weld fusion zone) has a high tendency to diffuse into the HAZ. The parameters which affect the diffusion of hydrogen in deposited metal depends on temperature, residual stress, solubility, the microstructure of metal and trapping effect. The microstructure of weld fusion zone and HAZ of P92 steel weldment is martensitic with some delta ferrite patches. The susceptibility to HAC is increased due to high hardenability and lath martensitic microstructure of P92 steel weldments. This resulted, the solubility of hydrogen in HAZ matrix decreases and hydrogen present in HAZ becomes supersaturated. The re-distribution of hydrogen atom during cooling makes the HAZ more susceptible to HAC. The diffusion of a hydrogen atom from weld metal (ferrite) to HAZ (austenite) occurs because hydrogen has lower solubility in ferrite as compared to austenite.

In the present investigation, the diffusible hydrogen level shows a great variation in all three cases considered. The diffusible hydrogen test results are depicted in Table 6.3. The minimum level of diffusible hydrogen was measured for the case I (electrode dried at 300 ^{o}C for 2h), i.e. 2.345±0.26 ml/100 g of deposited metal. The case III had a highest diffusible hydrogen level of 12.45±2.97 ml/100 g of deposited metal. The level of diffusible hydrogen was measured 2.925±0.39 ml/100 g of deposited metal (case II). To study the effect of diffusible hydrogen content on the performance of weldments, the hydrogen atoms are introduced forcefully in case III by dipping electrode in 15W grade oil. Hence, the selection of consumable is very important to attain lower hydrogen level in weld fusion zone.

Table 6.3 Diffusible hydrogen content for different condition of weld consumable

Electrode condition	Diffusible hydrogen content (ml/100g)			
	Trial 1	Trial 2	Mean	Standard deviation
Dried	2.16	2.53	2.345	0.26163
Without drying	2.43	3.2	2.925	0.388909
Oil dipped	10.35	14.55	12.45	2.969848

6.2.1.2 Granjon implant test

The top and side views of welded implant specimen with base plate are shown in Fig. 6.4(a-b), respectively. For the case I, the unfractured implant test specimen sectioned near implant axis is represented in Fig. 6.5. For each case, the microcracks are clearly observed in weld fusion zone and coarse grain heat affected zone (CGHAZ) because of rapid quenching in water and presence of diffusible hydrogen. It was observed that the HAZ is formed in the threaded region as shown in Fig. 6.5.

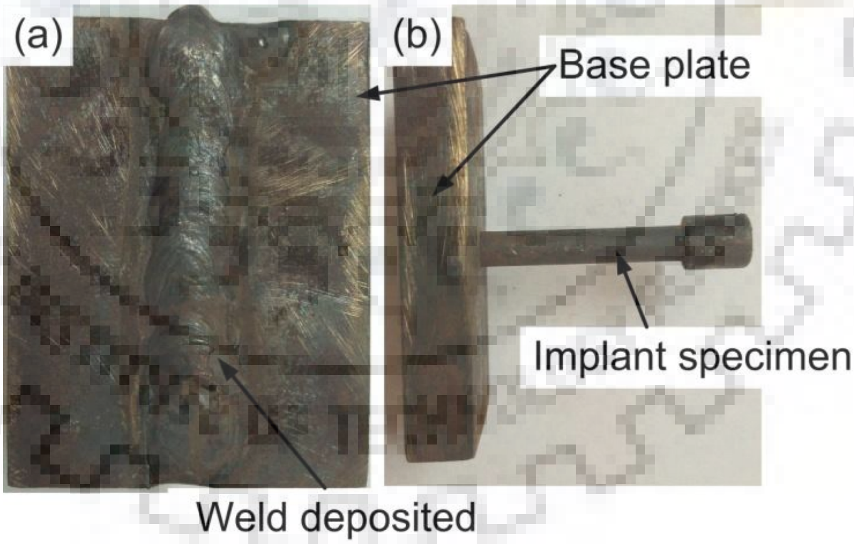

Figure 6.4 Implant test assembly (a) top view and (b) side view

Due to the difference in heat flow, it was clearly observed that the width of HAZ is more in implant specimen compared to the adjacent plate, from Fig. 6.5. It was occurred due to a shallower temperature gradient. At the time of welding, the hydrogen gas decomposed to atoms of hydrogen. During solidification of the weld, a large reduction in solubility of hydrogen occurred. From the weld fusion zone, the hydrogen atom tries to diffuse out. As the result of rapid cooling, some atoms of hydrogen are trapped in deposited metal. This resulted in the formation of porosity and microcracks in weld fusion zone. In weldments (weld fusion zone and HAZ), the atomic hydrogen penetrates deeper, which are responsible for HAC to occur.

Table 6.4 Implant test results for different condition of weld consumable

Electrode condition	Diffusible hydrogen content (ml/100 g)	CGHAZ max hardness (HV5)	CGHAZ tensile strength (MPa)	Lower critical stress (MPa)	NCSR	Embrittlement index (%)
Dried	2.345	545	1886	237	0.456	12.56
Without drying	2.925	540	1866	225	0.432	12.05
Oil dipped	12.45	535	1847	190	0.365	10.28

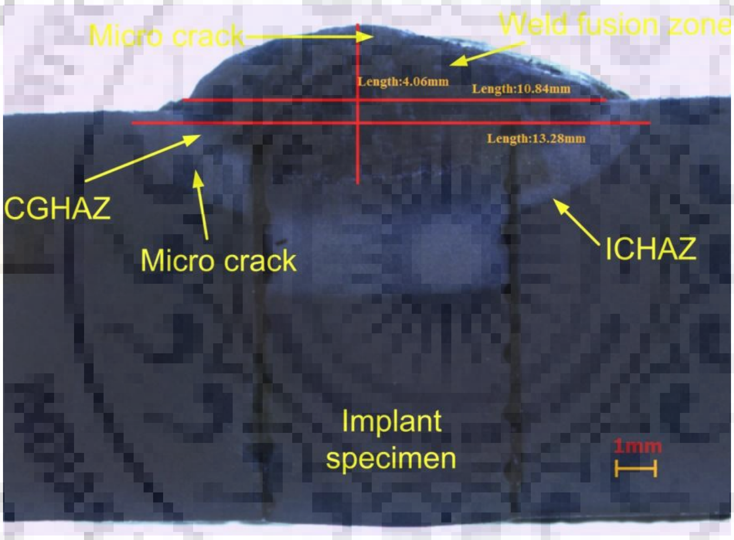

Figure 6.5 Unfractured implant test specimen sectioned near implant axis for Case I

It was observed that during tensile loading the thread into the implant specimen acted as a stress concentrator and failure occurred in the CGHAZ (stress concentrated HAZ) region instead of weld fusion zone. Fig. 6.6(a-b) represents the fractured implant specimen for case II and case III, respectively. It was clearly observed that the CGHAZ region is more prone to HAC. It was observed that crack initiates from CGHAZ region and propagates, as a result of coarse PAGBs and highly susceptible martensitic microstructure with high hardness. The crack initiation occurred from the un-fused helical notch present in the CGHAZ as shown in Fig. 6.6(a-b) and crack may propagate either through weld fusion zone or HAZ region.

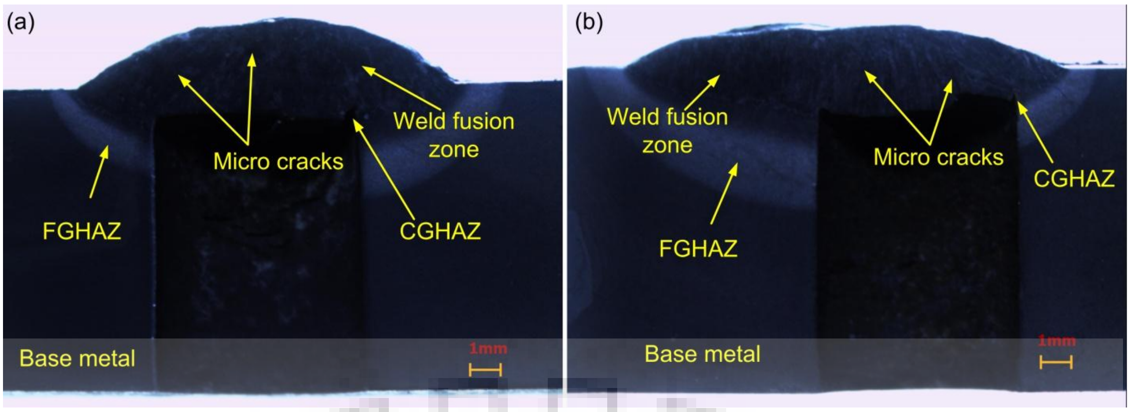

Figure 6.6 Fractured implant test specimen (a) Case II and (b) Case III

The Vickers hardness of unfractured implant samples was measured along the axis of the implant specimen in all three cases, starting from the weld fusion zone and through the HAZ to the unaffected base metal, as shown in Fig. 6.7(a-c). For all three cases, the weld fusion zone hardness exists in the range of 503 HV to 561 HV. The high hardness of weld fusion zone is found because of the presence of untempered lath martensitic structure. The minimum and maximum hardness in weld fusion zone occurred in case I.

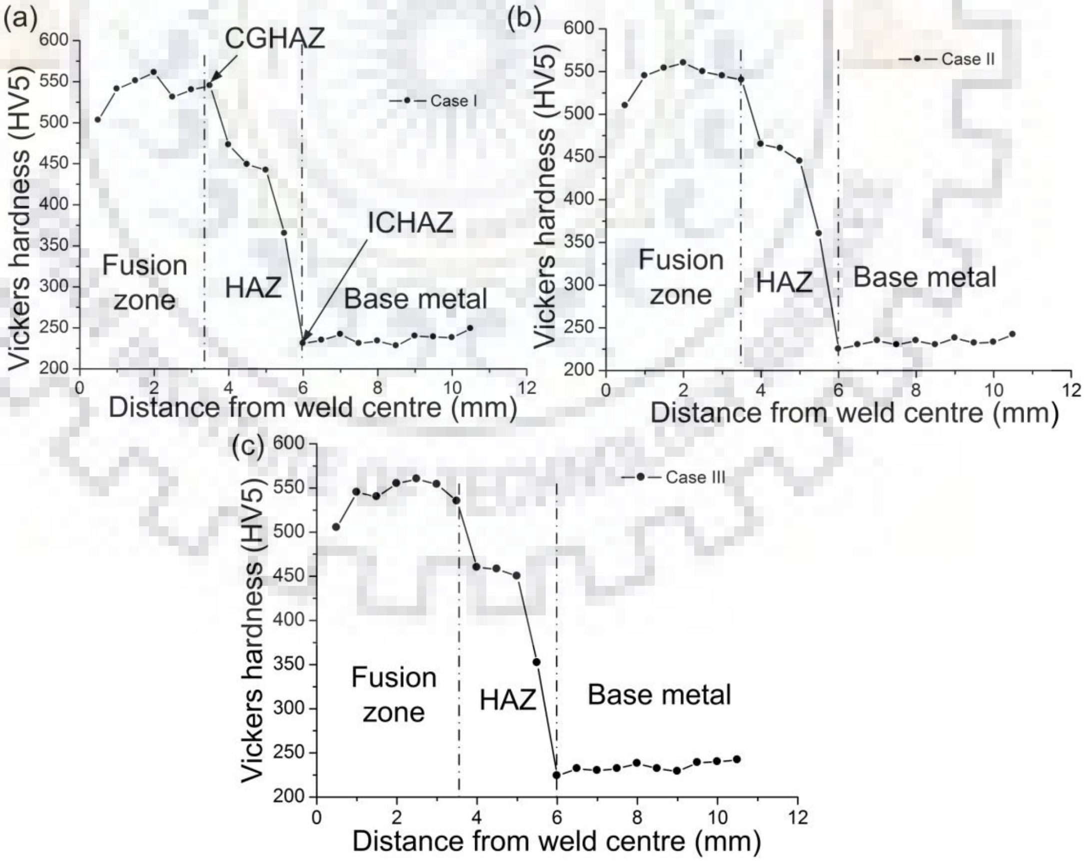

Figure 6.7 Vickers hardness measurement along the axis of implant specimen: (a) Case I, (b) Case II and (c) Case III

The variation in hardness value across the HAZ for all three cases is a direct notation of presence of different microstructure. In case I, the hardness value of HAZ was decreased from CGHAZ to fine-grained heat affected zone (FGHAZ) and into inter-critical heat affected zone (ICHAZ) as shown in Fig. 6.7(a). The minimum hardness value for HAZ was measured in the ICHAZ zone. The similar hardness pattern was obtained in rest two cases. The CGHAZ hardness was measured in the range of 494 HV to 545 HV for all three cases, which is much higher than the ICHAZ hardness value (231 HV to 224 HV). The lower hardness in ICHAZ indicates the softening in HAZ. The strength of soft zone (ICHAZ) can be improved by PWHT (Pandey and Mahapatra, 2016c). The CGHAZ maximum hardness was found 545, 540, and 535 HV for the case I, case II, and case III, respectively. Similar hardness variation is found in case II and case III as shown in Fig. 6.7(b) and (c), respectively.

Lower critical stress (LCS) was determined by plotting a curve between applied stress (MPa) and failure time (min) which showed that for lower applied stress, longer incubation time was required for fracture.

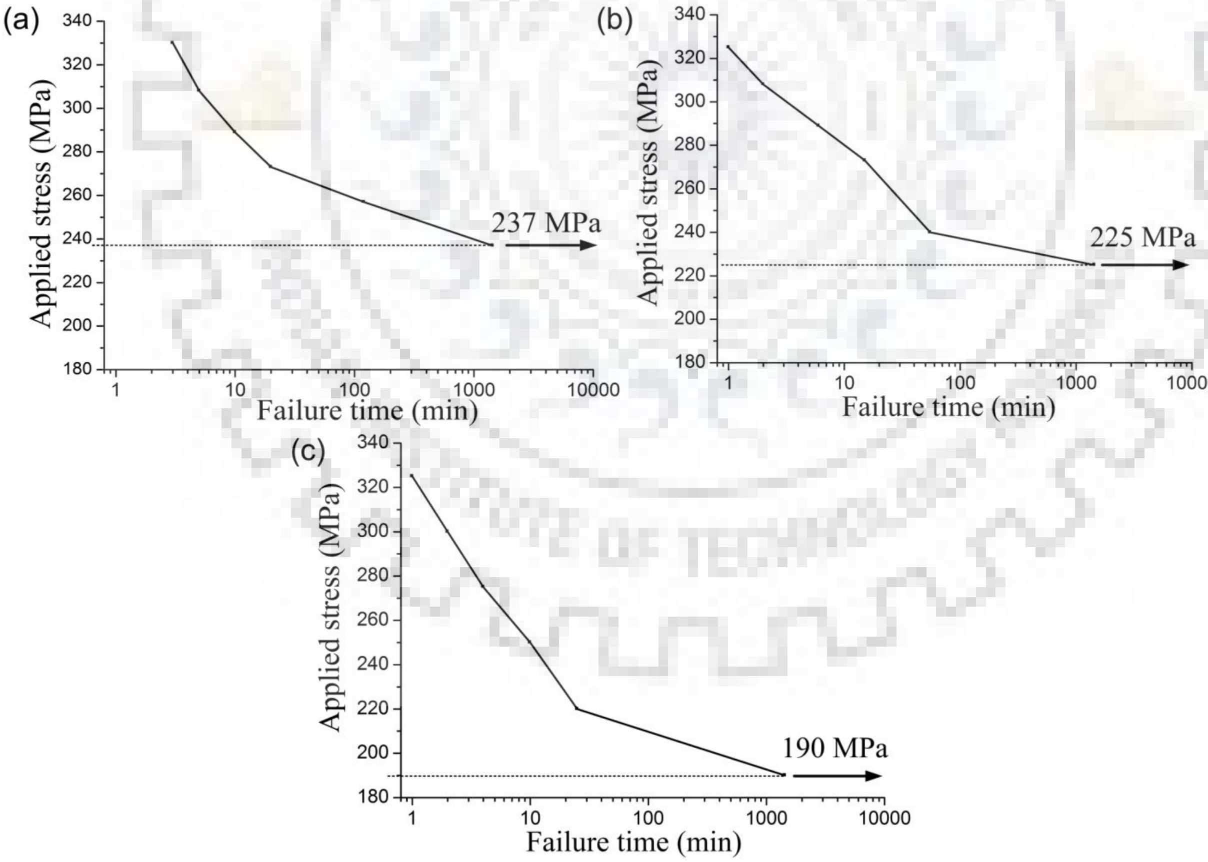

Figure 6.8 Implant test results for different test cases: (a) case I, (b) case II and (c) case III

By using the ASTM hardness conversion chart [46], the hardness value of CGHAZ was converted to CGHAZ tensile strength. The implant test results for the three different cases of the electrode are shown in Fig. 6.8(a-c). For all three cases, a similar trend has been obtained. Initially, the stress applied to the implant specimen for the case I was 330 MPa at the load of 10.08 kN. The applied stress is much lower than the YS of N&T P92 steel (520 MPa) and lower than the CGHAZ tensile strength (1886 MPa) but implant specimen fractured after 3 min of the loading. The lower time fracture of implant specimen indicates the high susceptibility of P92 steel to HAC. Hence, implant specimen fails in a short period of time at the high-stress level. For the case I (unfractured sample), at the stress of 237 MPa, the implant specimen did not fracture for 24 h of loading as shown in Fig. 6.8(a).

The Granjon implant test results are presented in Table 6.4. The LCS value was obtained from the experiments to be 237 MPa, 225 MPa and 190 MPa for the case I, case II and case III, respectively. The normalized critical stress ratio (NCSR) denotes that ratio of LCS evaluated from implant experiment to nominal yield strength of N&T P92 steel. To quantify the influence of hydrogen, the ratio of LCS to CGHAZ tensile strength is used to represent the embrittlement index of material.

The diffusible hydrogen level present in the deposited metal directly affects the LCS, i.e. performance of material. The effect of diffusible hydrogen level on LCS value and embrittlement index (EI) is shown in Fig. 6.9. As the diffusible hydrogen level increases in deposited metal, the LCS value decreases. From implant test, the lowest diffusible hydrogen level was measured for the case I (2.345 ml/100 g) for which high value of LCS (237 MPa) was obtained. The maximum value of diffusible hydrogen was measured about 12.45 ml/100 g in deposited metal for case III and for the same condition LCS value was determined about 190 MPa. The decrease in LCS value directly affects the EI and a decrease in the value of EI may be the cause of degradation in the performance of material.

The secondary electron fractographs of implant specimen in case II (electrode without drying) are represented in Fig. 6.10(a-b). The general fracture appearance of implant specimen in case II is shown in Fig. 6.10(a). The implant specimen was loaded under a stress of 325 MPa and failure was occurred after 2 min of loading. Cleavage type failure can be observed in the crack initiation zone. Generally, crack initiation zone is present near the root of the unfused helical thread. Both quasi-cleavage facets and ductile dimples were observed in the final fracture surface of implant specimen in case II as shown in Fig. 6.10(b).

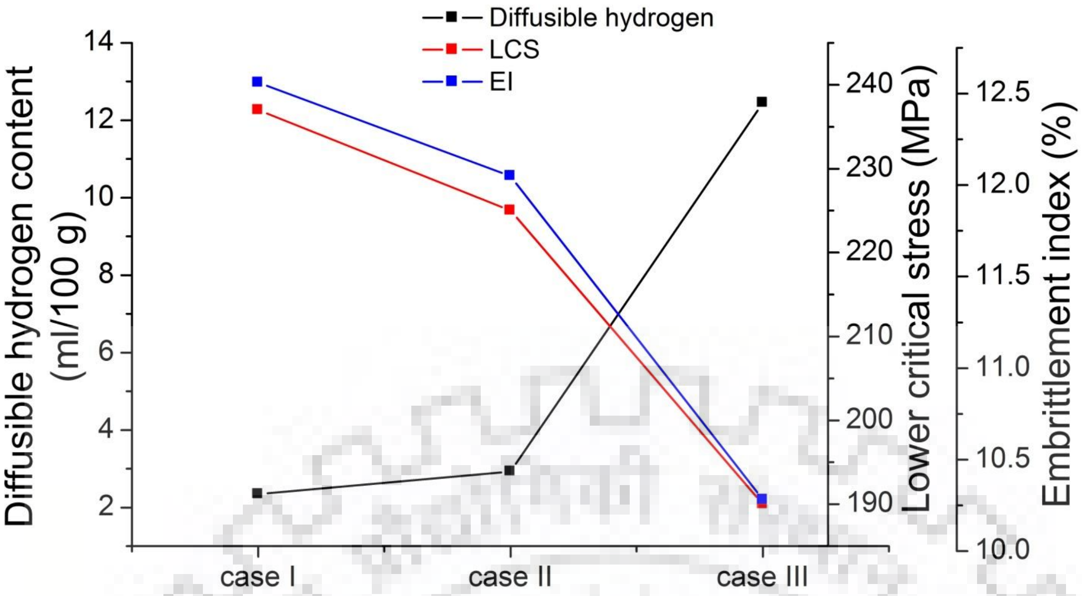

Figure 6.9 Effect of diffusible hydrogen content on embrittlement index and lower critical stress

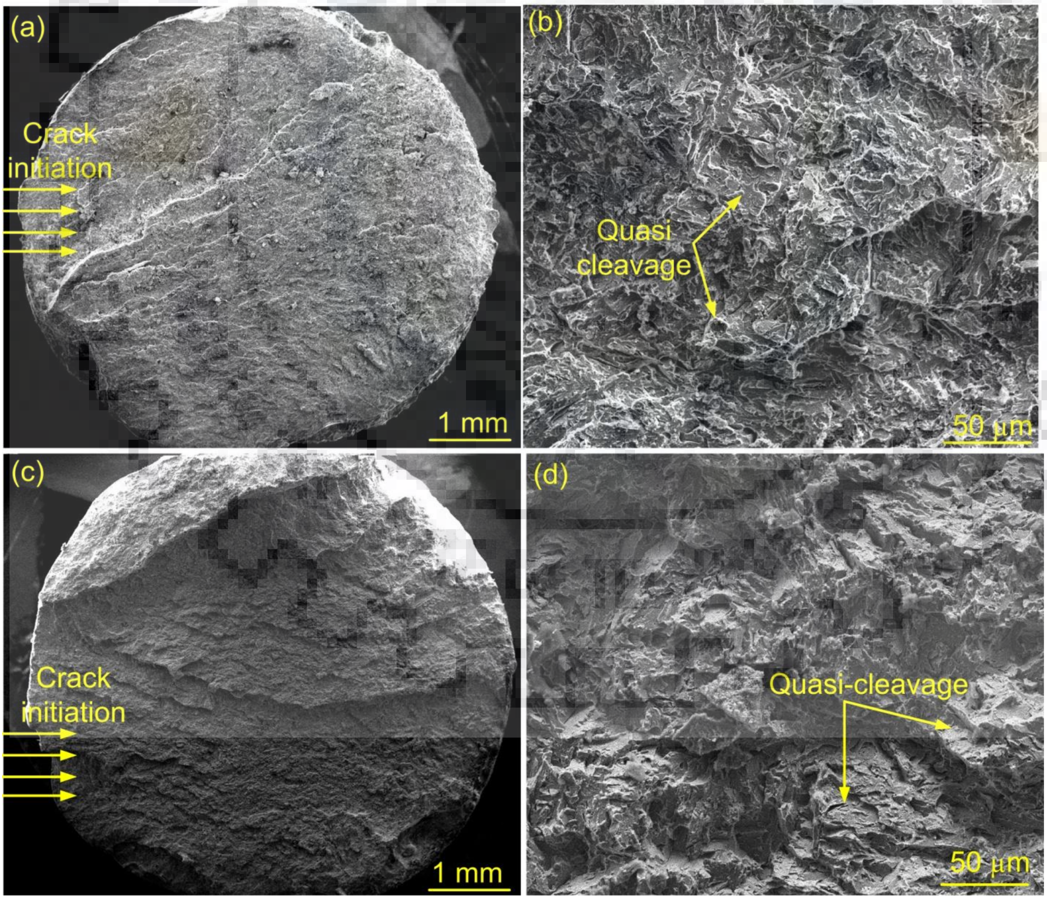

Figure 6.10 Fracture surface morphology of implant specimen in: (a) & (b) case II under a stress of 325 MPa with failure after 2 min of loading, (c) & (d) case III under a stress of 325 MPa with failure after 1 min of loading

A large area of quasi-cleavage facets is observed as compared to the small area of ductile dimples. The mixed mode fracture was observed in the final fracture surface of implant specimen as shown in Fig. 6.10(b). The final fracture occurred due to coalescence of microvoids. Fig. 6.10(c) represents the general appearance of the final fracture surface of implant specimen in case III. The crack initiates from the un-fused helical thread and propagates intergranularly as shown in Fig. 6.10(c). The final fracture zone is characterized with quasi-cleavage facets and a negligible amount of ductile dimples as shown in Fig. 6.10(d). The final fracture of implant specimen in case III occurred in a brittle manner. The increase in the level of hydrogen with crack propagation might be the cause of the change of fracture sequence from mixed mode to brittle (quasi-cleavage coalescence) fracture.

6.2.2 *Effect of welding conditions on diffusible hydrogen content and their effect on embrittlement of P92 steel*

6.2.2.1 Diffusible hydrogen measurement

The diffusible hydrogen results for Grade P92 steel welds from the mercury method are presented in Table 6.5. The measured diffusible hydrogen content was maximum for condition I (lower heat input). The average diffusible hydrogen was 8.2±0.77 ml/100 g of deposited metal in low heat input welds. An increase in the welding current (high heat input) resulted in a decreased level of diffusible hydrogen. The diffusible hydrogen content for condition II was 5.08±0.51ml/100 g of deposited metal. The condition III had the lowest diffusible hydrogen content of 2.5±0.72 ml/100 g of deposited metal. Table 6.5 suggested that the diffusible hydrogen content will increase with an increase in heat input during welding of Grade P92 steel. Hence, to achieve lower hydrogen content in the welds, the selection of welding parameters is very crucial. The HAZ HAC susceptibility is amplified due to hydrogen atom diffuses from ferrite (weld metal) to austenite (HAZ). Because hydrogen has higher solubility in austenite as compared to ferrite.

Table 6.5 Diffusible hydrogen values for different welding conditions

S.N.	Sample condition	Diffusible hydrogen (H_D)			
		Trial 1	Trial 2	Mean	Standard deviation
1	condition I	7.662	8.754	8.2	0.77
2	condition II	4.647	5.369	5.08	0.51
3	condition III	3.049	2.032	2.5	0.72

6.2.2.2 Granjon implant test

After welding, static tensile loading was applied to implant samples and hold for 24 hrs until a fracture occurs. The Granjon implant test results for Grade P92 steel welds are presented in Table 6.6. A curve applied stress (MPa) versus failure time (min) was plotted to determine the lower critical stress (LCS). This curve represents that the longer incubation time required before fracturing for low-stress values. The implant test results for all welding conditions are grouped, as shown in Fig. 6.11. A similar trend has been observed for all welding parameters. Initially, the applied stress to the implant sample was 280 MPa (load-9.3 kN) for condition I which was much lower than the yield strength of the Grade P92 steel (520MPa). But the sample was fractured just after 4 min of loading. The fracture of sample in such a small time indicates the higher susceptibility of Grade P92 steel to hydrogen assisted cracking (HAC). The sample did not fracture at 121 MPa of stress after 24 hrs of loading. Hence, lower critical stress (LCS) value for condition I was 121 MPa. The same procedure repeated to find out the LCS values for other two conditions. The LCS values were 170 MPa and 184 MPa for condition II and condition III, respectively.

Table 6.6 Implant test results for different welding process parameters

S.N.	Sample condition	Stress (MPa)	Load (KN)	Failure time
1	condition I	280	9.3	4 min
		250	8.3	7 min
		230	7.6	8 min
		200	6.6	15 min
		170	5.6	30 min
		121	4	24 hrs
2	condition II	280	9.3	8 min
		250	8.3	12 min
		230	7.6	31 min
		200	6.6	35 min
		170	5.6	24 hrs
3	condition III	280	9.3	10 min
		250	8.3	15 min
		230	7.6	35 min
		200	6.6	40 min
		184	6.1	24 hrs

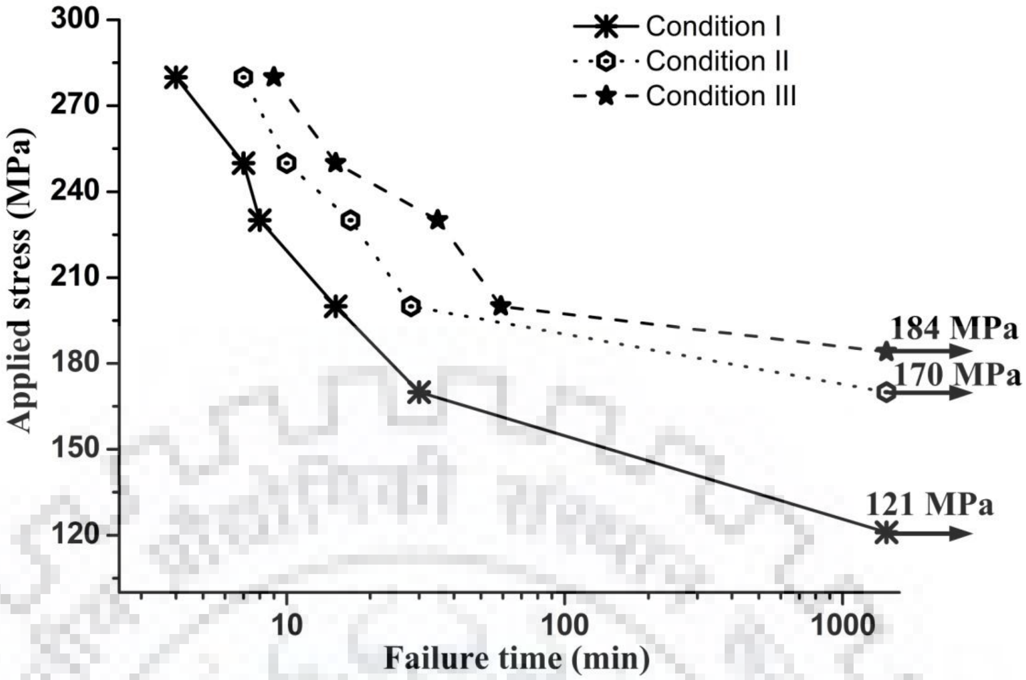

Figure 6.11 LCS for all welding conditions from applied stress versus failure time (min) curve

The fractured cross-section of implant tested samples are shown for the condition I, II and III, respectively (Fig. 6.12(a-c)). For all conditions, the fracture was observed in the coarse grain heat-affected zone (CGHAZ) instead of weld fusion zone due to thread in the implant sample which acted as a stress raiser or concentrator. The crack initiation occurred from the CGHAZ and crack may propagate either trough FGHAZ or weld fusion zone (Fig. 6.12(a-c)). Hence, we can say that the CGHAZ region was more prone to HAC due its high hardness, coarse prior austenite grain boundaries (PAGB's) and martensitic microstructure.

A schematic representation of crack propagation through deposited weld metal i.e., weld fusion zone at a higher level of stresses or shorter time for fracture is shown in Fig. 6.13(a). In this study, the fracture was in the CGHAZ instead of weld fusion zone due to thread in the implant sample which acted as stress concentrator. A schematic of crack propagation through CGHAZ at lower stress level (higher time for fracture) is shown in Fig. 6.13(b). To initiate cracking at lower level of stress, the critical hydrogen content is higher and required higher time to reach that level at the notch tip of thread. During that time more hydrogen diffuses into CGHAZ from weld fusion zone and makes hydrogen distribution uniform. Hence diffusion hydrogen level of CGHAZ increases and cracks initiated from CGHAZ i.e., notch tip. The cracks propagate in the FGHAZ or in the weld fusion zone. The previous studies on the susceptibility of CSEF steels towards HAC have shown that both CGHAZ and weld fusion zone are susceptible to HAC (Kalbert et al., 2003; Chandan Pandey et al., 2016).

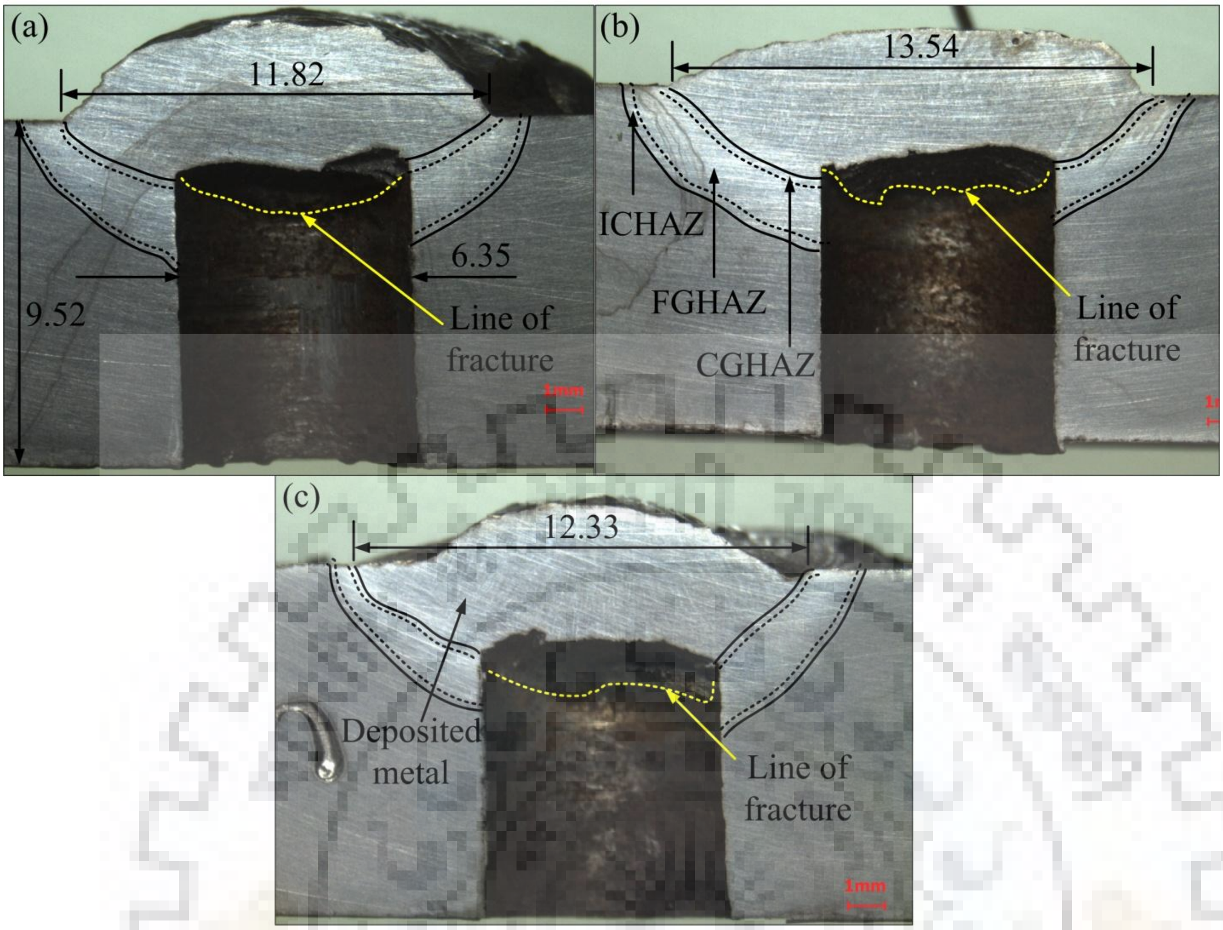

Figure 6.12 Fractured implant test samples showing line of fracture (a) condition I, (b) Condition II and (c) condition III

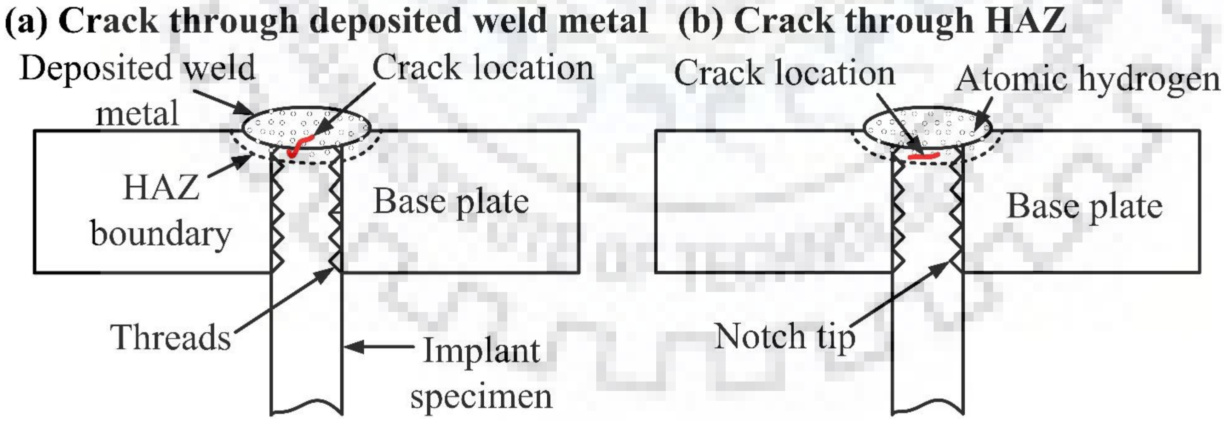

Figure 6.13 Schematic of crack propagation in the implant sample through (a) deposited weld metal (at higher stress levels), and (b) CGHAZ (at lower stress levels)

All unfractured implant specimens for different welding conditions were measured for The microhardness (Vickers) along the axis of implant sample. Figure 6.14 shows the Vickers microhardness plots for different welding process parameters stating from the weld center to the base material. Three rows of matrix were performed for each condition using the automated microhardness tester and average of three-row microhardness was plotted. The hills and valleys were observed in the hardness of weld fusion zone for all three conditions. This variation in microhardness across weld fusion zone is a notation of presence of soft δ-ferrite phases. The presence of soft δ-ferrite zones in the weld fusion zone is responsible for lower hardness while untampered lath martensite for higher hardness. Microhardness of HAZ decreases from CGHAZ to base material for all conditions. To calculate embrittlement index (EI), the maximum CGHAZ hardness was measured as 504, 496 and 484 HV for condition I, condition II and condition III, respectively.

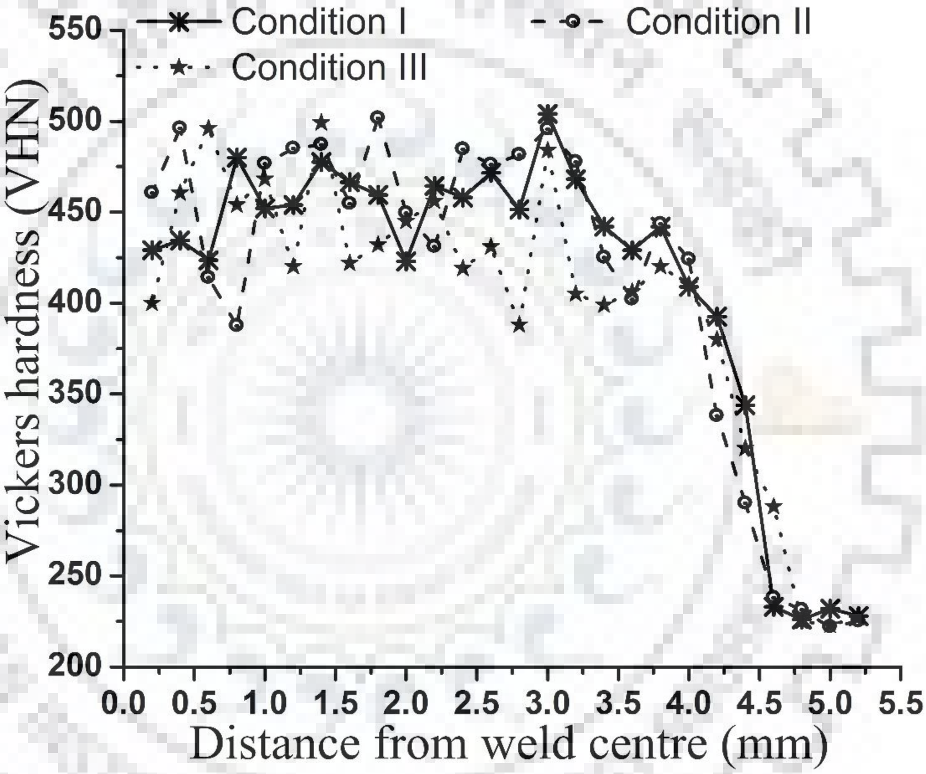

Figure 6.14 Microhardness of unfractured implant samples for different welding conditions

Table 6.7 Embrittlement index calculation from Granjon implant test results

Different welding parameters	Diffusible hydrogen (ml/100 g)	CGHAZ max hardness (HV)	CGHAZ tensile strength (MPa)	Lower critical stress (MPa)	Embrittlement index (%)
Condition I	8.2±0.77	504	1709	121	7.08
Condition II	5.08±0.51	496	1676	170	10.14
Condition III	2.5±0.72	484	1626	184	11.31

The CGHAZ tensile strength was predicted using the ASTM hardness conversion chart corresponding to maximum CGHAZ hardness values (Table 6.7). The ratio of LCS to CGHAZ tensile strength was calculated for all three conditions and presented as EI in Table 6.7. The value of EI was increased with decreased content of diffusible hydrogen. The effect of heat inputs on diffusible hydrogen contents as well as on EI (performance of welded joint) is shown in Fig. 6.15. The LCS increases with decrease in diffusion hydrogen content. The highest value of LCS (184 MPa) was measured for condition III (lower level of diffusible hydrogen). Hence, welding process parameters severe affect the contents of diffusible hydrogen in welds which influence the LCS and performance of the welded joint.

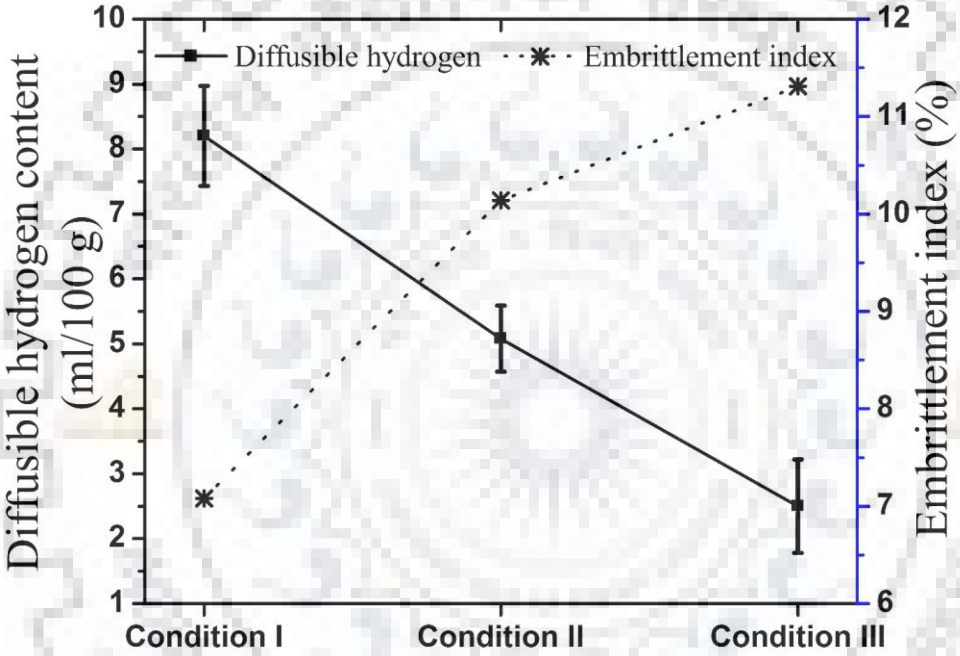

Figure 6.15 Effect of heat inputs on diffusible hydrogen content and on embrittlement index

The secondary electron micrograph of fractured implant sample for the condition I is shown in Fig. 6.16(a). For condition I, only quasi cleavage facets are seen in the fracture surface of implant sample. Quasi cleavage facets and ductile dimples with negligible amount observed for condition II in the fracture surface of implant sample (Fig. 6.16(b)). So, brittle mode of fracture occurred in implant specimen for condition I and II. The higher diffusible hydrogen content in welds might be the cause of brittle fracture. Figure 6.16(c) shows the fracture surface of implant sample in condition III which shows both quasi cleavage facets and ductile dimples. The mixed mode of fracture observed in condition III. The decrease in diffusible hydrogen content might be the cause for change of fracture mode from brittle to mixed mode.

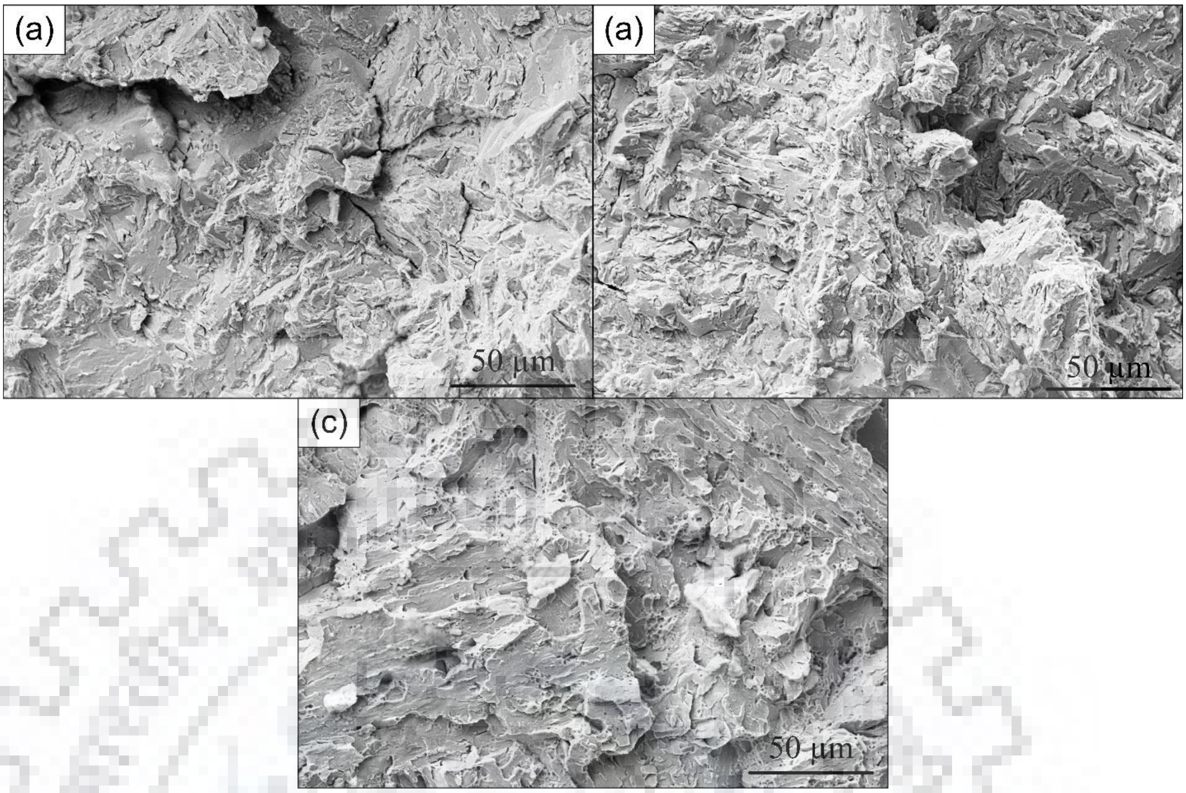

Figure 6.16 Fracture surface morphology of implant specimen under a stress of 280 MPa (a) condition I, (b) condition II and (c) condition III

6.3 Conclusions

- The diffusible hydrogen measurement and implant test to evaluate susceptibility for HAZ hydrogen cracking of P92 steel were successfully performed with welding electrode of E-911(Metrode: CH12MV-40). It was found that CGHAZ of P92 steel is highly susceptible to HAC because of the martensitic microstructure.
- A continuous increase was observed in the lower critical stress value with the decrease in the diffusible hydrogen content. Taking both the normalized critical stress ratio and embrittlement index in consideration along with hydrogen level for HAC susceptibility of HAZ, P92 steel in case I offer better resistance to HAC of HAZ compared to other cases.
- The Granjon implant test and mercury method were successfully used to evaluate susceptibility towards embrittlement (HAZ-HAC) of Grade P92 steel with different welding conditions using MAILARC–P92 filler. Both CGHAZ and weld fusion zone are observed highly susceptible to HAZ HAC due to its martensitic microstructure.
- The higher heat input resulted in decrease in diffusible hydrogen content in deposited weld metal. The weld deposited using higher heat input also shows higher resistance to

HAZ HAC as compared to other two conditions due to low content of diffusible content.

CHAPTER 7. CONCLUSIONS AND FUTURE SCOPE

The conclusions and scope of future research are discussed in this Chapter.

7.1 Conclusions

From the optimization of C&F P92 steel the following conclusions can be drawn:

- The distributions and size of precipitates were more prominent at the PAGBs than the interior of the matrix from SEM micrographs of as-received C&F P92 steel. It was also observed from the EDS spectra that the coarse white precipitates present at PAGBs were enriched with Cr and W as compared to fine precipitates present in matrix region. The size of precipitates accumulated along the PAGBs was found to be increase with increase in normalizing temperature.

- The Cr/Fe ratio continuously increased for normalizing at 950 °C and 1000 °C, and then, it started to decrease with normalizing temperature from 1050 °C to 1150 °C. The minimum and maximum Cr/Fe ratio was calculated for the normalizing temperature at 950 °C and 1050 °C, respectively. The diffusion of Cr into the carbides results to the evolution of meta-stable $M_{23}C_6$ phase, which is a consequence of the increase in Cr/Fe ratio.
- The yield strength (YS) and ultimate tensile strength (UTS) decreases with an increase in normalizing temperature. With the increase in normalizing temperature, the ductility was found to be increased and a decrease was found at the normalizing temperature of 1050 ^{o}C.
- Based on the observation of an optimum combination of strength, ductility, and toughness, the maximum normalizing temperature upto 1050 ^{o}C has been suggested for C&F P92 steel.
- The tensile fracture surfaces for the various normalizing temperature of as-received P92 steel were characterized by ductile tear ridges, transgranular cleavage facets, and transgranular ductile dimple tearing. The tensile fracture surfaces for normalized test samples at 1100 °C and 1150 °C were characterized by cleavage facets and with less number of dimples.
- The Charpy fracture surface of various normalized specimens showed mainly dimples and the cleavage facets and the mode of fracture was mixed type up to 1050 °C. After tempering the mixed mode of fracture mechanism was observed up to 1100 °C. The

fracture surfaces are characterized by transgranular ductile dimple tearing and some areas of quasi-cleavage facets.

- After thermal exposure, the embrittling effect occurred due to coarsening of secondary phase carbide precipitates along the PAGBs and within the grains. This effect was more pronounced in impact toughness testing as compared to tensile testing.

From the long-term aging of P92 steel the following conclusions can be drawn:

- During ageing, the evolution of Laves phase was found to have pronounced effect on mechanical properties of P92 steel. The presence of Laves phase was confirmed in all the aged samples.
- The strength and ductility and Charpy toughness were decreased after 720 h of ageing and this is attributed due to a loss in solid solution strengthening and formation of Laves phase. The rate of decrement was faster at the initial stage of ageing (720 h) and after that it become stable due to slow coarsening rate of Laves phase.
- The $M_{23}C_6$ precipitate size was measured to be 152 ± 22 nm and 178 ± 40 nm for aged samples of 720 hrs and 3000 hrs, respectively while the size of Laves phase was observed to be increased from 180 ± 20 nm to 300 ± 35 nm with increase in ageing time from 720 hrs to 3000 hrs.
- The Mo/Fe and W/Fe ratio increased continuously with increase in ageing time. The XRD analysis of thermal aged samples also confirms the presence of Fe_2W Laves phase after the ageing of 720 h at 650 ^{o}C.
- The Charpy toughness decreased continuously in thermal aged specimens due to coarse Laves phase. Hence, Laves phase evolution during ageing of P92 steel is a critical factor that governs the thermal degradation of P92 steel structures.

From effect of normalizing and tempering on dissolution of Laves phase following conclusions can be drawn:

- After aging, the presence of the Laves phase was confirmed using XRD peaks and secondary electron micrographs (SEMs). The coarsening of $M_{23}C_6$ precipitates was also confirmed using SEM results. The higher coarsening rate of the Laves phase was simulated as compared to $M_{23}C_6$ precipitates during prolonged exposure to tempering.
- The dissolution of the Laves phase was confirmed using XRD and SEM results after Aged+N&T4 treatment. After N&T of aged specimens, the grain size and microhardness were not changed significantly while the average precipitate size was

achieved almost similar to the base material. The effort of recovering the microstructure using re-austenitization and tempering treatment can be achieved.

- A model is suggested to predict dissolution time for Laves phase. The driving force for Laves phase precipitation decreases with increasing temperature above 620 ^{o}C. The precipitation map for the Laves phase suggested that the steel composition can be designed to avoid precipitation of Laves phase.
- A re-austenitization and tempering treatment was suggested following aging of P92 steel. Re-austenitization may be performed at 1050 ^{o}C for 1h and tempering may be performed at 760 ^{o}C for 4 hrs to maintain precipitation strengthening effect.

From the double austenitizing treatment the following conclusions can be drawn:

- After two-stage austenitizing treatment, the prior austenite grain size was refined to 19 µm (1150^{o}C/1 h//water quench, 1040 ^{o}C/1 h/air cool' and'760 ^{o}C/2 h/air cool') as compared to 33 µm of a conventional normalizing treatment (CNT).
- A homogenous tempered microstructure was obtained after 'double austenitization based normalizing and tempering' (DNT) treatment. For CNT, DNT 1, DNT 2 and DNT 3 treatment, hardness was measured to be 225, 230, 224 and 219 HV which clearly confirmed the softening of the material after the DNT 3 treatments as compared to CNT and DNT 1 treatment.
- A drastic reduction in hardness and strength was observed after the DNT 2 and DNT 3 treatment. The reduction in strength and hardness was attributed to a reduction in solid solution strengthening.
- The optimum microstructure stability and mechanical properties were obtained for the DNT 3 treatment (1150^{o}C/1 h//water quench, 1040 ^{o}C/1 h/air cool' and'760 ^{o}C/2 h/air cool') as a result of the grain refinement.
- The tensile fracture surface revealed the mixed mode of fracture and showed the presence of ductile fine dimples, deep dimples, shear lip, cleavage facets and tear ridges. The shear lip zone was also observed near the deep dimples as a result of the plastic deformation. The formation of deep dimples was associated with the with the coarse $M_{23}C_6$ particles that act as the crack nucleation sites due to their brittle nature. The triple point associated with higher density of precipitates facilitate the most preferential sites for the crack nucleation.

From optimization of preheating temperature and prediction of preheating temperature for thin plates in autogenous TIG welds by using Rosenthal equation the following conclusions can be drawn:

- The depth of penetration (DOP) was maximum with preheat temperature of 300 ^{o}C. The weld area, DOP and the ratio of DOP to bead width were increased with preheat temperature, which might affect the microstructure or evolution of δ-ferrite in the weld pool.
- A relation was successfully developed which can predict a preheat temperature for a given plate thickness of thin plates (maximum of 7.5 mm).
- Based on empirical formula's calculation, the possibility of δ-ferrite was low, but retention of δ-ferrite was observed in all weld joints.
- The volume fraction of δ-ferrite was found to be reduced with a reduction in cooling rate. The lowest volume fraction of δ-ferrite was measured 5 ± 2 % for preheat temperature of 300 ^{o}C. Though the P92 base material was free from δ-ferrite, it would be difficult to produce δ-ferrite free weld fusion zone of P92 steel with heat input higher than 2.5 KJ/mm.

From the dissolution of δ-ferrite using post-weld heat treatments the following conclusions can be drawn:

- In the as-welded condition, the presence of δ-ferrite was confirmed using XRD, secondary electron micrographs (SEMs) and optical micrographs. After PWHT, no effect on δ-ferrite was observed. But after PWNT, the dissolution of δ-ferrite was confirmed from XRD, SEMs and optical micrographs.
- The microhardness variation throughout the weld fusion zone was greater in the as-welded and PWHT conditions due to the presence of δ-ferrite. After PWNT, uniform microhardness across the weldments was achieved which indicates elimination of heterogeneity in the microstructure across the welded joint.
- After PWNT, the Charpy toughness of the weld fusion zone was improved to similar to that of the as-received base metal while the tensile strength did not change significantly.
- Scheil's solidification calculation is performed to confirm that the δ-ferrite is not stable at PWNT temperature. A model is used to analyze the dissolution kinematics

of δ-ferrite. The model predicts with sufficient accuracy that 27 min is required to hold the welded plates at 1050 ^{o}C to dissolve the δ-ferrite.

From effect of different filler on microstructure evolution and mechanical properties of SMAW welded joints of P92 steel the following conclusions can be drawn:

- In as-welded condition, the higher strength in P92 filler was attributed to the higher weight percentage of W and Mo in P92 weld fusion zone as compared to E911 filler welds. The UTS after PWHT was found to be increased in the transverse direction of the weld whereas the value decreased in the longitudinal direction for both the fillers.
- In as-welded condition, transverse tensile specimens were fractured from fine grain heat affected zone or inter-critical heat affected zone (FGHAZ/ICHAZ) but after PWHT, the fracture location was shifted to over tempered base metal from FGHAZ/ICHAZ.
- The as-welded hardness of weld zone was measured to be 451 ± 20 and 571 ± 24 HV for E911 and P92 fillers, respectively. After PWHT, a considerable lowering in hardness was observed throughout the weldments.
- In as-welded condition, the weld fusion zone shows the poor Charpy toughness of P92 steel welds for both the fillers. In as-welded condition, poor Charpy toughness was measured for P92 filler due to the higher weight percentage of V and Nb in weld fusion zone. In as-welded condition, Charpy toughness was measured to be lower than the minimum required Charpy toughness value for both the filler. After PWHT, the weld fusion zone Charpy toughness of P92 steel welds was incresed which was higher than the minimum required Charpy toughness value.
- The charpy toughness of HAZs in as-welded condition was measured to be 120 ± 7 and 128 ± 8 J for E911 and P92 fillers, respectively. HAZ Charpy toughness of P92 steel welds after PWHT was measured to be 142± 8 and 140 ± 5 Joules for E911 and P92 filler, respectively.

From effect of post-weld heat treatments on the microstructure evolution and mechanical properties of dissimilar SMAW welded joints of P911 and P92 steel using P911 filler the following conclusions can be drawn:

- In as-received P911 and P92 steel, the microstructure is characterized with tempered lath martensitic microstructure with coarse Fe and Cr-rich $M_{23}C_6$ type carbide precipitates along the PAGBs and V and Nb-rich fine MX type precipitates within grain interior region.

- In as-welded and PWHT condition, a significant variation was observed in the microstructure of CGHAZ, FGHAZ, IC-HAZ and over tempered base metals for both P92 and P911 side. The N&T treatment resulted in a homogenize microstructure across the dissimilar weldments that lead to improve mechanical properties.
- For subsequent PWHT, the tensile strength and yield strength was increased as compared to as-welded state. Maximum tensile and yield strength were measured for N&T condition. The tensile fracture occurred from the over-tempered base metal zone in all cases. The % elongation and % reduction in the area was increased after subsequent PWHT and reached to maximum value for N&T treatment.
- The phases identified in weld fusion zone for different heat treatment conditions were Cr-rich $M_{23}C_6$, V-rich MX, Cr-rich M_7C_3, Cr and Fe-rich M_2X.
- In as-welded condition, considerable hardness gradient was observed across the weldments. PWHT resulted in a considerable lowering in the hardness gradient. Minimum hardness gradient across the dissimilar weldments was observed in N&T condition. After N&T treatment, a negligible variation in hardness was observed across the weldments.
- The Charpy toughness value of weld fusion zone was measured as 24±2, 68±4 and 110±7 Joules in as-welded, PWHT and N&T condition, respectively. The N&T treatment provides the Charpy toughness value near to the as-received P911 steel.

From the effect of filler compositions on mechanical properties of dissimilar SMAW welded joints of P91 and P92 steel the following conclusions can be drawn:

- The microstructure of weld fusion zone revealed the untempered lath martensite with high solid solution hardening for both as-welded-P91 and as-welded-P92 welded joint. The PWHT resulted in the tempering of the martensite with the evolution of new $M_{23}C_6$ and MX precipitates in the weld fusion zone. In P92 filler rod, the higher weight percentage of the ferrite stabilizer resulted in the formation of the soft δ ferrite patches in weld fusion zone that did not respond to the PWHT.
- The FGHAZ for both the filler showed the complex microstructure. In as-welded condition, FGHAZ is characterized with some undissolved coarse precipitates of size in the range of 250-300 nm with untempered lath martensite. The PWHT led to the evolution of the precipitates along with tempering of the martensite.
- The tensile strength was measured 1178 ± 16 and 1348 ± 18 MPa for P91 and P92 filler, respectively in the as-welded condition and reduced drastically after PWHT and was

measured 760 ± 10 and 858 ± 12 MPa. In the as-welded condition, maximum and minimum joint efficiency were measured 199 and 174 %, respectively for as-welded-P91 and as-welded-P92 welded joint, respectively. The higher strength and weld efficiency for P92 filler was attributed to high W percentage that enhanced the solid solution hardening.

- The 521 ± 16 and 500 ± 18 HV microhardness were measured for the as-welded-P91 and as-welded-P92 welded joint, respectively which gets reduced drastically after the PWHT and was measured 318 ± 7 and 357 ± 10 HV for PWHT-P91 and PWHT-P92 welded joint. The large heterogeneity in the hardness of the subzones was measured in the as-welded condition which was observed to reduce after the PWHT.
- The Charpy impact toughness was measured 85 ± 5 and 43 ± 7 J for PWHT-P91 and PWHT-P92 welded joint after the PWHT. The required toughness value (minimum value 47 J) was achieved for the P91 filler as per PWHT reaction. However, it was still less in case of P92 filler.

From the effect of filler conditions on diffusible hydrogen content the following conclusions can be drawn:

- The diffusible hydrogen measurement and implant test to evaluate susceptibility for HAZ hydrogen cracking of P92 steel were successfully performed with welding electrode of E-911(Metrode: CH12MV-40). It was found that CGHAZ of P92 steel is highly susceptible to HAC because of the martensitic microstructure.
- The diffusible hydrogen levels measured for the case I, case II, and case III were 2.345, 2.925 and 12.45 ml/100 g in deposited metal, respectively.
- The deposited metal using dried electrode at 300 ^{o}C for 2 h (case I) offered a greater resistance to HAC compared to other cases because of the presence of low hydrogen level.
- The Vickers hardness measured in CGHAZ was 545, 540, and 535 HV for case I, case II, and case III, respectively. Hence it can be said that for same welding process and parameters, electrode condition does not show a great impact on CGHAZ hardness and microstructure.
- The lower critical stress (LCS) value obtained for the case I, case II, and case III were 237, 225 and 190 MPa, respectively. A continuous increase was observed in the LCS value with the decrease in the diffusible hydrogen content. Taking both the normalized critical stress ratio and embrittlement index in consideration along with hydrogen level

for HAC susceptibility of HAZ, P92 steel in case I offer better resistance to HAC of HAZ compared to other cases.

- The fracture surface of implant specimen in case II revealed the presence of quasi-cleavage facets and ductile dimples. In case III, the final fracture zone mainly consisted of quasi-cleavage facets and a negligible amount of dimples.

From the effect of welding conditions on diffusible hydrogen content and their effect on embrittlement of P92 steel the following conclusions can be drawn:

- The Granjon implant test and mercury method were successfully used to evaluate susceptibility towards embrittlement (HAZ-HAC) of Grade P92 steel with different welding conditions using MAILARC–P92 filler.
- Both CGHAZ and weld fusion zone are observed highly susceptible to HAZ HAC due to its martensitic microstructure.
- The higher heat input resulted in decrease in diffusible hydrogen content in deposited weld metal. The weld deposited using higher heat input also shows higher resistance to HAZ HAC as compared to other two conditions due to low content of diffusible content.
- A small decrease in Vickers microhardness of CGHAZ observed with an increase in heat input. The higher values of lower critical stress observed for lower values of diffusible hydrogen in deposited metal using higher heat inputs. However, the weld deposited using highest heat input (condition III) offers better resistance to HAZ HAC by considering embrittlement index and diffusible hydrogen content. In condition III, the fracture surface of implant specimen shows mixed mode of failure as compared to brittle in other two conditions.

7.2 Scope of future research work

- The effect of double austenitizing based normalizing and tempering treatment on behaviour of long term aging can be studied.
- The influence of normalizing and tempering process on aging specimens and their effect on mechnaical properties can be studied.
- Effect of Inconel fillers on mechanical properties of P92 steel welds can be studied.

LIST OF PUBLICATIONS

Output of present work:

International Journal

1. N. Saini, R.S. Mulik, M.M. Mahapatra, Influence of filler metals and PWHT regime on the microstructure and mechanical property relationships of CSEF steels dissimilar welded joints, International Journal of Pressure Vessels and Piping, 170, 2019, 1-9.
2. N. Saini, R.S. Mulik, M.M. Mahapatra, Prior-austenite grain refinement in P92 steel using double austenitization treatment, Materials Research Express, 6(2), 2018.
3. N. Saini, R.S. Mulik, M.M. Mahapatra, Study on the effect of ageing on laves phase evolution and their effect on mechanical properties of P92 steel, Materials Science and Engineering: A, 716, 2018, 179–188.
4. N. Saini, C. Pandey, M.M. Mahapatra, R.S. Mulik, Characterization of P92 steel weldments in as-welded and PWHT conditions, Welding Journal, 2018.
5. N. Saini, C. Pandey, M. M. Mahapatra, Effect of diffusible hydrogen content on embrittlement of P92 steel, International Journal of Hydrogen Energy A, 42(27), 2017, 17328-17338.
6. N. Saini, C. Pandey, M. M. Mahapatra, Characterization and evaluation of mechanical properties of CSEF P92 steel for varying normalizing temperature, Materials Science and Engineering: A, 688, 2017, 250-261.
7. N. Saini, C. Pandey, M.M. Mahapatra, Effect of normalizing temperature on fracture characteristic of tensile and impact tested creep strength enhanced ferritic P92 steel, Journal of Materials Engineering and Performance, 26, 2017, 5414–5424.
8. N. Saini, C. Pandey, M.M. Mahapatra, Microstructure evolution and mechanical properties of dissimilar welded joint of P911 and P92 Steel for subsequent PWHT and N & T treatment, Transactions of the Indian Institute of Metals, 2017.

Paper Under Review:

1. N. Saini, R.S. Mulik, M.M. Mahapatra, Effect of welding process parameters on embrittlement of Grade P92 steel using Granjon implant testing of welded joints (Journal of Hydrogen Energy).
2. N. Saini, R.S. Mulik, M.M. Mahapatra, L. Li, Dissolution of Laves Phase by Re-austenitization and Tempering of Grade P92 Steel (Materials Science and Technology, Taylor and Francis).
3. N. Saini, R.S. Mulik, M.M. Mahapatra, L. Li, Dissolution of δ-ferrite and its effect on mechanical properties of P92 steel welds (Materials Science and Engineering: A).

REFERENCES

Abe, F., 2009. Analysis of creep rates of tempered martensitic 9 % Cr steel based on microstructure evolution. Mater. Sci. Eng. A 510–511, 64–69. doi:10.1016/j.msea.2008.04.118

Abe, F., 2005. Effect of fine precipitation and subsequent coarsening of Fe2W laves phase on the creep deformation behavior of tempered martensitic 9Cr-W steels. Metall. Mater. Trans. A Phys. Metall. Mater. Sci. 36 A, 321–332. doi:10.1007/s11661-005-0305-y

Abe, F., 2004. Coarsening behavior of lath and its effect on creep rates in tempered martensitic 9Cr-W steels. Mater. Sci. Eng. A 389, 565–569. doi:10.1016/j.msea.2004.01.057

Abson, D.J., Rothwell, J.S., 2013a. Review of type IV cracking of weldments in 9 – 12 % Cr creep strength enhanced ferritic steels. Int. Mater. Rev. 58, 437–473. doi:10.1179/1743280412Y.0000000016

Abson, D.J., Rothwell, J.S., 2013b. Review of type IV cracking of weldments in 9 – 12 % Cr creep strength enhanced ferritic steels Review of type IV cracking of weldments in 9 – 12 % Cr creep strength enhanced ferritic steels. Int. Mater. Rev. 58, 437–473. doi:10.1179/1743280412Y.0000000016

Albert, S.K., Ramasubbu, V., Raj, S.I.S., Bhaduri, A.K., 2011. Hydrogen assited cracking susceptibility of modified 9Cr-1Mo steel and its weld metal. Weld. World 55, 66–74.

Alvaro, A., Thue Jensen, I., Kheradmand, N., Lovvik, O.M., Olden, V., 2015. Hydrogen embrittlement in nickel, visited by first principles modeling, cohesive zone simulation and nanomechanical testing. Int. J. Hydrogen Energy 40, 16892–16900. doi:10.1016/j.ijhydene.2015.06.069

American, A., Standard, N., 2006. Standard methods for determination of the diffusible hydrogen content of martensitic , bainitic , and ferritic steel weld. ANSI/AWS A4.3 93.

Arivazhagan, B., Srinivasan, G., Albert, S.K., Bhaduri, A.K., 2011. A study on influence of heat input variation on microstructure of reduced activation ferritic martensitic steel weld metal produced by GTAW process. Fusion Eng. Des. 86, 192–197. doi:10.1016/j.fusengdes.2010.12.035

Arivazhagan, B., Vasudevan, M., 2014. A comparative study on the effect of GTAW processes on the microstructure and mechanical properties of P91 steel weld joints. J. Manuf. Process. 16, 305–311. doi:10.1016/j.jmapro.2014.01.003

Armaki, H.G., Chen, R., Maruyama, K., Lgarashi, M., 2011. Creep behavior and degradation of subgrain structures pinned by nanoscale precipitates in strength-enhanced 5 to 12 % Cr ferritic steels. Metall. Mater. Trans. A Phys. Metall. Mater. Sci. 42, 3084–3094. doi:10.1007/s11661-011-0726-8

ASTM_A370-17, 2017. Standard test methods and definitions for mechanical testing of steel products. doi:10.1520/A0370-17.2

ASTM: E8/E8M, 2009. Standard test methods for tension testing of metallic materials. doi:10.1520/E0008

Babu, S.H., Amarendra, G., Rajaraman, R., Sundar, C.S., 2013. Microstructural characterization of ferritic / martensitic steels by positron annihilation spectroscopy. Int. Conf. Positron Annihil. J. Phys. 443, 1–6. doi:10.1088/1742-6596/443/1/012010

Baek, J.W., Nam, S.W., Kong, B.O., Ryu, S.H., 2005. The Effect of Delta-Ferrite in P92 Steel on the Formation of Laves Phase and Cavities for the Reduction of Low Cycle Fatigue and Creep-Fatigue Life. Key Eng. Mater. 297–300, 463–470. doi:10.4028/www.scientific.net/kem.297-300.463

Baltusnikas, A., Levinskas, R., Lukošiute, I., 2007. Kinetics of carbide formation during ageing of pearlitic 12X1M phi Steel. Mater. Sci. 13, 286–292.

Barbadikar, D.R., Deshmukh, G.S., Maddi, L., Laha, K., Parameswaran, P., Ballal, A.R., Peshwe, D.R., Paretkar, R.K., Nandagopal, M., Mathew, M.D., 2015. Effect of normalizing and tempering temperatures on microstructure and mechanical properties of P92 steel. Int. J. Press. Vessel. Pip. 132–133, 97–105. doi:10.1016/j.ijpvp.2015.07.001

BIS, 1986. Methods for determination of diffusible hydrogen content of deposited weld metal from covered electrodes in welding mild and low alloy steels.

Biswas, P., Mandal, N.R., Das, S., 2011. Prediction of welding deformations of large stiffened panels using average plastic strain method. Sci. Technol. Weld. Join. 16, 227–231. doi:10.1179/1362171811Y.0000000004

Biswas, Pankaj, Mandal, N.R., Vasu, P., Padasalag, S.B., 2011. A study on port plug distortion caused by narrow gap combined GTAW & SMAW and Electron Beam Welding. Fusion Eng. Des. 86, 99–105. doi:10.1016/j.fusengdes.2010.08.040

Blach, J., Falat, L., Sevc, P., 2009. Fracture characteristics of thermally exposed 9Cr-1Mo steel after tensile and impact testing at room temperature. Eng. Fail. Anal. 16, 1397–1403.

doi:10.1016/j.engfailanal.2008.09.003

Bradley, J., 1981. Use of implant testing to evaluate the susceptibility of HY-130 steel weldments to hydrogen embrittlement.

Bruscato, R., 1970. Temper Embrittlement and Creep Embrittlement of IV\ Cr-1 Mo Shielded Metal-Arc Weld Deposits. Weld. Res. Suppl. 148–156.

Cao, J., Gong, Y., Zhu, K., Yang, Z.G., Luo, X.M., Gu, F.M., 2011. Microstructure and mechanical properties of dissimilar materials joints between T92 martensitic and S304H austenitic steels. Mater. Des. 32, 2763–2770. doi:10.1016/j.matdes.2011.01.008

Cerjak, H., Letofsky, E., 1996. The effect of welding on the properties of advanced 9–12%Cr steels. Sci. Technol. Weld. Join. 1, 36–42. doi:10.1179/136217196790108414

Chalk, K.M., Shipway, P.H., Allen, D.J., 2011. Austenite formation during heat treatment of P92 power plant steel welds: dependence of A1 temperature on compositional changes. Sci. Technol. Weld. Join. 16, 613–618. doi:10.1179/1362171811Y.0000000042

Chhibber, R., Arora, N., Gupta, S.R., Dutta, B.K., 2008. Estimation of Gurson material parameters in bimetallic weldments for the nuclear reactor heat transport piping system. Proc. Inst. Mech. Eng. Part C J. Mech. Eng. Sci. 222, 2331–2349. doi:10.1243/09544062JMES1001

Chhibber, R., Singh, H., Arora, N., Dutta, B.K., 2012. Micromechanical modelling of reactor pressure vessel steel. Mater. Des. 36, 258–274. doi:10.1016/j.matdes.2011.10.027

Choudhary, B.K., Christopher, J., Rao Palaparti, D.P., Isaac Samuel, E., Mathew, M.D., 2013. Influence of temperature and post weld heat treatment on tensile stress-strain and work hardening behaviour of modified 9Cr-1Mo steel. Mater. Des. 52, 58–66. doi:10.1016/j.matdes.2013.05.020

Cipolla, L., Danielsen, H.K., Venditti, D., Emilio, P., Nunzio, D., Hald, J., Somers, M.A.J., 2010. Conversion of MX nitrides to Z -phase in a martensitic 12 % Cr steel. Acta Mater. 58, 669–679. doi:10.1016/j.actamat.2009.09.045

Coussement, C., Dhooge, A., de Witte, M., Dobbelaere, R., van der Donckt, E., 1991. High temperature properties of improved 9% Cr steel weldments. Int. J. Press. Vessel. Pip. 45, 163–178. doi:10.1016/0308-0161(91)90090-O

Cui, H., Sun, F., Chen, K., Zhang, L., Wan, R., Shan, A., Wu, J., 2010. Precipitation behavior of Laves phase in 10%Cr steel X12CrMoWVNbN10-1-1 during short-term creep exposure. Mater. Sci. Eng. A 527, 7505–7509. doi:10.1016/j.msea.2010.08.013

Danielsen, H.K., Emilio, P., Nunzio, D.I., Hald, J., 2013. Kinetics of Z-Phase Precipitation in 9 to 12 pct Cr Steels. Metall. Mater. Trans. A 44, 2445–2452. doi:10.1007/s11661-012-1583-9

Danielsen, H.K., Hald, J., 2009. On the nucleation and dissolution process of Z-phase Cr (V , Nb) N in martensitic 12 % Cr steels. Mater. Sci. Eng. A 505, 169–177. doi:10.1016/j.msea.2008.11.019

Danielsen, H.K., Hald, J., 2007. A thermodynamic model of the Z-phase Cr(V, Nb)N. Calphad 31, 505–514. doi:10.1016/j.calphad.2007.04.001

Danielsen, H.K., Hald, J., Grumsen, F.B., Somers, M., 2006. On the Crystal Structure of Z-Phase Cr (V , Nb) N. Metall. Mater. Trans. A 37, 2633–2640. doi:10.1007/BF02586098

Dayal, R.K., Parvathavarthini, N., 2003. Hydrogen embrittlement in power plant steels. Sadhana 28, 431–451. doi:10.1007/BF02706442

Dickinson, D.W., Ries, G.D., 1977. Implant testing of medium to high strength steel - A model for predicting delayed cracking susceptibility. Weld. Res. Suppl. 205–211.

Dimmler, G., Weinert, P., Kozeschnik, E., Cerjak, H., 2003. Quantification of the Laves phase in advanced 9-12% Cr steels using a standard SEM. Mater. Charact. 51, 341–352. doi:10.1016/j.matchar.2004.02.003

Dix, A.W., Savage, W.F., Dix, W., Arbor, A., 1974. Modified implant test for studying delayed cracking. Weld. Res. Suppl. 554–560.

Dodo, M.R., Ause, T., Adamu, M.A., Ibrahim, Y.M., 2016. Effect of post-weld heat treatment on the microstructure and mechanical properties of arc welded medium carbon steel. Niger. J. Technol. 35, 337–343.

Doremus, R.H., 1985. Rates of Phase Transformations. Acadmic press. doi:10.1557/S0883769400068913

Dudko, V., Belyakov, A., Kaibyshev, R., 2012. Effect of tempering on mechanical properties and microstructure of a 9 % Cr heat resistant steel. Mater. Sci. Forum 706, 841–846. doi:10.4028/www.scientific.net/MSF.706-709.841

Ennis, P.J., Czyrska-Filemonowicz, A., 2003. Recent advances in creep-resistant steels for power plant applications. Sadhana 28, 709–730. doi:10.1007/BF02706455

Ennis, P.J., Lipiec, A.Z., Wachter, O., Filemonowicz, A.C., 1997. Microstructural stability and creep rupture strength of the martensitic steel P92 for advanced power plant. Acta Mater. 45, 4901–4907. doi:10.1016/S1359-6454(97)00176-6

Falat, L., Kepic, J., Ciripova, L., Sevc, P., Dlouhy, I., 2016. The effects of postweld heat treatment and isothermal aging on T92 steel heat-affected zone mechanical properties of T92/TP316H dissimilar weldments. J. Mater. Res. 31, 1532–1543. doi:10.1557/jmr.2016.134

Fedoseeva, A., Dudova, N., Kaibyshev, R., Belyakov, A., 2017. Effect of tungsten on creep behavior of 9%Cr–3%Co martensitic steels. Metals (Basel). 7, 17–19. doi:10.3390/met7120573

Fydrych, D., 2017. An experimental study of high - hydrogen welding processes. Rev. Metal. 51, 1–11.

Fydrych, D., Rogalski, G., 2011. Effect of shielded-electrode wet welding conditions on diffusion hydrogen content in deposited metal. Weld. Int. 25, 166–171. doi:10.1080/09507116.2010.540828

Gedeon, S.A., Eagar, T.W., 1990. Assessing hydrogen-assisted cracking fracture modes in high-strength steel weldments. Weld. J. 213s-220s.

Golpayegani, A., Andr, H., Danielsen, H., Hald, J., 2008. A study on Z-phase nucleation in martensitic chromium steels. Mater. Sci. Eng. A 489, 310–318. doi:10.1016/j.msea.2007.12.022

Gómez, M., Rancel, L., Medina, S.F., 2009. Effects of aluminium and nitrogen on static recrystallisation in V-microalloyed steels. Mater. Sci. Eng. A 506, 165–173. doi:10.1016/j.msea.2008.11.049

Guo, X., Gong, J., Jiang, Y., Rong, D., 2013. The influence of long-term aging on microstructures and static mechanical properties of P92 steel at room temperature. Mater. Sci. Eng. A 564, 199–205. doi:10.1016/j.msea.2012.10.024

Gustafson, Å., Hättestrand, M., 2002. Coarsening of precipitates in an advanced creep resistant 9% chromium steel - quantitative microscopy and simulations. Mater. Sci. Eng. A 333, 279–286. doi:10.1016/S0921-5093(01)01874-3

Hald, J., 2008. Microstructure and long-term creep properties of 9 – 12 % Cr steels. Int. J. Press. Vessel. Pip. 85, 30–37. doi:10.1016/j.ijpvp.2007.06.010

Hald, J., Korcakova, L., 2003. Precipitate Stability in Creep Resistant Ferritic Steels – Experimental Investigations and Modelling. ISIJ Int. 43, 420–427.

Hättestrand, M., Andrén, H.O., 2001. Evaluation of particle size distributions of precipitates in a 9% chromium steel using energy filtered transmission electron microscopy. Micron 32, 789–797. doi:10.1016/S0968-4328(00)00086-X

Helis, L., Toda, Y., Hara, T., Miyazaki, H., Abe, F., 2009. Effect of cobalt on the microstructure of tempered martensitic 9Cr steel for ultra-supercritical power plants. Mater. Sci. Eng. A 510–511, 88–94. doi:10.1016/j.msea.2008.04.131

Hofer, P., Cerjak, H., Bernhard, S., 1999. The Influence of microstructural as pects on the service behaviour of advanced power plant pteels. ISIJ Int. 39, 874–888.

Hosoi, Y., Wade, N., Kunimitsu, S., Urita, T., 1986. Precipitation behavior of laves phase and its effect on toughness of 9Cr-2Mo Ferritic-martensitic steel. J. Nucl. Mater. 141–143, 461–467. doi:10.1016/S0022-3115(86)80083-6

Hu, X., Xiao, N., Luo, X., Li, D., 2010. Transformation behavior of precipitates in a W-alloyed 10 wt pct Cr steel for ultra-supercritical power plants. J. Mater. Sci. Technol. 26, 817–822. doi:10.1016/S1005-0302(10)60130-2

Hurtado-noreña, C., Danón, C.A., Luppo, M.I., Bruzzoni, P., 2015. Evolution of minor phases in a P91 steel normalized and tempered at different temperatures. Procedia Mater. Sci. 8, 1089–1098. doi:10.1016/j.mspro.2015.04.172

I A Shibli, D.G.R., 2006. Review of the use of new high strength steels in conventional and HRSG boilers R&D and plant experience.

Isik, M.I., Kostka, A., Eggeler, G., 2014. On the nucleation of Laves phase particles during high-temperature exposure and creep of tempered martensite ferritic steels. Acta Mater. 81, 230–240. doi:10.1016/j.actamat.2014.08.008

Janaki Ram, G.D., Reddy, A.V., Rao, K.P., Reddy, G.M., 2005. Improvement in stress rupture properties of inconel 718 gas tungsten arc welds using current pulsing. J. Mater. Sci. 40, 1497–1500. doi:10.1007/s10853-005-0590-2

Janaki Ram, G. D., Reddy, A.V., Rao, K.P., Reddy, G.M., 2004. Control of laves phase in inconel 718 GTA welds with current pulsing. Sci. Technol. Weld. Join. 9, 390–398. doi:10.1179/136217104225021788

Janaki Ram, G.D., Venugopal Reddy, A., Prasad Rao, K., Madhusudhan Reddy, G., 2004.

Control of laves phase in Inconel 718 GTA welds with current pulsing. Sci. Technol. Weld. Join. 9, 390–398. doi:10.1179/136217104225021788

Jandová, D., Kasl, J., Rek, a, 2010. Electron microscopy and microanalysis of steel weld joints after long time exposures at high temperatures. IOP Conf. Ser. Mater. Sci. Eng. 7, 012012. doi:10.1088/1757-899X/7/1/012012

Johnson, W.H., 1874. On some remarkable changes produced in iron and steel by the action of hydrogen and acids. Proc. R. Soc. London 23, 168–179.

Jones, W.B., Hills, C.R., Polonis, D.H., 1991. Microstructural Evolution of Modified 9Cr-lMo Steel. Metall. Trans. A 22, 1049–1058.

Kafexhiu, F., Vodopivec, F., Tuma, J.V., 2012. Effect of tempering on the room-temperature mechanical properties of X20CrMoV121 and P91 steels. Mater. Technol. 46, 459–464.

Kalbert, S., Ramasubbu, V., Parvathavarthini, N., Gill, T.P.S., 2003. Influence of alloying on hydrogen-assisted cracking and diffusible hydrogen content in Cr-Mo steel welds. Sadhana 28, 383–393. doi:10.1007/BF02706439

Kamal, S., Jayaganthan, R., Prakash, S., 2010. High temperature cyclic oxidation and hot corrosion behaviours of superalloys at 900°C. Bull. Mater. Sci. 33, 299–306. doi:10.1007/s12034-010-0046-4

Karthikeyan, T., Dash, M.K., Kirana, R., Mythili, R., Selvi, S.P., Moitra, A., Saroja, S., 2017. Effect of prior-austenite grain refinement on microstructure , mechanical properties and thermal embrittlement of 9Cr-1Mo-0 . 1C steel. J. Nucl. Mater. 494, 260–277. doi:10.1016/j.jnucmat.2017.07.019

Karthikeyan, T., Thomas Paul, V., Saroja, S., Moitra, A., Sasikala, G., Vijayalakshmi, M., 2011. Grain refinement to improve impact toughness in 9Cr-1Mo steel through a double austenitization treatment. J. Nucl. Mater. 419, 256–262. doi:10.1016/j.jnucmat.2011.08.010

Kern, T., Staubli, M., Scarlin, B., 2002. The European Efforts in Material Development for 650 ° C USC Power Plants-COST522. ISIJ Int. 42, 1515–1519.

Kim, S.H., Moon, H.K., Kang, T., Lee, C.S., 2003. Dissolution kinetics of delta ferrite in AISI 304 stainless steel produced by strip casting process. Mater. Sci. Eng. A 356, 390–398. doi:10.1016/S0921-5093(03)00152-7

Klueh, R L, 2005. Elevated temperature ferritic and martensitic steels and their application to future nuclear reactors. Int. Mater. Rev. 50, 287–310. doi:10.1179/174328005X41140

Klueh, R. L., 2005. Elevated temperature ferritic and martensitic steels and their application to future nuclear reactors. Int. Mater. Rev. 50, 287–310. doi:10.1179/174328005X41140

Knezevic, V., Sauthoff, G., Vilk, J., Inden, G., Schneider, A., Agamennone, R., Blum, W., 2002. Martensitic/ferritic super heat-resistant 650 °C steels- design and testing of model alloys. ISIJ Int. 42, 1505–1514.

Korcakova, L., Hald, J., Somers, M.A.J., 2001. Quantification of Laves phase particle size in 9CrW steel. Mater. Charact. 47, 111–117. doi:10.1016/S1044-5803(01)00159-0

Kou, S., 2002. Welding Metallurgy, second. ed, A. A Wiley-Interscience publication. doi:10.22486/iwj.v4i3.150243

Kumar, P.G., Yu-ichi, K., 2013. Diffusible Hydrogen In Steel Weldments. Trans. JWRI 42, 39–62.

Kunimitsu, S., You, Y., Kasuya, N., Sasaki, Y., Hosoi, Y., 1991. Effect of thermo-mechanical treatment on toughness of 9Cr-W ferritic-martensitic steels during aging. J. Nucl. Mater. 181, 689–692.

Kuper, M.W., Alexandrov, B.T., 2019. Retention of delta ferrite in the heat-affected zone of Grade 91 steel dissimilar metal welds. Metall. Mater. Trans. A 50, 2732–2747. doi:10.1007/s11661-019-05182-4

Laha, K., Chandravathi, K.S., Parameswaran, P., Rao, K.B.S., Mannan, S.L., 2007. Characterization of microstructures across the heat-affected zone of the modified 9Cr-1Mo weld joint to understand its role in promoting type IV cracking. Metall. Mater. Trans. A 38, 58–68. doi:10.1007/s11661-006-9050-0

Lee, J.S., Armaki, H.G., Maruyama, K., Muraki, T., Asahi, H., 2006. Causes of breakdown of creep strength in 9Cr-1 . 8W-0 . 5Mo-VNb steel. Mater. Sci. Eng. A 428, 270–275. doi:10.1016/j.msea.2006.05.010

Li, X., Cabrillat, M.T., Lejeail, Y., 2006. Study of modified 9Cr-lMo welds.

Liu, C., Liu, Y., Zhang, D., Yan, Z., 2011. Kinetics of isochronal austenization in modified high Cr ferritic heat-resistant steel. Appl. Phys. A Mater. Sci. Process. 105, 949–957. doi:10.1007/s00339-011-6517-7

Liu, J., Yu, H., Zhou, T., Song, C., Zhang, K., 2014. Effect of double quenching and tempering heat treatment on the microstructure and mechanical properties of a novel 5Cr steel processed by electro-slag casting. Mater. Sci. Eng. A 619, 212–220. doi:10.1016/j.msea.2014.09.063

Liu, X.Y., Fujita, T., 1989. Effect of chromium on creep rupture properties of a high chromium ferritic heat resistant steel. ISIJ Int. 29, 680–686.

Louthan, M.R., 2008. Hydrogen embrittlement of metals: A primer for the failure analyst. J. Fail. Anal. Prev. 8, 289–307. doi:10.1007/s11668-008-9133-x

Maddi, L., Deshmukh, G.S., Ballal, A.R., Peshwe, D.R., Paretkar, R.K., Laha, K., Mathew, M.D., 2016. Effect of Laves phase on the creep rupture properties of P92 steel. Mater. Sci. Eng. A 668, 215–223. doi:10.1016/j.msea.2016.05.074

Magudeeswaran, G., Balasubramanian, V., Madhusudhan Reddy, G., 2008. Hydrogen induced cold cracking studies on armour grade high strength, quenched and tempered steel weldments. Int. J. Hydrogen Energy 33, 1897–1908. doi:10.1016/j.ijhydene.2008.01.035

Mahesh, R.A., Jayaganthan, R., Prakash, S., 2008a. Evaluation of hot corrosion behaviour of HVOF sprayed NiCrAl coating on superalloys at 900 °C. Mater. Chem. Phys. 111, 524–533. doi:10.1016/j.matchemphys.2008.05.006

Mahesh, R.A., Jayaganthan, R., Prakash, S., 2008b. A study on hot corrosion behaviour of Ni-5Al coatings on Ni- and Fe-based superalloys in an aggressive environment at 900 °C. J. Alloys Compd. 460, 220–231. doi:10.1016/j.jallcom.2007.05.092

Mandziej, S.T., Výrostková, A., Chovet, C., 2011. Microstructure and creep rupture of P92-grade weld metal. Weld. World 55, 37–51.

Mannan, S.L., Chetal, S.C., Raj, B., Bhoje, S.B., 2003. Selection of materials for prototype fast breeder reactor. Trans. Indian Inst. Met. 1–35.

Maruyama, K, Sawada, K., Koike, J., 2001. Strengthening mechanisms of creep resistant tempered martensitic steel. ISIJ Int. 41, 641–653. doi:10.2355/isijinternational.41.641

Maruyama, Kouichi, Sawada, K., Koike, J., 2001. Strengthening mechanisms of creep resistant tempered martensitic steel. ISIJ Int. 41, 641–653. doi:10.2355/isijinternational.41.641

Masuyama, F., 2001. History of power plants and progress in heat resistant steels. ISIJ Int. 41, 612–625.

Mayr, P., Schlacher, C., Siefert, J.A., Parker, J.D., 2019. Microstructural features, mechanical properties and high temperature failures of ferritic to ferritic dissimilar welds. Int. Mater. Rev. 64, 1–26. doi:10.1080/09506608.2017.1410943

Milovic´, L., Vuherer, T., Vrhovac, M., Stankovic, M., 2013. Microstructures and mechanical properties of creep resistant steel for application at elevated temperatures. Mater. Des. 46, 660–667. doi:10.1016/j.matdes.2012.10.057

Narasimha Rao, B. V., Thomas, G., 1975. Design of Fe/4Cr/0.4C martensitic steels eliminating quench cracking. Mater. Sci. Eng. 20, 195–202. doi:10.1016/0025-5416(75)90149-4

Nisho, Y., Ohmae, T., Yoshida, Y., Miura, Y., 1971. Weld cracking and mechanical properties of 17 % chromium steel weldment. Weld. J. 50, 9-s-18-s.

Onoro, J., 2006. Weld metal microstructure analysis of 9-12% Cr steels. Int. J. Press. Vessel. Pip. 83, 540–545. doi:10.1016/j.ijpvp.2006.03.005

Ozturk, F., Pekel, H., Halkaci, H.S., 2011. The effect of strain-rate sensitivity on formability of AA 5754-O at cold and warm temperatures. J. Mater. Eng. Perform. 20, 77–81. doi:10.1007/s11665-010-9652-y

Padhy, G.K., Ramasubbu, V., Murugesan, N., Remash, C., Albert, S.K., 2012. Effect of preheat and post-heating on diffusible hydrogen content of welds. Sci. Technol. Weld. Join. 17, 408–413. doi:10.1179/1362171812Y.0000000023

Panait, C., Bendick, W., Fuchsmann, A., Besson, J., Panait, C., Bendick, W., Fuchsmann, A., 2010. Study of the microstructure of the Grade 91 steel after more than 100,000 h of creep exposure at 600 °C. Int. J. Press. Vessel. Pip. 0–13. doi:10.1016/j.ijpvp.2010.03.017

Panait, C.G., Bendick, W., Fuchsmann, A., Gourgues-Lorenzon, A.F., Besson, J., 2010a. Study of the microstructure of the Grade 91 steel after more than 100,000 h of creep exposure at 600 °C. Int. J. Press. Vessel. Pip. 87, 326–335. doi:10.1016/j.ijpvp.2010.03.017

Panait, C.G., Bendick, W., Fuchsmann, A., Gourgues-Lorenzon, A.F., Besson, J., 2010b. Study of the microstructure of the Grade 91 steel after more than 100,000 h of creep exposure at 600 °C. Int. J. Press. Vessel. Pip. 87, 326–335. doi:10.1016/j.ijpvp.2010.03.017

Panait, C.G., Zieli´nska-Lipiec, A., Koziel, T., Czyrska-filemonowicz, A., Gourgues-Lorenzon, A.F., Bendick, W., 2010c. Evolution of dislocation density , size of subgrains and MX-type precipitates in a P91 steel during creep and during thermal ageing at 600◦C for more than 100,000h C. Mater. Sci. Eng. A 527, 4062–4069. doi:10.1016/j.msea.2010.03.010

Pandey, C., Giri, A., Mahapatra, M.M., 2016. Effect of normalizing temperature on microstructural stability and mechanical properties of creep strength enhanced ferritic P91 steel. Mater. Sci. Eng. A 657, 173–184. doi:10.1016/j.msea.2016.01.066

Pandey, C., Giri, A., Mahapatra, M.M., Kumar, P., 2017. Characterization of microstructure of HAZs in as-welded and service condition of P91 pipe weldments. Met. Mater. Int. 23, 148–162. doi:10.1007/s12540-017-6394-5

Pandey, C., Mahapatra, M.M., 2016a. Effect of Groove Design and Post-Weld Heat Treatment on Microstructure and Mechanical Properties of P91 Steel Weld. J. Mater. Eng. Perform. 25, 2761–2775. doi:10.1007/s11665-016-2127-z

Pandey, C., Mahapatra, M.M., 2016b. Effect of long-term ageing on the microstructure and mechanical properties of creep strength enhanced ferritic P91 Steel. Trans. Indian Inst. Met. 69, 1657–1673. doi:10.1007/s12666-015-0826-z

Pandey, C., Mahapatra, M.M., 2016c. Effect of heat treatment on microstructure and hot impact toughness of various zones of P91 welded pipes. J. Mater. Eng. Perform. 25, 2195–2210. doi:10.1007/s11665-016-2064-x

Pandey, Chandan, Mahapatra, M.M., Kumar, P., Saini, N., 2018a. Comparative study of autogenous tungsten inert gas welding and tungsten arc welding with filler wire for dissimilar P91 and P92 steel weld joint. Mater. Sci. Eng. A 712, 720–737. doi:10.1016/j.msea.2017.12.039

Pandey, C., Mahapatra, M.M., Kumar, P., Saini, N., 2018. Some studies on P91 steel and their weldments. J. Alloys Compd. 743, 332–364. doi:10.1016/j.jallcom.2018.01.120

Pandey, Chandan, Mahapatra, M.M., Kumar, P., Saini, N., 2018b. Dissimilar joining of CFEF steels using autogenous tungsten-inert gas welding and gas tungsten arc welding and their effect on δ-ferrite evolution and mechanical properties. J. Manuf. Process. 31, 247–259. doi:10.1016/j.jmapro.2017.11.020

Pandey, Chandan, Mahapatra, M.M., Kumar, P., Saini, N., 2018c. Homogenization of P91 weldments using varying normalizing and tempering treatment. Mater. Sci. Eng. A 710, 86–101. doi:10.1016/j.msea.2017.10.086

Pandey, Chandan, Mahapatra, M.M., Kumar, P., Saini, N., 2018d. Comparative study of autogenous tungsten inert gas welding and tungsten arc welding with filler wire for dissimilar P91 and P92 steel weld joint. Mater. Sci. Eng. A 712C, 720–737. doi:10.1016/j.msea.2017.12.039

Pandey, Chandan, Mahapatra, M.M., Kumar, P., Saini, N., Thakre, J.G., 2017a. Nano-size Particle Evolution During Heat Treatment of P91 Steel and Their Effect on Micro

Hardness. Trans. Indian Inst. Met. doi:10.1007/s12666-017-1215-6

Pandey, Chandan, Mahapatra, M.M., Kumar, P., Vidyrathy, R.S., Srivastava, A., 2017b. Microstructure-based assessment of creep rupture behaviour of cast-forged. Mater. Sci. Eng. A 695, 291–301. doi:10.1016/j.msea.2017.04.037

Pandey, Chandan, Saini, N., Mahapatra, M.M., Kumar, P., 2017c. Study of the fracture surface morphology of impact and tensile tested cast and forged (C&F) Grade 91 steel at room temperature for different heat treatment regimes. Eng. Fail. Anal. 71, 131–147. doi:10.1016/j.engfailanal.2016.06.012

Pandey, Chandan, Saini, N., Mahapatra, M.M., Kumar, P., 2016. Hydrogen induced cold cracking of creep resistant ferritic P91 steel for different diffusible hydrogen levels in deposited metal. Int. J. Hydrogen Energy 41, 17695–17712. doi:10.1016/j.ijhydene.2016.07.202

Pandey, P.M., Reddy, N. V., Dhande, S.G., 2003. Real time adaptive slicing for fused deposition modelling. Int. J. Mach. Tools Manuf. 43, 61–71. doi:10.1016/S0890-6955(02)00164-5

Pandey, P.M., Venkata Reddy, N., Dhande, S.G., 2007. Part deposition orientation studies in layered manufacturing. J. Mater. Process. Technol. 185, 125–131. doi:10.1016/j.jmatprotec.2006.03.120

Penalba, F., Gomez-Mitxelena, X., Jimenez, J.A., Carsi, M., Ruano, O.A., 2016. Effect of temperature on mechanical properties of 9%Cr ferritic steel. ISIJ Int. 56, 1662–1667. doi:10.14429/dsj.61.774

Picu, R.C., Vincze, G., Gracio, J.J., Barlat, F., 2006. Effect of solute distribution on the strain rate sensitivity of solid solutions. Scr. Mater. 54, 71–75. doi:10.1016/j.scriptamat.2005.09.002

Qian, L., Guo, P., Zhang, F., Meng, J., Zhang, M., 2013. Abnormal room temperature serrated flow and strain rate dependence of critical strain of a Fe-Mn-C twin-induced plasticity steel. Mater. Sci. Eng. A 561, 266–269. doi:10.1016/j.msea.2012.10.087

Qiao, S., Wei, Y., Xu, H., Cui, H., Lu, F., 2019. The evolution behavior of second phases during long-term creep rupture process for modified 9Cr-1.5Mo-1Co steel welded joint. Mater. Charact. 151, 318–331. doi:10.1016/j.matchar.2019.03.020

Richardot, D., Vaillant, J.C., Arbab, A., Bendick, W., 2000. The T92/P92 Book. Vallourec-

Mannesmann tubes.

Robson, J.D., Upadhyay, P., Reynolds, A.P., 2010. Modelling microstructural evolution during multiple pass friction stir welding. Sci. Technol. Weld. Join. 15, 613–618. doi:10.1179/136217110X12813393169651

Rosenthal, D., 1946. The theory of moving source of heat and its application to metal treatments, Trans. A.S.M.E., 68 (1949) 849-866. Trans. A.S.M.E.

Sakthivel, T., Laha, K., Parameswaran, P., Panneer Selvi, S., Chandravathi, K.S., Mathew, M.D., 2015. Effect of thermal aging on microstructure and mechanical properties of P92 steel. Trans. Indian Inst. Met. 68, 411–421. doi:10.1007/s12666-014-0480-x

Sam, S., Das, C.R., Ramasubbu, V., Albert, S.K., Bhaduri, A.K., Jayakumar, T., Rajendra Kumar, E., 2014. Delta ferrite in the weld metal of reduced activation ferritic martensitic steel. J. Nucl. Mater. 455, 343–348. doi:10.1016/j.jnucmat.2014.07.008

Sawada, K., Kushima, H., Kimura, K., Tabuchi, M., 2007. TTP Diagrams of Z Phase in 9 – 12 % Cr Heat-Resistant Steels 47, 733–739.

Sawada, K., Tabuchi, M., Hongo, H., Watanabe, T., Kimura, K., 2008. Z-Phase formation in welded joints of high chromium ferritic steels after long-term creep. Mater. Charact. 59, 1161–1167. doi:10.1016/j.matchar.2007.09.009

Schafer, L., 1998a. Influence of delta ferrite and dendritic carbides on the impact and tensile properties of a martensitic chromium steel. J. Nucl. Mater. 263, 1336–1339.

Schafer, L., 1998b. Influence of delta ferrite and dendritic carbides on the impact and tensile properties of a martensitic chromium steel 263, 1336–1339.

Schäfer, L., 1998. Influence of delta ferrite and dendritic carbides on the impact and tensile properties of a martensitic chromium steel. J. Nucl. Mater. 258–263, 1336–1339. doi:10.1016/S0022-3115(98)00200-1

Sharma, L., Chhibber, R., 2019. Experimental Investigation of Thermo-Physical Properties of SAW Slag. Silicon. doi:10.1007/s12633-019-00286-3

Shibli, A., Starr, F., 2007. Some aspects of plant and research experience in the use of new high strength martensitic steel P91. Int. J. Press. Vessel. Pip. 84, 114–122. doi:10.1016/j.ijpvp.2006.11.002

Shrestha, T., Alsagabi, S.F., Charit, I., Potirniche, G.P., Glazoff, M. V, 2015. Effect of heat treatment on microstructure and hardness of Grade 91 Steel. Metals (Basel). 5, 131–149.

doi:10.3390/met5010131

Shrestha, T., Basirat, M., Charit, I., Potirniche, G.P., Rink, K.K., Sahaym, U., 2012. Creep deformation mechanisms in modified 9Cr-1Mo steel. J. Nucl. Mater. 423, 110–119. doi:10.1016/j.jnucmat.2012.01.005

Sikka, V.K., Patriarca, P., 1984. Analysis of weldment mechanical proprties of modified 9Cr-1Mo steel.

Silwal, B., Li, L., Deceuster, A., Griffiths, B., 2013. Effect of Postweld Heat Treatment on the Toughness of Heat-Affected Zone for Grade 91 Steel. Weld. J. 92, 80s-87s.

Sket, F., Dzieciol, K., Borbély, A., Kaysser-pyzalla, A.R., Maile, K., Scheck, R., 2010. Microtomographic investigation of damage in E911 steel after long term creep. Mater. Sci. Eng. A 528, 103–111. doi:10.1016/j.msea.2010.07.029

Sklenicka, V., Kucharova, K., Svobodová, M., Kvapilová, M., Král, P., Horváth, L., 2016. Creep properties in similar weld joint of a thick-walled P92 steel pipe. Mater. Charact. 119, 1–12. doi:dx.doi.org/10.1016/j.matchar.2016.06.033

Sourmail, T., 2001. Precipitation in creep resistant austenitic stainless steels. Mater. Sci. Technol. 17, 1–14. doi:10.1179/026708301101508972

Srinivas Prasad, S.P., Rajkumar, R., Hari Kumar, H.K., 2012. Numerical simulation of precipitate evolution in ferriticmartensitic power plant steels. Calphad Comput. Coupling Phase Diagrams Thermochem. 36, 1–7. doi:10.1016/j.calphad.2011.10.006

Sun, N., Jiang, Y., Weng, X., Gong, J., 2017. Microstructural evolution of P92 steel during long-term aging. J. Fail. Anal. Prev. 1–8. doi:10.1007/s11668-017-0312-5

Swada, K., Takeda, M., Maruyama, K., Ishii, R., Yamada, M., Nagae, Y., Komine, R., 1999. Effect of W on recovery of lath structure during creep of high chromium martensitic steels 267, 19–25.

Thomas Paul, V., Saroja, S., Vijayalakshmi, M., 2008. Microstructural stability of modified 9Cr-1Mo steel during long term exposures at elevated temperatures. J. Nucl. Mater. 378, 273–281. doi:10.1016/j.jnucmat.2008.06.033

Tkachev, E., Odnobokova, M., Kipelova, A., Belyakov, A., Kaibyshev, R., 2016. Effect of Tempering on Microstructure and Creep Properties of P911 Steel. Mater. Sci. Forum 879, 1963–1968. doi:10.4028/www.scientific.net/MSF.879.1963

Upadhyay, P., Reynolds, A.P., 2015. Thermal management in friction-stir welding of precipitation-hardened aluminum alloys. Jom 67, 1022–1031. doi:10.1007/s11837-015-1381-0

Vasudevan, R., Stout, R.D., Pense, A.W., 1981. Hydrogen-assisted cracking in HSLA pipeline steels. Weld. J. 60, 155–168.

Vitek, J.M., Vitek, S.A., David, S.A., 1995. Numerical modeling of diffusion-controlled phase transformations in ternary systems and application to the ferrite/austenite transformation in the Fe-Cr-Ni system. Metall. Mater. Trans. A 26, 2007–2025. doi:10.1007/BF02670673

Vodopivec, F., Kmetic, D., Vojvodi-Tuma, J., Skobir, D.A., 2004. Effect of operating temperature on microstructure and creep resistance of X20CrMoV121 steel. Mater. inTechnologije 38, 233–239.

Vyrostkova, A., Homolova, V., Pecha, J., Svoboda, M., 2008. Phase evolution in P92 and E911 weld metals during ageing. Mater. Sci. Eng. A 480, 289–298. doi:10.1016/j.msea.2007.07.036

Wang, J., Lu, S., Li, Y., Hu, Q., Rong, L., Li, D., 2016. Cold cracking sensitivity of a newly developed 9Cr2WVTa steel. J. Mater. Eng. Perform. doi:10.1007/s11665-016-2432-6

Wang, S.S., Peng, D.L., Chang, L., Hui, X.D., 2013. Enhanced mechanical properties induced by refined heat treatment for 9Cr – 0 . 5Mo – 1 . 8W martensitic heat resistant steel. Mater. Des. 50, 174–180. doi:10.1016/j.matdes.2013.01.072

Wang, X., Du, C., Liu, Hong, Liu, Hongwei, 2019. Effect of Laves phase on the toughness of P92 weld metals. Fatigue Fract. Eng. Mater. Struct. 42, 686–697. doi:10.1111/ffe.12943

Wang, X., Xu, Q., Yu, S., Hu, L., Liu, H., Ren, Y., 2015. Laves-phase evolution during aging in 9Cr-1.8W-0.5Mo-VNb steel for USC power plants. Mater. Chem. Phys. 163, 219–228.

Wang, Y., Kannan, R., Li, L., 2018a. Correlation Between Intercritical Heat-Affected Zone and Type IV Creep Damage Zone in Grade 91 Steel. Metall. Mater. Trans. A Phys. Metall. Mater. Sci. 49, 1264–1275. doi:10.1007/s11661-018-4490-x

Wang, Y., Kannan, R., Li, L., 2016a. Characterization of as-welded microstructure of heat-affected zone in modified 9Cr-1Mo-V-Nb steel weldment. Mater. Charact. 118, 225–234. doi:10.1016/j.matchar.2016.05.024

Wang, Y., Kannan, R., Li, L., 2016b. Identification and Characterization of Intercritical Heat-Affected Zone in As-Welded Grade 91 Weldment. Metall. Mater. Trans. A Phys. Metall. Mater. Sci. 47, 5680–5684. doi:10.1007/s11661-016-3736-8

Wang, Y., Kannan, R., Zhang, L., Li, L., 2017. Microstructural analysis of the as-welded heat-affected zone of a grade 91 steel heavy section weldment. Weld. J. 96, 203–219.

Wang, Y., Li, L., 2016. Microstructure evolution of fine-grained heat-affected zone in type IV failure of P91 welds. Weld. J. 95, 27s-36s.

Wang, Y., Li, L., Kannan, R., 2018b. Transition from Type IV to Type I cracking in heat-treated grade 91 steel weldments. Mater. Sci. Eng. A 714, 1–13. doi:10.1016/j.msea.2017.12.088

Wang, Y., Mayer, K., Scholz, A., Berger, C., Chilukuru, H., Durst, K., Blum, W., 2009. Development of new 11 % Cr heat resistant ferritic steels with enhanced creep resistance for steam power plants with operating steam temperatures up to 650 ◦ C 511, 180–184. doi:10.1016/j.msea.2008.04.116

Woodtli, J., Kieselbach, R., 2000. Damage due to hydrogen embrittlement and stress corrosion cracking. Eng. Fail. Anal. 7, 427–450. doi:10.1016/S1350-6307(99)00033-3

Xiong, X., Yang, F., Zou, X., Suo, J., 2012. Effect of twice quenching and tempering on the mechanical properties and microstructures of SCRAM steel for fusion application. J. Nucl. Mater. 430, 114–118. doi:10.1016/j.jnucmat.2012.06.047

Xu, L., Wang, Y., Jing, H., Zhao, L., Han, Y., 2016. Deformation Mechanism and Microstructure Evolution of T92/S30432 Dissimilar Welded Joint During Creep. J. Mater. Eng. Perform. 25, 3960–3971. doi:10.1007/s11665-016-2254-6

Xu, Y., Zhang, X., Tian, Y., Chen, C., Nan, Y., He, H., Wang, M., 2016. Study on the nucleation and growth of M23C6 carbides in a 10% Cr martensite ferritic steel after long-term aging. Mater. Charact. 111, 122–127. doi:10.1016/j.matchar.2015.11.023

Xue, W., Pan, Q. gang, Ren, Y. yao, Shang, W., Zeng, H. qiang, Liu, H., 2012. Microstructure and type IV cracking behavior of HAZ in P92 steel weldment. Mater. Sci. Eng. A 552, 493–501. doi:10.1016/j.msea.2012.05.076

Yadav, S.D., Sonderegger, B., Stracey, M., Poletti, C., 2016. Modelling the creep behaviour of tempered martensitic steel based on a hybrid approach. Mater. Sci. Eng. A 662, 330–341. doi:10.1016/j.msea.2016.03.071

Yaghi, A.H., Tanner, D.W.J., Hyde, T.H., Becker, A.A., Sun, W., 2012. Finite element thermal analysis of the fusion welding of a P92 steel pipe. Mech. Sci. 3, 33–42. doi:10.5194/ms-3-33-2012

Yin, F., Jung, W., Chung, S., 2007. Microstructure and creep rupture characteristics of an ultra-low carbon ferritic / martensitic heat-resistant steel 57, 469–472. doi:10.1016/j.scriptamat.2007.05.034

Yin, Y.F., Faulkner, R.G., Morris, P.F., Clarke, P.D., 2008. Modelling and experimental studies of alternative heat treatments in Steel 92 to optimise long term stress rupture properties. Energy Mater. Mater. Sci. Eng. Energy Syst. 3, 232–242. doi:10.1179/174892409X12596773881522

Yoshino, M., Mishima, Y., Toda, Y., Kushima, H., Sawada, K., Kimura, K., 2005. Phase equilibrium between austenite and MX carbonitride in a 9Cr-1Mo-V-Nb steel. ISIJ Int. 45, 107–115.

Yue, X., 2014. Investigation on heat-affected zone hydrogen-induced cracking of high-strength naval steels using the Granjon implant test. Weld. World 59, 77–89. doi:10.1007/s40194-014-0181-4

Yue, X., Feng, X.L., Lippold, J.C., 2013. Quantifying heat-affected zone hydrogen-induced cracking in high-strength naval steels. Weld. J. 92, 265–273.

Zheng-fei, H., Zhen-guo, Y., 2003. Identification of the precipitates by TEM and EDS in X20CrMoV12.1 after long-term service at elevated temperature. J. Mater. Eng. Perform. 12, 106–111.

Zhu, M.L., Xuan, F.Z., 2010. Effects of temperature on tensile and impact behavior of dissimilar welds of rotor steels. Mater. Des. 31, 3346–3352. doi:10.1016/j.matdes.2010.01.055

Zhu, S., Yang, M., Song, X.L., Tang, S., Xiang, Z.D., 2014. Characterisation of Laves phase precipitation and its correlation to creep rupture strength of ferritic steels. Mater. Charact. 98, 60–65. doi:10.1016/j.matchar.2014.10.004


भारतीय प्रौद्योगिकी संस्थान रुड़की
INDIAN INSTITUTE OF TECHNOLOGY ROORKEE